Cancer Cell Cycle Modulation by Metabolic Gene Expression and Role of Photoreceptor Phosphodiesterase 6H in Cancer Cell Growth



Ceren Yalaz

Jesus College

University of Oxford

Michaelmas Term, 2018

This thesis is submitted to the Department of Oncology, University of Oxford, in partial fulfilment of the requirements for the degree of Doctor of Philosophy.

Abstract

While the deregulation of cancer metabolism through oncogenic signalling, and the effect of the latter on proliferation and cell cycle control are widely studied, little is known on how metabolism in cancer cells leads to cell cycle control and progression. This project aimed to identify metabolic genes whose inhibition causes cell cycle arrest, which would allow further study of candidate genes in the context of cancer metabolism and cell proliferation. The screen was conducted with a custom siRNA library targeting metabolic genes commonly amplified in primary tumours, as well as those known to be involved in the key regulatory points of metabolic pathways.

Results show that TCA cycle, fatty acid metabolism and nucleotide metabolism are especially important during the transition into S phase, whereas enzymes of electron transport chain, glycolysis and pentose phosphate pathway are significant for the completion of both G1 and G2 phases. Among the genes whose knockdown caused G1, cone phosphodiesterase 6H (*PDE6H*) of the retina was selected for further study as a novel controller of cancer cell cycle and metabolism, recognised for a role in controlling retinal metabolism.

Besides causing G1 cell cycle arrest and disruption of G1/S checkpoint mechanism, *PDE6H* knockdown induced apoptosis and mitochondrial dysfunction. PDE6H depletion also inhibited cell proliferation and lowered basal levels of cellular metabolism. In xenograft experiments of *PDE6H* CRISPR/Cas9 knockout HCT116 cells we showed that *PDE6H* deletion slowed down tumour growth and improved animal survival. PDE6 inhibition via a drug, zaprinast, caused similar increase in tumour hypoxia and necrosis as well as an inhibition of tumour cell proliferation. Our results report PDE6H as a controller of cancer cell metabolism and proliferation, making it a potential target for therapy.

Acknowledgements

I would like to thank my supervisors, Prof. Adrian Harris for his endless support and for inspiring a set of standards in research and mentorship that will continue to guide me throughout my career, and Prof. Ruth Muschel for her supervision and showing me the importance of determination. I am grateful for the help and warm guidance I have received from members of Harris and Muschel labs: Christos, Jianzhou, Esther, Su Lim, Remko, Ana, Yunhong, Karim, Pavitra, Serena, and Shaunna. I am also thankful to my other invaluable mentors and teachers who have helped instil in me a passion for research: Dr. Gaby McDonald, Prof. Banu Onaral, Prof. Esra Battaloğlu, Prof. Katherine Weilbaecher, and Prof. Yoram Rudy. I feel very lucky to have learned from you.

I am also thankful the support I have received from Cancer Research UK, Department of Oncology, Clarendon Fund, and Jesus College without whom this work would not be possible.

My sincere gratitude goes to friends who have made Oxford home: Sorana, Janak, Vanessa, Kayla, Mashael, and Zeynep, as well as those who have remained close despite the distance: Katherine, Yasemin, Aycan, Neha, and Sarah. Thank you for your continuous and loving support even through times when I could not leave the lab. I am also thankful to Christina, Irini, Mari-lenna, Mary-Ann, Angela, Apolinario family, and Koon Hwee for brightening up the busier days.

I am especially indebted to my family: my mother for not only initiating an interest in science and life-long learning, but also for teaching me the meaning of hard-work and her command over multiple time-zones; my brother Ali for his incredible support and the happiness he brings me; my aunts and grandmother for their constant encouragement. It is the strength, calm and joy you give me that guides me through everything I aspire to.

This thesis is dedicated to Bedriye Odabaşı.

“Önümüz Bahar'dır, biliyorum. Umut kaçınılmaz gerçektir çünkü.”

List of abbreviations

4EBP	eukaryotic translation initiation factor 4e-binding protein
aa	amino acid
Ant	antimycin
APC	anaphase-promoting complex
ATP	adenosine triphosphate
bp	base pair
BrdU	bromodeoxyuridine
CA9	carbonic anhydrase 9
cAMP	cyclic adenosine monophosphate
Cas9	CRISPR associated protein 9
CDC	cell decision cycle
CDK	cyclin-dependent kinase
cGMP	cyclic guanosine monophosphate
CHK	checkpoint kinase
CMS	core metabolic signature
CMS-R	core metabolic signature-related
CPT	carnitine palmitoyltransferase
CRISPR	Clustered Regularly Interspaced Short Palindromic Repeats.
Ctrl	control
DMSO	dimethyl sulfoxide
DNA	deoxyribonucleic acid
ECAR	extracellular acidification rate
EdU	5-ethynyl-2´-deoxyuridine
EMT	epithelial-mesenchymal transition
ERK	extracellular regulated kinase
ETC	electron transport chain
FACS	fluorescence-activated cell sorting
FASN	fatty acid synthase
FCCP	carbonyl cyanide-4-(trifluoromethoxy)phenylhydrazone
FL	fluorochrome laser
FSC	forward scatter
GAF	cGMP-specific phosphodiesterases, adenylyl cyclases and FhlA
Gln	glutamine
GLS	glutaminase

Glu	glutamate
GLUT	glucose transporter
GMP	guanosine monophosphate
GSH	glutathione
GSK	glycogen synthase kinase
GTP	guanosine triphosphate
HE	haematoxylin & eosin
HIF	hypoxia-inducible factor
HK	hexokinase
IMP	inosine monophosphate
IMS	intermembrane space
KEGG	Kyoto Encyclopedia of Genes and Genomes
ko	knockout
KRAS	Kirsten RAt Sarcoma virus
LDH	lactate dehydrogenase
MCT	monocarboxylate transporter
MDA231	MDA-MB-231
MDA468	MDA-MB-468
MOM	mitochondrial outer membrane
MPT	mitochondrial permeability transition
mRNA	messenger RNA
mTORC	target of rapamycin complex
NADH	nicotinamide adenine dinucleotide
NADPH	nicotinamide adenine dinucleotide phosphate
NT	non-targeting
OAA	oxaloacetate
OCR	oxygen consumption rate
Oli	oligomycin
OXPHOS	oxidative phosphorylation
PAM	protospacer adjacent motif
PBS	phosphate-buffered saline
PD	palbociclib
PDE	phosphodiesterase
PDK	pyruvate dependent kinase
PFKFB3	6-phosphofructo-2- kinase/fructose-2,6-biphosphatase 3
PI	propidium iodide
PIk3	phosphatidylinositol-4,5- bisphosphate 3-kinase
PK	pyruvate kinase
PLK1	polo-like kinase 1
PPP	pentose phosphate pathway
PRPP	phosphoribosyl pyrophosphate
PTEN	phosphatase and tensin homolog

PYCR	pyrroline-5-carboxylate reductase
Rb	retinoblastoma protein
Rheb	Ras homolog enriched in brain
RISC	RNA-induced silencing complex
RNA	ribonucleic acid
ROS	reactive oxygen species
Rot	rotenone
rpm	revolutions per minute
RT	room temperature
RT-qPCR	real time quantitative polymerase chain reaction
SEM	standard error of the mean
sgRNA	single guide RNA
siRNA	small interfering RNA
SOD	superoxide dismutase
SREBP	sterol regulatory element-binding protein
SSC	side scatter
TBS	tris-buffered saline
TCA	tricarboxylic acid
TIGAR	TP53-inducible glycolysis and apoptosis regulator
VEGF	vascular endothelial growth factor
WT	wild-type
Zap	zaprinast
αKG	alpha ketoglutarate

List of figures

Figure 1.1: Summary of cell metabolism. 16
Figure 1.2: Cell cycle progression relies on cyclin-CDK complexes and their stage-specific controllers. 22
Figure 1.3: Summary of cancer cell metabolism and oncogenes involved in signalling and transcription. 30
Figure 2.1: FlowJo allows for quantification of G1, S, and G2/M populations based on DNA content. 43
Figure 2.2: Calculation of percentage of cells with dysfunctional mitochondria. 46
Figure 2.3: Seahorse mitochondrial stress test 50
Figure 2.4: CRISPR/Cas9 system 52
Figure 2.5: Cas9 gene modification leads to deletion of the gene product through various genetic modifications via DSB or NHEJ. 54
Figure 3.1: Cell seeding density and volume of transfection reagent were determined. 80
Figure 3.2: Cell cycle distribution of HCT116 cells with positive control candidate siRNAs was used to determine the duration of screen transfection. 82
Figure 3.3: Cell cycle analysis of HCT116 cells transfected with a) siNT yielded a baseline cell cycle distribution while b) siCCND1 and c) siCDC2 resulted in G1/S and G2/M arrest, respectively. 84
Figure 3.4: a) Z-factors of potential positive controls were calculated b) RT-qPCR data shows that a 72-hour transfection with siRNAs for respective genes 86
Figure 4.1: Top G1/S candidates were listed according to their Z-scores. 90
Figure 4.2: Enrichment analysis results summarise metabolic pathways of G1/S candidates. 91
Figure 4.3: Top G2/M candidates were listed according to their Z-scores. 92
Figure 4.4: Enrichment analysis results summarise metabolic pathways of G2/M. 93
Figure 4.5: Population of dead cells were estimated using ungated population of HCT116 cells. 95
Figure 4.6: Sub-G1 HCT116 cells were calculated following siRNA transfections. 97
Figure 4.7: PYCR knockdown caused G2/M arrest. 105
Figure 4.8: PYCR knockdown altered CDC2 expression. 106
Figure 4.9: Proline metabolism pathway. 108
Figure 4.10: Radiosensitivity was not observed in HC116 following *PYCRL* knockdown. 109
Figure 4.11: *PDE2A* and *PDE6H* knockdowns caused G1/S arrest. 110
Figure 4.12: *CPT1C* and *FASN* knockdowns caused G1/S arrest. 111
Figure 4.13: *CPT1C* and *FASN* knockdowns changed mRNA levels of cyclins. 114
Figure 4.14: CPT1 and FASN contribute to TCA cycle. 115
Figure 4.15: CDK4/6 inhibitor palbociclib caused G1/S arrest in HCT116 and MCF7 cells. 116

Figure 4.16: Palbociclib treatment altered mRNA expression of cyclins and fatty acid metabolism genes CPT1C and FASN. 117
Figure 4.17: Palbociclib treatment decreased cyclin B1 and pRB protein levels. 118
Figure 5.1: Pentose phosphate pathway and guanine pools sustain purine production. 125
Figure 5.2: PDE6 complex structure. 127
Figure 5.3: Visual signal transduction. 128
Figure 5.4: PDE6 family member genes are differentially expressed at the mRNA level in various cancers compared to normal tissue. 137
Figure 5.5: Cancer cell lines (CCLE) data show that the majority of cell lines with PDE6H amplification also have amplification or gain-of-function mutations of KRAS. 139
Figure 5.6: FxCycle and EdU staining was used to determine cell cycle distribution of HCT116 cells following transfection with positive control siRNAs. 140
Figure 5.7: *PDE6A, PDE6D*, and *PDE6H* knockdowns caused G1/S arrest in HCT116 cells. 141
Figure 5.8: *PDE6A, PDE6C, PDE6D, PDE6G* and *PDE6H* knockdowns caused an increase in HCT116 cell death. 142
Figure 5.9: Knockdown of PDE6 isoforms caused an increase in mitochondrial ROS in HCT116 cells. 143
Figure 5.10: siPDE6H transfection caused G1 arrest in HCT116, MDA-MB-23 and MDA-MB-468 cells. 144
Figure 5.11: Knockdown of the cone PDE6 isoforms, *PDE6C* and *PDE6H*, caused an increase in cyclin D1 and a decrease in phospho-RB Ser807/811 protein levels in HCT116 cells. 145
Figure 5.12: *PDE6H* knockdown changed mRNA expression of cell cycle regulators in HCT116. 146
Figure 5.13: PDE6H depletion resulted in lower levels of G1 regulators in HCT116 cells. 146
Figure 5.14: siPDE6H transfection increased cell death in HCT116, MDA-MB-231 and MDA-MB-468 cell populations. 149
Figure 5.15: Knockdown of PDE6 isoforms caused an increase in mitochondrial ROS in HCT116, DLD1, MDA-MB-231, and MDA-MB-468 cells. 150
Figure 5.16: Calculating dysfunctional mitochondria in HCT116 cells based on MitoTracker signals. 151
Figure 5.17: MitoTracker and MitoSOX MFI analyses following siPDE6H transfection. 153
Figure 5.18: *PDE6H* knockdown lowered basal levels of oxidative phosphorylation and glycolysis as well as the maximal respiration capacity in DLD1 cells. 156
Figure 5.19: *PDE6H* knockdown lowered basal levels of oxidative phosphorylation and glycolysis in HCT116 cells. 156
Figure 5.20: *PDE6H* knockdown lowered basal levels of oxidative phosphorylation and glycolysis as well as the maximal respiration capacity in MDA-MB-468 cells. 157
Figure 5.21: *PDE6H* knockdown lowered ECAR levels and maximum OCR capacity in MDA-MB-231. 157
Figure 5.22: *PDE6*H knockdown did not affect basal levels of oxidative phosphorylation or glycolysis in MCF7 cells. 158
Figure 5.23: *PDE6H* knockdown altered mitochondrial function. 159
Figure 5.24: PDE6 inhibition via siPDE6C and siPDE6H as well through zaprinast and administration of cGMP analogue increase cGMP levels in HCT116. 160

Figure 5.25: *PDE6H* knockdown caused mTORC1 and ERK1/2 activation, HIF-1α stabilisation. 161
Figure 5.26: cDNA template and amino acid sequence of PDE6H. 163
Figure 5.27: *PDE6H* CRISPR knockout and knockdown HCT116 cells were depleted of cone PDE6 gamma protein. 166
Figure 5.28: *PDE6H* knockout HCT116 clones had activated mTORC1, VASP and ERK1/2. Data are representative of two independent experiments. 167
Figure 5.29: *PDE6H* knockout clones do not have altered cell cycle profiles. 168
Figure 5.30: *PDE6H* knockout clones had altered basal OXPHOS and glycolysis compared to WT HCT116. 169
Figure 5.31: *PDE6H* knockout clones 6 and 14 had lower levels of oxidative phosphorylation and glycolysis compared to WT HCT116. 170
Figure 5.32: *PDE6H* knockout alters mitochondrial function. 171
Figure 5.33: PDE6H inhibition might affect metabolism through modulation of glucose and glutamine use. 172
Figure 5.34: OCR and ECAR levels of *PDE6H* ko HCT116 clones over a 12-hour Gln depletion. 173
Figure 5.35: Summary of NO/GC/cGMP/PKG pathway. 176
Figure 6.1: Cell viability of HCT116 cells decreased following siPDE6 transfection under both normoxic and hypoxic (1% O_2) conditions. 181
Figure 6.2: PDE6H depletion through a) siPDE6H transfection and b) CRISPR/Cas9 gene deletion resulted in formation of fewer HCT116 colonies. 182
Figure 6.3: PDE6H depletion disrupted spheroid growth in HCT116 183
Figure 6.4: PDE6 inhibitor zaprinast and cGMP analogue induced dysfunctional mitochondria in HCT116. 185
Figure 6.5: 24-hour treatment of HCT116 with Zaprinast (100nM) and 8-Br-cGMP (1 μM) did not change the percentage of live/apoptotic/dead cells. 187
Figure 6.6: Zaprinast and 8-Br-cGMP treatments resulted in G1 arrest in HCT116.. 187
Figure 6.7: *PDE6H* knockout tumours took longer to reach maximum volume than control or zaprinast treatment group, on average. 190
Figure 6.8: HCT116 tumours with PDE6H deletion grew slower compared to WT group. Zaprinast treatment did not affect tumour growth significantly. 191
Figure 6.9: *PDE6H* deletion in HCT116 affected animal survival. 193
Figure 6.10: Survival curve of complied PDE6H ko tumour growth data revealed that animals with PDE6H ko tumours had improved survival. 194
Figure 6.11: PDE6 inhibition and *PDE6H* deletion caused necrosis. 201
Figure 6.12: Immunostaining of tumour sections. 201
Figure 7.1: Working hypothesis on effect of PDE6H depletion on cell cycle progression, metabolism, mitochondrial function, and apoptosis. 213

List of tables

Table 2.1: Gene mutation information of cell lines used. 38
Table 2.2: Sequences of RT-qPCR primers used. 41
Table 2.3: Seahorse mitochondrial stress test drug concentrations. 51
Table 3.1: Core metabolic signature genes from Haider et al study (Haider et al., 2016). 62
Table 4.1: KEGG pathway classification of G1/S candidates reveal glycolysis and gluconeogenesis, amino acid synthesis and pyruvate metabolism as the top pathways. 91
Table 4.2: KEGG pathway classification of G2/M candidates reveal glycolysis, gluconeogenesis, and glucose derivative metabolisms as the top pathways. 93
Table 4.3: A summary of G1/S candidate genes. 100
Table 4.4: A summary of G2/M candidate genes. 102
Table 5.1: PDE6H CRISPR/Cas9 sgRNA primer pair 1 164
Table 5.2: PDE6H CRISPR/Cas9 sgRNA primer pair 2. 165
Table 5.3: Summary of effects of PDE6H knockdown in various cancer cell lines 174

Table of contents

ABSTRACT 2
ACKNOWLEDGEMENTS 3
LIST OF ABBREVIATIONS 4
LIST OF FIGURES 7
LIST OF TABLES 10
TABLE OF CONTENTS 11

1. CHAPTER 1: INTRODUCTION 15

A) Metabolic features of cancer cells 15
1. Glycolysis 15
2. Pyruvate and lactate production 17
3. TCA cycle 18
4. Glutaminolysis 19
5. Pentose phosphate pathway 20
6. Gluconeogenesis 21
7. Tumour microenvironment 21
B) Cell cycle progression and control mechanisms 22
C) Links between cancer cell metabolism and the cell cycle 24
1. Coordination of metabolic programming and cell cycle progression in yeast 24
2. Cell cycle effectors control metabolism 26
3. Cancer metabolism directs the cancer cell cycle 27
D) Oncogenic signalling that control cancer metabolism also affect cell cycle 29
1. MYC, HIF-1, and PI3K/AKT 29
2. ROS control and p53 31
3. KRAS 33
E) Proposed siRNA screen to determine metabolic genes involved HCT116 cell cycle 35
F) Aims of this thesis 37

2. CHAPTER 2: METHODS AND MATERIALS 38

A) Cell culture 38
1. Cell lines 38
B) Culture conditions and cell maintenance 39
C) siRNA reverse transfection 39

D) RNA isolation and reverse transcription polymerase chain reaction (RT-PCR) 40
E) Flow cytometry 42
1. High-throughput propidium iodide (PI) staining for cell cycle siRNA screen . 42
2. Click-iT EdU and FxCycle staining for cell cycle distribution 43
3. PI and Annexin V apoptosis assay 44
4. Mitochondria dyes 45
F) CyQuant viability measurement 46
G) Protein immunoblotting 47
H) cGMP ELISA 49
I) Seahorse metabolic assay 49
J) CRISPR/Cas9 nickase stable knockout cell line generation 52
1. Introduction to CRISPR Cas9 nickase 52
2. Generation of CRISPR/Cas9 PDE6H ko HCT116 54
K) Spheroid generation 55
L) Clonogenic survival assays 56
M) Statistical analysis 56
N) Xenograft mouse models 57
O) Immunohistochemistry 57

3. CHAPTER 3: DESIGN OF A METABOLIC SIRNA SCREEN WITH HCT116 CELL CYCLE ENDPOINT 59

A) Abstract 59
B) Introduction 60
C) Selection of the siRNA library and cell cycle assay 60
1. Rationale for siRNA screen and propidium iodide staining to process the endpoint 60
2. Compilation of core metabolic signature genes 62
3. Compilation of controllers of cellular metabolism 64
4. List of custom siRNA library genes 64
D) Setting up screen conditions and controls 79
E) Method of screen analysis 85
F) Discussion 87

4. CHAPTER 4: siRNA SCREEN IDENTIFIED THE METABOLIC DETERMINANTS OF CANCER CELL CYCLE 88

A) Abstract 88
B) Introduction 89
C) Results of the screen identified G1/S and G2/M arrest inducing siRNAs 90
1. G1/S candidates according to their Z-score 90
2. KEGG classification of G1/S candidates 91
3. G2/M candidates according to their Z-score 92
4. KEGG classification of G2/M candidates 93
5. Calculation of sub-G1 populations of transfected HCT116 94
D) Summary of results 98
E) Screen results for the candidates PYCR and PDE genes were validated 103

1. *PYCR2* and *PYCRL* knockdowns caused G2/M arrest 103
2. *PDE2A* and *PDE6H* knockdowns caused G1/S arrest 109
F) Screen results for candidates of fatty acid metabolism, CPT1C and FASN genes showed they altered G1/S progression 111
G) Discussion 119

5. CHAPTER 5: PDE6H CONTROLS G1 PROGRESSION AND CELL METABOLISM 122

A) Abstract 122
B) Introduction 123
C) PDE6 is at the crossroads of cancer metabolism and retinal physiology 123
1. Purine synthesis is a link between cell cycle progression and metabolism . 123
2. Retinal protein PDE6 takes part in purine metabolism 127
3. Parallels between retinal and cancer metabolism 130
D) PDE6 might play a role in tissue protection from exposure to hypoxia and reactive oxygen species 131
E) PDE6 isoforms are differentially expressed in cancer 133
F) Knockdown of PDE6 genes caused cell cycle arrest, cell death and accumulation of mitochondrial ROS in HCT116 139
G) *PDE6H* knockdown caused arrest at the G1/S checkpoint in colorectal and breast cancer cell lines 144
H) *PDE6H* knockdown induced cell death and dysfunctional mitochondria 147
I) siPDE6H transfection altered oxidative phosphorylation and glycolysis profiles of various cancer cell lines 155
J) PDE6H depletion altered cell signalling pathways 160
1. PDE6H inhibition increased cGMP levels in HCT116 160
2. *PDE6H* knockdown affected MAPK and mTOR signalling 161
K) sgRNA templates were designed for CRISPR/Cas9 double nickase gene editing. 162
1. Rationale for the selection of sgRNA-targeting site 162
2. Design of sgRNA primer pairs 164
3. Verification of *PDE6H* knockout in selected clones 165
L) *PDE6H* knockout clones had altered basal OXPHOS and glycolysis compared to WT HCT116 168
M) Discussion 174

6. CHAPTER 6: EFFECTS OF PDE6H DELETION ON GROWTH IN HCT116 XENOGRAFT TUMOURS 178

A) Abstract 178
B) Introduction 179
C) PDE6 depletion has antiproliferative effects on HCT116 179
D) *In vivo* experiment design 184
1. Zaprinast was selected as the PDE6 inhibitor 184
2. Tumour growth conditions 188
E) *PDE6H* deletion slowed HCT116 tumour growth 188
F) Discussion 201
3. *In vitro* work 202

4. In vivo work 202

7. CHAPTER 7: DISCUSSION 205

A) Future work 205
1. Senescence 205
2. Metabolomics 206
3. Downstream targets 207
4. Xenografts 211
5. Antibodies 212
B) Summarising PDE6H's control over cell cycle and metabolism 213

8. Bibliography 217

CHAPTER 1: INTRODUCTION

A)Metabolic features of cancer cells

Cancer metabolism is driven by the need to meet energetic and nutrient demands of high rates of proliferation and to provide a favourable microenvironment for tumour growth. Oncogenic signalling pathways that affect cancer metabolism also regulate cell cycle. Despite the known links between the cell cycle and metabolism, the metabolic control of cell cycle remains understudied.

A hallmark of cancer, “reprogramming of energy metabolism” (Hanahan and Weinberg, 2011) involves the rewiring of cancer cell metabolism which continues to develop as new pathways of biosynthesis and redox control are found to contribute to cancer growth. A summary of what are considered core pathways is described below (Figure 1.1).

1. Glycolysis

The initial interest in the cancer metabolism revolved around glycolysis. The first observation of the distinctive metabolism of cancer cells dates back to 1926 when Otto Warburg observed that tumour cells produce most of their energy through glycolysis, even under normoxic conditions (Gogvadze et al., 2008), an observation that is today referred to as “aerobic glycolysis”. Highly glycolytic tumour cells are thought to be those that are the most rapidly dividing.

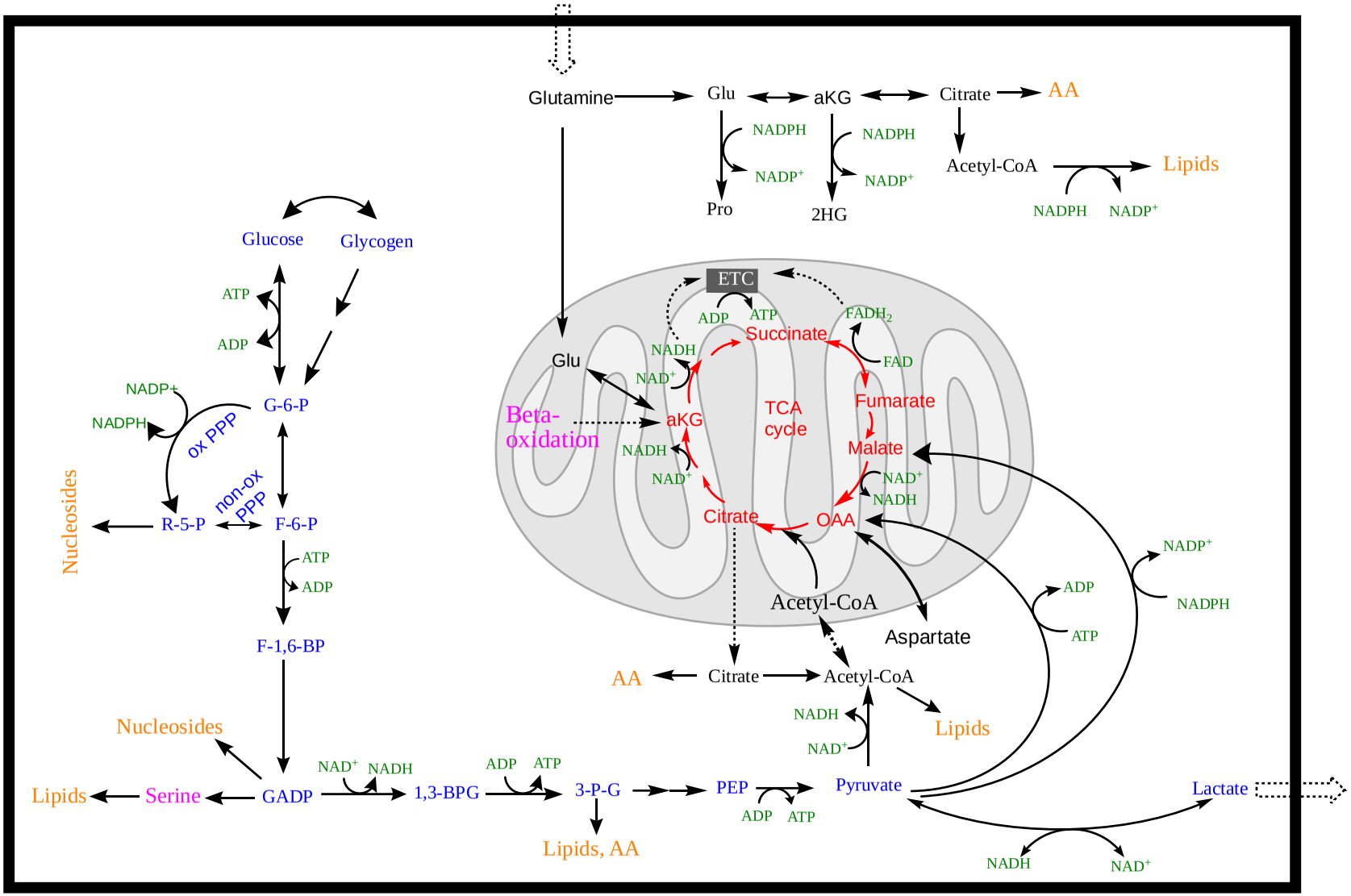


Figure 1.1: Summary of cell metabolism.
Main pathways of metabolism that are important for proliferation are glycolysis and glycogen catabolism, tricarboxylic acid (TCA) cycle, and glutaminolysis. Cell metabolism meets the needs of bioenergetics, biosynthesis, and redox balance. The following colours were used to show different components of metabolism; blue: sugar metabolism, green: cofactors, red; TCA cycle, orange: biosynthesis. Dashed arrows represent transport. ETC: Electron transport chain, αKG: alpha-ketoglutarate, F-6-P: fructose-6-phosphate, G-6-P: glucose-6-phosphate, GADP, glyceraldehyde-3-phosphate, Glu: glutamate, 2HG: 2-hydroxyglutarate, OAA: oxaloacetate, 3-PG: 3-phosphoglycerate, 1,3-BPG: 1,3-biphosphoglycerate, 1,3 PEP: phosphoenolpyruvic acid, R-5-P: ribose 5-phosphate.

Glycolysis rapidly produces ATP (Pfeiffer et al., 2001) (Shestov et al., 2014) and provides a carbon source for nucleotide synthesis through pentose phosphate pathway (PPP). It maintains redox homeostasis (Boros et al., 2000) (Wang et al., 2017), which depends on a balance between the ROS (reactive oxygen species) exposure and antioxidant defences of a cell (Acharya et al., 2010). Glycolysis is essential for cancer cell survival (Ros et al., 2012) (Figure 1.1).

The high level of glucose uptake in cancer cells allows them to proliferate rapidly and thrive even under unstable oxygen conditions, through aerobic glycolysis (Hamanaka and Chandel, 2012). Glycolysis produces lactic and bicarbonic acids, making the tumour microenvironment acidic. Tumours have a growth advantage from this feature, which helps to suppress the immune responses (Kroemer and Pouyssegur, 2008). Additionally, cancer cells can handle the acidic microenvironment by help from cancer associated fibroblasts that help alleviate the acidic burden through transcellular flow of H^+ (Hulikova et al., 2016) or through extracellular pH regulation via CA9 (carbonic anhydrase 9) activity (McIntyre et al., 2012).

Aerobic glycolysis of cancer cells is sustained with the aid of overexpression of certain glucose metabolism enzyme and transporters in cancer cells. GLUT1 and GLUT3, the high affinity glucose transporters, are overexpressed in cancer cells (Younes et al., 1997) and allow high uptake of glucose. Also overexpressed are the glycolysis enzymes PFKFB3 (6-phosphofructo-2-kinase/fructose-2,6-biphosphatase 3) and HK2 (hexokinase 2), which along with the M2 isoform of pyruvate kinase regulate the glycolytic flux (Gogvadze et al., 2008). mRNA levels of the glycolysis enzymes HK1 (hexokinase 1), LDHA (lactate dehydrogenase A), PKM2 (pyruvate kinase M2) and glucose transporter GLUT1 in primary tumours and liver metastases are significantly higher than in normal mucosa of colorectal cancer patients (Graziano et al., 2016).

2. Pyruvate and lactate production

Pyruvate is at a branch point between glycolysis and the Krebs cycle. It gets

transported to the mitochondria by mitochondrial pyruvate carriers (MPCs) and is broken down to acetyl CoA. High lactate levels in cancer cells are promoted by the prevalence of pyruvate kinase PKM2 (Christofk et al., 2008a). PKM2 gets inactivated by tyrosine kinase signalling in cancer cells (Christofk et al., 2008b). PKM1 function is also important for survival of nonproliferating tumour cells (Israelsen et al., 2013). PKM2, unlike PKM1 which only has a fully active form, can switch to a low-active form (Mazurek 2011). Switching to a low activity isoform of PKM slows down pyruvate production, allowing utilisation of glycolysis intermediates in biosynthesis of amino acids, lipids and nucleotides (Hsu & Hung, 2018). PKM2 inhibition hinders B16 tumour growth through its suppression of aerobic glycolysis (Zhao, 2018).

Lactate produced by glycolysis is circulated within/between tissues rapidly and enters TCA cycle by conversion to pyruvate by LDH (Hui et al., 2017). An isoform of lactate dehydrogenase (LDHA), is overexpressed in cancer cells (Gogvadze et al., 2008). This isoform helps direct pyruvate to lactate production rather than enter mitochondria to partake in the TCA cycle. In addition to the reduction of direct entry of pyruvate into TCA cycle via LDHA activity, TCA cycle is impeded by decreased Acetyl-CoA production, due to the inhibition of pyruvate dehydrogenase (PDH) complex via PDK1 activation in hypoxia (Diaz-Ruiz et al., 2011) (Kim et al., 2006). These modifications in cancer cells allow for the utilisation of pyruvate and TCA cycle intermediates outside of the TCA cycle, such as acetyl-CoA and citrate, which is transported out the mitochondrial matrix to be used in biosynthesis reactions (Diaz-Ruiz et al., 2011).

3. TCA cycle

Cancer cells upregulate biosynthesis without dismissing oxidative phosphorylation completely. The TCA cycle intermediate citrate is exported from the mitochondria to take part in fatty acid synthesis (Jones and Thompson, 2009). Fatty acid oxidation is also necessary in endothelial cells for nucleotide production and *CPT1A*

knockdown results in depletion of pyridines and purines required for DNA replication (Schoors et al., 2015).

Glycolysis alone cannot support tumour growth in absence of OXPHOS (Fogal et al., 2010) (Wheaton et al., 2014) which is necessary for production of energy as well as synthesis of lipids, amino acids, and nucleotides. A balance between mitochondrial function and redox status is needed for sustainable cancer cell proliferation. Redox balance is maintained via an upregulation of PGC1a that induce mitochondrial biogenesis and elevated OXPHOS in melanoma (Tan et al., 2016) (Vazquez et al., 2013), increase of superoxide dismutase protein expression in ovarian cancer (Hu et al., 2005) or activation of NRF2 signalling to promote glutathione production (DeNicola et al., 2011).

Electron transport chain (ETC) consists of a series of enzymes and coenzymes on the mitochondrial inner membrane, that facilitate the transport of electrons, reducing O_2, FADH2, and NADH, creating a proton gradient the energy of which is harnessed for ATP production (Bender, 2003). ETC plays an important role in biosynthesis through aspartate production (Birsoy et al., 2015). Gain of function mutation of isocitrate dehydrogenase 1 (IDH1) (Dang et al., 2009) and inactivation of fumarate hydratase (FH) (Sciacovelli et al., 2016) lead to aberrant epigenetic modifications that lead to EMT in glioma and renal cancer, respectively. Hypoxic tumours, where ETC is impeded, rely on extracellular aspartate for survival via SLC1A3 transport (Garcia-Bermudez et al., 2018). Limitation of ETC increases mitochondrial capacity and limits superoxide radical production, contributing to survival (Porporato et al., 2017).

4. Glutaminolysis

Glutamine is also important for biosynthesis, besides supplementing TCA cycle through glutaminolysis (DeBerardinis et al., 2007) (Hosios et al., 2016). As the most abundant amino acid in plasma and muscle, it is used in biosynthesis of nucleotides and nonessential amino acids; it also provides NADPH necessary for lipid synthesis and

antioxidant mechanisms (Vander Heiden and DeBerardinis, 2017). In rapidly proliferating cells, glutamine transporters are highly expressed through Myc activity and can be used as chemotherapeutic targets (Bhutia et al., 2015). A coordination between glucose and glutamine consumption across cancer cell lines has been suggested to be regulated by the mitochondrial enzyme SIRT4 which inhibits PDH and activates glutamate dehydrogenase, lowering levels of glutaminolysis under low glucose conditions (Wang et al., 2018). This suggests that balancing of metabolic activities and preventing the accumulation of intermediate substrates, such as pyruvate and lactate, is necessary for pH homeostasis (Wang et al., 2015a).

Under hypoxia, glycolysis is upregulated and pyruvate is converted into lactate instead of being used in mitochondria (Semenza, 2009). Under hypoxia, glycolytic enzyme phosphoglycerate kinase (PGK1) is translocated into mitochondria, activating PDHK1 which leads to inhibition of PDH complex, supressing TCA cycle and OXPHOS (Li et al., 2016). Expression of beta-F1-ATPase is reduced (Isidoro et al., 2004) as well as the activities of ETC complexes I, III and IV due to mtDNA mutations in tumours (Ishikawa et al., 2008). An integrated control of increased glycolysis and reduced OXPHOS helps sustained growth under hypoxia.

5. Pentose phosphate pathway

Cancer cells require a high synthesis rate of macromolecules to sustain a high level of proliferation. Besides glycolysis, glucose also supplies PPP substrates. PPP yields ribose-5-phosphate, which is a key intermediate in nucleotide synthesis. PPP produces NADPH as a metabolic substrate in fatty acid synthesis and as an antioxidant against the damages caused by chemotherapeutic agents (Jiang et al., 2014).

The transcription factor NRF2 enhances PPP through activation of G6PD (glucose-6-phosphate dehydrogenase) and de novo nucleotide synthesis genes (Mitsuishi et al., 2012). Besides inducing NADPH production through PPP, NRF2 signalling also mitigates the antiproliferative effect of oxidative PPP gene knockout by

increasing GSH levels through glutamine anaplerosis and cystine uptake (Harvey et al., 2009) (Muir et al., 2017). P53 inducible TIGAR results in an increase of pentose phosphate pathway activity by directing glucose away from glycolysis (Bensaad et al., 2006). Glucose also contributes to TCA cycle anaplerosis (Davidson et al., 2016).

6. Gluconeogenesis

Gluconeogenesis directs TCA cycle intermediates back to glycolysis. Cytosolic PEPCK1 (phosphoenolpyruvate carboxykinase 1), which converts OAA to PEP, promotes cancer cell proliferation by supporting anabolism even when the cell has limited supplies of glucose and/or glutamine (Montal et al., 2015). PEPCK1 is also overexpressed in colon cancer. PEP is converted to serine and purine biosynthesis precursors via mitochondrial PEPCK2, which is overexpressed in NSCLC (Vincent et al., 2015).

7. Tumour microenvironment

The effect of the inhibition of a metabolic gene may not reveal itself *in vitro* yet may be effective against tumour growth in vivo, as shifts in cancer cell metabolism has implications in tumour microenvironment. Cancer associated fibroblasts secrete lactate making the microenvironment more acidic, enhancing the epithelial-mesenchymal transition of neighbouring cancer cells, and impeding with drug action (Fiori et al., 2019). They also supply cancer cells with nutrients such as glutamine, lactate, and ketone bodies (Chiarugi and Cirri, 2016). Glucose depleted cancer cells can be sustained by upregulation of oxidative phosphorylation, due to increased MCT1 expression and lactate uptake induced by macrophages (De Saedeleer et al., 2014). As the tumour microenvironment gets hypoxic, HIF-1α functions as a survival factor and EMT promoter (Denko, 2008). Upregulation of tumour glycolysis produces lactic acid which impedes with activity of tumour reactive T-cells in melanoma and lung cancer (Cascone et al., 2018). Immunological checkpoint controller PD-L1 promotes expression of glycolytic

enzymes in cancer cells through PI3K/mTOR signalling (Joyal et al., 2016) whereas PD-1 activity compromises glycolysis and facilitates fatty acid oxidation in T-cells by inhibiting PI3K/AKT (Patsoukis et al., 2013).

B) Cell cycle progression and control mechanisms

Proliferation of eukaryotic cells includes progression through four phases of the cell cycle: gap 1 (G1), DNA synthesis (S), gap 2 (G2) and mitosis (M) (Figure 1.2). Mammalian cells advance through G1 phase and start DNA synthesis (S phase) under the control of cyclin-dependent kinases (CDKs) and their associated cyclins (Figure 1.2), which are directed by growth factor signalling and the availability of nutrients (Lapenna and Giordano, 2009). The major transitions in the cell cycle, controlled by CDK/cyclin complexes, are the entry from G0, quiescent phase, initiation of DNA synthesis (S

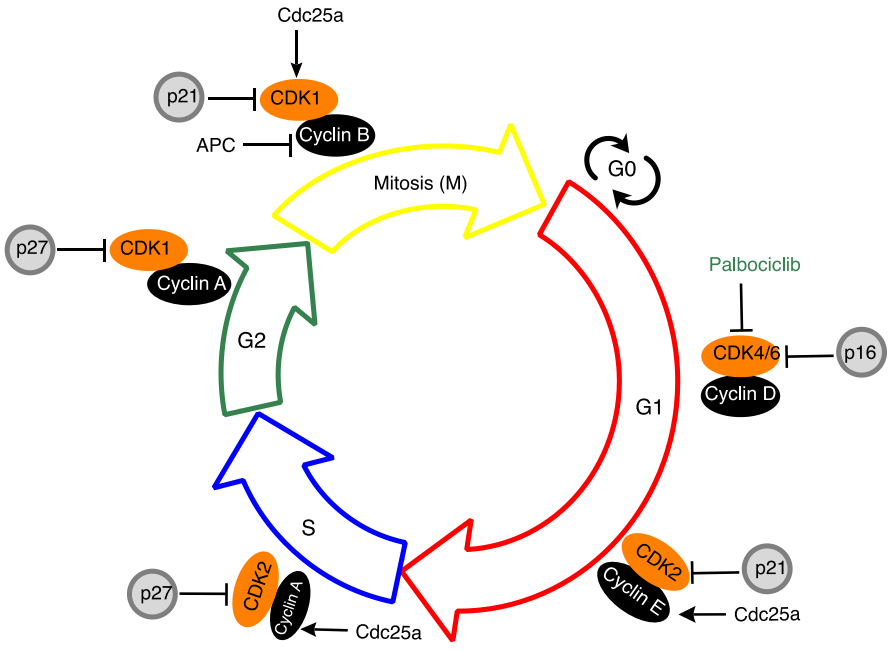


Figure 1.2: Cell cycle progression relies on cyclin-CDK complexes and their stage-specific controllers.
P16, p21, and p27 are cell cycle inhibitors that prevent the formation of their corresponding Cyclin-CDK complexes. Palbociclib is a drug that inhibits CDK4/6 (Jingwen et al., 2017).

phase), the passage from G2 into mitosis, and the process of cellular division (Nigg, 1995). Normal cells are unable to pass through the G1 or G2 checkpoints in the presence of DNA damage. The G1-S phase transition is controlled by phosphorylation of the retinoblastoma protein, Rb, by CDK4/CDK6, in complex with the D-type cyclins: D1, D2, or D3. In early G1, the CDK inhibitor, p16 prevents the interactions between CDK4/6 and the D-type cyclins. In late G1, cyclin D levels rise and outcompete p16 to bind to CDK4/6, allowing activation of CDK4/6.

When CDK4/6-cyclin D complexes hyperphosphorylate Rb, the repression of gene transcription through E2F is relieved, and the cell passes through the G1-S checkpoint. The catalytic activity of CDK4/CDK6 thus controls a cell's commitment to DNA replication. Hyperphosphorylation of Rb results in the upregulation of the genes controlled by E2F transcription factors. Rb phosphorylation is sustained by further cyclin A/B and CDK1/2 activity, and this hyperphosphorylated state ensures cell cycle progression. This results in the synthesis of genes necessary for DNA replication (Fry and Vassilev, 2005).

CDK1 is necessary for the progression through late G2 and M phases, as it prevents premature cytokinesis by ensuring chromatin condensation (Swain et al., 2007). It is primarily regulated by cyclin B, which increases in abundance during S and G2 phases, and peaks in late G2 (Vassilev et al., 2006). It is also regulated by WEE1, which inhibits CDK1 by phosphorylation at the tyrosine 15 residue. The CDC25 phosphatase overcomes the WEE1 inhibition by dephosphorylating CDK1 in order to promote progression into mitosis. Furthermore, cells arrest at the G2/M checkpoint in the presence of DNA damage via inhibition of CDC25 by CHK1 and CHK2, or via p53-mediated transcriptional activation of CDK1 inhibitors such as p21. CDK1 helps chromatin to achieve maximum condensation and controls the sequence of mitotic events. CDK1 activity is halted after the proteolysis of cyclin B by the anaphase-promoting complex (APC), which marks the beginning of mitosis (Lapenna and Giordano, 2009). CDK1 is an essential cell cycle driver, whereas the cell cycle can

progress without CDK2 and CDK4 (Santamaría et al., 2007).

Overexpression of CDKs or cyclins, or mutations in CDK genes lead to deregulation of the cell cycle, which may promote oncogenesis (Collins and Garrett, 2005). Cancer cells often do not have the functional cell cycle checkpoints found in normal cells. Bypassing the G1 to S restriction point allows cancer cells to replicate even in the absence of mitotic stimuli. However, for DNA repair and survival, tumour cells depend on the checkpoint arrest in the S or G2 phases (Lapenna and Giordano, 2009).

Key components of the checkpoints during G1 and G2 phases are CHK1 and CHK2. They act on CDK activity by inhibiting members of the CDC25 family of phosphatases that activate CDKs. Loss of CHK1 activity renders p53-deficient cells prone to the accumulation of DNA damage. Inhibition of CHK2 protects healthy cells from DNA damage and also leaves tumour cells sensitive to genotoxic agents (Collins and Garrett, 2005).

C) Links between cancer cell metabolism and the cell cycle

1. Coordination of metabolic programming and cell cycle progression in yeast

A better understanding of the metabolic control of cell cycle has the potential to elucidate cell growth, proliferation and tumorigenesis and find new therapy targets. The mechanisms by which cell growth and division are coordinated by metabolism are widely studied in unicellular organisms, in which the decision to enter the cell cycle mostly relies on the nutritional and metabolic status of the cell. Yeast metabolic cycle consist of the oxidative/respiratory (O/R), reductive/building (R/B), and reductive/charging (R/C) phases during which oxygen levels increase, decrease, and stay constant, respectively (Cai and Tu, 2012). Oxidative phase is dominated by oxidative phosphorylation that

produces ATP. R/B is when cell division happens and is dominated by mitochondrial biogenesis and glycolysis; OXPHOS is low during this phase, preventing oxidative damage to newly synthesised DNA. During R/C, acetyl-CoA accumulates through amino acid degradation and fatty acid oxidation, and is used up during the oxidative phase (Tu and McKnight, 2007).

Metabolite levels also oscillate during cell cycle, adding to its cyclic nature. Acetyl-CoA and NADPH levels are periodic during the yeast metabolic cycle. They both increase at the end of R/C and into the oxidative phase, which is the period during which transcription of genes encoding enzymes that function in PPP, fatty acid oxidation, glycolysis and breakdown of storage carbohydrates proteins are upregulated. Most metabolites, except for amino acids, also reach their maximum levels during the reductive/charging phase (Spellman et al., 1998).

In addition to the availability of nutrients, transcription of metabolic genes also plays a role in yeast cell cycle control. An investigation of periodic mRNA fluctuations across cell cycle stages revealed that nuclear encoded mitochondrial genes required for oxidative phosphorylation and glycolysis peaked only during G1 (Chumakov et al., 2006). Expression of genes encoding acid phosphatases and transport membranes for amino acids, ammonia, sugars and iron, also peak during M/G1 (Spellman et al., 1998).

Cells exit the quiescent cycle when sufficient nutrients are provided. Without interjection from other factors, the cell will complete a cycle and divide. In the case of depletion of an essential nutrient, the cell cycle will complete but will not restart, entering G0 phase instead. Yeast exits cell division cycle during carbon starvation, entering a more stable phase, G0 (Gray et al., 2004) (Yeung et al., 2008).

Lipid synthesis is crucial for both cell cycle progression and growth due to the contribution of lipids as building blocks of cell membrane, energy metabolism intermediates, and redox balance controllers. Lipid availability varies at different stages of the cell cycle: plasma membrane’s fluidity is highest during S phase, with increases in PC (phosphatidylcholine), DAG (diacylglycerol) and PI (phosphatidylinositol) fractions

(Furse and Shearman, 2018).

2. Cell cycle effectors control metabolism

Polo-like kinase 1 (PLK1), which is involved in mitosis, also regulates glycolysis and pentose phosphate pathway. PLK1 mediated activation of G6PD is important for cell cycle progression (Ma et al., 2017).

Cell cycle effector complex cyclin D3-CDK6 results in CDK6 activation, which phosphorylates and inhibits glycolysis enzymes PFK1 and PKM2. This inhibition directs intermediates of glycolysis into serine synthesis and pentose phosphate pathways resulting in increased de novo synthesis of nucleotides. By inhibiting catalytic activity of key glycolysis enzymes, CDK6 leads to increased levels of anti-ROS molecules NADPH and reduced glutathione. Inhibition of CDK4 and CDK6, however, does not alter NADPH or reduced glutathione levels, causing only a slight elevation in ROS levels (Wang et al., 2017).

The drug palbociclib (PD-0332991) inhibits CDK4/cyclin D1 kinase activity by selectively targeting CDK4/6. Recent reports show that this drug, in combination with fulvestrant, an estrogen receptor antagonist, improved survival among patients with HR+ HER2- breast cancer (Turner et al., 2018). G1 cell cycle arrest was observed along with antiproliferative effects of CDK4 inhibition in HCT116 and NCI-H460 tumour cell lines. Application of this single agent causes fast and reversible inhibition of the Ser780 and Ser795 sites of RB by CDK4 and CDK6. This response coincides with the elimination of RB phosphorylation at Ser780 and the downregulation of the gene products of the E2F transcription factor (Collins and Garrett, 2005). Furthermore, palbociclib leads to decreased primary tumour growth and recurrence in mouse models of patient-derived pancreatic ductal adenocarcinoma (Chou et al., 2018). Interestingly, palbociclib has a dual effect on the cell cycle and metabolism. It causes mitochondria accumulation, elevates glycolysis and OXPHOS levels, and increases ATP production in an Rb-dependent manner; these metabolic effects are reversed by the inhibition of

mTORC1 following palbociclib administration (Franco et al., 2016).

3. Cancer metabolism directs the cancer cell cycle

Metabolic status is an important factor for initiation of proliferation or exit into a quiescent phase (Duan and Pagano, 2011). The nutrient dependent nature of the G1 checkpoint is well described in both normal and abnormally proliferating cells. However, the metabolic statuses of different stages of the cell cycle in cancer cells are poorly studied. Therefore, it is important to investigate the relation of metabolic regulators to proteins governing cell cycle progression.

One example of a known link between metabolism and cell cycle regulation in cancer is the regulation of the G1/S checkpoint by 6-phophofructo-2-kinase/fructose-2,6-biphophatase isoform 3 (PFKFB3) and glutaminase 1 (GLS1) in HeLa cells (Colombo et al., 2010). Levels of the PFKFB3 enzyme, which promote glycolysis through increased levels fructose 2,6-bisphosphate, increase during cell division. This is observed during mid-to-late G1 in the cell cycle, and the inhibition of the enzyme prevents progression into S phase. PFKFB3 may be responsible for the upregulation of glycolysis in G1 in HeLa (Tudzarova et al., 2011). The regulation of this enzyme by the ubiquitin ligase APC/C-CDH1 highlights the coordination between cell metabolism and the cell cycle progression (Almeida et al., 2010). The ubiquitin ligase activity of APC/C-CDH1 maintains normal cells in G1, and its inactivation in mid or late G1 is necessary for transition into S phase.

In HeLa cells, the inhibition of PFKFB3 prevents cells from going into S phase. Additionally, levels of GLS1, which is degraded by APC/C-CDH1, increase along with those of PFKFB3 in HeLa cells, indicating that glutaminolysis and glycolysis are upregulated simultaneously at the G1/S restriction point (Duan and Pagano, 2011).

GLS1 is an essential enzyme in glutam§inolysis, and like PFKFB3, it is targeted for degradation by ubiquitin ligase APC/C-Cdh1 (Visintin et al., 1997). Both GLS1 and PFKFB3 accumulate in mid-to-late G1, when the APC/C-Cdh1 activity decreases (Li and

Zhang, 2009). An increase in PFKFB3 and glutamine levels coincides with the increased lactate generation and processing of glutamine, respectively (Colombo et al., 2010). Experiments done with HeLa cells deprived of glucose and glutamine, at distinct stages of the cell cycle, show that both substrates are required for progression through G1, but only glutamine is crucial for progression through S phase (Colombo et al., 2011).

PFKFB3 is regulated by HIF-1α, AKT and PTEN (Obach et al., 2004) (Garcia-Cao et al., 2012). It is overexpressed in cancer cells (Atsumi et al., 2002) and its activity is necessary for CDK activation that follows posttranscriptional degradation of p27. This leads to cell cycle progression and limits apoptosis. PFKFB3 silencing reduces CDK1 activity and leads to G1/S arrest and apoptosis (Yalcin et al., 2014). PFKFB3 binds to CDK4 and inhibit its degradation by ubiquitylation, resulting in its accumulation and activation of E2F transcription. Therefore, a dual targeting of PFKFB3 and CDK4 has therapeutic potential (Jia et al., 2018). Another glycolytic enzyme hexokinase 2 (HK2), is also overexpressed in many malignant cells and its inhibition causes G0/G1 arrest and apoptosis (Hu et al., 2014).

The transcription factor SREBP1 induces the expression of FASN and several other genes involved in fatty acid synthesis. It also induces accumulation of p27, which inhibits CDK1 and CDK2 activity (Nakakuki et al., 2007), resulting in G1 arrest. The inhibition of SREBP1 or SREBP2 lowers the expression of lipid biosynthesis genes in colon cancer cells and inhibit xenograft tumour growth in vivo (Wen et al., 2018).

A recent study, which aimed to identify metabolites associated with G1 and SG2M stages via mass spectroscopy analysis of cell cycle stage sorted cells, showed that mitochondrial arginase 2 can be targeted as a vulnerability of cancer cells while sparing untransformed cells; knockdown of ARG2 caused G2M arrest (Roci et al., 2019). Arginine is important for mTORC1 activation through arginine sensor SLC38A9, allowing transport of essential amino acids from lysosomes (Wyant et al., 2017).

D) Oncogenic signalling that control cancer metabolism also affect cell cycle

Signalling pathways that control growth and cell division also control mammalian cell metabolism (Figure 1.3).

1. MYC, HIF-1, and PI3K/AKT

MYC, which is activated in many types of human cancer is known to be involved in regulation of both cell cycle and metabolism. Overactivation of c-MYC in untransformed cells predisposes them to cell death induced by growth factor or nutrient deprivation (Wise et al., 2008). Its activation induces glutaminolysis (Liu et al., 2012), which provides substrates into the TCA cycle, leading to increased lipid and protein synthesis.

PI3K/AKT, MYC, and HIF-1 partake in a shift from OXPHOS to glycolysis in cancer cells by increasing glucose uptake and facilitating glycolysis (Zawacka-Pankau et al., 2011). MYC also upregulates pyruvate dehydrogenase kinase 1 (PDK1) to decrease entry of pyruvate into TCA cycle (Kim et al., 2007). While upregulating glycolysis, MYC also sustains oxidative phosphorylation through mitochondrial biogenesis and glutaminolysis by enhancing transport of glutamine carbon into TCA cycle (Yeung et al., 2008). MYC acts on multiple sites of cell cycle control. It induces transcription of cyclin D, cyclin B and multiple CDKs while decreasing expression of p21 and p27 (Bretones et al., 2015). Its downregulation causes G1 arrest in cancer cells (Qi et al., 2007). MYC enhances progression through G1 by repressing p21 transcription (Gartel et al., 2001). HIF-1α activates p21 transcription by functionally counteracting and displacing c-MYC from p21 promoter, even in the absence of hypoxia (Koshiji et al., 2004).

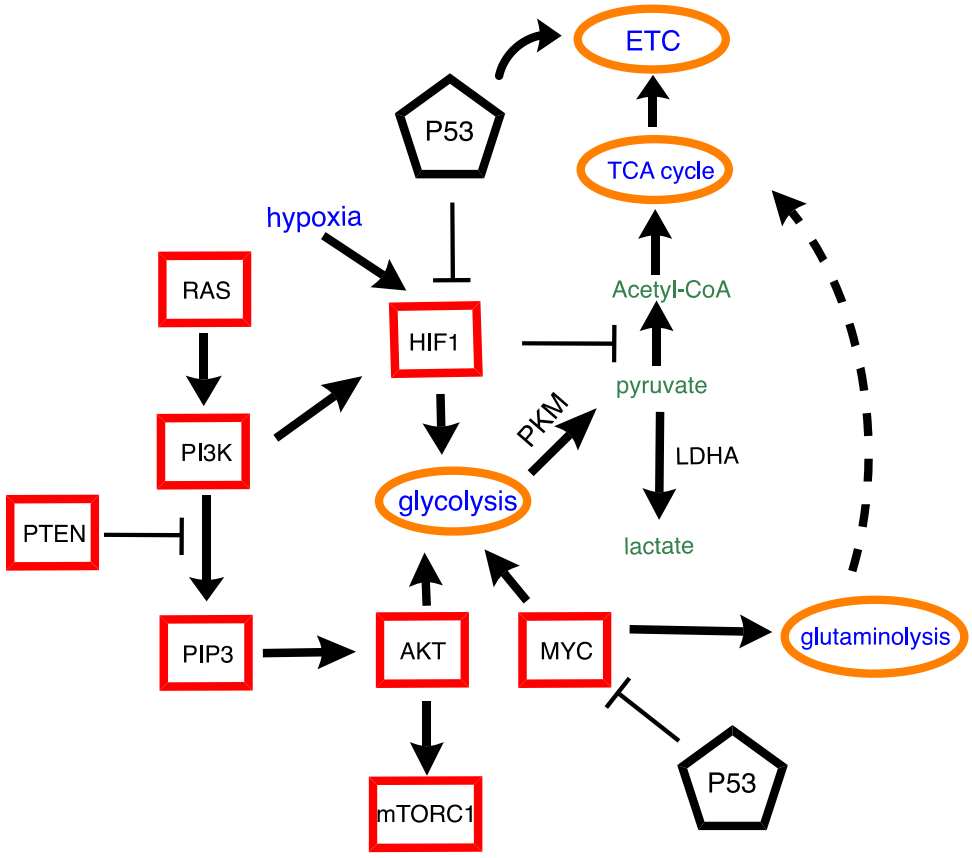


Figure 1.3: Summary of cancer cell metabolism and oncogenes involved in signalling and transcription.
See text for detailed explanation.

The transcription factor HIF-1 upregulates transcription of numerous glycolysis enzymes including GLUT1, PFK1 and aldolase, and downregulates oxidative phosphorylation by activating PDK1; it also upregulates LDHA which replenishes NAD+ to sustain glycolysis (Denko, 2008). HIF-1 dependent lipid droplet accumulation through fatty acid uptake also helps survival and ATP production after hypoxia reoxygenation (Bensaad et al., 2014). Mitochondria in cancer cells have increased ROS production due to mitochondrial dysfunction and NADPH activation, which results in activation of HIF-1α (Owusu-Ansah et al., 2008) (Kumari et al., 2018).

HIF-1 causes cell cycle arrest through cooperation with p53 and is a major controller of cell cycle under hypoxic conditions. Activation of MAPK pathway also activates HIF-1 under normoxic conditions in by increasing its translation (Sang et al.,

2003). HIF-1 activity increases glycolysis by increasing transcription of glucose transporters and glycolytic enzymes, promoting the flux of pyruvate to lactate. Hypoxic control of cell proliferation leads to apoptosis in oncogene-transformed cells whereas in primary cells G0/G1 arrest is observed (Schmaltz et al., 1998).

HIF-1α also slows cell division. CDK1 and 2 directly interact with HIF-1α and are positive and negative regulators of HIF-1α, respectively. CDK1 overexpression results in increased HIF-1α transcription and lowers its lysosomal degradation. Inhibition of CDK1 by roscovitine prevents hypoxic induction of HIF-1α targets GLUT1, PDK1 and VEGF at mRNA and protein levels. CDK2 activity, on the other hand, enhances degradation of HIF-1α. (Ma et al., 2017)

AKT is another oncogene that promotes the progression of cells from G1 to S phase of the cell cycle when phosphorylated. It has a dual effect on cell cycle progression and metabolism. It increases cyclin D1 translation by phosphorylating p21 and also increases glucose uptake of cells by promoting translocation of the glucose transporters to the cell membrane through insulin signalling (Gallagher and LeRoith, 2011). Inhibition of PI3K/AKT pathway results in cell cycle arrest by inducing p21 and p27 expression while inhibiting that of cyclin D1 in pancreatic cancer (Roy et al., 2010).

Insulin and GSK3B signalling are necessary for cell cycle progression since their activity stabilizes cyclin D1 levels by sequestering it in the nucleus. Insulin helps promote glucose homeostasis at cellular level following cell division (Lee et al., 2014). GSK3B plays a direct role in metabolism by inhibiting glycogen synthesis. PI3K inhibition leads to G3SK3B activation which is results in p53 inactivation. GSK3B is therefore a controller of p53 in apoptosis (Nayak and Cooper, 2012).

2. ROS control and p53

Reactive oxygen species (ROS) include oxygen derivatives which are free radicals (e.g. superoxide, peroxyl ion, hydroxyl ion, carbon dioxide radical) or non-radicals (e.g. hydrogen peroxide) which are oxidising agents (Costa et al., 2014). They

can be damaging due their ability to oxidise lipids, proteins and DNA (Halliwell, 2006). Cells need to control ROS for sustained proliferation.

SOD1 is antioxidant system that reduce superoxide radicals into hydrogen peroxide and oxygen. Glutathione is needed to remove hydrogen peroxide produced by SOD (Costa et al., 2014). SOD1 mutations are involved in conditions from heart disease to Down's Syndrome to Alzheimer's (Milani et al., 2011) and a SOD1 mutation leads to ALS phenotype in mice. Its depletion leads to an aging phenotype increased oxidative stress, cellular senescence and inflammation (Zhang et al., 2017).

Cellular energetics and cell cycle control are also coordinated through nutrient deprivation or mitochondrial stress. Mitochondrial reactive oxygen species (ROS) induce G1 arrest in Drosophila (Lee and Finkel, 2013). Disruption of mitochondrial complex 1 also causes G1/S arrest (Owusu-Ansah et al., 2008). A therapeutic strategy is to lower the antioxidant capacity of cancer cells to sensitize them to chemo- and radiotherapy. Cancer cells have higher basal levels of ROS compared to normal cells, thus targeting their inherent mechanism (SOD and glutathione peroxidase) to tolerate ROS can help improve their sensitivity to chemotherapeutic drugs over that of normal cells (Liou and Storz, 2010). This approach can help lower the dose necessary to potentiate chemotherapeutic effect and alleviate side-effects. While tolerable levels of ROS such as H_2O_2 can promote cancer cell survival and cell cycle progression (Qi et al., 2013), increasing their levels above the tipping point results in cell death (Verbon et al., 2012).

At low doses, oxidative or nitrosative ROS can activate p53 which can initiate a negative feedback through TIGAR action or enhance survival through autophagy (Kaminskyy and Zhivotovsky, 2014). P53 induced G1 arrest is also a survival strategy that allows cancer cells to repair DNA damage under low stress (Lane, 1992).

Under sufficient stress, p53 leads to growth arrest and apoptosis, as is observed in the absence of SOD1 activity (Watanabe et al., 2013). NRF2 (nuclear factor (erythroid-derived 2)-like 2) signalling increases SOD1 transcription, in cardiac myocytes (Dreger et al., 2009).

While DNA damage can activate p53-dependent apoptosis, p53 can induce cell cycle arrest through induction of p21 upon non-lethal DNA damage (Labuschagne et al., 2018). G1 checkpoint response results in the inhibition of CDK4 and CDK2 activities (He et al., 2005).

P53 function has cell specific effects and apoptosis or cell cycle arrest are not the only means through which p53 prevents tumour development. Since mice deficient in genes that confer P53 the ability to induce apoptosis or cell cycle Puma, Noxa, and p21 do not develop spontaneous tumours (Valente et al., 2013) (Aubrey et al., 2017). A fine balanced ROS production that does not drive the cancer cell to apoptosis is necessary for tumour growth. P53 inducible gene, TIGAR, is involved in this balance as its lowering of fructose-2,6-biphosphate levels downregulate glycolysis and has an antioxidant effect (Bensaad et al., 2006).

p53 inhibits glycolysis by downregulating *GLUT*1 and *GLUT4* expression (Schwartzenberg-Bar-Yoseph et al., 2004). Loss of p53 function activates NFKB signalling, which activates GLUT3 (Yeung et al., 2008). P53 also controls tumour growth by blocking ATP production through its downregulation of transcription factors c-MYC and HIF-1α.

P53 promotes OXPHOS by enhancing ETC function (Matoba et al., 2006), elevating fatty acid oxidation (Sanchez-Macedo et al., 2013), as well as increasing α-KG production through GLS2 activity which also increases glutathione levels (Hu et al., 2010). P53 also regulates ROS by lowering levels of glycolysis while promoting PPP, resulting in increased NADPH production (Duan et al., 2018). Interestingly, expression of SLC1A3, which is necessary for cancer cell survival and primary tumour growth under hypoxic and low glutamine conditions, is promoted by p53 (Tajan et al., 2018).

3. KRAS

Mutant KRAS is a main driver in lung, colorectal, and pancreatic cancer. From the RAS family GTPases include that also include HRAS and NRAS; KRAS is typically

mutated at codons 12,13, and 61 (Prior et al., 2012). These mutations results in GTP-bound and constitutively active KRAS. While KRAS mutations are typical of lung hyperplasia and adenomas, late stage adenocarcinoma tumours are also driven by p53 -/- status. KRAS driven PDAC relies on glutamine for ROS regulation (Son et al., 2013). Glycolytic genes and transporters are overexpressed in KRAS driven NSCLC where glycolysis and glutathione production is upregulated (Kerr and Martins, 2018).

RAS and MYC oncogenes, as well as mutant p53 lead to increased ROS generation (Sznarkowska et al., 2016). KRAS driven cancers have higher ROS levels due to activation of p38/PDPK1/PKCδ/p47 cascade but are able to tolerate them due to NRF2 signalling. Targeting NRF2 pathway reduces proliferation of KRAS(G12D) driven cancers (Sznarkowska et al., 2016). NRF2 signalling is activated by loss of KEAP1 and promotes KRAS-driven lung adenocarcinoma (Romero et al., 2017).

Oncogenic KRAS upregulates glutamine catabolism that leads to increased production of glutathione (GSH). Due to ROS scavenging properties of GSH, oncogenic KRAS leads to cisplatin resistance. The fast glutamine consumption that confers cisplatin resistance (Duan et al., 2018), as well as high intrinsic ROS levels (Yang et al., 2019) can also be a growth burden. Wild type KRAS is necessary for function of chemotherapeutic agents such as gemcitabine and cisplatin (Vogel et al., 2015). Cytotoxic resistance of KRAS mutant cancer cells can be overcome by MYC inhibitors. These drugs cause G1 cell cycle arrest, but the arrest does not confer protection from the cytotoxic effect of the drug since MYC inhibition results in cytochrome c release from the mitochondria and apoptosis (Ischenko et al., 2017).

RAS transformation also leads to elevated levels of micropinocytosis resulting in intake of albumin that increases intracellular glutamine (Commisso et al., 2013). KRAS mutated lung tumours have enhanced lipid metabolism. When KRAS G12D mutation is coupled with p53-/- however, autophagy is downregulated, which results in defective fatty acid oxidation and lipid accumulation (Guo et al., 2013). Further dependence of RAS driven cells on extracellular nutrients is evident in their high rates of unsaturated

fatty acid scavenging, allowing them to synthesize lipids independent of input from glycolysis via Acetyl-CoA, similar to behaviour of hypoxic cells (Kamphorst et al., 2013).

ROS generation through mitochondrial metabolism can aid with KRAS-induced anchorage independent growth (Weinberg et al., 2010) and loss of this function results in reduced tumorigenesis in KRAS-driven lung cancer in mice. These mitochondria retain less Ca^{2+}, leading to a decrease in mitochondrial apoptosis (Wallace, 2012).

E) Proposed siRNA screen to determine metabolic genes involved HCT116 cell cycle

Previous work of Prof. Harris's group set out to define genes involved in metabolism that were regulated by copy number that is associated with increased transcription, displaying the importance of metabolic genes in tumour growth (Haider et al., 2016). Prior to the Haider work, there had been an effort to profile an *in vivo* genetic signature of hypoxia in head and neck squamous cell cancers by identifying genes, that were strongly upregulated at mRNA level, which clustered with the expression of well-established hypoxia-regulated genes (Winter et al., 2007). Haider et al. compiled a list of metabolic enzyme and transporter genes from KEGG database to cover metabolic genes that are associated with stemness and aggressive breast cancers. They aimed to build a gene amplification signature that covers genes that are upregulated in primary tumours of at least three of the major ten types of cancer. For the gene to be included in the signature, it had to upregulated on both genomic and transcriptional level with a $\log_2$ fold change >0.5 (Haider et al., 2016). This allowed for the identification of a series of metabolic enzymes strongly related to an *in vivo* hypoxia signature. The group showed a significant overlap between upregulation of metabolic enzymes and *in vivo* hypoxia signature, both of which can be induced by oncogenic signalling pathways as part of the Warburg effect (Harris, 2002) (Bensaad and Harris, 2014) (Abu-Jamous et

al., 2017).

At the same time work was ongoing in Higgins and Muschel labs to identify drugs that can alter mitochondrial oxygen consumption. This work resulted in identification the anti-malarial drug atovaquone which inhibits mitochondrial complex 3 (Ashton et al., 2016) and PI3K/mTOR inhibitors (Kelly et al., 2014) as agents that alleviate tumour and the spheroid 3D model of hypoxia by lowering oxidative phosphorylation. The next step was to target these metabolic genes, investigated by both groups, in an siRNA screen to determine which genes may be most critical for cell cycle proliferation at defines cell cycle stages.

Levels of cell cycle regulators regulate the effectiveness of drugs like estrogen antagonist fulvestrant (Alves et al., 2016) and CDK 4/6 inhibitor palbociclib (Raspé et al., 2017), which can be used together in treating metastatic breast cancer (Turner et al., 2018). Palbociclib has a dual effect on cell cycle and metabolism (Franco et al., 2016). Prof. Muschel's group has previously studied the effect of S stage cell-cycle-arrest-inducing chemotherapeutic agent gemcitabine on oxidative phosphorylation (Grimes et al., 2016). Therefore, we also considered that combining an inhibitor of cell cycle progression through a metabolic route could enhance the effect of other drugs that target the same checkpoint.

Based on work from Harris and Muschel groups, we were then interested in determining metabolic genes that are important for cancer cell growth, but not previously identified in a role of regulating cell cycle.

The aim of studying the effect of metabolic genes on cell cycle progression was to understand whether certain metabolic pathways regulate cell cycle progression at G1/S or G2/M stages of the cell cycle and individually identify metabolic genes the function of which are indispensable to cell cycle progression.

siRNA screen was described in Chapter 3. Screen validation results and selection of PDE6H for further study were covered in Chapter 4. Chapter 5 presents a review of PDE6 biology and investigation of PDE6H for its effect on cell cycle and metabolism. A

constitutive knockout of *PDE6H* was developed by CRISPR/Cas9 technology (Chapter 5) to conduct longer term and in vivo experiments (Chapter 6).

F) Aims of this thesis

The aim of this thesis was to identify metabolic regulators of cell cycle progression in HCT116 cells to determine metabolic genes that were not previously recognised to have a role in cancer cell growth and proliferation, that can be targeted to prevent or slow cancer cell growth. The objectives are therefore:

1) To design and conduct a custom siRNA screen of 487 metabolic genes that encode important enzymes of cell metabolism or metabolite transporters as well as those that known to be upregulated at a genetic level in at least three types of primary tumours. The end-point of the screen was cell cycle distribution of the siRNA transfected HCT116 cells (Chapter 3).

2) To classify the genes as G1/S or G2/M regulators and , and validate some of novel main candidates from both classes (Chapter 4).

3) To investigate the pathway through which the main candidate chosen for further study controls cell cycle regulation, oncogene signalling, and cell metabolism in cancer cells (Chapter 5).

4) To examine tumour growth of CRISPR/Cas9 *PDE6H* knockout HCT116 cells in CD1 mouse model (Chapter 6).

CHAPTER 2: METHODS AND MATERIALS

A) Cell culture

1. Cell lines

Cancer cell lines used were HCT116 (colorectal carcinoma), DLD1 (colorectal adenocarcinoma, MCF7 (breast adenocarcinoma), MDA-MB-231 (breast adenocarcinoma), and MDA-MB-468 (breast adenocarcinoma), obtained from ATCC and were expanded from Harris and Muschel laboratory stocks, used at low passage. Cell line authentication was conducted through Eurofins Genomics. Our cell line selection aimed to include more than one type of cancer cell line that would include different statuses for p53 and KRAS. Gene mutation information (CBioportal) of the cell lines is shown in Table 2.1

Table 2.1: Gene mutation information of cell lines used.

	P53	KRAS	PIK3CA	BRAF
HCT116		gain of function	gain of function	
DLD1	loss of function	gain of function	gain of function	
MCF7			gain of function	
MDA-MB-231	loss of function	gain of function		gain of function
MDA-MB-468	loss of function		gain of function	

The cell lines used did not have overexpression of MYC (CBioportal).

B) Culture conditions and cell maintenance

Cells were grown in DMEM (Dulbecco Modified Eagle Medium, Gibco), containing 10% FBS (Fetal Bovine Serum, Gibco), 100 U/ml of penicillin, and 50 g/ml of streptomycin and supplemented with 4.5 g/L glucose (11965) or 1 g/L glucose (11885) and kept at 37 °C in water-saturated incubators containing 5% CO_2 and 95% air. Once they reached 70 to 90% confluency every three days, cell culture was split 1:10; cells were washed with 1 x PBS (phosphate buffered solution), trypsinised in 0.05% trypsin (Gibco) for 10 min at 37 °C and added to fresh medium. Cell suspension with trypsin was centrifuged for 5 minutes at 1200 rpm (Thermo Scientific™ Sorvall™ Legend™). Old medium was decanted, and cells were resuspended in fresh media. Concentration of viable cells in single cell suspensions was determined using a Nucleocounter (Chemometec). Cell suspensions were then divided into fresh tissue flasks or plated in the desirable format.

Cells to be frozen were resuspended in freezing media following removal of old media after centrifugation. Freezing medium consisted of 60% culture medium, an additional 30% FBS, and 10% DMSO (BioReagent, Sigma). Cells were then transferred to cryo-vials and kept overnight in isopropanol filled freezing containers (Thermo Fisher). Cells were stored at -80 °C for six months or kept in liquid nitrogen for longer for longer storage. To recover frozen cells, they were thawed in 37 °C water bath and resuspended in fresh media. This medium with DMSO was removed via centrifugation and cells were replated following suspension in fresh media.

C) siRNA reverse transfection

Dharmacon Human siGENOME SMARTpool siRNAs (Dharmacon) were resuspended in 1x siRNA buffer 60 mM KCl, 6 mM HEPES-pH 7.5, and 0.2 mM $MgCl_2$) by a series of centrifugation and vortexing to prepare a stock of 2 µM for siRNA screen

and 10 µM for all other transfections. Reverse transfection for the siRNA screen was carried out in flat-bottom 96-well plates using DharmaFECT Cell Culture Reagent (DCCR) (Dharmacon). The siRNA-DCCR was complexed with DharmaFECT transfection reagent by incubating the solution for 25 mins at RT. HCT116 cells, which were prepared for passaging in 25 mM glucose DMEM without antibiotics, were then added to wells of the plate containing 20 µL of the complex. The final volume per well was 100 µL. Transfected cells were incubated at 37 ºC and were assessed for cell-cycle distribution via PI staining after 72 hours of incubation. siRNA reverse transfection for sample preparation towards all other phenotypical analyses was carried out in 6-well or 12-well plates using 5 mM glucose DMEM without antibiotics. Ratio of transfection medium to cell suspension was kept at 1:5 as was the reverse transfection protocol of the siRNA screen. 2 µL of DharmaFECT transfection reagent was used per mL of total transfection volume. RNA extraction was carried out after 48 hours of reverse transfection. All other siRNA transfected sample collections including protein extraction or collection of cells for replating were carried out on the third day of transfection; following refeeding of transfected cells with complete culture media including antibiotics.

D) RNA isolation and reverse transcription polymerase chain reaction (RT-PCR)

Cells grown to 80% confluency in 12-well plates were lysed directly by adding 300 µL of Tri-Reagent (Sigma). 60 µL chloroform was added to the cell lysate. The aqueous upper phase was obtained in a clean tube containing glycogen (Thermo Fisher) and RNA was precipitated by adding isopropanol. The RNA pellet was centrifuged and washed twice with cold 75% ethanol. RNA was quantitated using Nanodrop (Thermo Fisher).

cDNA was synthesised from 1 µg of total RNA. Annealing step was performed

using 5uM of oligo(dT)$_{20}$ (Thermo Fisher) and 1 mM dNTP (Thermo Fisher) through an incubation 5 minutes at 65°C, followed by one minute of incubation at 4 °C. The reverse transcriptase master mix was prepared with 5x SSIV buffer, 100 mM DTT, RNAout Ribonuclease inhibitor, and SSIV reverse transcriptase (Thermo Fisher) as per manufacturer's instructions. RT reaction was carried out by incubating the mixture at 55°C for 10 minutes, followed by an incubation at 80°C for 10 minutes. RT-qPCR reaction was carried out by using 400 nM of primer mix (Sigma) and 2xSYBR No-ROX mastermix (Bioline). Primers were designed to produce a product of size 70-250 base pairs, GC content of above 50%, with the minimum melting temperature of 57 ºC, and maximum melting temperature of 63 ºC. Maximum melting temperature between primer pairs were kept at 3 ºC. Primers were also designed to span exon-exon junctions. Specificity of primers was checked using Primer-Blast software (Ye et al., 2012). Beta-actin (Bactin) was used as the housekeeping gene to which the mRNA expressions of other genes were normalised. Forward (fwr) and reverse (rev) primer sequences are shown in Table 2.2.

Table 2.2: Sequences of RT-qPCR primers used.

PDE6H_fwr	TTGTCTTTTGCAAAGAAGGCAGC
PDE6H_rev	GGCTGATGTTTCCCTTTCAGC
CCNA1_fwr	TCCCGCAATCATGTACCCTG
CCNA1_rev	ATTGCTTCAGACTCCACGGG
CCNB1_fwr	AAACTTTGGTCTGGGTCGGC
CCNB1_rev	TGTTGCTCGACATCAACCTCT
CCND1_fwr	GATGCCAACCTCCTCAACGA
CCND1_rev	GTTCCTCGCAGACCTCCAG
CCNE1_fwr	GCAAACGTGACCGTTGATCC
CCNE1_rev	TAATCCGAGGCTTGCACGTT
CDK2_fwr	CATCTTTGCTGAGATGGTGACTC
CDK2_rev	TGTTAGGGTCGTAGTGCAGC
CDK4_fwr	CTTTGGCAGCTGGTCACATGG
CDK4_rev	ATTCTCAGATCAAGGGAGACCCTCA
CPT1C_fwr	ATGGGAATGCGCCCCTTATG
CPT1C_rev	AGGTGGCGGATGTAGTCTTTT
FASN_fwr	AAGGACCTGTCTAGGTTTGATGC

FASN_rev	TGGCTTCATAGGTGACTTCCA
ANAPC1_fwr	TCCTTTTGGTCGAGACCACTG
ANAPC1_rev	CAGCTTTCCTTCTGTTTCTCGT
CDC25a_fwr	TCTTCACACAGAGGCAGAACTC
CDC25a_rev	GCATCGGTTGTCAAGGTTTGTA
Bactin_fwr	CTTCGCGGGCGACGAT
Bactin_rev	CCACATAGGAATCCTTCTGACC

E) Flow cytometry

1. High-throughput propidium iodide (PI) staining for cell cycle siRNA screen

Transfected cells in 96-well plates were lifted after a 5-minute incubation with 35 µL trypsin/well. The cell suspension was added to the V-bottom plates containing the old media and centrifuged at 2000 rpm for 10 minutes at room temperature (RT). The supernatant was discarded. Cells were resuspended in 50 µL of 1:1 PBS:Accumax (Sigma-Aldrich) solution and were kept at RT for 15 minutes. The suspension was then added dropwise to a fresh v-bottom 96-well plate containing 130 µL/well of ice-cold absolute ethanol and incubated at 4 °C for 90 minutes. The fixed cells were washed with 80 µL of cold PBS by centrifuging at 4°C 2000 rpm for 10 minutes. PBS was discarded, and the cells were resuspended in 100 µL of PI solution (200 µg/mL RNAse A (Sigma-Aldrich), 50 µg/mL PI solution (Sigma-Aldrich) and 1xPBS). and incubated 4 ◦C for at least 30 minutes. A high-throughput DNA content analysis via flow cytometry was carried out base on FL2 laser readings using FACSCalibur (BD Biosciences) and the data were assessed to draw cell cycle distribution histograms using FlowJo software. FSC-H, an indicator of size, vs SSC-H, an indicator of granularity, plots were used for gating cells. A second gate was applied on FL2-W vs FL2-A graph to omit doublets. Single cell population was used to determine cell cycle distribution based on PI signal detected via FL2-A (Figure 2.1). DNA content histogram was used for quantifying population of cells in G1, which corresponded to PI signal of “n”, and for quantifying

population of cells in G2/M, which corresponded to PI signal of “2n”. Once the two peaks corresponding to G1 and G2/M populations were determined, FlowJo automatically determined the middle region in the histogram as S population.

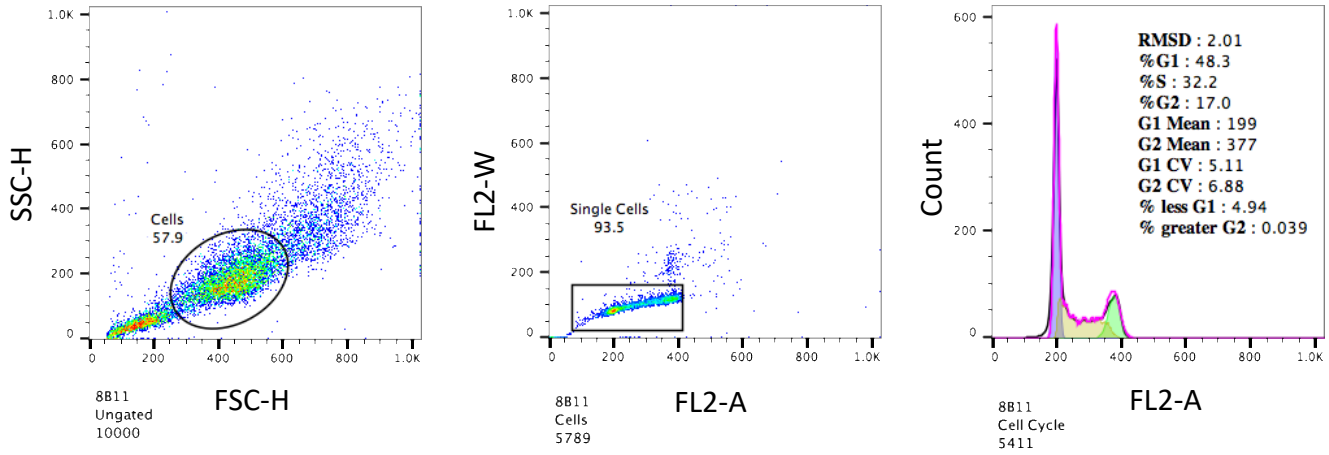


Figure 2.1: FlowJo allows for quantification of G1, S, and G2/M populations based on DNA content.
HCT116 cells are plotted. Purple peak corresponds to G1 population, green to G2/M and yellow to S.

2. Click-iT EdU and FxCycle staining for cell cycle distribution

10 mM solution of EdU was prepared by dissolving the lyophilised EdU dye provided with the Alexa Fluor 647 Click-iT EdU Flow Cytometry Assay Kit (Thermo Fisher). EdU solution was added to the media of adherent cells which were incubated with the dye for 2.5 hours. Cells were washed with 1x PBS trypsinised, lifted via trypsinisation, resuspended in fresh medium and obtained in round-bottom polystyrene FACS tubes (Falcon). The cell pellet that contained about 250,000-1,000,000 cells was washed with 1 mL of 1% BSA (bovine serum albumin) in PBS and the supernatant was discarded. 200 µL of Fixation/Permeabilisation solution (BD Biosciences) was added to the pellet. Fixed cells were incubated overnight at 4 ºC, protected from light. The cells were washed with 1 mL of 1% BSA and repelleted. 250 µL of Click-iT reaction cocktail was added to the pellet. The reaction cocktail consisted of 219 µL PBS, 5 µL CuSO4,

1.25 µL fluorescent dye azide, and 25 µL of reaction buffer. The reaction mixture was incubated for 30 minutes, protected from light, at RT. The cells were washed with 1 mL of 1% BSA in 1x Perm/Wash Buffer (BD Biosciences) and repelleted. The pellet was resuspended in 1xPBS containing 1 µL of 1 x FxCycle Violet stain (Thermo Fisher) and analysed via FACS Attune (Thermo Fisher).

FSC-A vs SSC-A plots were used for gating cells. EdU (5-ethynyl-2´-deoxyuridine) stains newly synthesised DNA as a thymidine analogue and is detected via click chemistry that covalently binds the ethynyl moiety of EdU to Alexa Fluor 647 coupled azide. Click-iT EdU dye allowed S-phase cells to be detected by RL1, while FxCycle Violet stained cells were detected by VL1. FxCycle acts as a PI substitute. EdU + FxCycle staining allowed for an analysis of cell cycle distribution where percentage of S phase cells were more accurate than that determined by PI staining on its own. The cell cycle distribution was determined using FlowJo software. At least 20,000 cells were used for analysis.

3. PI and Annexin V apoptosis assay

Cells were lifted via trypsinisation, resuspended in old culture medium that was retained and obtained in round-bottom polystyrene FACS tubes (Falcon). The medium was removed via centrifugation as in cell passaging. The cell pellet that contained about 250,000-1,000,000 cells was washed with PBS and was resuspended in 1 mL Annexin V+PI solution. The solution consisted of 5 µL of Brilliant Violet 711 Annexin V (BioLegend), 200 µg/mL RNAse A (Sigma-Aldrich), 50 µg/mL PI solution (Sigma-Aldrich) in 1xPBS. FACS Attune (Thermo Fisher) was used for analysis and cells were gated on FSC-A vs SSC-A plots. Single cells were further gated using FL2-W vs FL-1 plots. BV 711 Annexin V was detected by VL4 and PI was detected by BL2. Annexin V vs PI plots were used to determine populations of cells corresponding to live and non-apoptotic (Annexin V–PI–), apoptotic cells (Annexin +) as well as necrotic cells (Annexin V–PI+) (Ravi Hingorani, 2011). At least 50,000 cells were used for analysis.

4. Mitochondria dyes

MitoSOX Red

Lyophilised MitoSOX Red Mitochondrial Superoxide Indicator (Thermo Fisher) was dissolved in 13 µL of DMSO (BioReagent, Sigma) to prepare 5 mM stock solution. The stock solution was diluted 1:10 in culture medium and added to the media of adherent cells to make up a final concentration of 5 µM. Cells were incubated with the dye for 30 minutes. Adherent cells were then trypsinised and washed in PBS as was described in 2.1. The resulting cell pellet was resuspended in 1 mL PBS and analysed via FACS Attune (Thermo Fisher) BL2 laser. FSC-A vs SSC-A plots were used for gating cells as shown in Figure 2.1. Median of MitoSOX signal was used as an indication of mitochondrial superoxide reactive oxygen species (ROS). At least 50,000 cells were used for analysis.

MitoTracker Deep Red and MitoTracker Green

Lyophilised MitoTracker Deep Red (Invitrogen) and MitoTracker Green (Invitrogen) were dissolved in DMSO (BioReagent, Sigma) to produce 1 mM stock solution. The stock solutions were diluted 1:100 in culture media and together added to the media of adherent cells to make up a final solution of 25 nM. Cells were incubated with the dyes for 45 minutes. Adherent cells were then trypsinised and washed in PBS as was described in 2.1. The resulting cell pellet was resuspended in 1 mL PBS and analysed via FACS Attune (Thermo Fisher) BL1 (Green) and YL2 (Deep Red) laser after cells were gated using FSC-A vs SSC-A plots as shown in Figure 2.1.. At least 50,000 cells were used for analysis.

MitoTracker Deep Red stained intact mitochondria utilising the mitochondrial membrane potential, whereas MitoTracker Green stained all mitochondria. MitoTracker Deep Red vs MitoTracker Green plots were used to determine populations of cells with dysfunctional mitochondria (Deep Red- Green+) that have lost their membrane potential (IP et al, 2017) (Figure 2.2).

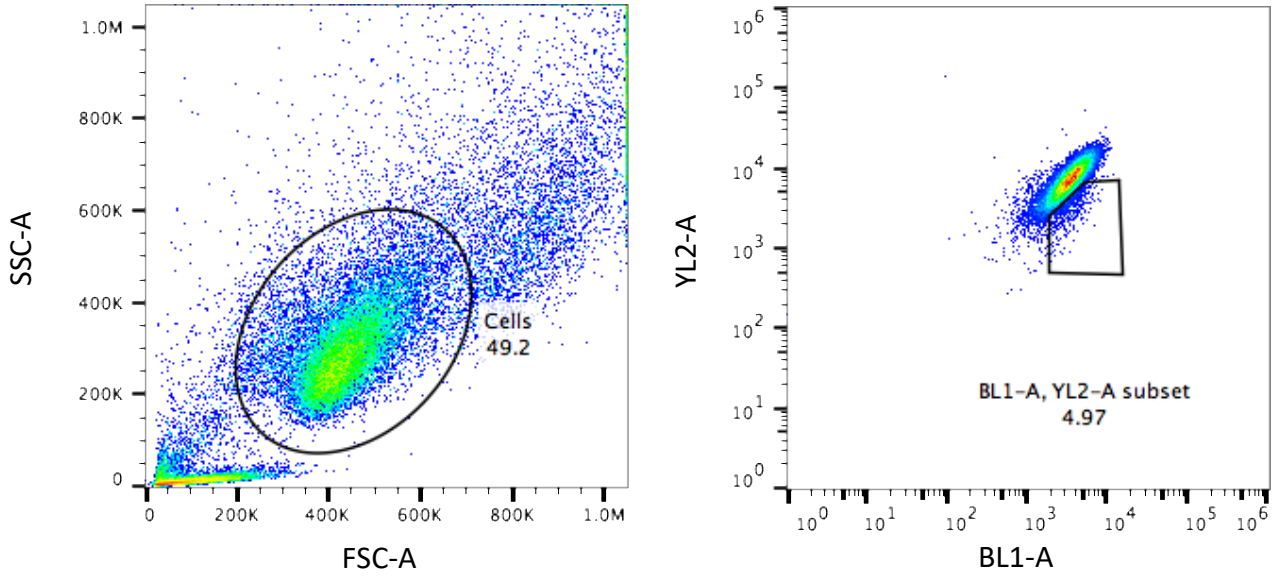


Figure 2.2: Calculation of percentage of cells with dysfunctional mitochondria. HCT116 cells were gated using FSC that indicates size, and SSC that indicates granularity. BL1 detects MitoTracker Green and YL2 detects MitoTracker Deep Red.

F) CyQuant viability measurement

CyQuant (Thermo Fisher) dye was used to determine cell viability of adherent cells 1x lysis and cell dye solution was prepared by diluting the 20x cell-lysis buffer and 400x CyQuant GR dye to 1x each in MilliQ water. The assay was conducted on cells grown in 96-well plates. Medium was removed from each well and plates were frozen in -80 ºC for at least two hours. At the time of the assay, plates were thawed, and cells were incubated with 200 µL working solution after being lysed by mixing through pipetting. After a ten-minute incubation at RT on a plate shaker, protected from light, stained cell lysates were transferred to black-bottom 96-well plates (3603, Corning). Fluorescence of samples were measured using a fluorescence microplate reader at

excitation/emission wavelengths 485 nm/520 nm.

G) Protein immunoblotting

Adherent cells were washed with PBS. They were next sheared with 1x RIPA buffer (Sigma) containing 1x Protease/Phosphatase Inhibitor Cocktail (Cell Signaling Technology -CST) and obtained in Eppendorf Tubes. Lysates were shaken on an orbital shaker for 30 minutes in 4 ºC and centrifuged to remove cell debris for 30 minutes at 4 ºC and 13,000 rpm. The supernatant was obtained in a clean Eppendorf Tube and protein concentration determined via DC protein assay (Bio-Rad) as per manufacturer's instructions. Protein gel electrophoresis samples were prepared by heating 20 µg of total protein with 1x NuPAGE® LDS Sample Buffer (Invitrogen), and 1 mM DTT (BioUltra, Sigma) at 90 ºC for 5 minutes. Gel electrophoresis was carried out in 1x NuPAGE MES SDS Running Buffer (Invitrogen).

PDE6H, 4EBP1, and phospho-4EBP1 blot samples were run on NuPAGE 10% Bis-Tris, 1.5 mm (Invitrogen) protein gels for 1.5 hours at RT under constant voltage of 100 V. VASP, phospho-VASP, cyclin D1, cyclin B1, CDK4, CDK6, p21, ERK1/2, phospho-ERK1/2, HIF-1α, Rb, and Phospho-Rb (Ser807/811) blot samples were run on NuPAGE 4-12% Bis-Tris, 1.5 mm (Invitrogen) protein gels for 1 hour at RT under constant voltage of 100 V. mTOR, phospho-mTOR (Ser2448), and phospho-mTOR (Ser2481) samples were run on NuPAGE Novex 3-8% Tris-Acetate, 1.5 mm (Invitrogen) protein gels, for 3 hours at 4 ºC under constant voltage of 60 V. Gels of 4EBP1, phospho-4EBP1, and PDE6H were transferred to 0.2 µM pore Immobilon-PSQ Membrane (Merck). Gels of VASP, phospho-VASP, cyclin D1, cyclin B1, p21, ERK1/2, phospho-ERK1/2, HIF-1α , mTOR, phospho-mTOR (Ser2448), and phospho-mTOR (Ser2481) were transferred to 0.45 µM pore size Immobilon-P PVDF Membrane (Merck). Proteins to be detected via fluorescent imager (Odyssey Fc, Licor) were

transferred Immobilon®-FL PVDF (Licor).

Transfer of each Bis-Tris gel was carried out at 4 ºC in TE62 transfer cooled unit (GE Healthcare) under constant voltage of 50 V. PDE6H blots were transferred for 1 hour and VASP, phospho-VASP (Ser239), 4EBP1, phospho-4EBP1 (Thr37/46) for 2.5 hours. Transfer HIF-1α, mTOR, phospho-mTOR (Ser2448), and phospho-mTOR (Ser2481) blots, which were run on Tris-Acetate gels, were transferred for 14 hours at 4ºC under constant voltage of 20 V. Transfer solution of 4EBP1, phospho-4EBP1, and PDE6H samples consisted of 10% methanol (Sigma) in 1x NuPAGE Transfer Buffer (Invitrogen). Transfer solution of the remaining samples consisted of 20% methanol in 1x NuPAGE Transfer Buffer. Membranes were allowed to dry for an hour at RT following transfer. They were then rewetted, washed with 1x TBS and blocked for an hour using 5% BSA (A9647, Sigma) in TBS.

Primary antibody solution contained 0.02% Tween 20 (Sigma) in 1x TBS (TBST), with 5% BSA. The antibodies used were against VASP (3132, CST), Phospho-VASP (Ser239) (3114, CST), cyclin D1 (2922, CST), cyclin B1 (4138), CDK4 (12790, CST), CDK6 (13331, CST), HIF-1α (610958, BD Biosciences), mTOR (2983, CST), phospho-mTOR(Ser2448) (5536, CST), phospho-mTOR (Ser2481) (2974, CST), 4EBP1 (9644, CST), phospho-4EBP1 (Thr37/46) (2855, CST), Rb (9309, CST), Phospho-Rb (Ser807/811) (9308, CST), PDE6H (156104, ABCAM), p44/42 ERK1/2 (9102, CST), phospho-p44/42 ERK1/2 (Thr202/Tyr204) (9101, CST), p21 (2947, CST) anti-β-Actin (Beta actin/Bactin) (3700, CST). All antibodies were used at 1:1000 dilution except for anti-PDE6H which was used at 1:250 and for Bactin which was used at 1:5000 dilution.

Secondary incubation of membranes was conducted with HRP-linked antibodies (7074 and 7076) in a 5% BSA TBST solution for an hour at RT. Chemiluminescent blots were washed and incubated with 1:10,000 diluted HRP-conjugated beta actin (60008, Proteintech) in 5% BSA TBST solution for beta actin staining. These blots were imaged via LAS 4000 biomolecular imager (GE Healthcare). Fluorescent blots were incubated for secondary antibodies in 5% BSA TBST solutions containing 1:15,000 dilutions of

800CW 680RD (32210 and 68071, Licor). These blots were imaged via Odyssey Fc (Licor).

H) cGMP ELISA

Basal levels of cGMP in cell lysates were measured using cGMP ELISA Kit (Cayman, 581021). Adherent cells grown in 6-well plates were washed and incubated with 0.5 mL of 0.1 M HCl for 20 minutes at room temperature. The cells were then scraped off with a cell scraper and were homogenously suspended by pipetting up and down. The cell suspension was obtained in an Eppendorf tube which was centrifuged at 1000xg for 10 minutes at 4 ºC. The supernatant was obtained in a clean test tube. cGMP standards were reconstituted in ELISA buffer and were diluted as per manufacturer's instructions. Buffer, standards/samples and antiserum were added in the wells assigned according to manufacturer's instructions. The plate was covered with plastic film and incubated for 18 hours at 4 ºC in dark. The plate was later washed five times with the Wash Buffer and was developed with the addition of Ellman's Reagent followed by the tracer. Development was carried out at room temperature in dark, for 90 minutes, using an orbital shaker. Absorbance reading of the plate was done at 405 nm and analysis was conducted using Cayman's online ELISA analysis tool: (https://www.caymanchem.com/analysisTools/elisa).

I) Seahorse metabolic assay

Cells were grown for 16 hours in 96-well XF plates (Seahorse Biosciences). Prior to the assay, the Seahorse calibration plate filled with XF calibration solution was placed in the 37°C non-CO_2 Seahorse chamber overnight. Two hours prior to the run, the Seahorse medium was prepared as follows: 5 mM glucose, 1 mM pyruvate, 4 mM

glutamine, XF media, and NaOH unless otherwise specified to bring the pH up to 7.4. The cells were washed twice and resuspended in assay media. Drugs of interest, which were diluted in the assay media were added to treatment groups. The cells in Seahorse media were kept in the non-CO2 incubator for 45 minutes prior to the mitotic stress test run.

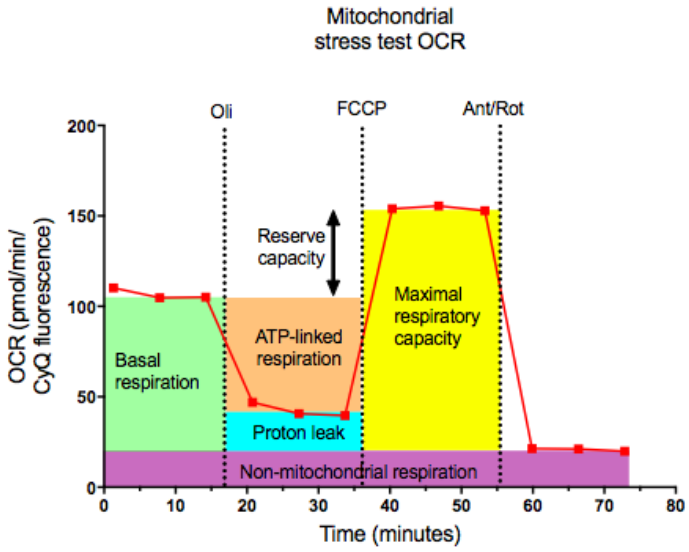


Figure 2.3: Seahorse mitochondrial stress test measures the contributions of various components of mitochondrial respiration to oxygen consumption rate (OCR) (Gueven et al., 2014).

Oxygen consumption profiles were determined via measurements prior to and following sequential injection of oligomycin, FCCP, and antimycin and rotenone (Figure 2.3). Oligomycin blocks ATP synthase, forcing the basal oxygen consumption levels to drop. The drop in OCR levels following oligomycin injection is used to obtain the level of oxygen consumption that is used for mitochondrial ATP generation, beyond the level required to overcome the natural proton leak across the ATP synthase of the inner mitochondrial membrane. The proton leak occurs when there is incomplete coupling of the ATP-producing respiration through ETC to OXPHOS, allowing the protons to enter the mitochondrial matrix from intermembrane space via proton channels (Winer and Wu, 2014). It is postulated that he leaked protons protect the mitochondria by oxidising superoxide ions (Brookes 2005). Following the administration of oligomycin, the cell relies on glycolysis for energy production.

FCCP administration results in the uncoupling of the proton transfer across the mitochondrial inner-membrane from the proton channel of ATP synthase complex V (Kenney et al., 2014). Following the uncoupling of ATP synthesis from oxygen consumption, H^+ follows its concentration gradient back into the mitochondrial matrix; ETC consumes oxygen as the electron acceptor to move H^+ back into the intermembrane space (Van der Windt et al., 2016). The oxygen consumption reaches its peak value as the proton conductance across the mitochondrial inner membrane increases. Due to the collapse of the mitochondrial potential, ATP is not generated, and a rapid consumption of energy and oxygen is observed, with both OCR and ECAR increasing; OCR due to uncoupling, and ECAR due to the cell's efforts to sustain energy levels. Antimycin A and rotenone act as electron transport chain inhibitors that shut down ETC (Van der Windt et al., 2016). These inhibitors are added to determine non-mitochondrial respiration. Reserve/spare capacity, which is the difference between maximal and basal OCR values, indicates a spare ETC capacity that allows for a surge of ATP generation upon short-term metabolic demand (Fern, 2003).

Seahorse assay was conducted as per conditions specified for each cell line. OCR and ECAR data were obtained from the Seahorse mitochondrial stress test. The cell medium was then removed, and Seahorse plates were placed in -80 °C overnight for CyQuant viability test. ECAR and OCR values were normalised to cell viability values, determined by CyQuant fluorescence intensity values per well.

Table 2.3: Seahorse mitochondrial stress test drug concentrations.

Cell line	Cell number/well	Oligomycin (µM)	FCCP (µM)	Antimycin (µM)
HCT116 WT	22,500	1	0.5	0.5
DLD1	22,500	1	0.5	0.5
MCF7	20,000	1	0.25	0.5
MDA-MB-231	20,000	0.25	0.25	0.5
MDA-MB-468	25,000	1.5	1.25	0.5

J) CRISPR/Cas9 nickase stable knockout cell line generation

1. Introduction to CRISPR Cas9 nickase

CRISPR/Cas9 *PDE6H* knockout HCT116 cells were developed with the aim of comparing WT HCT116 cells with those with a stable knockout of *PDE6H* gene. CRISPR/Cas mediated knockout of *PDE6H* was carried out with paired Cas9 nickases. The CRISPR/Cas system utilizes the RNA-based adaptive immune system of bacteria and archaea that detects and destroys foreign bodies of viruses and plasmids by targeting nucleic acid in a sequence-specific manner. CRISPR DNA repeats are separated by proto-spacer spacers (Horvath and Barrangou, 2010).

The CRISPR/Cas system is designed to produce gene deletion in human cells *in vitro* by causing double strand breaks at target of interest using a synthetic single-guide RNA and Cas9 (Yang et al., 2013). Knockout is accomplished by using the Cas9 endonuclease to target a unique DNA sequence that immediately follows a protospacer adjacent motif PAM (Figure 2.4).

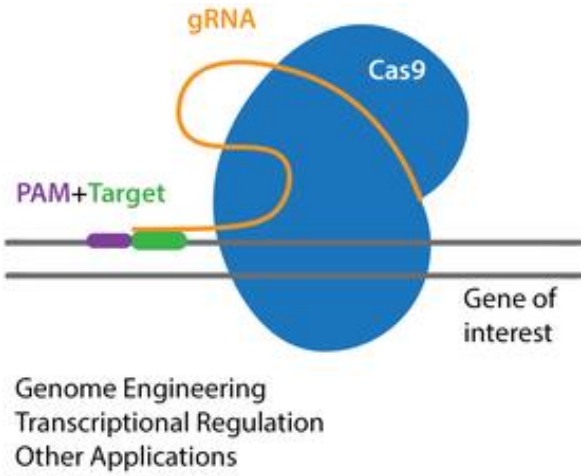


Figure 2.4: CRISPR/Cas9 system targets a unique DNA sequence adjacent to protospacer adjacent motif (PAM) using a (single) guideRNA (sgRNA or gRNA). Permission was obtained for use of image (Addgene, 2017).

The CRISPR system consists of the Cas9 protein and a guide RNA (sgRNA) which contains a scaffold sequence that allows the Cas9 to bind to target sequence and

a nucleotide spacer homologous to the target sequence (Wang et al., 2013). The scaffold sequence is about 20 base pairs long. Cas9 is activated upon sgRNA binding and cleaves once bound to the target sequence (Figure 5.6) (Ran et al., 2013b), (Adli, 2018). Plasmids for expression of Cas9 or Cas9-nickase (D10A) were obtained from the Addgene plasmid repository supplied by Zhang laboratory.

Wild-type Cas9 allows gene editing via guidable DNA cleavage while the catalytically impaired nickase Cas9 enzyme mutant Cas9 (mtCas9), consisting of Cas9D10A and Cas H840A, can be used for gene editing without double strand breaks (Adli, 2018). Off-target effects of CRISPR/Cas gene editing can be ameliorated by using the mtCas9 nickase in pairs with two guide RNAs to generate nicks on different DNA strands, resulting in two single-strand breaks in close proximity. These nicks on homologous strands lead to single strand breaks that lead to overhangs (Cho et al., 2013).

Cas9 induced breaks are prone to being repaired by non-homologous end joining than those caused by Cas9 nickases. However, homology-dependent repair occurs at a similar rate with both strategies although the genome-editing outcome depends on the context (Miyaoka et al., 2016). The products of Cas9D10A nicking might lead to indels, base mismatches with considerably less off-targeted mutations and unwanted translocations compared to CRISPR/Cas9 system (Cho et al., 2013). The nickase system that results in nicks on homologous DNA strands is highly specific since double strand breaks take place only when the two Cas9 nickases cleave simultaneously. Induction of nicks at off-target sites is unlikely to cause non-homologous end joining since any mutation introduced outside the PAM and sgRNA targeting sequence remain intact after repair by HDR, which result in re-nicking by the CRISPR/Cas9 system until the PAM-sgRNA sequence is disrupted via error-prone NHEJ (Satomura et al., 2017).

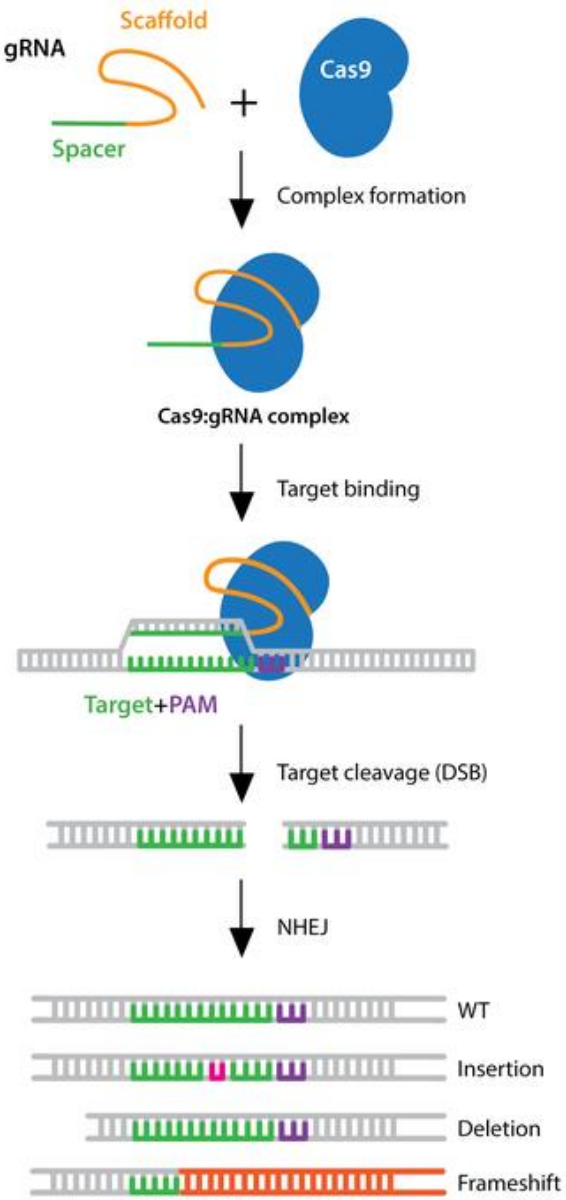


Figure 2.5: Cas9 gene modification leads to deletion of the gene product through various genetic modifications via DSB or NHEJ. Permission was obtained for use of image (Addgene, 2017).

2. Generation of CRISPR/Cas9 PDE6H ko HCT116

As part of our CRISPR ko cell line generation, plasmids were prepared by Dr. Yunhong Chao from Muschel lab as per Zhang lab protocol (Zhang, 2017). The two pairs of sgRNAs targeting *PDE6H* were designed (Chapter 5) and configured into plasmids. The plasmids were based on PX461: SpCas9n-2A-EGFP (D10A nickase) and PX462: SpCas9n-2A-Puro (D10 nickase). 100,000 HCT116 cells were plated in one well of a 12-well plate in complete culture medium of 5 mM glucose DMEM. A day after

seeding, the transfection reagents “A” and “B” were prepared. “A” included 150 µL Opti-MEM reduced serum medium (Gibco) and 8 µL of Lipofectamine 3000 reagent (Thermo Fisher). “B” included 150 µL Opti-MEM reduced serum media, 8 µL of P3000 reagent with 2 µg of each plasmid. A and B were incubated together for 15 minutes. Medium of the adherent cells to be transfected was replaced with the transfection medium made of A and B mixture. 24 hours after transfection, transfection efficiency was determined using Zoe Fluorescent Cell Imager (Bio-Rad) to be 70%. Transfection reagent was changed with full culture medium without pen/strep but with 1.5 µg/mL puromycin for selection. After two days of puromycin selection, puromycin medium was replaced with complete culture medium (including pen/strep) and remaining cells were incubated for another day. Cells were then counted and diluted in a single cell suspension to yield 0.5 cells/well. 200 µL of the cell suspension was seeded into each well of 96-well plates. After ten days, cells that grew into single colonies were replated and expanded in 6-well plates up to 80% confluency. The resulting clones were tested via western blotting to confirm the deletion of the gene product.

K) Spheroid generation

HCT116 cells were prepared into single a cell suspension at a concentration of 10^4 cells/mL. 200 µL of the cell suspension was added to a 96-well spheroid microplate with a round-bottom low-attachment surface (4515, Corning). The microplate was centrifuged for 5 minutes at 1500 rpm at RT and placed in an incubator. Four days after seeding, spheroids started to form. They were imaged with a Zeiss Axiovert 135 microscope.

L) Clonogenic survival assays

HCT116 cells were seeded in 6-well plates (3516, Corning) at varying densities depending on their colony forming ability: 0 Gy group at 400 cells/well, 2 Gy at 800 cells/well, and 4 Gy at 1600 cells/well. Six hours after plating, cells were irradiated by a Caesium-137 irradiator (Gamma Service: GSR D1; dose rate 1.94 Gy min^{-1}). Cells were allowed to grow to log phase for about a week until countable colony growth was observed. Once colonies had formed, the medium was removed, and then the colonies were stained with crystal violet and counted with a Gelcount automated colony counter (Oxford Optronics).

M) Statistical analysis

When only one independent variable was being measured, unpaired t-test was used for comparing the means between two groups; one-way ANOVA was used for comparing more than two groups. Two-way ANOVA analysis was used for analyses involving multiple independent variables. Analyses were conducted using Prism 7 (GraphPad Software Inc.). Degree of statistical significance was denoted by "$*$" when $P < 0.05$, "$**$" when $P < 0.01$, "$***$" when $P < 0.001$, and "$****$" when $P<0.0001$. Error bars represent standard deviation unless otherwise specified.

Paired tests were used when results pertain the same biological replicate. Difference-paired tests were used when difference between control and treated groups is consistent. Ratio-paired tests were used when the ratio between control and treated groups is consistent and the differences grow with the control values (GraphPad).

Post hoc tests: Tukey's test was used to compare every mean with every other mean, as part of one- and two-way ANOVA. Dunnett's test was used when each mean was compared to a control mean as part of one- and two-way ANOVA. Sidak's test was used after two-way ANOVA, when independently comparing means at various time-points.

N) Xenograft mouse models

All protocols were carried out under Home Office regulations, under license PPL 30/3197. Dr. Esther Bridges conducted the xenograft study. 2.5 x106 HCT116 cells in 200 µL of Matrigel (BD Bioscience) were implanted subcutaneously into female CD1 nude mice. Intratumoural injections were given to one group when tumours reached an average group tumour volume of 50mm3. Tumour volume was calculated from a formula ($V = L \times W \times H \times \pi/6$). Tumour growth was monitored and measured using calipers. Tumours of the zaprinast treatment group were treated for four weeks with three doses given on days 1, 3, and 5 of the week. 12 injections were given in total. 3 mg/mL of zaprinast (10010421, Cayman) in 1% DMSO in PBS was administered via intratumoural injection (100 µL) using insulin needles (28G and ½ inch). When the tumors reached 1000 mm3, the mice were sacrificed by cervical dislocation.

O) Immunohistochemistry

Paraffin-embedded cell pellets or tissue sections were retrieved, dewaxed and rehydrated according to standard procedures. Antigen retrieval was conducted in sodium citrate buffer pH 6 (ABCAM). Slides were stained using the FLEX staining kit (Agilent). As part of tumour section preparation, endogenous peroxidase activity was blocked. Primary antibodies were diluted in PBS (0.2% 9w/v sodium azide and 10% bovine serum) (Sigma-Aldrich). Slides were stained with rabbit anti-Ki67 at 1:100 dilution (M7240; Dako, Glostrup, Denmark), rabbit anti-CA9 at 1:100 dilution (M75; BD Biosciences) and anti-endomucin at 1:50 dilution (106100 ABCAM) for 1h at room temperature. Slides were washed in PBS and were incubated with the Flex anti-rabbit/anti-mouse secondary antibody for 30 minutes at room temperature and washed in Flex buffer. 3,3′-Diaminobenzidine (Flex-DAB) was applied to the sections for 10 minutes for visualisation. After PBS washing, the slides were counterstained by

immersing in Flex haematoxylin solution for 20 seconds, air-dried and mounted with mounting medium (Sigma). Secondary-only control staining was done routinely, these were negative. HE slides were either stained for Giles haematoxylin (Sigma-Aldrich) and counter stained with eosin (Sigma-Aldrich). Necrosis was assessed histologically on the haematoxylin-stained sections. Necrotic areas were identified as areas displaying cells with basophilic pyknotic nuclei undergoing karyorrhexis and/or karyolysis. Xenograft study and staining were conducted by Dr. Esther Bridges.

Scoring was conducted with the help of Dr. Bridges, using the Visiopharm Integrator System protocol written by Dr. Nasullah Khalid Alham. Viable and necrotic areas were determined via threshold classification. Thresholds levels were adjusted from default values against control xenograft staining; the xenografts from all groups were then analysed using the same values. The protocol determined tumour region of interest (ROI). Necrotic/viable areas were determined via Haematoxylin (H)—3,3'-Diaminobenzidine (DAB) colour deconvolution. Haematoxylin-positive necrotic regions were determined within the total tumour area. Nuclei were detected within tumour ROI and classified as Ki-67 positive or negative. CA9 positive regions within the cytoplasm were also determined. Analysis of full slides were conducted in a tile-by-tile fashion. Ki-67 positive nuclei and CA9 positive cells were scored within viable tumour regions.

CHAPTER 3: DESIGN OF A METABOLIC SIRNA SCREEN WITH HCT116 CELL CYCLE ENDPOINT

A) Abstract

An siRNA screen was conducted to monitor cell cycle distribution HCT116 colorectal cancer cells following siRNA transfection. The aim was to identify metabolic genes the knockdown of which caused cell cycle arrest at G1/S and G2/M points of the cell cycle. A custom siRNA library of 487 genes was developed, containing: 1) genes from KEGG (Kyoto Encyclopedia of Genes and Genomes) defined metabolic pathways (Kanehisa and Goto, 2000) (Kanehisa et al., 2014), that produce enzymes and transporters involved in key regulatory pathways of metabolism, such as glycolysis and glucose metabolism, tricarboxylic acid (TCA) cycle, pentose phosphate pathway (PPP), fatty acid metabolism, nucleotide synthesis, in addition to transcription factors involved in hypoxia and AMPK signalling; 2) isoforms of genes that make up a core metabolic signature (Haider et al., 2016) of primary tumours. Metabolic genes as well as positive controls were organised in a 96-well setting that would allow for reverse transfection of HCT116 cells, followed by propidium-iodide staining of DNA content to allow for determination of G1/S and G2/M arrest inducing siRNAs. siCCND1 was used as a positive control for G1/S arrest- and siCDC2 was used as a positive control for G2/M

arrest-inducting candidates.

B) Introduction

Oncogenes control cancer cell proliferation, which is tightly linked to metabolism. Most oncogenes that trigger proliferative signals also cause metabolic changes (Fritz and Fajas, 2010). While the deregulation of cancer metabolism through oncogenic signalling, and the effect of the latter on proliferation and cell cycle control is widely studied, little is known about the mechanisms through which metabolism in cancer cells leads to cell cycle control and progression. Inhibiting metabolic pathways to cause cell cycle arrest will allow us to find anti-proliferative measures against the cancer cell by finding metabolic vulnerabilities of the HCT116 colorectal cancer cells, as well as bringing to light the links between metabolism and cell cycle regulation. The aim of this chapter is to identify metabolic genes whose inhibition cause cell cycle arrest in HCT116 cancer cell line to allow selection for further study of candidate genes that are important in regulating cancer metabolism and cancer cell proliferation.

C)Selection of the siRNA library and cell cycle assay

1. Rationale for siRNA screen and propidium iodide staining to process the endpoint

Suppressing gene function via RNA interference can identify new cancer targets (Bric et al., 2009). RNA induced silencing complexes (RISCs) target specific mRNAs for cleavage or translational repression (Tang, 2005). RNA silencing is carried out by short double stranded RNAs (dsRNAs) which are part of the immune response against RNA viruses and transposable elements (Meister and Tuschl, 2004). Formation and activation of endogenous siRNA consists of: cleavage of long double stranded RNA

strands into 21-25 base pair siRNA dimers with characteristic 2-nucleotide overhangs at the 3' ends by the endonuclease RNase Dicer enzyme that then incorporates the guide strand to the RISC, and the degradation of the "passenger strand" that is not included in the complex, by the nuclease during RISC activation (Leuschner et al., 2006). After the destruction of mRNA, RISC can be regenerated for multiple rounds of cleavage (Zamore and Aronin, 2003).

The shorter the dsRNAs, the more specific the binding to mRNA is and less of a risk the siRNA transfection carries of evoking an immune response in the host; generally siRNAs longer than 23 bps induce a strong interferon response and affect cell viability (Reynolds, 2006). Off-target effects can be limited by using the lowest amount of siRNA that still achieves gene suppression (Dharmacon, 2014).

Cell cycle stage can be analysed based on DNA content quantification, expression levels of cell cycle regulators, and BrdU incorporation into newly synthesised DNA (Pozarowski and Darzynkiewicz, 2004). DNA content can be determined via flow cytometry (FC) or microscopic detection via DNA stains (Mukherji et al., 2006). FC gives a fast quantification of DNA that can detect significant changes in cell cycle distribution. Flow cytometry was preferable in our case due to our access to a 96-well BD FACSCalibur that allows for high throughput flow cytometry readings. The 96-well FC setting also enables the use of the same siRNA sample during transfection and flow cytometry reading at the end-point of the assay.

Propidium iodide, DAPI/Hoechst, and BrdU staining, as well as FUCCI platform (Sakaue-Sawano et al., 2008) were considered for measuring cell cycle distribution. DAPI/Hoechst was eliminated due to its poor compatibility with our FC instrument. Our experience with FUCCI cells showed that the fused red- and green-emitting fluorescent probes affected the cell cycle distribution of the cells, therefore this method was deemed unreliable and was discarded. BrdU signal depends heavily on the duration of incubation. BrdU can be used as an indicator of population of cells in S only when the incubation time is limited to the duration of that phase. Since we planned on using

unsynchronised cells, BrdU staining was not suitable in the high-throughput setting. Propidium iodide staining gave the flexibility needed to conduct the screen for the scale of our siRNA screen, with the staining period having less of an effect on the results compared to BrdU method. Propidium iodide staining was therefore selected for determining the main hits of the screen that would later be followed up through more extensive methods.

2. Compilation of core metabolic signature genes

The metabolic genes that Dr. Syed Haider from Buffa and Harris groups (Haider et al., 2016) reported to be amplified in primary tumours (Table 3.1), were included in the library. Haider et al. compiled a list of metabolic enzyme and transporter genes from KEGG database to cover metabolic genes that are associated with stemness and aggressive breast cancers. The aim was to build a gene signature that covers genes that are upregulated in primary tumours of at least three of the major ten types of cancer. For a gene to be included in the signature, it had to upregulated on both genomic and transcriptional level with a log2 fold change >0.5 (Haider et al., 2016). The initial list of genes, the family members of which we included in our siRNA screen are listed as the 49 genes below.

The list of genes compiled by Haider et al. will be referred to as the Core Metabolic Signature (CMS) and the genes that are not included in their list but are related to the CMS will be referred to as CMS-R.

Table 3.1: Core metabolic signature genes from Haider et al study (Haider et al., 2016).

Gene Symbol	Description
ABCC5	ATP-binding cassette, sub-family C (CFTR/MRP), member 5 [Source:HGNC Symbol;Acc:56]
AHCY	adenosylhomocysteinase [Source:HGNC Symbol;Acc:343]
ALDOA	aldolase A, fructose-bisphosphate [Source:HGNC Symbol;Acc:414]
ALG3	asparagine-linked glycosylation 3, alpha-1,3- mannosyltransferase homolog (S. cerevisiae) [Source:HGNC Symbol;Acc:23056]
B4GALT3	UDP-Gal:betaGlcNAc beta 1,4- galactosyltransferase, polypeptide 3 [Source:HGNC Symbol;Acc:926]

CAD	carbamoyl-phosphate synthetase 2, aspartate transcarbamylase, and dihydroorotase [Source:HGNC Symbol;Acc:1424]
CLCN2	chloride channel 2 [Source:HGNC Symbol;Acc:2020]
CYC1	cytochrome c-1 [Source:HGNC Symbol;Acc:2579]
DHCR7	7-dehydrocholesterol reductase [Source:HGNC Symbol;Acc:2860]
DHRS13	dehydrogenase/reductase (SDR family) member 13 [Source:HGNC Symbol;Acc:28326]
DHTKD1	dehydrogenase E1 and transketolase domain containing 1 [Source:HGNC Symbol;Acc:23537]
EDEM2	ER degradation enhancer, mannosidase alpha-like 2 [Source:HGNC Symbol;Acc:15877]
FLAD1	FAD1 flavin adenine dinucleotide synthetase homolog (S. cerevisiae) [Source:HGNC Symbol;Acc:24671]
FLVCR1	feline leukemia virus subgroup C cellular receptor 1 [Source:HGNC Symbol;Acc:24682]
GAPDH	glyceraldehyde-3-phosphate dehydrogenase [Source:HGNC Symbol;Acc:4141]
GGH	gamma-glutamyl hydrolase (conjugase, folylpolygammaglutamyl hydrolase) [Source:HGNC Symbol;Acc:4248]
GMPS	guanine monophosphate synthetase [Source:HGNC Symbol;Acc:4378]
GPI	glucose-6-phosphate isomerase [Source:HGNC Symbol;Acc:4458]
HCN3	hyperpolarisation activated cyclic nucleotide-gated potassium channel 3 [Source:HGNC Symbol;Acc:19183]
IMPDH1	IMP (inosine 5'-monophosphate) dehydrogenase 1 [Source:HGNC Symbol;Acc:6052]
ITPA	inosine triphosphatase (nucleoside triphosphate pyrophosphatase) [Source:HGNC Symbol;Acc:6176]
KCNMB3	potassium large conductance calcium-activated channel, subfamily M beta member 3 [Source:HGNC Symbol;Acc:6287]
LPCAT1	lysophosphatidylcholine acyltransferase 1 [Source:HGNC Symbol;Acc:25718]
NAT9	N-acetyltransferase 9 (GCN5-related, putative) [Source:HGNC Symbol;Acc:23133]
NME1	non-metastatic cells 1, protein (NM23A) expressed in [Source:HGNC Symbol;Acc:7849]
NUDT1	nudix (nucleoside diphosphate linked moiety X)-type motif 1 [Source:HGNC Symbol;Acc:8048]
PDE7A	phosphodiesterase 7A [Source:HGNC Symbol;Acc:8791]
PIGU	phosphatidylinositol glycan anchor biosynthesis, class U [Source:HGNC Symbol;Acc:15791]
PMM2	phosphomannomutase 2 [Source:HGNC Symbol;Acc:9115]
PSPH	phosphoserine phosphatase [Source:HGNC Symbol;Acc:9577]
PYCR1	pyrroline-5-carboxylate reductase 1 [Source:HGNC Symbol;Acc:9721]
PYCRL	pyrroline-5-carboxylate reductase-like [Source:HGNC Symbol;Acc:25846]
SHMT2	serine hydroxymethyltransferase 2 (mitochondrial) [Source:HGNC Symbol;Acc:10852]
SLC12A8	solute carrier family 12 (potassium/chloride transporters), member 8 [Source:HGNC Symbol;Acc:15595]
SLC25A10	solute carrier family 25 (mitochondrial carrier; dicarboxylate transporter), member 10 [Source:HGNC Symbol;Acc:10980]
SLC25A13	solute carrier family 25, member 13 (citrin) [Source:HGNC Symbol;Acc:10983]
SLC39A11	solute carrier family 39 (metal ion transporter), member 11 [Source:HGNC Symbol;Acc:14463]
SLC39A4	solute carrier family 39 (zinc transporter), member 4 [Source:HGNC Symbol;Acc:17129]
SLC4A2	solute carrier family 4, anion exchanger, member 2 (erythrocyte membrane protein band 3-like 1) [Source:HGNC Symbol;Acc:11028]
SLC5A6	solute carrier family 5 (sodium-dependent vitamin transporter), member 6 [Source:HGNC

	Symbol;Acc:11041]
SQLE	squalene epoxidase [Source:HGNC Symbol;Acc:11279]
SRD5A1	steroid-5-alpha-reductase, alpha polypeptide 1 (3-oxo-5 alpha-steroid delta 4-dehydrogenase alpha 1) [Source:HGNC Symbol;Acc:11284]
TK1	thymidine kinase 1, soluble [Source:HGNC Symbol;Acc:11830]
TPI1	triosephosphate isomerase 1 [Source:HGNC Symbol;Acc:12009]
TSTA3	tissue specific transplantation antigen P35B [Source:HGNC Symbol;Acc:12390]
TTYH3	tweety homolog 3 (Drosophila) [Source:HGNC Symbol;Acc:22222]
TYMS	thymidylate synthetase [Source:HGNC Symbol;Acc:12441]
UCK2	uridine-cytidine kinase 2 [Source:HGNC Symbol;Acc:12562]
UCKL1	uridine-cytidine kinase 1-like 1 [Source:HGNC Symbol;Acc:15938]

3. Compilation of controllers of cellular metabolism

In addition to the metabolic genes that related to the gene signature of Haider et al. list, genes that encode enzymes and transporters that are important for the regulation of the energy metabolism and oncogenic signalling were also included in the screen (Table 3.2). This second part of the list was compiled from seminal papers and pathway maps that summarize genes involved in cancer metabolism (Hsu and Sabatini, 2008) (Cairns et al., 2011); (Gallagher and LeRoith, 2011); (Vander Heiden et al., 2009); (Cantor and Sabatini, 2012).

4. List of custom siRNA library genes

Table 3.2: Genes of the custom metabolic siRNA screen. (Met.=metabolism)

	Pathway	Gene Symbol	Function
	Lipid met.	*ACAA1α*	acetyl-CoA acyltransferase 1
CMS-R	ABC transporter	*ABCC1*	ATP-binding cassette, sub-family C (CFTR/MRP), member 1
CMS-R	ABC transporter	*ABCC10*	ATP-binding cassette, sub-family C (CFTR/MRP), member 10
CMS-R	ABC transporter	*ABCC12*	ATP-binding cassette, sub-family C (CFTR/MRP), member 12
CMS-R	ABC transporter	*ABCC2*	ATP-binding cassette, sub-family C (CFTR/MRP), member 2
CMS-R	ABC transporter	*ABCC3*	ATP-binding cassette, sub-family C (CFTR/MRP), member 3
CMS-R	ABC transporter	*ABCC4*	ATP-binding cassette, sub-family C (CFTR/MRP), member 4
CMS	ABC transporter	*ABCC5*	ATP-binding cassette, sub-family C (CFTR/MRP), member 5
CMS-R	ABC transporter	*ABCC6*	ATP-binding cassette, sub-family C (CFTR/MRP), member 6
CMS-R	ABC transporter	*ABCC8*	ATP-binding cassette, sub-family C (CFTR/MRP), member 8
CMS-R	ABC transporter	*ABCC9*	ATP-binding cassette, sub-family C (CFTR/MRP), member 9

	Lipid met.	*ACAA2*	acetyl-CoA acyltransferase 2
	Lipid met.	*ACACA*	acetyl-CoA carboxylase alpha
	Lipid met.	*ACACB*	acetyl-CoA carboxylase beta
	Lipid met.	*ACADL*	acyl-Coenzyme A dehydrogenase, long chain
	Lipid met.	*ACADM*	acyl-Coenzyme A dehydrogenase, C-4 to C-12 straight chain
	Lipid met.	*ACADS*	acyl-Coenzyme A dehydrogenase, C-2 to C-3 short chain
	Lipid met.	*ACADSB*	acyl-Coenzyme A dehydrogenase, short/branched chain
	Lipid met.	*ACADVL*	acyl-Coenzyme A dehydrogenase, very long chain
	Lipid met.	*ACAT1*	acetyl-CoA acetyltransferase 1
	Lipid met.	*ACAT2*	acetyl-CoA acetyltransferase 2
	Lipid met.	*ACLY*	ATP citrate lyase
	TCA cycle	*ACO1*	aconitase 1
	Lipid met.	*ACOT2*	acyl-CoA thioesterase 2
	Lipid met.	*ACOT4*	acyl-CoA thioesterase 4
	Lipid met.	*ACOT6*	acyl-CoA thioesterase 6
	Lipid met.	*ACOT7*	acyl-CoA thioesterase 7
	Lipid met.	*ACOT8*	acyl-CoA thioesterase 8
	Lipid met.	*ACOT9*	acyl-CoA thioesterase 9
	Lipid met.	*ACOT12*	acyl-CoA thioesterase 12
	Lipid met.	*ACOX1*	acyl-Coenzyme A oxidase 1, palmitoyl
	Lipid met.	*ACOX2*	acyl-Coenzyme A oxidase 2, branched chain
	Lipid met.	*ACOX3*	acyl-Coenzyme A oxidase 3, pristanoyl
	Lipid met.	*ACSBG1*	acyl-CoA synthetase bubblegum family member 1
	Lipid met.	*ACSBG2*	acyl-CoA synthetase bubblegum family member 2
	Lipid met.	*ACSL1*	acyl-CoA synthetase 1
	Lipid met.	*ACSL3*	acyl-CoA synthetase long-chain family member 3
	Lipid met.	*ACSL4*	acyl-CoA synthetase long-chain family member 4
	Lipid met.	*ACSL5*	acyl-CoA synthetase long-chain family member 5
	Lipid met.	*ACSL6*	acyl-CoA synthetase long-chain family member 6
	Lipid met.	*ACSM1*	acyl-CoA synthetase medium-chain family member 1
	Lipid met.	*ACSM3*	acyl-CoA synthetase medium-chain family member 3
	Lipid met.	*ACSS1*	acyl-CoA synthetase short-chain family member 1
	Lipid met.	*ACSS2*	acyl-CoA synthetase short-chain family member 2
CMS	Amino acid met.	*AHCY*	s-adenosylhomocysteine hydrolase
	Proliferation	*AKT1*	v-akt murine thymoma viral oncogene homolog 1
	Proliferation	*AKT1S1*	AKT1 substrate 1 (proline-rich)
	Proliferation	*AKT2*	v-akt murine thymoma viral oncogene homolog 2
	Proliferation	*AKT3*	v-akt murine thymoma viral oncogene homolog 3 (protein kinase B, gamma)
	Lipid met.	*ALDH2*	aldehyde dehydrogenase 2 family (mitochondrial)
	Glycolysis	*ALDOA*	aldolase A

	Glycolysis	*ALDOB*	aldolase B, fructose-bisphosphate
	Glycolysis	*ALDOC*	aldolase C, fructose-bisphosphate
CMS-R	Glucose met.	*ALG1*	asparagine-linked glycosylation 1 homolog (S. cerevisiae, beta-1,4-mannosyltransferase)
CMS-R	Glucose met.	*ALG10B*	asparagine-linked glycosylation 10 homolog B (yeast, alpha-1,2-glucosyltransferase)
CMS-R	Glucose met.	*ALG2*	asparagine-linked glycosylation 2 homolog (S. cerevisiae, alpha-1,3-mannosyltransferase)
CMS	Glucose met.	*ALG3*	asparagine-linked glycosylation 3 homolog (S. cerevisiae, alpha-1,3-mannosyltransferase)
CMS-R	Glucose met.	*ALG5*	asparagine-linked glycosylation 5 homolog (S. cerevisiae, dolichyl-phosphate beta-glucosyltransferase)
CMS-R	Glucose met.	*ALG6*	asparagine-linked glycosylation 6 homolog (S. cerevisiae, alpha-1,3-glucosyltransferase)
CMS-R	Glucose met.	*ALG8*	asparagine-linked glycosylation 8 homolog (S. cerevisiae, alpha-1,3-glucosyltransferase)
CMS-R	Glucose met.	*ALG9*	asparagine-linked glycosylation 9 homolog (S. cerevisiae, alpha- 1,2-mannosyltransferase)
CMS-R	Glucose met.	*ALG11*	asparagine-linked glycosylation 11 homolog (S. cerevisiae, alpha-1,2-mannosyltransferase)
CMS-R	Glucose met.	*ALG12*	asparagine-linked glycosylation 12 homolog (S. cerevisiae, alpha-1,6-mannosyltransferase)
CMS-R	Glucose met.	*ALG13*	asparagine-linked glycosylation 13 homolog (S. cerevisiae)
CMS-R	Glucose met.	*ALG14*	asparagine-linked glycosylation 14 homolog (yeast)
	Cell signalling	*ARHGEF9*	Cdc42 guanine nucleotide exchange factor (GEF) 9
	Complex 5	*ATP5A1*	ATP synthase, H+ transporting, mitochondrial F1 complex, alpha subunit 1, cardiac muscle
	Complex 5	*ATP5B*	ATP synthase, H+ transporting, mitochondrial F1 complex, beta polypeptide
	Complex 5	*ATP5C1*	ATP synthase, H+ transporting, mitochondrial F1 complex, gamma polypeptide 1
	Complex 5	*ATP5D*	ATP synthase, H+ transporting, mitochondrial F1 complex, delta subunit
	Complex 5	*ATP5E*	ATP synthase, H+ transporting, mitochondrial F1 complex, epsilo bunit
	Complex 5	*ATP5F1*	ATP synthase, H+ transporting, mitochondrial F0 complex, subunit B1
	Complex 5	*ATP5G1*	ATP synthase, H+ transporting, mitochondrial F0 complex, subunit C1 (subunit 9)
	Complex 5	*ATP5G2*	ATP synthase, H+ transporting, mitochondrial F0 complex, subunit C2 (subunit 9)
	Complex 5	*ATP5G3*	ATP synthase, H+ transporting, mitochondrial F0 complex, subunit C3 (subunit 9)
	Complex 5	*ATP5H*	ATP synthase, H+ transporting, mitochondrial F0 complex, subunit d
	Complex 5	*ATP5I*	ATP synthase, H+ transporting, mitochondrial F0 complex, subunit E
	Complex 5	*ATP5J*	ATP synthase, H+ transporting, mitochondrial F0 complex, subunit F6
	Complex 5	*ATP5J2*	ATP synthase, H+ transporting, mitochondrial F0 complex, subunit F2
	Complex 5	*ATP5L*	ATP synthase, H+ transporting, mitochondrial F0 complex, subunit G

	Complex 5	*ATP5O*	ATP synthase, H+ transporting, mitochondrial F1 complex, O subunit
	Complex 5	*ATP5S*	ATP synthase, H+ transporting, mitochondrial F0 complex, subunit s (factor B)
	Complex 5	*ATP6*	ATP synthase F0 subunit 6
	Complex 5	*ATP8*	ATP synthase F0 subunit 8
	Complex 5	*ATPAF1*	ATP synthase mitochondrial F1 complex assembly factor 1
	Complex 5	*ATPAF2*	ATP synthase mitochondrial F1 complex assembly factor 2
CMS-R	Glucose met.	*B4GALT1*	UDP-Gal:betaGlcNAc beta 1,4- galactosyltransferase, polypeptide 1
CMS-R	Glucose met.	*B4GALT2*	UDP-Gal:betaGlcNAc beta 1,4- galactosyltransferase, polypeptide 2
CMS	Glucose met.	*B4GALT3*	UDP-Gal:betaGlcNAc beta 1,4- galactosyltransferase, polypeptide 3
CMS-R	Glucose met.	*B4GALT5*	UDP-Gal:betaGlcNAc beta 1,4- galactosyltransferase, polypeptide 5
CMS-R	Glucose met.	*B4GALT6*	UDP-Gal:betaGlcNAc beta 1,4- galactosyltransferase, polypeptide 6
CMS-R	Glucose met.	*B4GALT7*	xylosylprotein beta 1,4-galactosyltransferase, polypeptide 7 (galactosyltransferase I)
	Lipid met.	*BDH1*	3-hydroxybutyrate dehydrogenase, type 1
	Lipid met.	*BDH2*	3-hydroxybutyrate dehydrogenase, type 2
	Pentose phosphate	*C12orf5*	Blocks glycolysis and promotes pentose phosphate (TIGAR)
CMS	Pyrimidine met.	*CAD*	carbamoyl-phosphate synthetase 2, aspartate transcarbamylase, and dihydroorotase
CMS-R	Anion channel	*CLCN1*	chloride channel 1, skeletal muscle (Thomsen disease, autosomal dominant)
CMS	Anion channel	*CLCN2*	chloride channel 2
CMS-R	Anion channel	*CLCN3*	chloride channel 3
CMS-R	Anion channel	*CLCN4*	chloride channel 4
CMS-R	Anion channel	*CLCN5*	chloride channel 5 (nephrolithiasis 2, X-linked, Dent disease)
CMS-R	Anion channel	*CLCN6*	chloride channel 6
CMS-R	Anion channel	*CLCN7*	chloride channel 7
CMS-R	Anion channel	*CLCNKA*	chloride channel Ka
CMS-R	Anion channel	*CLCNKB*	chloride channel Kb
	Complex 4	*COX1*	cytochrome c oxidase subunit I
	Complex 4	*COX2*	cytochrome c oxidase subunit II
	Complex 4	*COX3*	cytochrome c oxidase subunit III
	Complex 4	*COX4I1*	cytochrome c oxidase subunit IV isoform 1
	Complex 4	*COX4I2*	cytochrome c oxidase subunit IV isoform 2 (lung)
	Complex 4	*COX5A*	cytochrome c oxidase subunit Va
	Complex 4	*COX5B*	cytochrome c oxidase subunit Vb
	Complex 4	*COX6A1*	cytochrome c oxidase subunit VIa polypeptide 1
	Complex 4	*COX6A2*	cytochrome c oxidase subunit VIa polypeptide 2
	Complex 4	*COX6C*	cytochrome c oxidase subunit VIc
	Complex 4	*COX7A1*	cytochrome c oxidase subunit VIIa polypeptide 1
	Complex 4	*COX7A2*	cytochrome c oxidase subunit VIIa polypeptide 2
	Complex 4	*COX7B*	cytochrome c oxidase subunit VIIb

	Complex 4	*COX7B2*	cytochrome c oxidase subunit VIIb2
	Complex 4	*COX7C*	cytochrome c oxidase subunit VIIc
	Complex 4	*COX8A*	cytochrome c oxidase subunit VIIIA (ubiquitous)
	Complex 4	*COX8C*	cytochrome c oxidase subunit VIIIC
	Lipid met.	*CPT1A*	carnitine palmitoyltransferase 1A (liver)
	Lipid met.	*CPT1B*	carnitine palmitoyltransferase 1B (muscle)
	Lipid met.	*CPT1C*	carnitine palmitoyltransferase 1C (brain)
	Lipid met.	*CPT2*	carnitine palmitoyltransferase 2
	Lipid met.	*CRAT*	carnitine acetyltransferase
	Lipid met.	*CROT*	carnitine O-octanoyltransferase
	TCA cycle	*CS*	citrate Synthase
	Cell signalling	*CXCR4*	chemokine (C-X-C motif) receptor 4
	Complex 3	*CYC1*	cytochrome c-1
	Complex 4	*CYCS*	cytochrome c, somatic
	Lipid met.	*DECR1*	2,4-dienoyl CoA reductase 1, mitochondrial
	Lipid met.	*DECR2*	2,4-dienoyl CoA reductase 2, peroxisomal
CMS	Lipid met.	*DHCR7*	7-dehydrocholesterol reductase
CMS-R	Beta oxidation	*DHRS1*	dehydrogenase/reductase (SDR family) member 1
CMS	Beta oxidation	*DHRS13*	dehydrogenase/reductase (SDR family) member 13
CMS-R	Beta oxidation	*DHRS3*	dehydrogenase/reductase (SDR family) member 3
CMS-R	Beta oxidation	*DHRS4*	dehydrogenase/reductase (SDR family) member 4
CMS-R	Beta oxidation	*DHRS7*	dehydrogenase/reductase (SDR family) member 7
CMS-R	Beta oxidation	*DHRS7B*	dehydrogenase/reductase (SDR family) member 7B
CMS-R	Beta oxidation	*DHRS9*	dehydrogenase/reductase (SDR family) member 9
CMS-R	Beta oxidation	*DHRSX*	dehydrogenase/reductase (SDR family) X-linked
CMS	Beta oxidation	*DHTKD1*	dehydrogenase E1 and transketolase domain containing 1
	PDH complex	*DLAT*	pyruvate dehydrogenase subunit
	Pyruvate met.	*DLD*	dihydrolipamide dehydrogenase
	Lipid met.	*ECHS1*	enoyl coenzyme A hydratase, short chain, 1, mitochondrial
CMS-R	Beta oxidation	*EDEM1*	ER degradation enhancer, mannosidase alpha-like 1
CMS	Glucose met.	*EDEM2*	ER degradation enhancer, mannosidase alpha-like 2
CMS-R	Glucose met.	*EDEM3*	ER degradation enhancer, mannosidase alpha-like 3
	Proliferation	*EIF4EBP1*	eukaryotic translation initiation factor 4E binding protein 1
	Glycolysis	*ENO1*	enolase 1
	Glycolysis	*ENO2*	enolase 2 (gamma, neuronal)
	Glycolysis	*ENO3*	enolase 3 (beta, muscle)
	TCA cycle	*EPHB2*	EPH receptor B2
	Lipid met.	*FA2H*	fatty acid 2-hydroxylase
	Lipid met.	*FAAH*	fatty acid amide hydrolase
	Lipid met.	*FABP1*	fatty acid binding protein 1, liver
	Lipid met.	*FABP2*	fatty acid binding protein 2, intestinal

	Lipid met.	*FABP3*	fatty acid binding protein 3, muscle and heart (mammary-derived growth inhibitor)
	Lipid met.	*FABP4*	fatty acid binding protein 4, adipocyte
	Lipid met.	*FABP6*	fatty acid binding protein 6, ileal (gastrotropin)
	Lipid met.	*FABP7*	fatty acid binding protein 7, brain
	Lipid met.	*FADS1*	fatty acid desaturase 1
	Lipid met.	*FADS2*	fatty acid desaturase 2
	Lipid met.	*FADS3*	fatty acid desaturase 3
	Lipid met.	*FADS6*	fatty acid desaturase domain family, member 6
	Lipid met.	*FASN*	fatty acid synthase
	Glycolysis	*FBP1*	fructose-1,6-bisphosphatase 1
	Glycolysis	*FBP2*	fructose-1,6-bisphosphatase 2
	TCA cycle	*FH*	Fumarate hydratase
CMS	Glucose met.	*FLAD1*	FAD1 flavin adenine dinucleotide synthetase homolog (S. cerevisiae)
CMS	Transporter	*FLVCR1*	feline leukemia virus subgroup C cellular receptor
	Proliferation	*FRAP1*	FK506 binding protein 12-rapamycin associated protein 1
	Gluconeogenesis	*G6PC*	glucose-6-phosphatase, catalytic subunit
	Gluconeogenesis	*G6PC2*	glucose-6-phosphatase, catalytic, 2
	Gluconeogenesis	*G6PC3*	glucose 6 phosphatase, catalytic, 3
	Gluconeogenesis	*G6PD*	glucose 6-phosphate dehydrogenase
CMS	Glycolysis	*GAPDH*	glyceraldehyde-3-phosphate dehydrogenase
	Glycolysis	*GCK*	glucokinase
	Glycolysis	*GFOD1*	glucose-fructose oxidoreductase domain containing 1
	Glycolysis	*GFOD2*	glucose-fructose oxidoreductase domain containing 2
	Glutaminolysis	*GFPT1*	glutamine-fructose-6-phosphate transaminase 1
	Glutaminolysis	*GFPT2*	glutamine-fructose-6-phosphate transaminase 2
CMS	Pyrimidine met.	*GGH*	gamma-glutamyl hydrolase (conjugase, folylpolygammaglutamyl hydrolase)
	Lipid met.	*GK2*	glycerol kinase 2
	Glucose met.	*GLO1*	glyoxalase I
	TCA cycle	*GLS*	glutaminase
	TCA cycle	*GLS2*	glutaminase
	Glutaminolysis	*GLUD1*	glutamate dehydrogenase 1
	Glutaminolysis	*GLUL*	glutamate-ammonia ligase (glutamine synthetase)
	Glutaminolysis	*GLULD1*	glutamate-ammonia ligase (glutamine synthetase) domain containing 1
CMS	Purine met.	*GMPS*	guanine monophosphate synthetase
	Lipid met.	*GPD2*	glycerol-3-phosphate dehydrogenase 2 (mitochondrial)
	Pentose phosphate	*GPI*	glucose-6-phosphate isomerase
	Glucose met.	*GSK3A*	glycogen synthase kinase 3 alpha
	Glucose met.	*GSK3B*	glycogen synthase kinase 3 beta
	Lipid met.	*HADH*	hydroxyacyl-Coenzyme A dehydrogenase

	Lipid met.	*HADHA*	hydroxyacyl-Coenzyme A dehydrogenase alpha subunit
	Lipid met.	*HADHB*	hydroxyacyl-Coenzyme A dehydrogenase beta subunit
	Glucose met.	*HAGH*	hydroxyacylglutathione hydrolase
	Lactate production	*HAGHL*	hydroxyacylglutathione hydrolase-like
CMS-R	Cation channel	*HCN1*	hyperpolarisation activated cyclic nucleotide-gated potassium channel 1
CMS-R	Cation channel	*HCN2*	hyperpolarisation activated cyclic nucleotide-gated potassium channel 2
CMS	Cation channel	*HCN3*	hyperpolarisation activated cyclic nucleotide-gated potassium channel 3
CMS-R	Cation channel	*HCN4*	hyperpolarisation activated cyclic nucleotide-gated potassium channel 4
	Hypoxia	*HIF-1A*	Hypoxia inducible factor
	Hypoxia	*HIF-1AN*	hypoxia-inducible factor 1, alpha subunit inhibitor
	Hypoxia	*HIF3A*	hypoxia inducible factor 3, alpha subunit
	Hypoxia	*HIG2*	hypoxia-inducible protein 2
	Glycolysis	*HK1*	hexokinase 1
	Glycolysis	*HK2*	hexokinase 2
	Glycolysis	*HK3*	hexokinase 3 (white cell)
	Glucose met.	*HKDC1*	hexokinase domain containing 1
	Lipid met.	*HMGCL*	3-hydroxymethyl-3-methylglutaryl-Coenzyme A lyase (hydroxymethylglutaricaciduria)
	Lipid met.	*HMGCLL1*	3-hydroxymethyl-3-methylglutaryl-Coenzyme A lyase-like 1
	Lipid met.	*HMGCR*	3-hydroxy-3-methylglutaryl-CoA reductase
	Lipid met.	*HMGCS1*	3-hydroxy-3-methylglutaryl-CoA synthase 1
	Lipid met.	*HMGCS2*	3-hydroxy-3-methylglutaryl-CoA synthase 2 (mitochondrial)
	Proliferation	*HNF4A*	hepatocyte nuclear factor 4, alpha
	Proliferation	*HNF4G*	hepatocyte nuclear factor 4, gamma
	Hypoxia	*HSPBAP1*	HSPB (heat shock 27kDa) associated protein 1
	Hypoxia	*HSPBP1*	hsp70-interacting protein
	Hypoxia	*HYOU1*	hypoxia up-regulated 1
	TCA cycle	*IDH1*	Isocitrate dehydrogenase 1
	TCA cycle	*IDH2*	Isocitrate dehydrogenase 2
CMS	Nucleotide met.	*IMPDH1*	IMP (inosine monophosphate) dehydrogenase 1
CMS-R	Nucleotide met.	*IMPDH2*	IMP (inosine monophosphate) dehydrogenase 2
CMS	Nucleotide met.	*ITPA*	inosine triphosphatase (nucleoside triphosphate pyrophosphatase)
CMS-R	Cation channel	*KCNMA1*	potassium large conductance calcium-activated channel, subfamily M, alpha member 1
CMS-R	Cation channel	*KCNMB1*	potassium large conductance calcium-activated channel, subfamily M, beta member 1
CMS-R	Cation channel	*KCNMB2*	potassium large conductance calcium-activated channel, subfamily M, beta member 2
CMS	Cation channel	*KCNMB3*	potassium large conductance calcium-activated channel, subfamily M beta member 3
CMS-R	Cation channel	*KCNMB4*	potassium large conductance calcium-activated channel, subfamily

			M, beta member 4
	Glycolysis	*LDHA*	lactate dehydrogenase
	Glucose met.	*LDHAL6B*	lactate dehydrogenase A-like 6B
	Glucose met.	*LDHB*	lactate dehydrogenase B
	Glucose met.	*LDHC*	lactate dehydrogenase C
	Glucose met.	*LDHD*	lactate dehydrogenase D
	Lipid met.	*LDLR*	low density lipoprotein receptor (familial hypercholesterolemia)
	Lipid met.	*LDLRAD1*	low density lipoprotein receptor class A domain containing 1
	Lipid met.	*LDLRAD2*	low density lipoprotein receptor class A domain containing 2
	Lipid met.	*LDLRAD3*	low density lipoprotein receptor class A domain containing 3
	Lipid met.	*LDLRAP1*	low density lipoprotein receptor adaptor protein 1
	Lipid met.	*LIPA*	lipase A, lysosomal acid, cholesterol esterase (Wolman disease)
	Lipid met.	*LIPC*	lipase, hepatic
	Lipid met.	*LIPE*	lipase, hormone-sensitive
	Lipid met.	*LIPF*	lipase, gastric
	Lipid met.	*LIPG*	lipase, endothelial
	Lipid met.	*LIPH*	lipase, member H
	Lipid met.	*LOC646486*	fatty acid binding protein
CMS	Lipid met.	*LPCAT1*	lysophosphatidylcholine acyltransferase 1
	Lipid met.	*LPL*	lipoprotein lipase
	TCA cycle	*MAP2K1*	mitogen-activated protein kinase kinase 1
	TCA cycle	*MAP2K2*	mitogen-activated protein kinase kinase 2
	Lipid met.	*MCEE*	methylmalonyl CoA epimerase
	TCA cycle	*MDH1*	malate dehydrogenase 1, NAD (soluble)
	TCA cycle	*MDH2*	malate dehydrogenase 2, NAD (mitochondrial)
	Pyruvate met.	*ME1*	malic enzyme 1
	Pyruvate met.	*ME2*	malic enzyme 2
	Pyruvate met.	*ME3*	malic enzyme 3
	Proliferation	*MEF2A*	MADS box transcription enhancer factor 2, polypeptide A (myocyte enhancer factor 2A)
	Proliferation	*MEF2B*	MADS box transcription enhancer factor 2, polypeptide B (myocyte enhancer factor 2B)
	Proliferation	*MEF2C*	MADS box transcription enhancer factor 2, polypeptide C (myocyte enhancer factor 2C)
	Proliferation	*MEF2D*	MADS box transcription enhancer factor 2, polypeptide D (myocyte enhancer factor 2D)
	Complex 1	*MT-ND1*	NADH dehydrogenase 1, mitochondrial EC
	Complex 1	*MT-ND2*	NADH dehydrogenase 2, mitochondrial EC
	Complex 1	*MT-ND3*	NADH dehydrogenase 3, mitochondrial EC
	Complex 1	*MT-ND4*	NADH dehydrogenase 4, mitochondrial EC
	Complex 1	*MT-ND4L*	NADH dehydrogenase 4L, mitochondrial EC
	Complex 1	*MT-ND5*	NADH dehydrogenase 5, mitochondrial EC
	Complex 1	*MT-ND6*	NADH dehydrogenase 6, mitochondrial EC

	Lipid met.	*MUT*	methylmalonyl CoA mutase
CMS	Lipid met.	*NAT9*	N-acetyltransferase 9
	Complex 1	*NDUFS1*	NADH-ubiquinone oxidoreductase 75 kDa subunit, mitochondrial EC
	Complex 1	*NDUFS2*	NADH dehydrogenase [ubiquinone] iron-sulfur protein 2, mitochondrial EC
	Complex 1	*NDUFS3*	NADH dehydrogenase [ubiquinone] iron-sulfur protein 3, mitochondrial EC
	Complex 1	*NDUFS7*	NADH dehydrogenase [ubiquinone] iron-sulfur protein 7, mitochondrial EC
	Complex 1	*NDUFS8*	NADH dehydrogenase (ubiquinone) Fe-S protein 8, mitochondrial EC
	Complex 1	*NDUFV1*	NADH dehydrogenase [ubiquinone] flavoprotein 1, mitochondrial EC
	Complex 1	*NDUFV2*	NADH dehydrogenase [ubiquinone] flavoprotein 2, mitochondrial EC
CMS	Pyrimidine met.	*NME1*	non-metastatic cells 1, protein (NM23A) expressed in
CMS	Nucleotide met.	*NUDT1*	nudix (nucleoside diphosphate linked moiety X)-type motif 1
CMS-R	Nucleotide met.	*NUDT10*	nudix (nucleoside diphosphate linked moiety X)-type motif 10
CMS-R	Nucleotide met.	*NUDT2*	nudix (nucleoside diphosphate linked moiety X)-type motif 2
CMS-R	Nucleotide met.	*NUDT3*	nudix (nucleoside diphosphate linked moiety X)-type motif 3
CMS-R	Nucleotide met.	*NUDT4*	nudix (nucleoside diphosphate linked moiety X)-type motif 4
CMS-R	Nucleotide met.	*NUDT5*	nudix (nucleoside diphosphate linked moiety X)-type motif 5
	TCA cycle	*OGDH*	alpha-ketoglutarate dehydrogenase
	lutaminolysis	*OXGR1*	oxoglutarate (alpha-ketoglutarate) receptor 1
	TCA cycle	*PC*	pyruvate carboxylase
	TCA cycle	*PCK1*	phosphoenolpyruvate carboxykinase 1 (soluble)
	TCA cycle	*PCK2*	phosphoenolpyruvate carboxykinase 2 (mitochondrial)
CMS-R	Purine met.	*PDE1A*	phosphodiesterase 1A, calmodulin-dependent
CMS-R	Purine met.	*PDE1B*	phosphodiesterase 1B, calmodulin-dependent
CMS-R	Purine met.	*PDE1C*	phosphodiesterase 1C, calmodulin-dependent 70kDa
CMS-R	Purine met.	*PDE2A*	phosphodiesterase 2A, cGMP-stimulated
CMS-R	Purine met.	*PDE3A*	phosphodiesterase 3A, cGMP-inhibited
CMS-R	Purine met.	*PDE3B*	phosphodiesterase 3B, cGMP-inhibited
CMS-R	Purine met.	*PDE4A*	phosphodiesterase 4A, cAMP-specific (phosphodiesterase E2 dunce homolog, Drosophila)
CMS-R	Purine met.	*PDE4B*	phosphodiesterase 4B, cAMP-specific (phosphodiesterase E4 dunce homolog, Drosophila)
CMS-R	Purine met.	*PDE4C*	phosphodiesterase 4C, cAMP-specific (phosphodiesterase E1 dunce homolog, Drosophila)
CMS-R	Purine met.	*PDE4D*	phosphodiesterase 4D, cAMP-specific (phosphodiesterase E3 dunce homolog, Drosophila)
CMS-R	Purine met.	*PDE4DIP*	phosphodiesterase 4D interacting protein (myomegalin)
CMS-R	Purine met.	*PDE5A*	phosphodiesterase 5A, cGMP-specific
CMS-R	Purine met.	*PDE6A*	phosphodiesterase 6A, cGMP-specific, rod, alpha
CMS-R	Purine met.	*PDE6B*	phosphodiesterase 6B, cGMP-specific, rod, beta (congenital stationary night blindness 3, autosomal dominant)

CMS-R	Purine met.	*PDE6C*	phosphodiesterase 6C, cGMP-specific, cone, alpha prime
CMS-R	Purine met.	*PDE6D*	phosphodiesterase 6D, cGMP-specific, rod, delta
CMS-R	Purine met.	*PDE6G*	phosphodiesterase 6G, cGMP-specific, rod, gamma
CMS-R	Purine met.	*PDE6H*	phosphodiesterase 6H, cGMP-specific, cone, gamma
CMS	Purine met.	*PDE7A*	phosphodiesterase 7A
CMS-R	Purine met.	*PDE7B*	phosphodiesterase 7B
CMS-R	Purine met.	*PDE8A*	phosphodiesterase 8A
CMS-R	Purine met.	*PDE8B*	phosphodiesterase 8B
CMS-R	Purine met.	*PDE9A*	phosphodiesterase 9A
CMS-R	Purine met.	*PDE10A*	phosphodiesterase 10A
CMS-R	Purine met.	*PDE11A*	phosphodiesterase 11A
	PDH complex	*PDHA1*	pyruvate dehydrogenase subunit
	PDH complex	*PDHA2*	pyruvate dehydrogenase (lipoamide) alpha 2
	PDH complex	*PDHB*	pyruvate dehydrogenase subunit
	PDH complex	*PDHX*	pyruvate dehydrogenase subunit
	PDH complex	*PDK1*	pyruvate dehydrogenase kinase
	PDH complex	*PDP1*	pyruvate dehydrogenase subunit
	Glycolysis	*PFKFB1*	6-phosphofructo-2-kinase/fructose-2,6-biphosphatase 1
	Glycolysis	*PFKFB2*	6-phosphofructo-2-kinase/fructose-2,6-biphosphatase 2
	Glycolysis	*PFKFB3*	6-phosphofructo-2-kinase/fructose-2,6-biphosphatase 3
	Glycolysis	*PFKFB4*	6-phosphofructo-2-kinase/fructose-2,6-biphosphatase 4
	Glycolysis	*PFKL*	phosphofructokinase, liver
	Glycolysis	*PFKM*	Phosphofructokinase
	Glycolysis	*PFKP*	phosphofructokinase, platelet
	Pentose phosphate	*PGD*	phosphogluconate dehydrogenase
	Glycolysis	*PGK1*	phosphoglycerate kinase
	Pentose phosphate	*PGLS*	6-phosphogluconolactonase
	Glycolysis	*PGM1*	phosphoglucomutase
CMS-R	Lipid met.	*PIGS*	phosphatidylinositol glycan anchor biosynthesis, class S
CMS-R	Lipid met.	*PIGT*	phosphatidylinositol glycan anchor biosynthesis, class T
CMS	Lipid met.	*PIGU*	phosphatidylinositol glycan anchor biosynthesis, class U
CMS-R	Lipid met.	*PIGV*	phosphatidylinositol glycan anchor biosynthesis, class V
CMS-R	Lipid met.	*PIGW*	phosphatidylinositol glycan anchor biosynthesis, class W
CMS-R	Lipid met.	*PIGX*	phosphatidylinositol glycan anchor biosynthesis, class X
CMS-R	Lipid met.	*PIGY*	phosphatidylinositol glycan anchor biosynthesis, class Y
CMS-R	Lipid met.	*PIGZ*	phosphatidylinositol glycan anchor biosynthesis, class Z
	Glycolysis	*PKM*	pyruvate kinase
CMS-R	Glycolysis	*PMM1*	phosphomannomutase 1
CMS	Glycolysis	*PMM2*	phosphomannomutase 2
	Proliferation	*PPARA*	peroxisome proliferator-activated receptor alpha

	Proliferation	*PPARBP*	PPAR binding protein
	Proliferation	*PPARD*	peroxisome proliferator-activated receptor delta
	Proliferation	*PPARG*	peroxisome proliferator-activated receptor gamma
	Proliferation	*PPARGC1A*	peroxisome proliferator-activated receptor gamma, coactivator 1 alpha
		PPARGC1B	peroxisome proliferator-activated receptor gamma, coactivator 1 beta
	Lipid met.	*PRKAA1*	protein kinase, AMP-activated, alpha 1 catalytic subunit
	Lipid met.	*PRKAA2*	protein kinase, AMP-activated, alpha 2 catalytic subunit
	Lipid met.	*PRKAB1*	protein kinase, AMP-activated, beta 1 non-catalytic subunit
	Lipid met.	*PRKAB2*	protein kinase, AMP-activated, beta 2 non-catalytic subunit
	Lipid met.	*PRKAG1*	protein kinase, AMP-activated, gamma 1 non-catalytic subunit
	Lipid met.	*PRKAG2*	protein kinase, AMP-activated, gamma 2 non-catalytic subunit
	Lipid met.	*PRKAG3*	protein kinase, AMP-activated, gamma 3 non-catalytic subunit
CMS	Glycolysis	*PSPH*	phosphoserine phosphatase
CMS	Arginine and proline met.	*PYCR1*	pyrroline-5-carboxylate reductase 1
CMS-R	Arginine and proline met.	*PYCR2*	pyrroline-5-carboxylate reductase family, member 2
CMS	Arginine and proline met.	*PYCRL*	pyrroline-5-carboxylate reductase-like
	Pentose phosphate	*RPE*	ribulose-5-phosphate-3-epimerase
	Pentose phosphate	*RPIA*	ribose 5-phosphate isomerase A
	Nucleotide met.	*RRM1*	ribonucleotide reductase M1 polypeptide
	Nucleotide met.	*RRM2*	ribonucleotide reductase M2 polypeptide
	Nucleotide met.	*RRM2B*	ribonucleotide reductase M2 B (TP53 inducible)
	Lipid met.	*SCARB1*	scavenger receptor class B, member 1
	Electron transport chain	*SCO2*	cytochrome x oxidase
	Complex 2	*SDHA*	succinate dehydrogenase A
	Complex 2	*SDHB*	succinate dehydrogenase B
	Complex 2	*SDHC*	succinate dehydrogenase C
	Complex 2	*SDHD*	succinate dehydrogenase D
CMS	Amino acid met.	*SHMT2*	serine hydroxymethyltransferase 2 (mitochondrial)
	TCA cycle	*SIRT3*	NAD-dependent deacetylase sirtuin-3, mitochondrial
	Hypoxia	*SIRT6*	Sirtuin 6
CMS-R	Cation transporter	*SLC12A1*	solute carrier family 12 (sodium/potassium/chloride transporters), member 1
CMS-R	Cation transporter	*SLC12A2*	solute carrier family 12 (sodium/potassium/chloride transporters), member 2
CMS-R	Cation transporter	*SLC12A3*	solute carrier family 12 (sodium/chloride transporters), member 3
CMS-R	Cation transporter	*SLC12A4*	solute carrier family 12 (potassium/chloride transporters), member 4
CMS-R	Cation	*SLC12A6*	solute carrier family 12 (potassium/chloride transporters), member

	transporter		6
CMS-R	Cation transporter	*SLC12A7*	solute carrier family 12 (potassium/chloride transporters), member 7
CMS	Cation transporter	*SLC12A8*	solute carrier family 12 (potassium/chloride transporters), member 8
CMS-R	Cation transporter	*SLC12A9*	solute carrier family 12 (potassium/chloride transporters), member 9
	TCA cycle	*SLC1A5*	glutamine transporter
CMS-R	Mitochondrial transporter	*SLC25A1*	solute carrier family 25 (mitochondrial carrier; citrate transporter), member 1
CMS-R	Mitochondrial transporter	*SLC25A11*	solute carrier family 25 (mitochondrial carrier; oxoglutarate carrier), member 11
CMS-R	Mitochondrial transporter	*SLC25A12*	solute carrier family 25 (mitochondrial carrier, Aralar), member 12
CMS	Mitochondrial transporter	*SLC25A13*	solute carrier family 25, member 13 (citrin)
CMS-R	Mitochondrial transporter	*SLC25A14*	solute carrier family 25 (mitochondrial carrier, brain), member 14
CMS-R	Mitochondrial transporter	*SLC25A15*	solute carrier family 25 (mitochondrial carrier; ornithine transporter) member 15
CMS-R	Mitochondrial transporter	*SLC25A16*	solute carrier family 25 (mitochondrial carrier; Graves disease autoantigen), member 16
CMS-R	Mitochondrial transporter	*SLC25A17*	solute carrier family 25 (mitochondrial carrier; peroxisomal membrane protein, 34kDa), member 17
CMS-R	Mitochondrial transporter	*SLC25A18*	solute carrier family 25 (mitochondrial carrier), member 18
CMS-R	Mitochondrial transporter	*SLC25A19*	solute carrier family 25 (mitochondrial deoxynucleotide carrier), member 19
CMS-R	Mitochondrial transporter	*SLC25A2*	solute carrier family 25 (mitochondrial carrier; ornithine transporter) member 2
CMS-R	Mitochondrial transporter	*SLC25A20*	solute carrier family 25 (carnitine/acylcarnitine translocase), member 20
CMS-R	Mitochondrial transporter	*SLC25A21*	solute carrier family 25 (mitochondrial oxodicarboxylate carrier), member 21
CMS-R	Mitochondrial transporter	*SLC25A22*	solute carrier family 25 (mitochondrial carrier: glutamate), member 22
CMS-R	Mitochondrial transporter	*SLC25A23*	solute carrier family 25 (mitochondrial carrier; phosphate carrier), member 23
CMS-R	Mitochondrial transporter	*SLC25A24*	solute carrier family 25 (mitochondrial carrier; phosphate carrier), member 24
CMS-R	Mitochondrial transporter	*SLC25A25*	solute carrier family 25 (mitochondrial carrier; phosphate carrier), member 25
CMS-R	Mitochondrial transporter	*SLC25A3*	solute carrier family 25 (mitochondrial carrier; phosphate carrier), member 3
CMS-R	Mitochondrial transporter	*SLC25A31*	solute carrier family 25 (mitochondrial carrier; adenine nucleotide translocator), member 31
CMS-R	Mitochondrial transporter	*SLC25A4*	solute carrier family 25 (mitochondrial carrier; adenine nucleotide translocator), member 4
CMS-R	Mitochondrial transporter	*SLC25A5*	solute carrier family 25 (mitochondrial carrier; adenine nucleotide translocator), member 5
CMS-R	Mitochondrial transporter	*SLC25A6*	solute carrier family 25 (mitochondrial carrier; adenine nucleotide translocator), member 6
	Lipid met.	*SLC27A1*	solute carrier family 27 (fatty acid transporter), member 1

	Lipid met.	*SLC27A2*	solute carrier family 27 (fatty acid transporter), member 2
	Lipid met.	*SLC27A3*	solute carrier family 27 (fatty acid transporter), member 3
	Lipid met.	*SLC27A4*	solute carrier family 27 (fatty acid transporter), member 4
	Lipid met.	*SLC27A5*	solute carrier family 27 (fatty acid transporter), member 5
	Lipid met.	*SLC27A6*	solute carrier family 27 (fatty acid transporter), member 6
	Mitochondrial transport	*SLC28A1*	solute carrier family 28 (sodium-coupled nucleoside transporter), member 1
	Mitochondrial transport	*SLC28A2*	solute carrier family 28 (sodium-coupled nucleoside transporter), member 2
	Mitochondrial transport	*SLC28A3*	solute carrier family 28 (sodium-coupled nucleoside transporter), member 3
	Mitochondrial transport	*SLC29A1*	solute carrier family 29 (nucleoside transporters), member 1
	Mitochondrial transport	*SLC29A2*	solute carrier family 29 (nucleoside transporters), member 2
	Mitochondrial transport	*SLC29A3*	solute carrier family 29 (nucleoside transporters), member 3
	Mitochondrial transport	*SLC29A4*	solute carrier family 29 (nucleoside transporters), member 4
	Glycolysis	*SLC2A1*	glucose transporter (GLUT1)
	Mitochondrial transport	*SLC2A10*	solute carrier family 2 (facilitated glucose transporter), member 10
	Mitochondrial transport	*SLC2A12*	solute carrier family 2 (facilitated glucose transporter), member 12
	Mitochondrial transport	*SLC2A13*	solute carrier family 2 (facilitated glucose transporter), member 13
	Glycolysis	*SLC2A2*	glucose transporter (GLUT2)
	Mitochondrial transport	*SLC2A3*	solute carrier family 2 (facilitated glucose transporter), member 3
	Mitochondrial transport	*SLC2A4*	solute carrier family 2 (facilitated glucose transporter), member 4
	Mitochondrial transport	*SLC2A5*	solute carrier family 2 (facilitated glucose/fructose transporter), member 5
	Mitochondrial transport	*SLC2A6*	solute carrier family 2 (facilitated glucose transporter), member 6
	Mitochondrial transport	*SLC2A7*	solute carrier family 2 (facilitated glucose transporter), member 7
	Mitochondrial transport	*SLC2A8*	solute carrier family 2, (facilitated glucose transporter) member 8
	Mitochondrial transport	*SLC2A9*	solute carrier family 2 (facilitated glucose transporter), member 9
CMS-R	Senescence and autophagy	*SLC39A1*	solute carrier family 39 (zinc transporter), member 1
CMS-R	Senescence and autophagy	*SLC39A10*	solute carrier family 39 (zinc transporter), member 10
CMS	Senescence and autophagy	*SLC39A11*	solute carrier family 39 (metal ion transporter), member 11
CMS-R	Senescence and autophagy	*SLC39A12*	solute carrier family 39 (zinc transporter), member 12
CMS-R	Senescence and autophagy	*SLC39A13*	solute carrier family 39 (zinc transporter), member 13

CMS-R	Senescence and autophagy	*SLC39A14*	solute carrier family 39 (zinc transporter), member 14
CMS-R	Senescence and autophagy	*SLC39A2*	solute carrier family 39 (zinc transporter), member 2
CMS-R	Senescence and autophagy	*SLC39A3*	solute carrier family 39 (zinc transporter), member 3
CMS	Senescence and autophagy	*SLC39A4*	solute carrier family 39 (zinc transporter), member 4
CMS-R	Senescence and autophagy	*SLC39A5*	solute carrier family 39 (metal ion transporter), member 5
CMS-R	Senescence and autophagy	*SLC39A6*	solute carrier family 39 (zinc transporter), member 6
CMS-R	Senescence and autophagy	*SLC39A7*	solute carrier family 39 (zinc transporter), member 7
CMS-R	Senescence and autophagy	*SLC39A8*	solute carrier family 39 (zinc transporter), member 8
CMS-R	Senescence and autophagy	*SLC39A9*	solute carrier family 39 (zinc transporter), member 9
CMS-R	Anion channel	*SLC4A1*	solute carrier family 4, anion exchanger, member 1 (erythrocyte membrane protein band 3, Diego blood group)
CMS-R	Anion channel	*SLC4A10*	solute carrier family 4, sodium bicarbonate transporter-like, member 10
CMS-R	Anion channel	*SLC4A11*	solute carrier family 4, sodium bicarbonate transporter-like, member 11
CMS-R	Anion channel	*SLC4A1AP*	solute carrier family 4 (anion exchanger), member 1, adaptor protein
CMS-R	Anion channel	*SLC4A2*	solute carrier family 4, anion exchanger, member 2 (erythrocyte membrane protein band 3-like 1)
CMS-R	Anion channel	*SLC4A3*	solute carrier family 4, anion exchanger, member 3
CMS-R	Anion channel	*SLC4A5*	solute carrier family 4, sodium bicarbonate cotransporter, member 5
CMS-R	Anion channel	*SLC4A7*	solute carrier family 4, sodium bicarbonate cotransporter, member 7
CMS-R	Anion channel	*SLC4A8*	solute carrier family 4, sodium bicarbonate cotransporter, member 8
CMS-R	Anion channel	*SLC4A9*	solute carrier family 4, sodium bicarbonate cotransporter, member 9
CMS-R	Sodium/sugar cotransporter	*SLC5A1*	solute carrier family 5 (sodium/glucose cotransporter), member 1
CMS-R	Sodium/sugar cotransporter	*SLC5A10*	solute carrier family 5 (sodium/glucose cotransporter), member 10
CMS-R	Sodium/sugar cotransporter	*SLC5A11*	solute carrier family 5 (sodium/glucose cotransporter), member 11
CMS-R	Sodium/sugar cotransporter	*SLC5A12*	solute carrier family 5 (sodium/glucose cotransporter), member 12
CMS-R	Sodium/sugar cotransporter	*SLC5A2*	solute carrier family 5 (sodium/glucose cotransporter), member 2
CMS-R	Sodium/sugar cotransporter	*SLC5A3*	solute carrier family 5 (inositol transporters), member 3
CMS-R	Sodium/sugar cotransporter	*SLC5A4*	solute carrier family 5 (low affinity glucose cotransporter), member 4
CMS-R	Sodium/sugar cotransporter	*SLC5A5*	solute carrier family 5 (sodium iodide symporter), member 5

CMS	Sodium/sugar cotransporter	*SLC5A6*	solute carrier family 5 (sodium-dependent vitamin transporter), member 6
CMS-R	Sodium/sugar cotransporter	*SLC5A7*	solute carrier family 5 (choline transporter), member 7
CMS-R	Sodium/sugar cotransporter	*SLC5A8*	solute carrier family 5 (iodide transporter), member 8
CMS-R	Sodium/sugar cotransporter	*SLC5A9*	solute carrier family 5 (sodium/glucose cotransporter), member 9
	Lipid met.	*SNCA*	synuclein, alpha (non A4 component of amyloid precursor)
CMS	Lipid met.	*SQLE*	squalene epoxidase
CMS	Lipid met.	*SRD5A1*	steroid-5-alpha-reductase, alpha polypeptide 1 (3-oxo-5 alpha-steroid delta 4-dehydrogenase alpha 1)
CMS-R	Lipid met.	*SRD5A2*	steroid-5-alpha-reductase, alpha polypeptide 2 (3-oxo-5 alpha-steroid delta 4-dehydrogenase alpha 2)
	Lipid met.	*SREBF1*	sterol regulatory element binding transcription factor 1
	Lipid met.	*SREBF2*	sterol regulatory element binding transcription factor 2
	Amino acid met.	*STK11IP*	serine/threonine kinase 11 interacting protein
	Pentose phosphate	*TALDO1*	transaldolase 1
	Proliferation	*TCEB2*	transcription elongation factor B (SIII), polypeptide 2 (18kDa, elongin B)
	Proliferation	*TCEB3*	transcription elongation factor B (SIII), polypeptide 3 (110kDa, elongin A)
CMS	Pyrimidine met.	*TK1*	thymidine kinase 1, soluble
	Pentose phosphate	*TKTL1*	transkelotase
	Proliferation	*TP53*	tumour protein p53 (Li-Fraumeni syndrome)
	Glycolysis	*TPI1*	triosephosphate isomerase
CMS	Glucose met.	*TSTA3*	tissue specific transplantation antigen P35B
CMS	Anion channel	*TTYH3*	tweety homolog 3 (Drosophila)
CMS	Pyrimidine met.	*TYMS*	thymidylate synthetase
CMS-R	Pyrimidine met.	*UCK1*	uridine-cytidine kinase 1
CMS	Pyrimidine met.	*UCK2*	uridine-cytidine kinase 2
CMS	Pyrimidine met.	*UCKL1*	uridine-cytidine kinase 1-like 1
	Complex 3	*UQCC1*	ubiquinol-cytochrome c reductase complex assembly factor 1
	Complex 3	*UQCC2*	ubiquinol-cytochrome c reductase complex assembly factor 2
	Complex 3	*UQCR10*	ubiquinol-cytochrome c reductase, complex III subunit X
	Complex 3	*UQCR11*	ubiquinol-cytochrome c reductase, complex III subunit XI
	Complex 3	*UQCRB*	ubiquinol-cytochrome c reductase binding protein
	Complex 3	*UQCRC1*	ubiquinol-cytochrome c reductase core protein I
	Complex 3	*UQCRC2*	ubiquinol-cytochrome c reductase core protein II
	Complex 3	*UQCRFS1*	ubiquinol-cytochrome c reductase, Rieske iron-sulfur polypeptide 1
	Complex 3	*UQCRH*	ubiquinol-cytochrome c reductase hinge protein
	Complex 3	*UQCRQ*	ubiquinol-cytochrome c reductase, complex III subunit VII
	Anion channel	*VDAC*	Voltage-dependent anion channel 1

D) Setting up screen conditions and controls

Dharmacon Smartpool siRNAs were used for the siRNA screen. By targeting four mRNA regions, these pools aim to reduce false negatives, and effective silencing can be achieved at low concentrations of siRNAs. This also reduces off-target silencing. These siRNAs aim specific knockdown by avoiding targeting common seed regions and produce siRNAs without perfect matches at the 3'UTR region of the antisense strand of the siRNA (Birmingham et al., 2006). Sense strand modification with 2′-O-methyl groups prevent its interaction with RISC and antisense strand phosphorylation at the 5'-end (Jackson, 2006). Off-target effects are important to avoid as they might lead to phenotypical changes that lead to the identification of false-positives of an siRNA screen. Since the concentration of the siRNA can play an important role in its off-target effects, the concentration of each siRNA for the screen was kept at 20 nM, the lowest concentration suggested by the manufacturer (Dharmacon, 2014).

HCT116 cells were selected for their ease of transfection (He et al., 2014), and near diploid karyotype and chromosome stability (Thompson and Compton, 2008). P53 mutations can alter cell cycle arrest (Sokolova et al., 2016), therefore wild-type p53 status of HCT116 cells played a role in our selection.

DharmaFECT2, which is the transfection reagent suggested for HCT116 cells (Dharmacon, 2018), was selected for the siRNA screen. The cell seeding density was aimed to be kept high, to allow enough cells for flow cytometry analysis in the 96-well format, while not exceeding 80% confluence in the negative control group (non-targeting siRNA: siNT) following a three-day transfection. It was preferred to not extend transfection length over three days to avoid having to change the media, which could cause cell loss and major metabolic changes. This would allow the cells to be analysed via high-throughput flow cytometry at the end-point of transfection.

Within the ranges suggested by the manufacturer, different concentrations of DharmaFECT were also tested (Figure 3.1). Two sets of positive controls were used for

assay optimisation: 1) cell viability positive control and 2) cell cycle arrest positive control. The first positive control group was PLK1, the knockdown of which was expected to cause cell death (Pezuk et al., 2013).

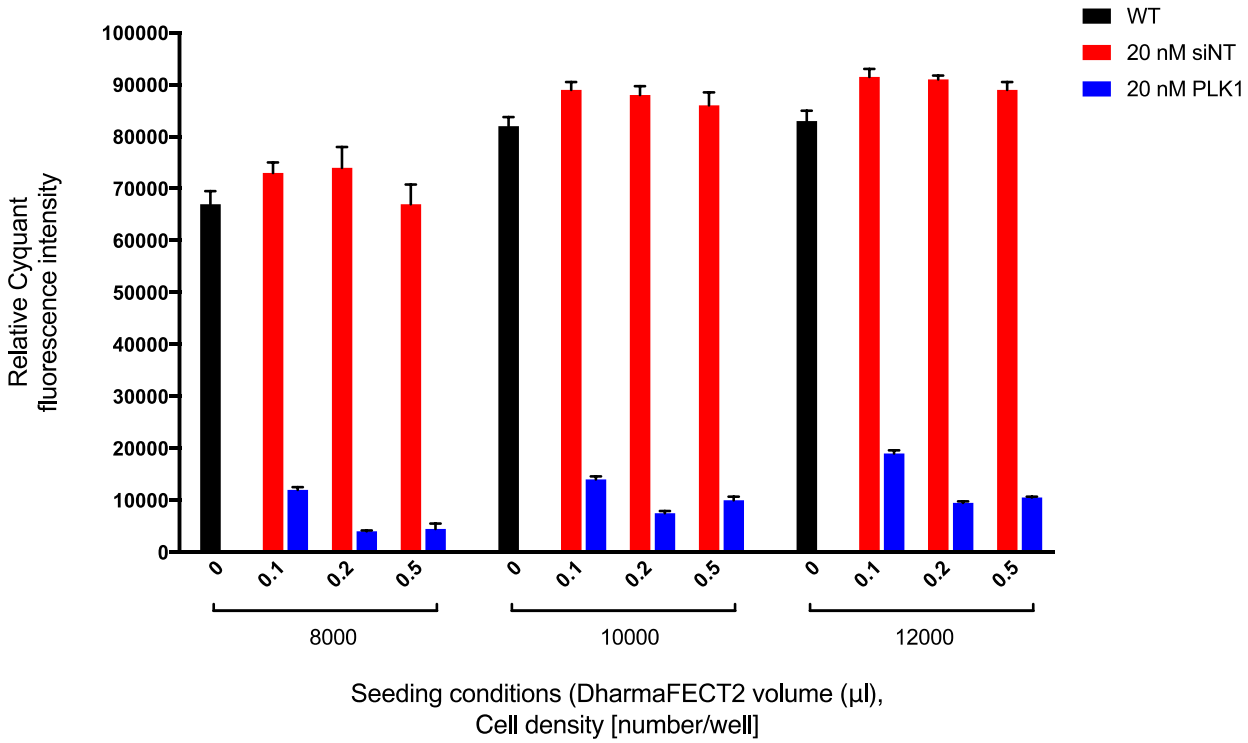


Figure 3.1: Cell seeding density and volume of transfection reagent were determined. siPLK1 was used a positive control to induce lowering of cell viability, indicated by the fluorescence signal of the CyQuant direct-cell assay. Data are mean±standard deviation, n=6 biological replicates. One-way ANOVA with Dunnett's multiple comparisons test was used to compare CyQuant signals of siNT and siPLK1 groups; P was determined to be less than 0.0001. Same test was used to compare CyQuant signals of siNT and siPLK1 groups; P was determined to be 0.49, hence the difference was not significant.

Cell seeding density and DharmaFECT2 volume were determined to be values that yield a successful transfection that does not change the viability of siNT group while lowering of viability of the positive control group significantly. HCT116 cell viability was tested for various DharmaFECT2 and cell seeding concentrations, using 20 nM siNT and 20 nM siPLK1 transfections. Increasing the DharmaFECT2 volume up to 0.5 µl caused slight decrease in viability compared to 0.2 µl. Raising the volume from 0.1 µl to 0.2 µl enhanced *PLK1* knockdown, causing a significant decrease in the viability of the *PLK1* knockdown cells. Therefore, 0.2 µl per transfection was decided upon for the 96-

well format transfections.

Transfection lengths of 24-72 hours were tested for the cell cycle screen, to give sufficient time (24-48 hours) for the mRNA levels to be suppressed (Dharmacon, 2014) and to allow unsynchronised HCT116 cells, whose cell division time is 22 hours, to go through at least an entire cell cycle. The siRNA screen was conducted under high glucose concentrations (25 mM) to ensure that there are plenty of cells across all siRNA group samples at the time of flow cytometry reading.

CCND1 (cyclin D1) and CDC2 (cell division cycle protein 2) siRNAs were determined as G1/S and G/2M arrest positive controls, respectively. In addition to PLK-1, positive control siRNAs were identified that would measure the efficiency of transfection in cell cycle arrest. CCND1 (cyclin D1) (Baldin et al., 1993) and CDC25a (Cell division protein 25a) (Busino et al., 2004) were tested as the cell cycle regulators whose inhibition would arrest cells before in G0/G1 or before S phase, respectively. ANAPC1 (Anaphase-promoting complex subunit 1) (Manchado et al., 2012) and CDC2 (Cell division cycle protein 2) (Wang et al., 2000) siRNAs were chosen as positive controls that would cause G2/M arrest. siNT values were taken as the baseline for cell cycle distribution values. As expected, ANAPC1 and CDC25a inhibitions did not cause cell cycle arrest at the G1 stage.

A 72-hour reverse transfection with positive controls siRNAs caused cell cycle arrest at the anticipated stages (Figure 3.2). siCCND1 transfection caused an increase in G1/S population of about 40% under both conditions. siCDC2 transfection caused an increase in G2/M population of 38% after a two-day and 25% after a three-day transfection. Cells transfected with ANAPC1 siRNA showed similar levels of G2/M population increase of 5% for both transfection durations. siCDC25S transfection caused an increase in G1/S population after a three-day transfection (5%) siPLK1 transfection caused significant G2/M arrest as well.

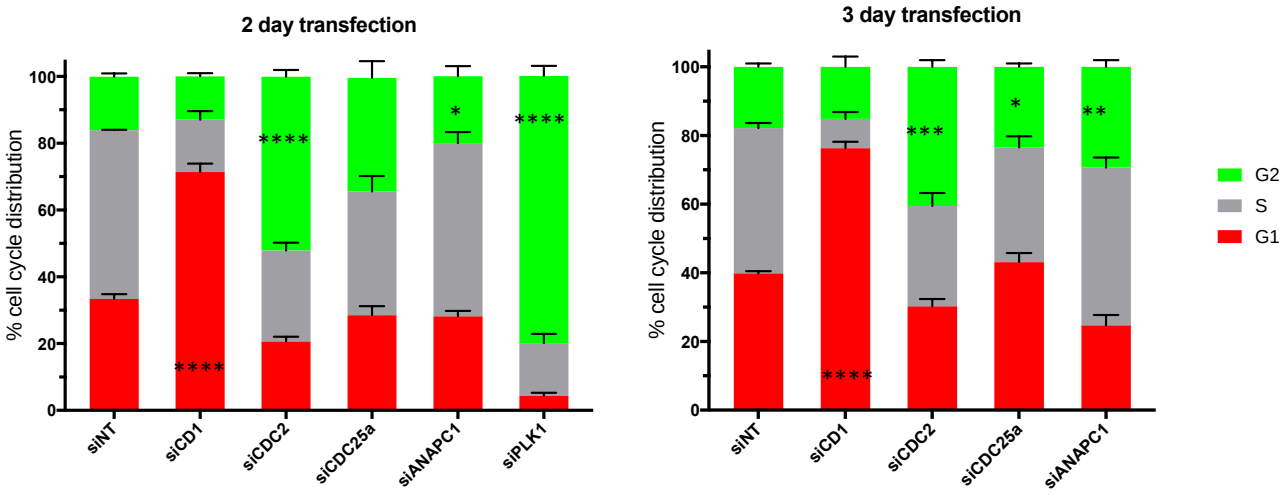
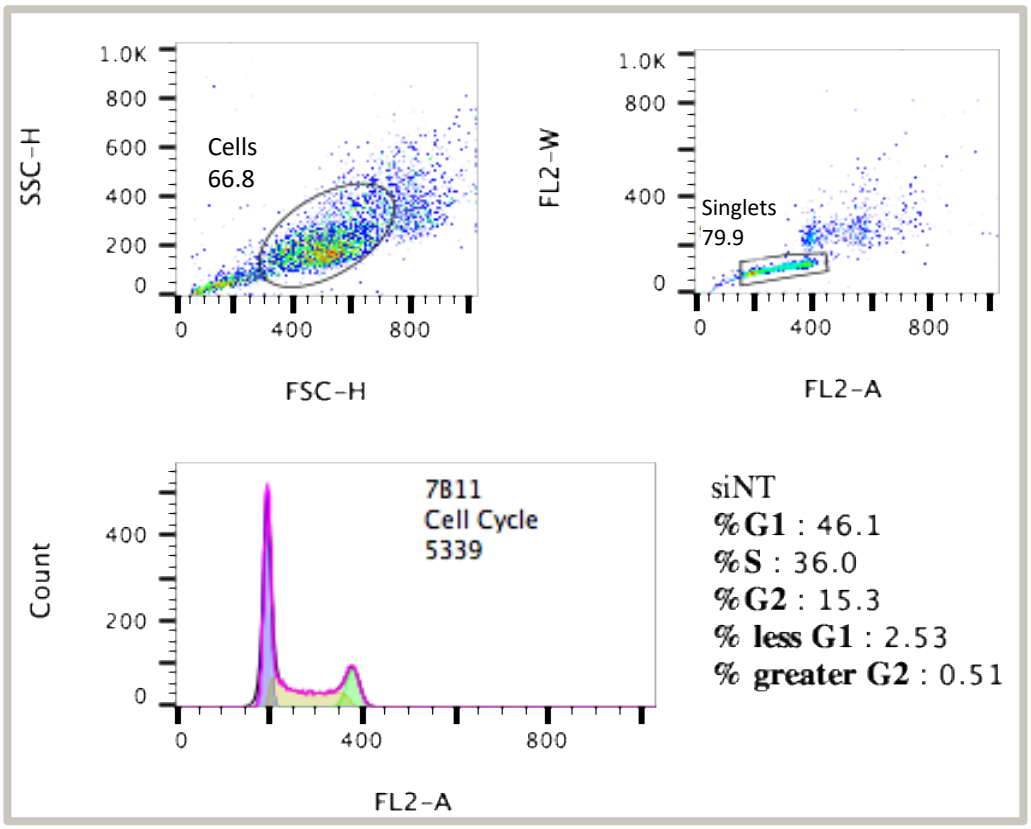


*Figure 3.2: Cell cycle distribution of HCT116 cells with positive control candidate siRNAs was used to determine the duration of screen transfection. Samples were analysed for propidium iodide staining on the second or third day of siRNA transfection via flow cytometry. The data are expressed as percentage of cells in G1, S, and G2 stage relative to the total number of viable cells. Data shown are mean values of n=4 biological replicates; error bars represent standard deviation. 2-way ANOVA followed by Dunnett's multiple comparisons test was used to determine the statistical significance between percentages of cells in G1/S or G2/M compared to the values of siNT group. * P<0.05, ** P<0.01, *** P<0.001, **** P<0.0001.*

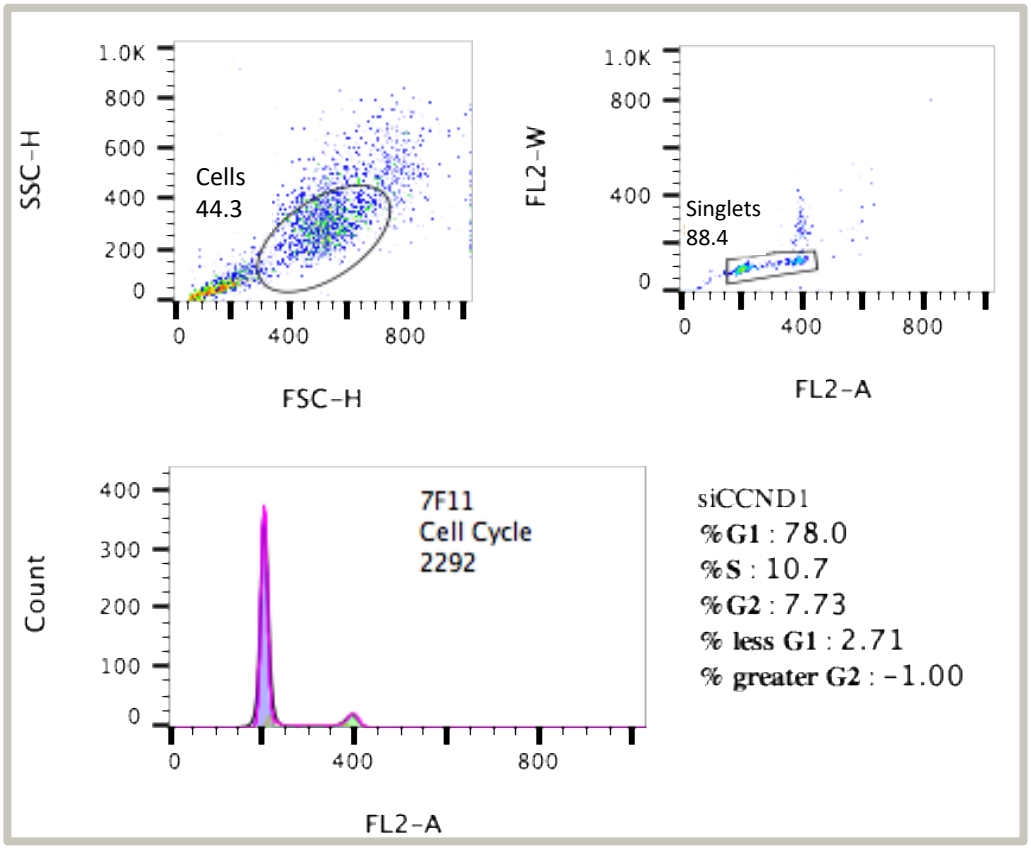
A three-day siPLK1 transfection did not yield enough viable cells for flow cytometry analysis. G1/S and G2/M arrests induced by CD1 and CDC2 siRNAs were more prominent than those caused by *CDC25c* and *ANAPC1* knockdowns. Due to all of the expected cell cycle distribution changes occurring after a three-day transfection, and as a longer transfection yields more cells at the time of the end-point assay, three-day transfection was chosen.

Watson model within FlowJo cell cycle analysis tool was used to determine G1, S, and G2 populations (Figure 3.3). Percentage distribution of each cell population was then normalised to 100%, to omit the cells with DNA content below the range set for G1 and above the range set for G2. This model approximates the G1 population as the first peak corresponding to the lower value on the DNA content histogram and the width of the peak is estimated as that of the distribution at 60% of the maximum value (FlowJo, 2018).

a)


SSC-H
FSC-H
Cells
66.8
FL2-W
FL2-A
Singlets
79.9
Count
FL2-A
7B11
Cell Cycle
5339
siNT
%G1 : 46.1
%S : 36.0
%G2 : 15.3
% less G1 : 2.53
% greater G2 : 0.51

b)


SSC-H
FSC-H
Cells
44.3
FL2-W
FL2-A
Singlets
88.4
Count
FL2-A
7F11
Cell Cycle
2292
siCCND1
%G1 : 78.0
%S : 10.7
%G2 : 7.73
% less G1 : 2.71
% greater G2 : -1.00

c)

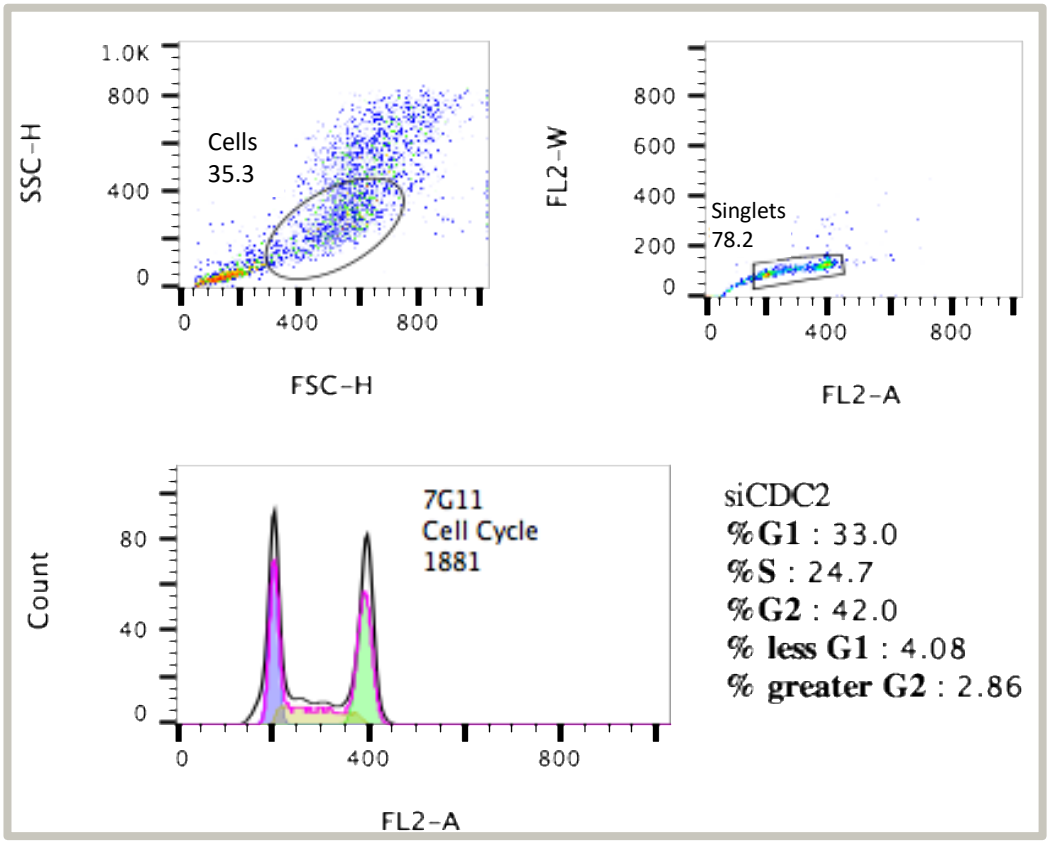


Figure 3.3: Cell cycle analysis of HCT116 cells transfected with a) siNT yielded a baseline cell cycle distribution while b) siCCND1 and c) siCDC2 resulted in G1/S and G2/M arrest, respectively. Side vs forward scatter plots were used to gate out debris and FL2 plots were used to gate for single cells (singlets) The numbers under the gate names show the percentage of the cells to which the gate applies. Cell cycle analysis was then carried out based on Watson univariate modelling which creates a fit to cell cycle data based on DNA content. This model assumes a normal distribution for G1/S and G2/M populations.

During the analysis of screen results, batch analysis was conducted based on gates and cell cycle peak selections of siNT wells of each plate. The gates and cell cycle settings determined for siNT wells of each plate were copied to the rest of samples on that plate. First, single cells were gated for. Next, using the “cell cycle tool” of FlowJo, the position of G1 was defined. G2 peak was set to be placed at between 1.9-2.0 times the position of G1 peak, based on the best-fitting determined for the siNT wells of each plate.

E) Method of screen analysis

The siRNA screen results were analysed based on the end-point of propidium iodide staining. The results of the screen were evaluated in two groups: G1/S and G2/M arrest causing siRNAs. The propidium iodide (PI) staining flow cytometry analysis was utilised for determining if the cell population of interest has a DNA content of n or 2n. The percentage of cells with n amount of DNA correspond to population of cells in G1/S phase and the percentage of cells with 2n amount of DNA help determine the cells in G2/M phase.

The cell percentage distributions across the three stages of cell cycle were calculated according to the propidium iodide staining intensity obtained from the flow cytometry results. These results were then analysed by FlowJo tool which helps determine the distribution across stages of the cell cycle based on flow cytometry data presented as a histogram. The percentage of increase in G1/S stage for siCCND1 and siCDC25a percentages and increases in G2/M for siANAPC1 and siCDC2 from siNT were used to decide on the degree of arrest at the cell cycle stage of interest. The percentage difference in G1/S or G2/M phases were then used to calculate a Z-score for each siRNA except for the negative control siNT. A high Z-score indicates a significant arrest at the stage of interest.

Z-factor is important as it reflects the power of the assay in hit identification by defining a screening window (Zhang, 1999) and is identified based on the means (μ) and standard deviations (σ) of negative (n) and positive (p) controls:

$$\text{Z-factor} = 1 - \frac{3(\sigma_p + \sigma_n)}{|\mu_p - \mu_n|}.$$

A successful assay has a Z-factor greater than 0.5 (Zhang, 1999). siCCND1 and siCDC2 caused a greater decrease in CCND1 and CDC2 mRNA levels, respectively than did siCDC25a and siANAPC1 of CDC25a and ANAPC1 mRNA levels, respectively

(Figure 3.4). siCDC25a's positive control is negative; since there is no separation band between the signal variants of the positive and negative control, siCDC25a cannot be used as a positive control. siANAPC1 is also eliminated since there is no adequate separation between this control and siNT cell population. Therefore, siCCND1 and siCDC2 were chosen as the main cell-cycle positive controls for the screen (Figure 3.4). siCCND1 served as the G1/S arrest positive control and siCDC2 served as the G2/M arrest positive control. mRNA levels after siRNA delivery with DharmaFECT2 for these genes were successfully lowered, suggesting that the knockdown is still valid 72 hours after transfection.

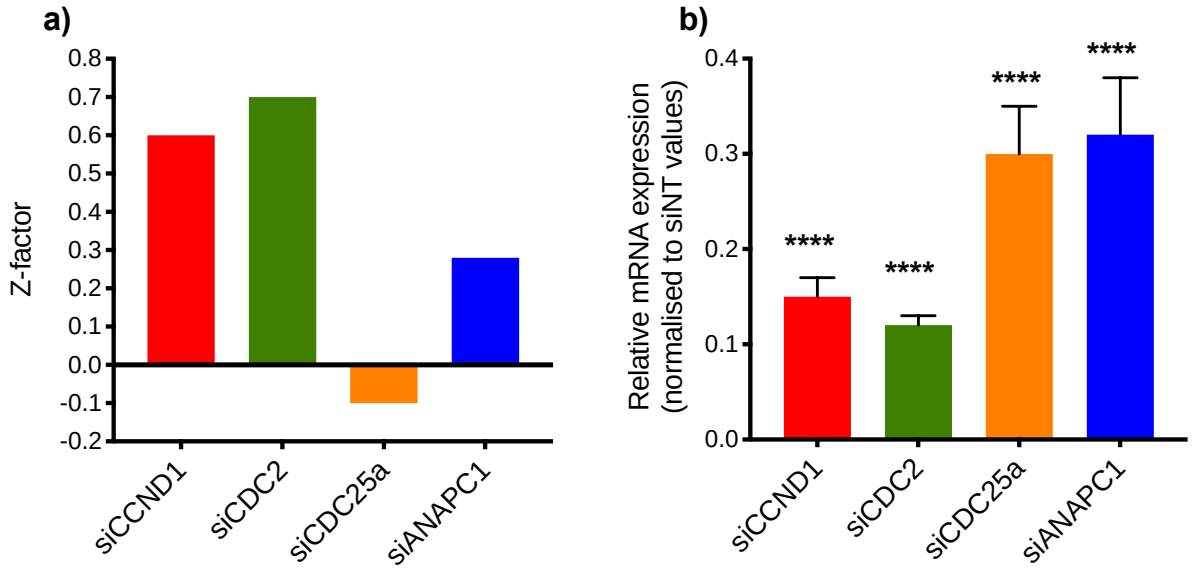


*Figure 3.4: a) Z-factors of potential positive controls were calculated b) RT-qPCR data shows that a 72-hour transfection with siRNAs for respective genes lowered mRNA expression about 90% for CCND1 and CDC2, and 70% for CDC25a and ANAPC1 in HCT116. N=3 biological replicates, error bars show standard deviation. One-way ANOVA with Dunnett's multiple comparisons test was used to determine the statistical significance between mRNA expressions of each siRNA compared to the values of siNT for each gene. **** P<0.0001.*

For high-throughput monitoring of cell-cycle progression, transfection methods were determined, and a 96-well plate flow protocol developed. Three independent screens were completed: the first run including all 487 siRNAs, the second run including 236 siRNAs, the transfection of which caused a G1 or G2 arrest of 5%, and a third run with a list of 347 siRNAs containing all the siRNAs of the second run as well as those that caused even a slight arrest in the first two runs. Two sets of Z-scores were

calculated for each run, based on the percentage distribution of HCT116 cells in G1/S and G2/M.

F) Discussion

A custom siRNA library of metabolic genes was assembled, including key components of cell metabolism as well as metabolic genes that are commonly amplified in primary tumours. Flow cytometry analysis of propidium iodide DNA staining was chosen as the end-point of the siRNA screen. Positive controls that lower cell viability were used to determine cell seeding density, length of transfection, and concentration of transfection media. Additional positive controls were utilised to test that the assay setup allowed for cell cycle arrest detection at both G1/S and G2/M stages with Z-scores above the threshold of 0.5.

The screen was conducted in a 96-well format in which reverse transfected HCT116 cells were analysed for cell cycle distribution. The candidate genes were identified based on separate G1/S and G2/M Z-scores. Candidates with Z-scores above 2 and were amongst the top 10% candidates in at least two independent runs are included in the list of top candidates.

CHAPTER 4: siRNA SCREEN IDENTIFIED THE METABOLIC DETERMINANTS OF CANCER CELL CYCLE

A) Abstract

Our studies identified genes that link metabolic pathways of energy production and biosynthesis to cell cycle progression. Results show that TCA cycle, fatty acid metabolism and nucleotide metabolism are especially important during the transition into S phase, whereas enzymes of electron transport chain, glycolysis, and pentose phosphate pathway are significant for the completion of both G1 and G2 phases. Validation of the screen was carried out by confirming the cell cycle arrest caused by G1/S and G2/M candidates with the highest Z-scores. Fatty acid metabolism genes *CPT1C* and *FASN*, and purine metabolism genes *PDE2A* and *PDE6H* were used to confirm the G1/S results. Proline metabolism genes, *PYCR2* and *PYCRL*, were used to confirm G2/M arrest causing genes. Among the genes whose knockdown caused G1 arrest, cone phosphodiesterase 6H (*PDE6H*) of the retina was selected for further study as a novel controller of cancer cell cycle and metabolism.

B) Introduction

G1/S and G2/M candidates of the metabolic siRNA screen were determined based on increases in cell population distribution at the corresponding cell cycle stages, determined via a flow cytometry at the end of an siRNA transfection. Three runs of the siRNA screen were conducted with the flow cytometry end-point to analyse propidium iodide staining of DNA content.

Transfection with the “G1/S candidate” siRNAs increased the G1/S population of HCT116 cells whereas transfection with the “G2/M candidate” siRNAs increased the G2/M population. The pathways in which the top candidate genes were involved were classified into those causing G1 or G2 arrest. siRNAs which had Z-scores greater than 2 in the last run are presented in Figure 4.1 and Figure 4.2.

C) Results of the screen identified G1/S and G2/M arrest inducing siRNAs

1. G1/S candidates according to their Z-score

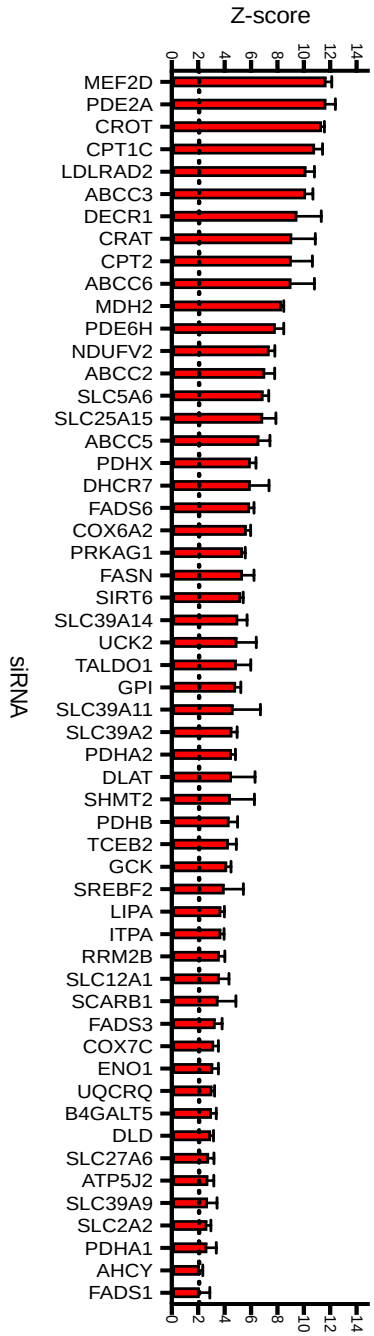


Figure 4.1: Top G1/S candidates were listed according to their Z-scores.
The results of the third run of the screen are presented. Z-score of 2 was taken as the cut-off. Only the candidates that were amongst the top 10% candidates in at least two independent runs are included in the list of top candidates. Data are mean±standard deviation, representative of three independent experiments, n=3 biological replicates.

2. KEGG classification of G1/S candidates

Table 4.1: KEGG pathway classification of G1/S candidates reveal glycolysis and gluconeogenesis, amino acid synthesis and pyruvate metabolism as the top pathways.

Term	Genes	P-value
glycolysis and gluconeogenesis	*GPI;PDHA2;PDHA1;DLAT;ENO1;PDHB;DLD;GCK*	2.32E-07
alanine and aspartate metabolism	*PDHA2;PDHA1;DLAT;PDHB;CRAT;DLD*	1.37E-06
pyruvate metabolism	*PDHA2;PDHA1;MDH2;DLAT;PDHB;DLD*	4.25E-06
valine leucine and isoleucine biosynthesis	*PDHA2;PDHA1;PDHB*	3.47E-04
abc transporters general	*ABCC3;ABCC2;ABCC5;ABCC6*	1.05E-03
oxidative phosphorylation	*UQCRQ;NDUFV2;COX6A2;COX7C;ATP5J2*	7.78E-03
polyunsaturated fatty acid biosynthesis	*FASN;FADS1*	8.78E-03
butanoate metabolism	*PDHA2;PDHA1;PDHB*	1.06E-02
maturity onset diabetes of the young	*SLC2A2;GCK*	2.54E-02
PPAR signalling pathway	*CPT2;SLC27A6;CPT1C*	2.90E-02
citrate cycle	*MDH2;DLD*	3.32E-02
adipocytokine signalling pathway	*CPT2;PRKAG1;CPT1C*	3.35E-02
purine metabolism	*PDE6H;RRM2B;PDE2A;ITPA*	4.71E-02

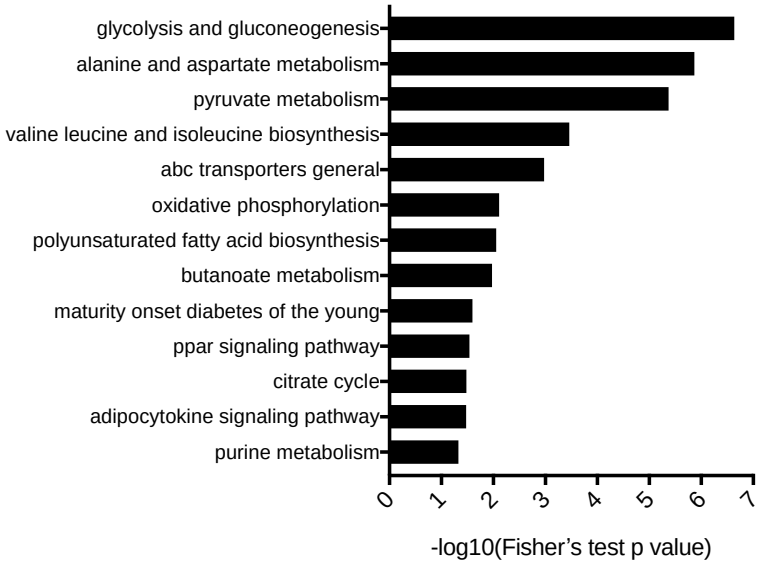


Figure 4.2: Enrichment analysis results summarise metabolic pathways of G1/S candidates.

3. G2/M candidates according to their Z-score

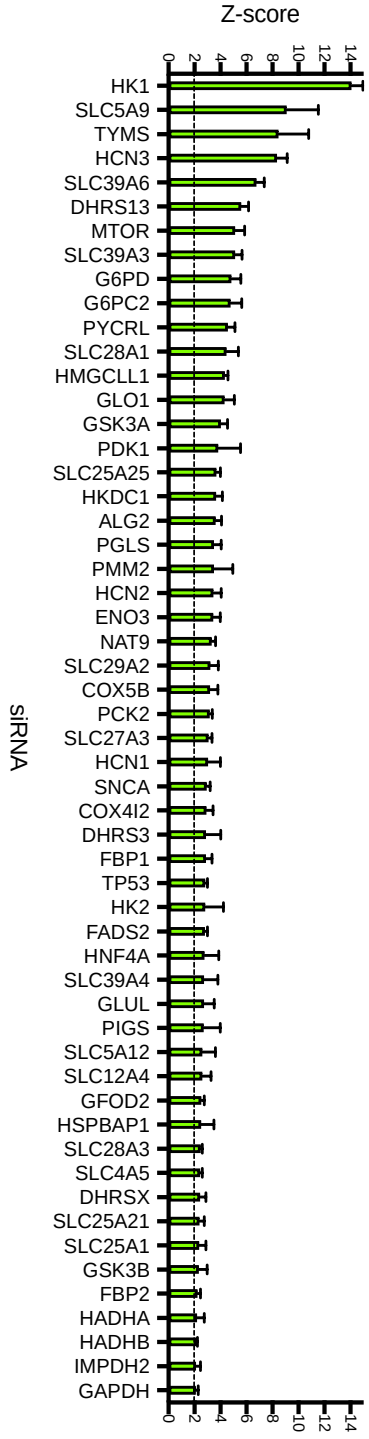


Figure 4.3: Top G2/M candidates were listed according to their Z-scores.
The results of the third run of the screen are presented. Z score of 2 was taken as the cut score. Only the candidates that were amongst the top 10% candidates in at least two independent runs are included in the list of top candidates. Data are mean±standard deviation, representative of three independent experiments, n=3 biological replicates.

4. KEGG classification of G2/M candidates

Table 4.2: KEGG pathway classification of G2/M candidates reveal glycolysis, gluconeogenesis, and glucose derivative metabolisms as the top pathways.

Term	Genes	P-value
glycolysis and gluconeogenesis	*G6PC2;PFKL;PGK1;ENO3;FBP1;GAPDH;FBP2;HK2;HK1*	6.29E-09
fructose and mannose metabolism	*PFKL;PMM2;FBP1;FBP2;HK2;HK1*	2.23E-06
galactose metabolism	*G6PC2;PFKL;HK2;HK1*	2.49E-04
benzoate degradation via coa ligation	*HADHA;DHRSX;DHRS3*	1.14E-03
carbon fixation	*PGK1;FBP1;FBP2*	1.28E-03
limonene and pinene degradation	*HADHA;DHRSX;DHRS3*	1.61E-03
Alzheimer's disease	*GSK3B;GAPDH;SNCA*	2.42E-03
valine leucine and isoleucine degradation	*HADHB;HADHA;HMGCL*	7.92E-03
adipocytokine signalling pathway	*G6PC2;PRKAG2;PCK2*	2.69E-02
Huntington's disease	*GAPDH;TP53*	3.40E-02
starch and sucrose metabolism	*G6PC2;HK2;HK1*	3.96E-02
arginine and proline metabolism	*PYCRL;PYCR2*	3.98E-02

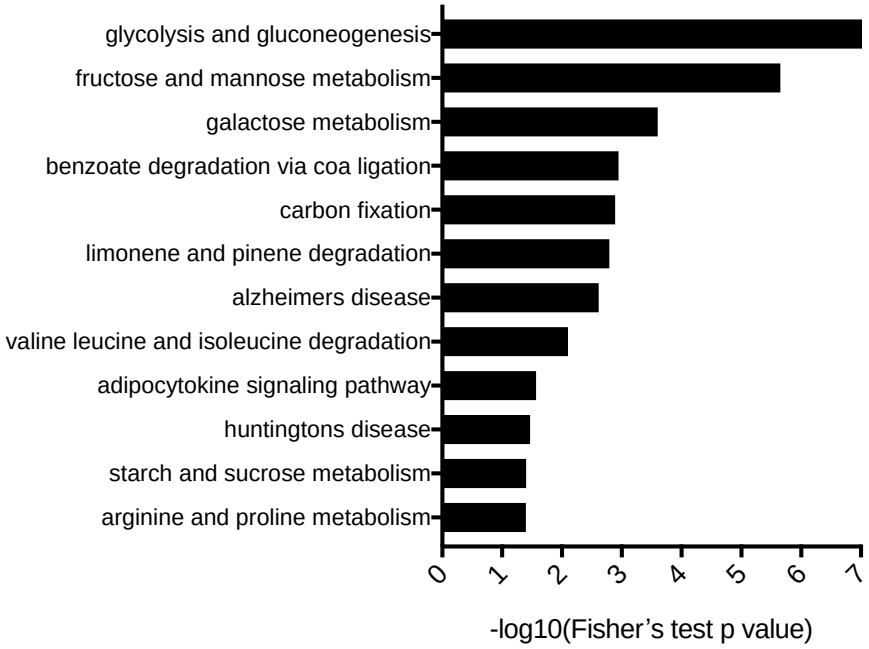


Figure 4.4: Enrichment analysis results summarise metabolic pathways of G2/M.

KEGG classification gives an idea about the pathways that the candidate genes belong to. It should not be taken as a method of quantification since a) Many genes appear in multiple places and b) Number of genes that were included in the screen from each pathway are not considered. The significance of a certain pathway would be presented more accurately if the number of candidate genes from each pathway was normalised to

the number of genes initially included in the screen, of that pathway.

A better representation of screen results would also involve getting rid of redundancy in pathway classification and reporting a ratio of the number of genes which were identified in the screen/number genes that were initially included in the screen, for each pathway.

5. Calculation of sub-G1 populations of transfected HCT116

Apoptotic cell population was estimated as the percentage of “dead cells” from the PI histograms of ungated cells. For the G1/S and G2/M analysis of flow cytometry results of the screen (Figures 4.1, 4.2), two gates were applied to select single cells which were then included in the cell cycle stage analysis, as described in the Chapter 2.

While apoptotic cell populations that appear as sub-G1 peaks need to be estimated after elimination of the debris (Riccardi & Nicoletti, 2006), population of sub-G1 cells in Figure 4.5a were determined on ungated cells, using all events (Figure 4.5b). The reason to use ungated cells in our study was: 1) Dead populations would stain PI+ if they had been stained prior to fixing, yet the cells of this screen were fixed prior to PI staining (Crowley et al, 2006) to be able to identify G1/S and G2/M population. 2) In our screen, the old supernatant was included in sample preparation to include any poorly-attached/dead cells/mitotic cells in the flow cytometry analysis. Given the limitations of our protocol, PI staining could not differentiate between debris and live/dead cells. Therefore, an attempt to quantify the debris separately from the cell population was made on the basis of size.

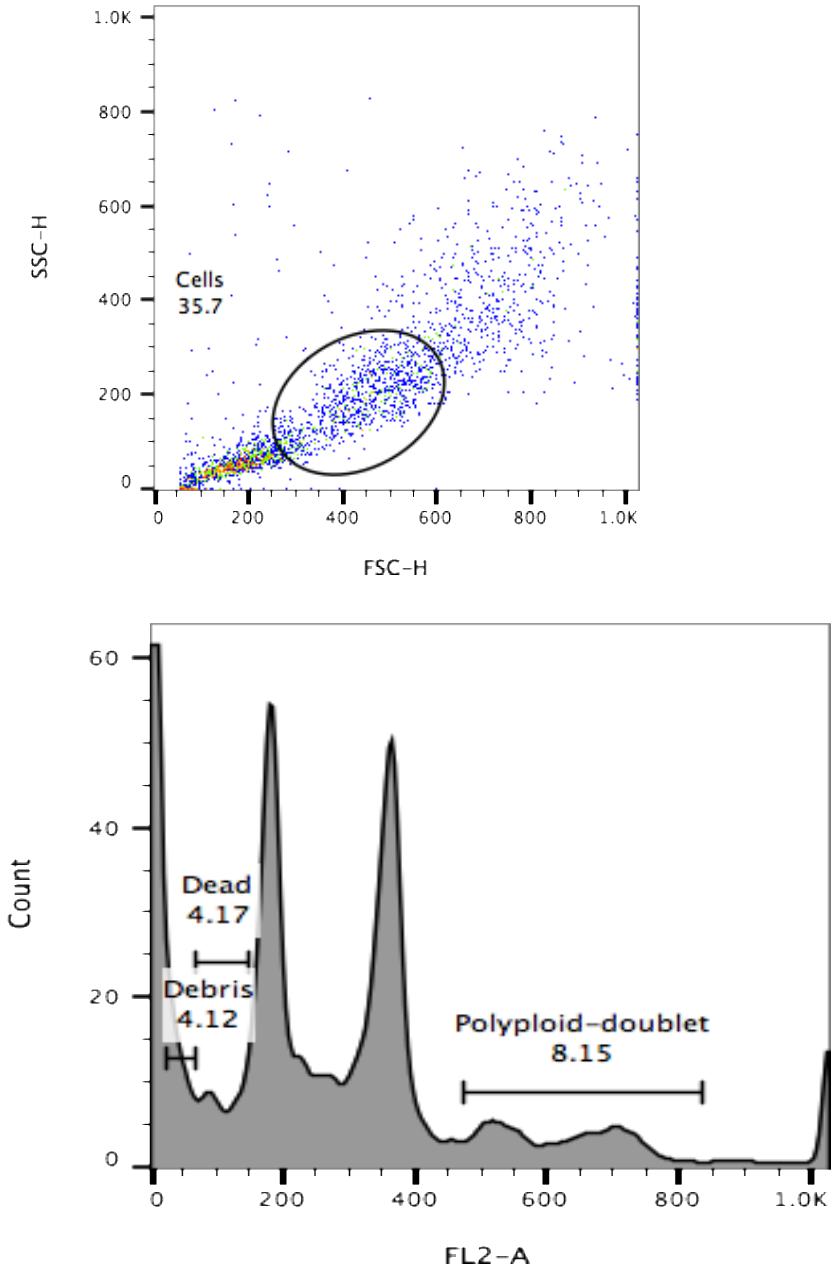


Figure 4.5: Population of dead cells were estimated using ungated population of HCT116 cells.

Our method does not allow for distinction between dead/apoptotic cells or debris. PBS washing prior to cell harvest is required for identification of apoptotic cells with PI staining of fixed cells (Riccardi & Nicoletti, 2006). If cells had been washed prior to fixing and PI staining, and if there were at least twice the number of cells (20k) to analyse, apoptotic cells would constitute a sub-G1 peak that is clearly separated from the G1 peak. Yet very few of our siRNAs resulted in a distinguishable sub-G1 peak.

Therefore, the results presented in Figure 4.6 are percentages of a sub-G1 population that estimate, but do not constitute an accurate representation of apoptotic/dead HCT116 populations of Run 3. Genes the knockdowns of which caused a sub-G1 population greater than 4% are presented in Figure 4.6. The control group siNT had 1.5% sub G1 population, consistent across the plates of the screen run. There was no clear trend between the siRNAs that caused a sub-G1 population of 4% and above, and a cell stage specific classification of candidate siRNAs. siRNAs that resulted in a sub-G1 population included both G1/S and G2/M candidates, as well as siRNAs that were not determined as cell cycle arresting candidates. Figure 4.6 includes G1/S candidates ACADVL, DLD, PDE6H,PDHA2, PDHB, PIGY, RRM2B, UCK2, and UQCRQ; G2/M candidates EPHB2, FADS2, FLAD1, GAPDH, NAT9, PCK2, PGLS, SLCA9; as well as genes that were not identified as candidates of the screen: ACOT6, ACSL6, ACSS2, FABP2, LDHAL6B, LALRAP1, NDUFS2, PDE6G, PFKFB2, PGK1, PRKAG3, RRM1, SLC5A10, SLC5A12, STK11IP, and TSTA3.

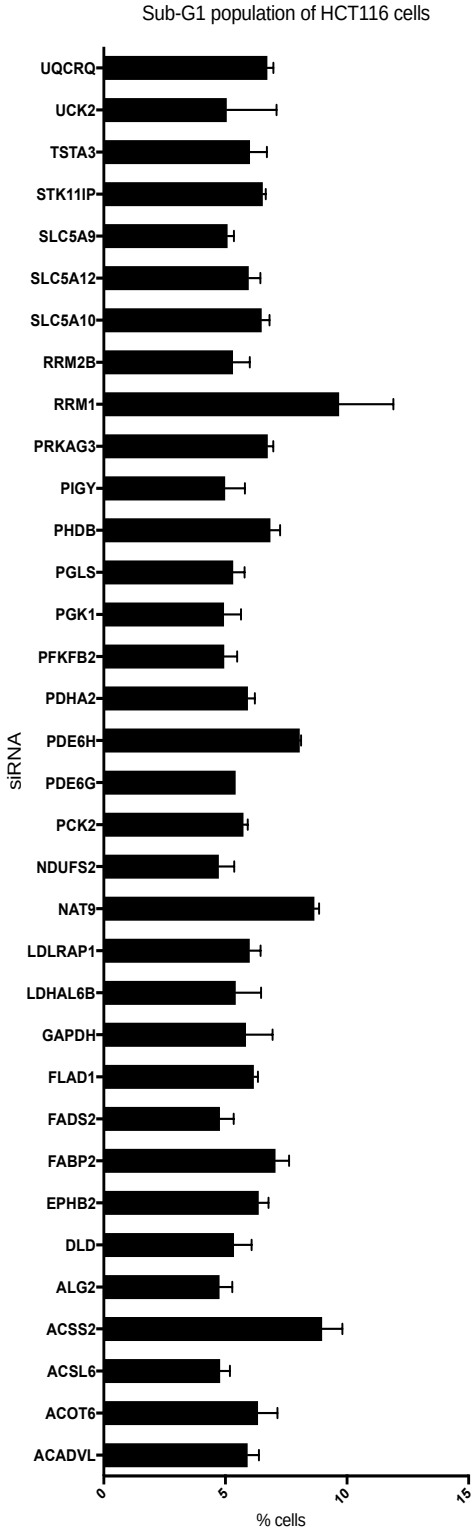


Figure 4.6: Sub-G1 HCT116 cells were calculated following siRNA transfections.

D) Summary of screen results

The results of the screen help identify the cell cycle stage during which the genes identified by the siRNA screen are important for proliferation. Knockdown of genes that are part of mitochondrial metabolism, the genes that encode pyruvate dehydrogenase (PDH) complex components and beta-oxidation enzymes, as well as genes of fatty acid desaturation and synthesis pathways, caused G1/S arrest. These results suggest the genes to be involved in G1/S transition and that mitochondrial function of HCT116 is significant for growth and procession through G1 or the G1/S checkpoint. The knockdown of *PDHA1, PDHA1, PDHB, PDHX, DLAT*, and *DLD* which code for enzymes of the PDH complex all caused arrest in G1/S. While transfection with PDH complex siRNAs had caused arrest in G1/S, knockdown of the PDH kinase *PDK1* had caused arrest in G2/M. An excess of PDH activity might impede with G2/M progression.

In addition to the inhibition of PDH complex, depletion of electron transport chain components through transfections with siNDUFV2, siCOX6A2, siCOX7C, siUQRC, and siATP5J2 all caused arrest in G1/S . Taken together with the arrest caused by PDH complex and beta-oxidation downregulation, a potential reason for this observed G1/S arrest is the indispensability of Acetyl-CoA and oxidative phosphorylation to HCT116 growth. Mitochondria might play a more important part than initially thought, as early as in G1. Other mitochondria related genes that provide substrates for the TCA cycle (beta-oxidation genes *HADHA*, *HADHB*) and electron transport chain genes such as *COX5B*, *COX4I2*, and *UQCRC2*, are important in G2. Mitochondrial metabolism was determined to be a driving force for cell growth throughout the HCT116 cell cycle.

Enzymes in glycolysis and gluconeogenesis pathways made up a significant portion of the G2/M candidates, while they also appear amongst the G1/S genes. This suggests that glucose metabolism is important in all stages of the cell cycle. Glycolytic genes were expected to come up in the G1 stage of the cell cycle (Bao et al., 2013) as levels of glycolysis are higher in G1 stage so their inhibition might have been expected to

result in G1 arrest. DNA synthesis is a high-energy demanding process (Dolfi et al., 2013) (Lane and Fan, 2015). Therefore, genes of enzymes that facilitate reactions that fuel the cell would show up in the G1/S stage, prior to or during DNA synthesis. Processes that increase the nucleotide pools in the cell were also expected to be amongst G1 candidates. In short, genes that enable reactions that produce the energy and building blocks of DNA synthesis were expected to make up G1 candidates.

PPP produces nucleotides that are necessary for DNA synthesis. Therefore, it was surprising that inhibition of the oxidative PPP arm which is upregulated in G1/S (Vizán et al., 2009b) caused G2 arrest, not G1 as expected. On the other hand, inhibition of the non-oxidative PPP caused G1 arrest. It was expected that the depletion of genes involved in nucleotide synthesis: *UCK2, ITPA*, and *RRM2B*, cause G1 arrest, since their end-products are necessary for DNA synthesis and crucial for G1/S transition Inhibition of purine metabolism genes *PDE2A* and PDE6H have also caused G1 arrest. *PDE2A* is known to regulate p21 activity and its suppression inhibits formation of cyclin D1-CDK complexes (Favot et al., 2004), that are necessary for G1/S transition. *PDE6H* was a significant hit and this gene's relation to cancer was unknown.

Transfection with siRNAs for genes that encode enzymes and transporters that control intracellular levels of secondary messengers also reveal that these genes: ABC transporters, HCN voltage gated cation channels and PDEs are relevant to both stages of cell cycle. Through their control of cGMP and cAMP levels, these genes can affect nucleotide pools since secondary messengers are intermediates in nucleotide production (Beavo et al., 2006). Overall, the genes whose main function is to regulate nucleotide pools were estimated to control the G1 stage of the cell cycle as they would be relevant to the DNA synthesis. On the other hand, the nucleotides can be precursors to amino acid production which can make them relevant throughout the cell cycle.

Some G1-arrest-causing candidate siRNAs were omitted from Figure 4.1 as although they had Z-scores greater than 2, they had not caused more than 10% increase in the G1 population in at least two independent runs: C12orf5, ACADVL, CLCN3, BDH1,

PIGY, LDLRAD1, PDE6C, MUT, PIGU, NUDT1, ALG6, DECR2, PIGZ, PIGX, PPARG, PFKFB2, PDE10A, CXCR4, ACSL1, HMGCR, MAP2K1, PPARGC1B, SLC12A9, TCEB3, PDE6D, PDE1A, OXGR1, UQCRC1, ATP5I, ACADL, PDE4C, SLC39A7, SLC2A9, SLC12A2, ACSBG1, SLC5A1. G2-arrest-causing candidate siRNAs RKAG2, UQCC2, PGK1, and PDP1 were omitted from the final list for the same reasons. 55 genes were identified as metabolic genes whose inhibition cause G1/S arrest (Figures 4.1). The inhibition of 65 genes was found to cause G2/M arrest (Figure 4.2).

While the siRNA screen was conducted under high glucose conditions (25mM), the validation experiments, were conducted under low glucose conditions of 5 mM glucose, to reflect physiological conditions more accurately. The previously established relation of some candidate genes, that were presented in Figures 4.1 and 4.3, to cell cycle are summarised in Tables 4.3 and 4.4.

Table 4.3: A summary of G1/S candidate genes.
TALDO1(Vizán et al., 2009a); (Du et al., 2013); (Jiang et al., 2014). CPT (Mashima et al., 2009); (Carracedo et al., 2013); (Pacilli et al., 2013); (Chuang et al., 2011; Martinez-Outschoorn et al., 2014; Menendez and Lupu, 2007). PDH (Dang, 2013; Koukourakis et al., 2005). DECR1(Young and Anderson, 2008). PDE (Favot et al., 2004); (Tiwari, 2007); (Dong et al., 2013). UCK2 (Murata, 2004). ITPA (Abolhassani et al., 2010). RRM2B (Liu et al., 2005).

NAME	FUNCTION	ROLE IN CANCER	ROLE IN CELL CYCLE REGULATION
TALDO1 Transaldolase 1	Provides ribose-5 phosphate for nucleic acid synthesis and NADPH for lipid synthesis through nonoxidative branch of PPP	PPP is upregulated by oncogene activity; its suppression impairs cancer growth	Oxidative branch of PPP is upregulated in G1/S
CPT1 Carnitine Palmitoyltransferase	Regulates β-oxidation and transport of long fatty acids into mitochondria	Upregulated in tumours	Inhibition of β-oxidation metabolism causes G1 arrest
CROT Carnitine O-Octanoyltransferase	Regulates transport of medium- and long-chain acyl-CoA molecules into cytosol	Same as above	Same as above

	and mitochondria		
DECR1 2,4-Dienoyl CoA Reductase 1, Mitochondrial	Regulates β-oxidation	Same as above	Same as above
PDHX *PDH2* *PDHB* *PDHA*	Controls first step of breakdown of pyruvate in TCA cycle Catalyses the conversion of pyruvate to acetyl coenzyme A	Repressed in non-small cell lung carcinomas, upregulated in fibroblasts in tumour stroma	Inhibited by PDKs, especially under hypoxia
PDE2A Phosphodiesterase 2A, CGMP-Stimulated	Regulates the action of second messenger cGMP Involved in purine metabolism	Plays role in melanoma metastasis	Its inhibition prevents cyclin D1-CDK4 complex formation through p21 in HUVEC
PDE6H Phosphodiesterase 6H, CGMP-Specific, Cone	Controls transmission and amplification of visual stimuli Involved in purine metabolism	Upregulated in breast cancer Could be related to exposure to artificial light at night being a potential risk factor for breast cancer	Intervention of purine metabolism can arrest DNA replication
UCK2 Uridine-Cytidine Kinase 2	Phosphorylates uridine to produce uridine monophosphate (UMP)	Inhibition of pyrimidine metabolism can halt cancer growth	Uridine cytidine pools are elevated in S phase
ITPA Inosine Triphosphatase	Converts deoxy- and ribose-phosphates into their monophosphate derivatives	Its inhibition in HeLa causes sensitivity to DNA break and apoptosis	Its deficiency causes G2/M arrest in mouse embryonic fibroblasts
RRM2B Ribonucleotide Reductase M2 B (TP53 Inducible)	DNA repair	Its suppression can sensitize colon and pancreas cancer cells to gemcitabine	Expressed in G1/S in KB cells, degraded in S

Table 4.4: A summary of G2/M candidate genes.
GSK3 (Eom and Jope, 2009); (Jacobs et al., 2012); (Villunger et al., 2013); (Li Chen et al., 2014). G6PD (Vizán et al., 2009a); (Jiang et al., 2014); ((Wang et al., 2015b). PYCR (Liu et al., 2009); (Phang et al., 2012); (Liu and Phang, 2012). PDK1 (Kim et al., 2006); (Madhok et al., 2010); (Fujiwara et al., 2012); (He et al 2018). HCN (Norberg et al., 2010)

NAME	FUNCTION	ROLE IN CANCER	ROLE IN CELL CYCLE REGULATION
GSK3β,α Glycogen Synthase Kinase 3 beta (brain), alpha (skeletal muscle)	Glycogen synthesis inhibition Regulates proliferation, cell motility and survival	Activity can be inhibited by PI3K and AKT Promotes p53-induced apoptosis	When active, degrades cyclin D1 Inactivating GSK3 through the PI3K/AKT signalling pathway might enhance CHK1 mediated G2/M checkpoint
G6PD glucose-6-phosphate dehydrogenase	Produces NADPH and ribose through oxidative branch of pentose phosphate pathway Directly controls the PPP flux	Inhibited by p53 Levels associated with breast cancer metastasis ROS scavenger	Its downregulation causes G1 arrest by decreasing cyclin D1 and CDK4 levels Oxidative branch of pentose phosphate pathway is activated in G1/S
PGLS *6-*phosphogluconolactonase	Produces NADPH and ribose through oxidative branch of pentose phosphate pathway	n/a	Same as the 2nd point above
PYCRL Pyrroline-5-Carboxylate Reductase-Like	Produces proline from glutamate Located in cytosol Generates $NADP^+$ Potentially linked with PPP	Possibly upregulated by MYC	POX, which catalyses its reverse reaction, is a regulator of G2 checkpoint, and is inhibited by MYC
PYCR2 Pyrroline-5-Carboxylate Reductase 2	Produces proline from glutamate Located in mitochondrial matrix Produces NAD^+ Potentially linked with glycolysis	Same as above	Same as above
PDK1 Pyruvate Dehydrogenase	Inhibits pyruvate dehydrogenase subunits PDHA1 and PDHA2	Activity lowers OXPHOS, retains proliferation under	Repression of *PDK2* by miR-422a causes G1 arrest.

Kinase Isoform 1	Regulates glucose and fatty acid metabolism	hypoxia Induced by HIF-1 under hypoxia	
HCN 1,2,3 Hyperpolarisation Activated Cyclic Nucleotide Gated Potassium Channel	Regulates the cellular uptake of Ca^{2+} which acts through signal transduction pathways involving cell motility and transport, DNA transcription, and apoptosis.	n/a	n/a

E) Screen results for the candidates PYCR and PDE genes were validated

Top candidates that previously had not been explored for effect in HCT116 cell cycle regulation were selected for validation across a broader panel of cell lines: colorectal cancer cell lines HCT116 and DLD1, as well as breast cancer cell lines MCF7 and MDA-MB-231. siCCND1 was included in validation work as a G1/S arrest positive control and siCDC2 was included as G2/M positive control siRNA. G2/M candidates PYCR2 and PYCRL are part of proline synthesis pathway and G1/S candidates PDE2A, PDE6H partake in purine metabolism.

1. *PYCR2* and *PYCRL* knockdowns caused G2/M arrest

PYCR enzymes partake in the conversion of glutamate to proline (Liu et al., 2012). Proline can protect cells against oxidative stress from H_2O_2 incubation and this effect is reported to be due to PRODH activity and not PYCR1/2 (Natarajan et al., 2012). On the other hand, in IDH1 mutated cancers such as gliomas where the redox homeostasis is disrupted, excess proline synthesis via PYCR1 uncouples TCA cycle activity from the electron transport chain. This leads to a reduction in the $NADH/NAD^+$ ratio and lowering of OXPHOS. (Natarajan et al., 2012), ROS control can be double-edged sword and its impact can depend on tumour microenvironment that functions as a tumour suppressor to

induce apoptosis or as an oncogenic factor through ATP production and biosynthesis of ROS-induced autophagy (Liu et al., 2012). Therefore, the effect of PYCR knockdown depends on the metabolic requirements of energy and redox balance of a particular cell line.

All four cell lines underwent G2 arrest upon transfection with *PYCR2* or *PYCRL* siRNAs. siPYCRL caused a greater increase in G2/M population than did siPYCR2. The validation work reflected the results of the initial screen of the HCT116 cells. The siRNAs for the positive control genes also caused arrest at the anticipated cell cycle stages, to a greater extent than those for the candidate genes.

PYCRL knockdown caused G2/M arrest in HCT116, DLD1, MDA-MB-231, and MCF7 cells. *PYCR2* knockdown caused G2/M arrest only in HCT116 cells amongst the four cell lines (Figure 4.7). a) HCT116: *PYCR2* knockdown caused an increase of 6% and *PYCRL* knockdown caused an increase of 13% in G2/M. siPYCRL induced arrest is about half of that caused by siCDC2 transfection. b) DLD1: *PYCR2* knockdown caused an increase of 3% and *PYCRL* knockdown caused an increase of 5% in G2/M. siPYCRL induced arrest was only a fourth of that caused by siCDC2 transfection. c) and d): MDA-MB-231, MCF7: *PYCR2* knockdown did not cause an arrest. *PYCRL* knockdown caused a 4% increase in MDA-MB-231 and 5% increase in MCF7's G2/M populations, respectively. siPYCRL induced arrest was only a fourth of that caused by siCDC2 transfection in MCF7 and a third of that caused by siCDC2 transfection. The increase in G2/M population following siPYCRL transfection was followed with decrease in S populations, which suggest that cells were able to progress from S to G2 but went through arrest during G2, before going through mitosis. The results of the DLD1, MCF7, and MDA-MB-231 cell lines were consistent with the HCT116 results, in which the G2/M arrest

caused by *PYCRL* knockdown was more significant that that caused by that of *PYCR2*.

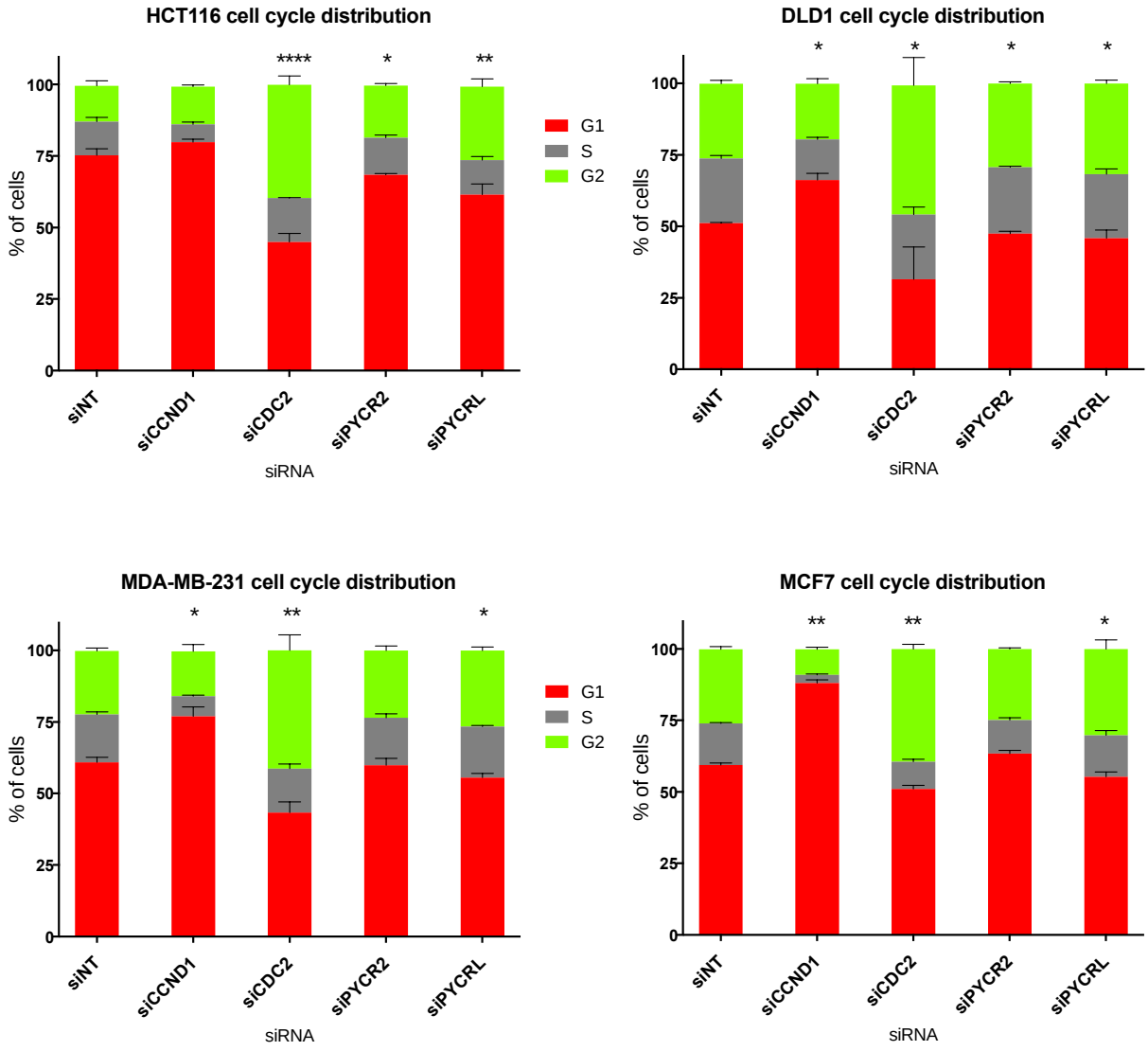


Figure 4.7: PYCR knockdown caused G2/M arrest.
*Samples were analysed for propidium iodide staining on the third day of siRNA transfection via flow cytometry. The data are expressed as percentage of cells in G1, S, and G2 stage relative to the total number of viable cells. Data shown are mean values of n=5 biological replicates; error bars represent standard deviation. 2-way ANOVA followed by Dunnett's multiple comparisons test was used to determine the statistical significance between percentage of cells in G2/M compared to the values of siNT group.*P<0.05, **P<0.01, ***P<0.001, ****P<0.0001.*

PYCR2 knockdown increased CDC2 mRNA expression 1.5-fold in HCT116, 1.2-fold in DLD1, and about four-fold in MCF7 (Figure 4.8). *PYCR2* knockdown causes a 1.5 increase in *PYCRL* mRNA in HCT116, a two-fold increase in MDA-MB-231 and a sixteen-fold increase in MCF7. On the other hand, *PYCR2* knockdown lowered *PYCRL* mRNA

levels in DLD1 four-fold.

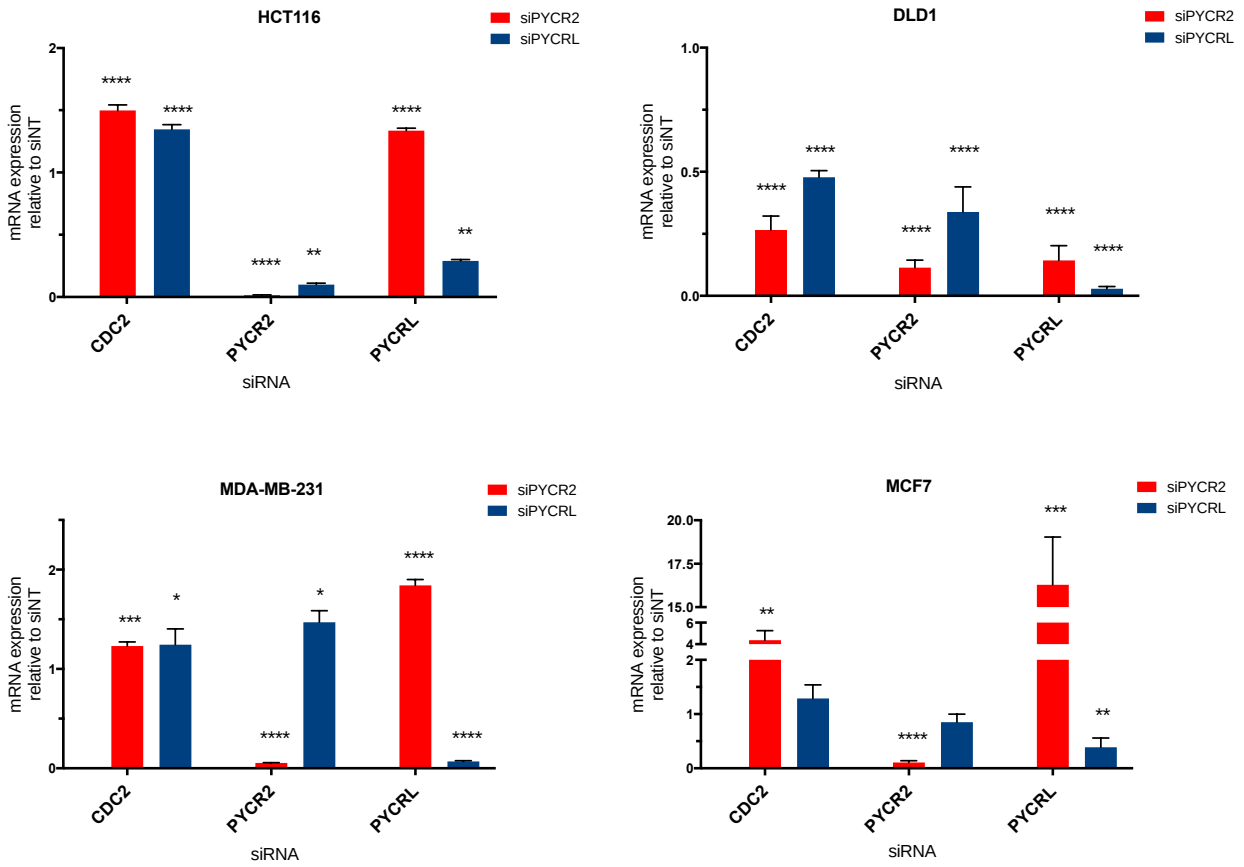


Figure 4.8: PYCR knockdown altered CDC2 expression.
*Transcriptional levels of PYCR2 and PYCRL mRNA regulates that of the other isoform. mRNA samples were collected on the second day of siRNA transfection. Data shown are mean values of n=3 biological replicates; error bars represent standard deviation. One-way ANOVA with Dunnett's multiple comparisons test was used to determine the statistical significance between mRNA expressions of each siRNA compared to the values of siNT for each gene. *P<0.05, **P<0.01, ***P<0.001, ****P<0.0001.*

PYCRL knockdown also caused a ten-fold decrease in *PYCR2* mRNA levels in HCT116 and a three-fold decrease in DLD1 cells. A similar decrease is not observed in the other cell lines. The significant decrease in *PYCR2* mRNA levels upon *PYCRL* knockdown might explain why G2/M arrest is strongest in HCT116. The slight G2/M arrest in DLD1 following siPYCR2 transfection can also be attributed to the decrease in PYCRL mRNA in DLD1, which occurs at a lower level than in HCT116. *PYCRL* knockdown upon the four cell lines. Since siPYCRL transfection causes a decrease in both *PYCR2* and *PYCRL* levels, its effect on cell cycle might be stronger in HCT116. In MDA-MB-231,

however, the *PYCR2* mRNA levels actually increase following siPYCRL transfection.

Despite the increase in CDC2 levels following both PYCR knockdowns and the increase in *PYCRL* mRNA following *PYCR2* knockdown, the G2/M arrest observed in HCT116 cells following PYCR knockdown was the most significant amongst the four cell lines. This may be due to the dependence of HCT116 on intracellular ROS control which PYCR is known to play an effect (Phang et al., 2012). Therefore, we tested whether PYCR knockdown would make HCT116 cells more sensitive to radiation and conducted clonogenic assays to observe colony growth at 2, 4 and 6 Gy radiation.

Since proline can protect cells against oxidative stress from H_2O_2 incubation and this effect is reported to be due to PRODH activity and not PYCR1/2 (Natarajan et al., 2012), and since chronic exposure to H_2O_2 can cause chromosomal instability (Limoli & Giedzinski, 2003) that can perpetuate the damage caused by ionising radiation (Dayal et al., 2003), we wanted to test whether the knockdown of *PYCRL* would result in radiosensitivisation of HCT116 cells. While cells are most radiosensitive at the G2/M phase (Pawlik & Keyomarsi, 2004), which is the stage in which *PYCRL* knockdown causes arrest, the increase in %G2M might have been insufficient to elicit radiosensitivity through this means. (Phang et al., 2012)

The proline cycle is an intermediate pathway that connects PPP, glycolysis, and glutaminolysis (Figure 4.9). It also acts as a redox shuttle maintaining redox homeostasis. Unlike PYCR1/2 which are located in the mitochondria and control NADH/NAD^+ shuttle, cytoplasmic PYCRL controls NADPH/$NADP^+$ levels (Liu et al., 2015).

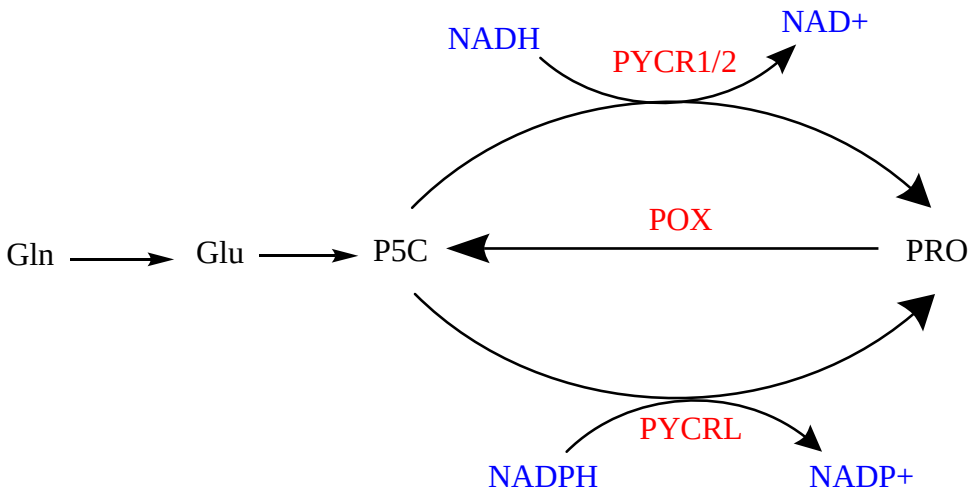


Figure 4.9: Proline metabolism pathway.
PYCR (pyrroline-5-carboxylate reductase), POX (proline oxidase. Enzymes are shown in red, cofactors in blue and intermediates in black (Phang et al., 2012).

While PRODH is involved in cellular superoxide defence (Natarajan et al., 2012) (Figure 4.9), our results did not report a role for PYCRs in superoxide damage control (Figure 4.10). The clonogenic assay performed with unirradiated HCT116 (0 Gy control group) and cells irradiated at doses of 2 Gy, 4 Gy, and 6 Gy showed that the siPYCRL transfected HCT116 cells had lower survival than the negative control group, especially after 4 Gy and 6 Gy radiation treatments. However, the decrease in colony numbers is not sufficient to conclude that PYCR knockdown elicits radiosensitivity in HCT116. The experiment was conducted twice with similar results. Results of one experiment presented are presented in Figure 4.10. We acknowledge that the experiment needs three biological replicates to arrive at any conclusions. The statistical analysis of the technical replicates, as it stands, is a measure of technical reproducibility only.

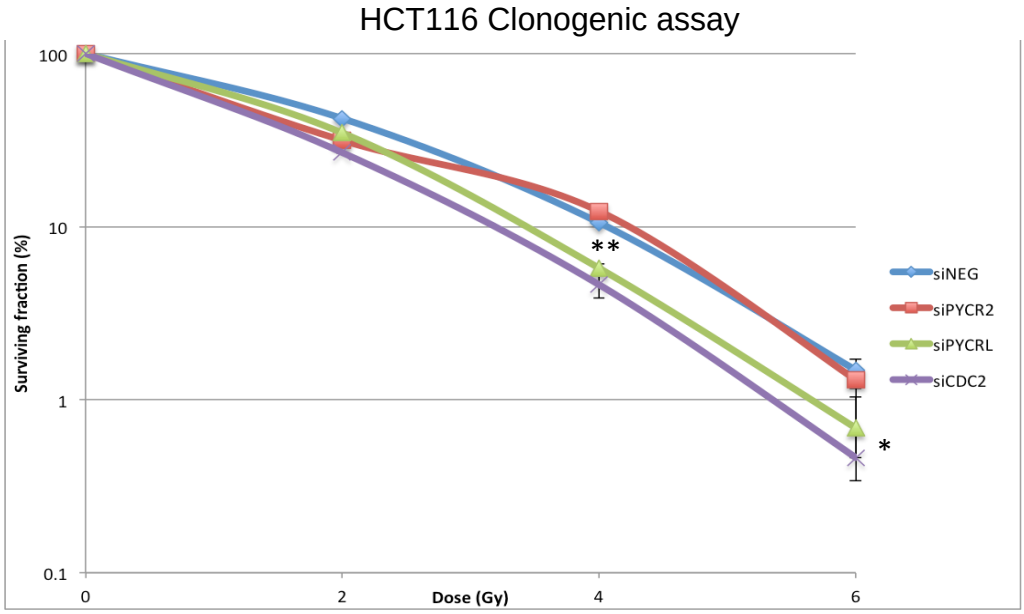


Figure 4.10: Radiosensitivity was not observed in HC116 following PYCRL knockdown. Clonogenic assay results of HCT116 cells grown for 10 days showed that PYCRL kd HCT116 cells had lower surviving fractions at 4 Gy (**) and 6 Gy (*) compared to the negative control group siNT. Data shown are mean values of 6 technical replicates, n=1. 2-way ANOVA followed by Dunnett's multiple comparisons test was used for analysis. Error bars represent standard deviation.

2. *PDE2A* and *PDE6H* knockdowns caused G1/S arrest

Purine metabolism genes were also verified across the four cell lines (Figure 4.11). *PDE6C* knockdown does not cause a cell cycle arrest, unlike that of the other cone PDE6 gene, *PDE6H* or the PDE2 family member *PDE2A*. siPDE2A transfection caused an increase of G1 population of 25% in HCT116, 17% in DLD1, 14% in MDA-MB-231, and 10% in MCF7. siPDE6H transfection caused G1/S arrest only in HCT116 and MDA-MB-231 cells, and to a lesser extent than siPDE2A transfection, with an increase of 14% in HCT116 and 11% in MDA-MB-231. The G1/S arrests caused by *PDE2A* and *PDE6H*

knockdowns in MDA-MB-231 were greater than that caused by the positive control siRNA, siCCND1.

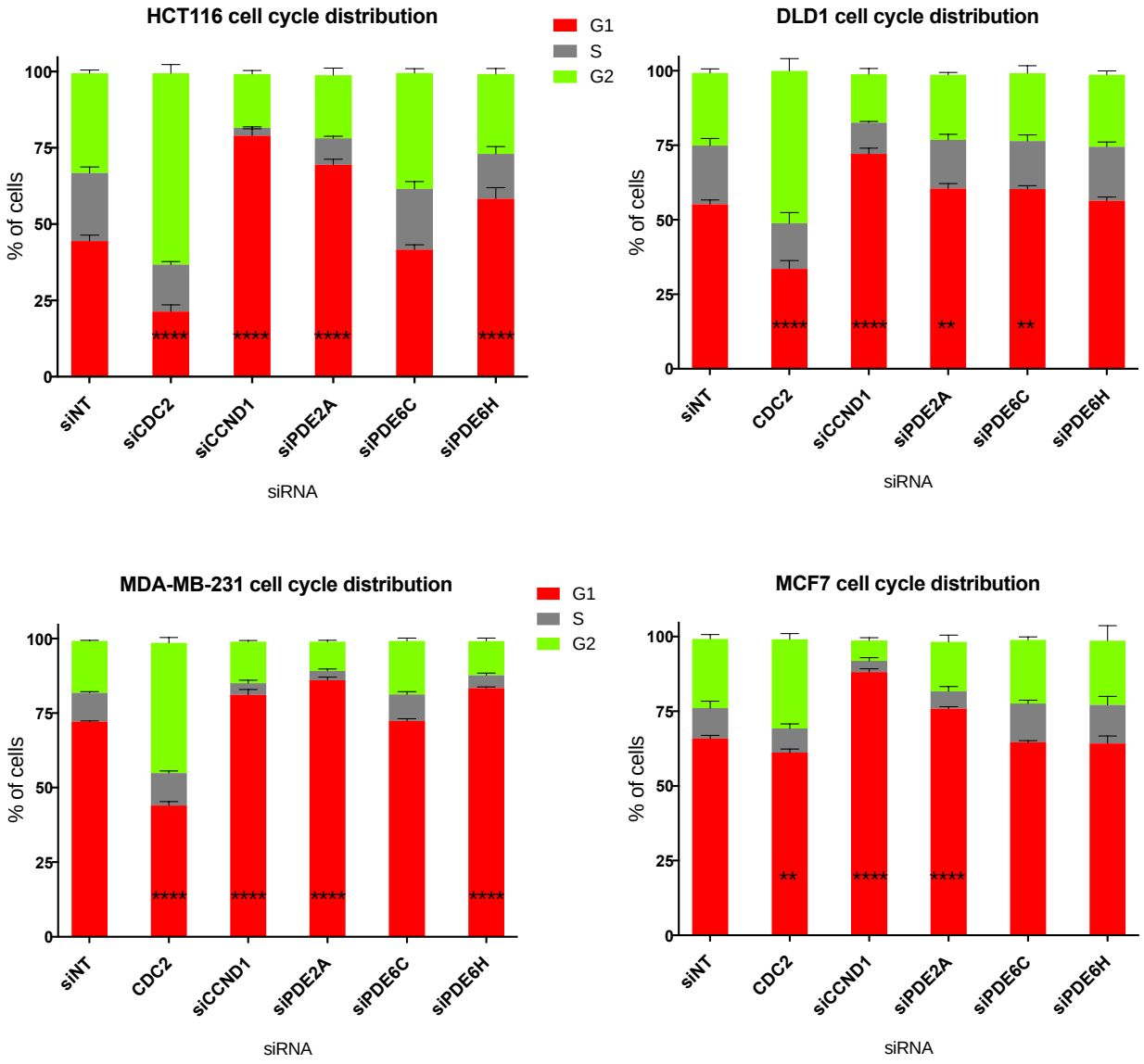


Figure 4.11: PDE2A and PDE6H knockdowns caused G1/S arrest.
*Samples were analysed for propidium iodide staining on the third day of siRNA transfection via flow cytometry. siPDE2A transfection causes G1/S arrest in all four cell lines: HCT116, DLD1, MDA-MB-231, and MCF7. siPDE6H transfection causes G1/S arrest in HCT116 and MDA-MB-231. The data are expressed as percentage of cells in G1, S, and G2 stage relative to the total number of viable cells. Data shown are mean values of n=5 biological replicates; error bars represent standard deviation. 2-way ANOVA followed by Dunnett's multiple comparisons test was used to determine the statistical significance between percentage of cells in G1/S compared to the values of siNT group.*P<0.05, **P<0.01, ***P<0.001, ****P<0.0001.*

F) Screen results for candidates of fatty acid metabolism, CPT1C and FASN genes showed they altered G1/S progression

Both CPT1 and *FASN* knockdown caused G1/S arrest across all four cell lines (Figure 4.12): colorectal cancer cell lines HCT116 and DLD1, and breast cancer cell lines MCF7 and MDA-MB-231.

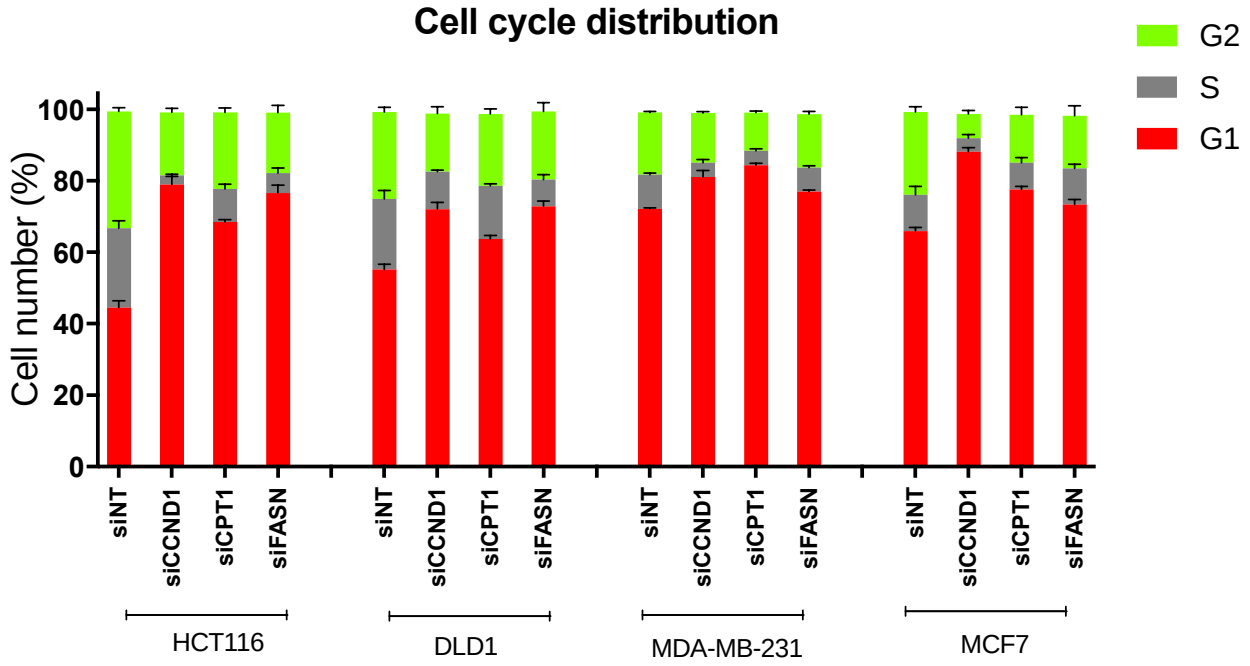


Figure 4.12: CPT1C and FASN knockdowns caused G1/S arrest.
*The arrest is observed across all four cell lines: HCT116, DLD1, MDA-MB-231, and MCF7. Samples were analysed for propidium iodide staining on the third day of siRNA transfection via flow cytometry. The data are expressed as percentage of cells in G1, S, and G2 stage relative to the total number of viable cells. Data shown are mean values of n=5 biological replicates; error bars represent standard deviation. 2-way ANOVA followed by Dunnett's multiple comparisons test was used to determine the statistical significance between percentage of cells in G1/S compared to the values of siNT group. Changes in G1/S population following siFASN and siCPT1C transfection were statistically significant across all four cell lines ****P<0.0001.*

Transfection with siCPT1C caused an increase in G1 populations of 24% in HCT116, 9% in DLD1, 12% in MDA-MB-231 and 12% in MCF7. Transfection with siFASN caused an increase in G1 populations of 32% in HCT116, 17% in DLD1, 5% in MDA-MB-

231, and 7% in MCF7 cells. The increase in G1 stage was accompanied with a decrease in a significant decrease in percentage of cells in S populations and a slight decrease in G2 populations. This observation indicates that the cells in S phase are progressing onto the G2 phase, and the G2 cells are going through mitosis. Along with the cells that are in G1 at the time of transfection, this may indicate that those G2 cells that have recently gone through mitosis also arrest in the G1 phase. We need BrdU staining to demonstrate this.

siCPT1 induced G1/S arrest was even greater than that caused by the positive control transfection siCCND1 in case of MDA-MB-231. Choosing the two cell lines from the colorectal and breast groups where the positive controls caused greater arrest than the candidate genes, the mRNA expression of cyclin B1 cyclin D1 as well that of the two lipid metabolism genes of interest were measured via RT-qPCR (Figure 4.13).

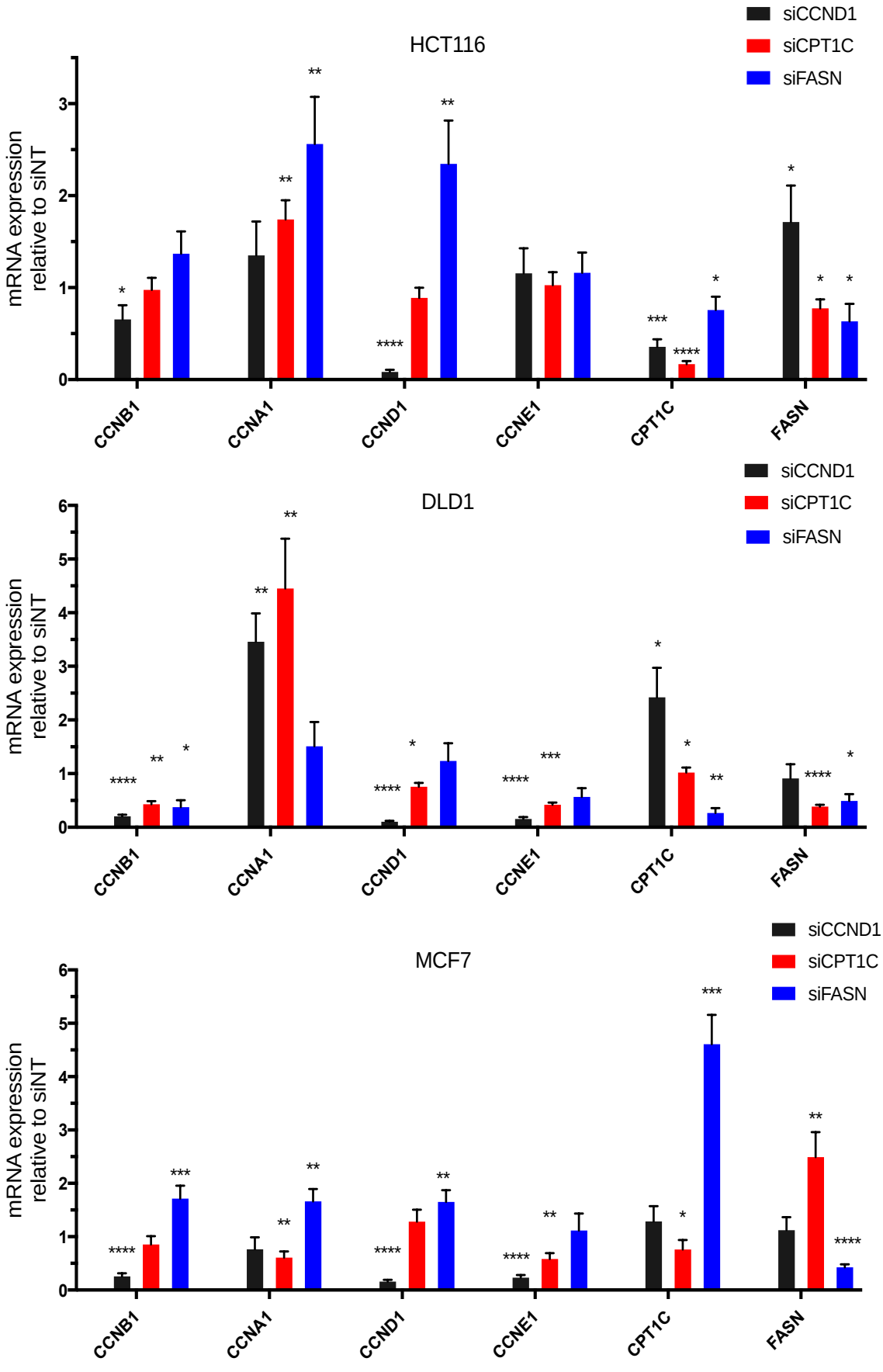

HCT116
siCCND1
siCPT1C
siFASN
mRNA expression relative to siNT
CCNB1
CCNA1
CCND1
CCNE1
CPT1C
FASN
DLD1
siCCND1
siCPT1C
siFASN
mRNA expression relative to siNT
CCNB1
CCNA1
CCND1
CCNE1
CPT1C
FASN
MCF7
siCCND1
siCPT1C
siFASN
mRNA expression relative to siNT
CCNB1
CCNA1
CCND1
CCNE1
CPT1C
FASN

*Figure 4.13: CPT1C and FASN knockdowns changed mRNA levels of cyclins. CPT1c and FASN knockdowns decrease the mRNA level of the other in HCT116 and DLD1 cells, whereas the knockdowns cause a compensatory response of the other gene in MCF7. Adherent cells were treated with 100 nM palbociclib for 24 hours. Data shown are mean values of 4 technical replicates n=1, representative of two independent experiments; error bars represent standard deviation. *P<0.05, **P<0.01, ***P<0.001, ****P<0.0001 One-way ANOVA with Dunnett's multiple comparisons test was used to determine the statistical significance between mRNA expressions of each siRNA compared to the values of siNT for each gene.*

Despite the G1/S arrest that occurred upon siCPT1C transfection, cyclin B1 and cyclin D1 mRNA levels of HCT116 and MCF7 do not change. siFASN transfection, however, causes a 1.5-fold increase of cyclin B1 mRNA in both cell lines and 2.3- and 1.6-fold increases in cyclin D1 mRNA in HCT116 and MCF7, respectively. Interestingly, change in *CPT1C* mRNA values follow an opposite trend in HCT116 and MCF7 following *FASN* knockdown: *CPT1C* mRNA levels lower 25% in HCT116 but increase 4.5-fold in MCF7 cells. A similar trend applies to both cell lines regarding *FASN* mRNA levels upon *CPT1C* knockdown. As with Figure 4.10, results presented in Figure 4.13 pertain to one biological replicate. Results of at least three biological replicates need to be presented and assessed. Statistical analyses shown here are merely intra-test assessments.

It is possible that CPT1C and FASN compensate for one another (Figure 4.14), and so might the other CPT isoforms in MCF7. In HCT116 cells however, CPT1 and FASN enzymes might be co-expressed so that the knockdown of one might decrease the mRNA expression of another. Alternatively, siFASN might be more effective in slowing down the fatty acid metabolism if the cell is relying upon intracellular production of triglycerides produced by FASN, as FASN depletion would yield fewer substrates for CPT1.

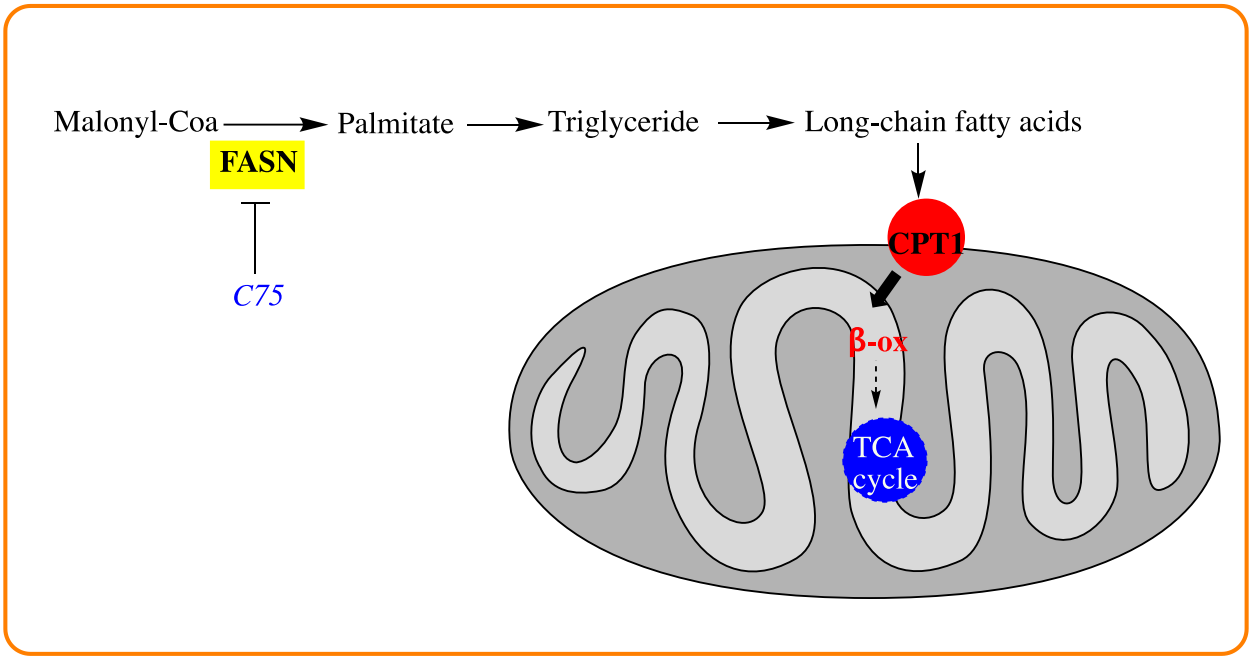


Figure 4.14: CPT1 and FASN contribute to TCA cycle.
FASN is important for production of long-chain fatty acids that enter the mitochondria through CPT1 to go through in beta-oxidation to partake in TCA cycle. C75 inhibits catalytic activity of FASN.

It is already known that breast cancer cells rely on lipid metabolism (Bougnoux et al., 2010), (Bensaad et al., 2014). Our results suggest that *CPT1C* depletion in MCF7 might interfere with the fatty acid transport into mitochondria, cutting the supply to TCA cycle, and the cell responded to this fatty acid deficit by increasing *FASN* expression. CDK4/6 inhibitor palbociclib, which causes arrest in G1/S stage where CPT1C and FASN seem to be important for cell cycle progression, also affected *CPT1C* and *FASN* expression.

Palbociclib causes G1 cell cycle arrest in HCT116 and MCF7 cells; the arrest of MCF7 is more prominent compared to that of HCT116 cells (Figure 4.15). Palbociclib treatment of MCF7 caused greater G1 arrest under high glucose conditions that were used in the siRNA screen (25 mM) compared to low glucose (5 mM). Palbociclib increased the G1 population by 10% in HCT116 and 13% in MCF7 under low glucose conditions. Under high glucose conditions, the drug increased G1 population of HCT116 14% and increased that of MCF7 by 21%.

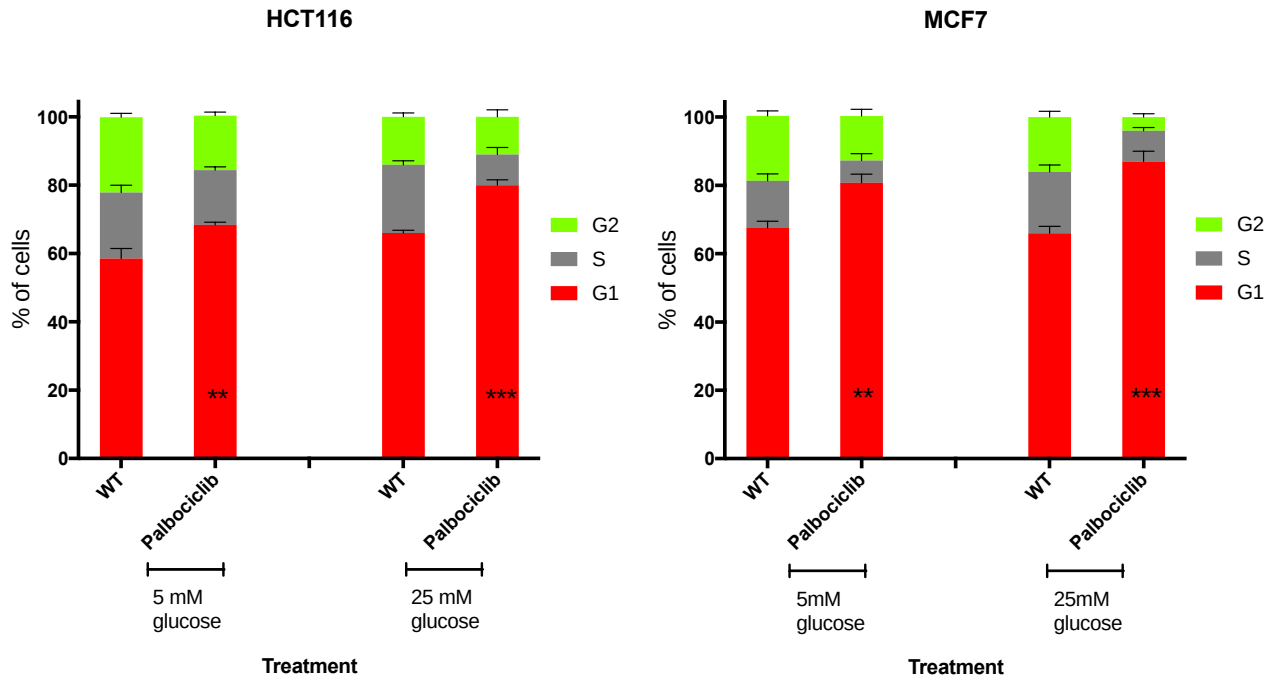


*Figure 4.15: CDK4/6 inhibitor palbociclib caused G1/S arrest in HCT116 and MCF7 cells. The arrest is greater in MCF7 compared to HCT116, and under high glucose conditions compared to low glucose. Adherent cells were treated with 100 nM palbociclib for 24 hours. The data are expressed as percentage of cells in G1, S, and G2 stage relative to the total number of viable cells. Data shown are mean values of n=4 biological replicates; error bars represent standard deviation. 2-way ANOVA followed by Dunnett's multiple comparisons test was used to determine the statistical significance between percentages of cells in G1/S compared to the values of siNT group for each glucose concentration. **P<0.01, ***P<0.001.*

Our results suggest that the difference in arrest inducing effect of the drug under different glucose conditions correlated with the different patterns of baseline CPT1C expression (Figure 4.16). Palbociclib increased *CPT1C* and *FASN* expression in MCF7 under low glucose concentrations and decreased its expression under high glucose concentrations. *CPT1C* expression was also higher under low glucose conditions compared to high glucose. Results presented in Figure 4.16 need to be repeated with at least three biological replicates. Insulin signalling would be overridden in high glucose media, under which the cells are likely to be insulin resistant. The mTOR activating effect of palbociclib (Franco et al., 2016) might be the reason for the increase in *CPT1C* and *FASN*, as mTOR is known to activate *SERB* transcription which induces expression of fatty acid synthase (FASN) (Soliman, 2011).

An upregulation of fatty acid metabolism might have resulted in some MCF7 cells overcoming the G1 Increase as seen in low glucose group, further suggesting that fatty acid synthesis is important for the G1/S progression. MCF7 cells were more sensitive to palbociclib treatment than HCT116 cells.

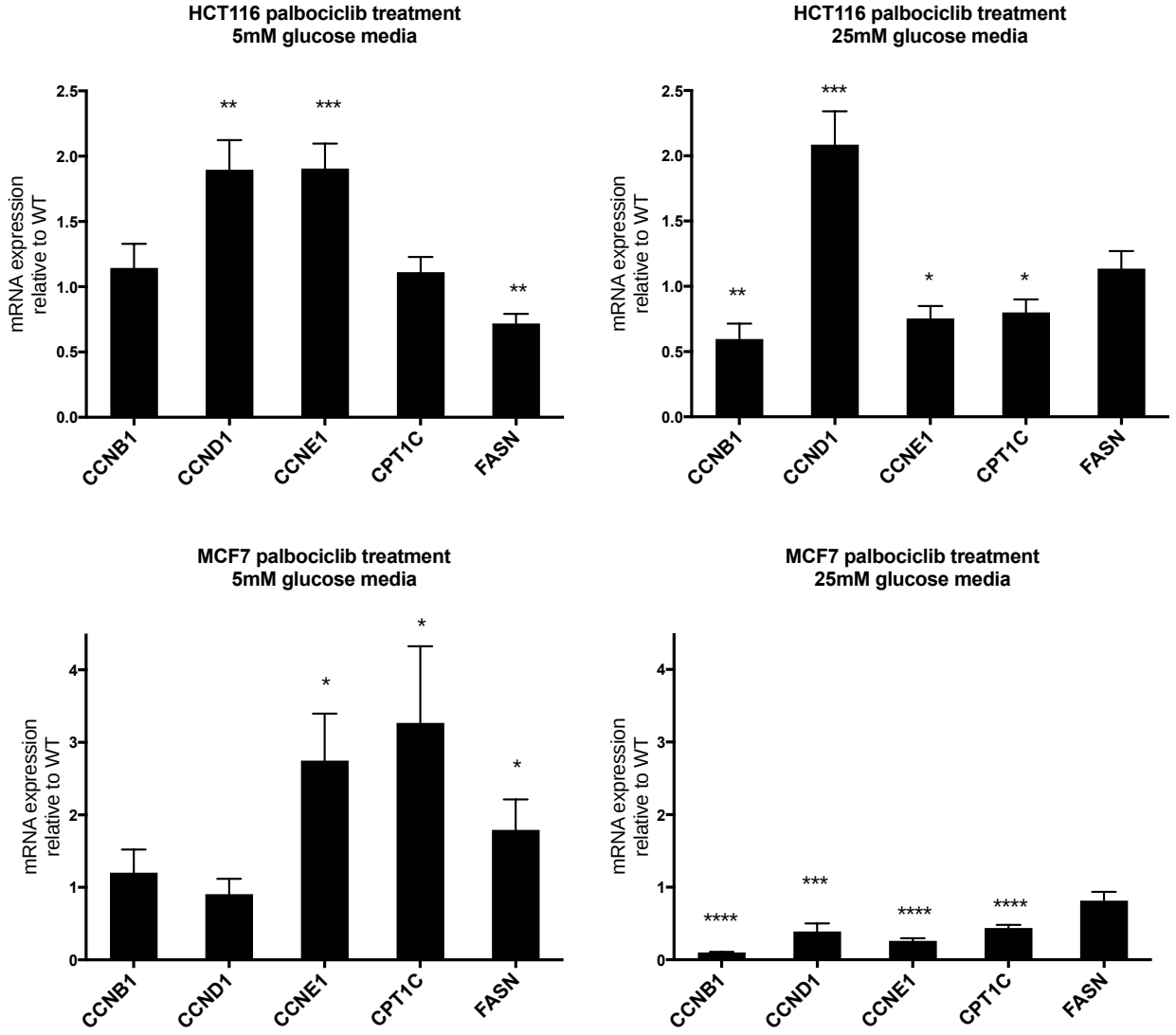


Figure 4.16: Palbociclib treatment altered mRNA expression of cyclins and fatty acid metabolism genes CPT1C and FASN.
*Adherent cells were treated with 100 nM Palbociclib for 24 hours. Data shown are mean values of n=4 technical replicates, representative of two independent experiments; error bars represent standard deviation. *P<0.05, **P<0.01, ***P<0.001, ****P<0.0001. One-way ANOVA with Dunnett's multiple comparisons test was used to determine the statistical significance between mRNA expressions of each siRNA compared to the values of siNT group.*

Under high glucose conditions, cyclin B1 mRNA and protein levels decreased in both HCT116 and MCF7 following palbociclib treatment. Cyclin B1 mRNA remained the same under low glucose conditions in both cell lines (Figures 4.16). These results explained the greater extent of G1 arrest observed in both cell lines under high glucose conditions compared to low glucose conditions. Under high glucose conditions, mRNA levels of cyclin E1, protein and mRNA levels of cyclin B1, and RB phosphorylation decreased significantly in MCF7 cells while the decrease was considerably less in HCT116 cells (Figures 4.16 and 4.17). Under both low and glucose concentrations, the cyclin D1 mRNA levels increased in HCT116 whereas they decreased in MCF7 cells. These results were in accordance with the higher sensitivity of MCF7 to the drug.

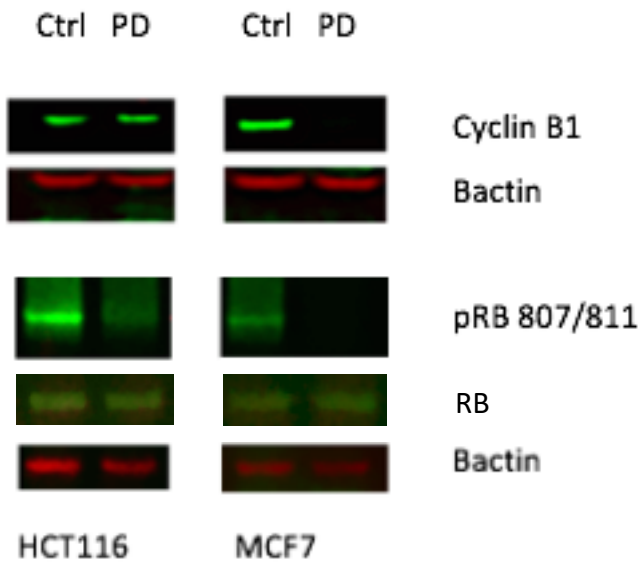


Figure 4.17: Palbociclib treatment decreased cyclin B1 and pRB protein levels. Adherent HCT116 and MCF7 cells were treated for 48 hours with 100 nM palbociclib (PD) in 25 mM glucose media. Data shown are representative of three independent experiments.

G) Discussion

The results showed that the TCA cycle, fatty acid metabolism and nucleotide metabolism were especially important during the transition into S phase, whereas enzymes of electron transport chain, glycolysis and pentose phosphate pathway were significant for the completion of both G1 and G2 phases. The screen was conducted under high glucose concentrations to ensure enough viable cells for flow cytometry analysis, whereas the validation work was conducted under low glucose concentrations that were closer to physiological concentrations. We acknowledge that a more throughout screen should be conducted using a larger set of cancer cell lines, as different cell types rely on different metabolic components for growth and proliferation. Variety in the oncogenic mutations, that might allow certain cancer cells to overcome cell cycle arrest, also underline the importance of using multiple cell lines in a metabolic siRNA screen. Another issue regarding the screen was the use of high glucose media, which might have pushed cells towards a more glycolytic metabolism, affecting the screen outcome. An improved screen would also include all runs conducted with the entire library, instead of using part of the library in the latter two runs.

The cell cycle distribution results that were obtained through the HCT116 metabolic siRNA screen were then validated in different cancer cell lines. Changes in levels of cell cycle regulators also confirmed the arrest caused by metabolic gene depletion.

The siRNAs for genes that were determined to be amongst top G1 candidates, *PDE2A, PDE6H, CPT1C*, and *FASN*, were confirmed to cause cell cycle arrest. The G1/S arrest induced by siFASN was greater than that of siCPT1 in the colorectal cancer cell lines. An opposite trend was observed in breast cancer cell lines where depletion of *FASN* caused a greater increase in G1 population than that of *CPT1C*. This might suggest a greater dependence on synthesis versus breakdown of long-chain fatty acids

in the colorectal cancer cell lines. The trend can also be explained by the presence of multiple CPT1 genes that produce transporter of the same function, whereas *FASN* is indispensable. Proline metabolism genes, *PYCR2* and *PYCRL* were analysed for cell cycle arrest in G2/M across four cell lines. The greater effect of cytosolic *PYCRL* in causing cell cycle arrest, compared to its cytosolic counterpart mitochondrial *PYCR2* suggests that NADPH/$NADP^+$ levels might play a greater role in cell cycle progression that those of NADH/NAD^+. However, *PYCR* knockdown resulted in modest amounts of G2 arrest, which can suggest that PYCR2 or PYCRL genes are not essential for cell cycle progression on their own and changes in their mRNA values might be compensated for through their isoforms.

Our results displayed the variation in how cells respond to modifications of their metabolism through metabolic gene knockdown. Effect of growth conditions on how cells responded to stress were implied through results which showed that palbociclib had a greater cell-cycle-arresting effect under high glucose conditions compared to low glucose. Our results had shown that glycolysis is vital for completion of S stage. High glucose levels might have pushed cells to be more glycolytic, making them more prone to G1/S arrest through palbociclib action.

Cell cycle arrest inducing drug palbociclib also altered metabolic gene expression, further signifying the connection between cell cycle and metabolism. Palbociclib's cell cycle control can be a tug-of-war with its metabolic effect through insulin regulated mTOR signalling that helps the cells overcome a G1 arrest (Franco et al., 2016). The complex effect of cell cycle modifications suggest that the metabolic implications should be considered when developing chemotherapeutic drugs targeting cell division.

Moving forward, we had planned to study a particular gene that can be targeted to halt growth and/or elicit a metabolic vulnerability in cancer cells. Amongst the genes that were not chosen for further study were G1/S candidates encoding enzymes of beta-oxidation, such as *CPT1C, CPT2 DECR1, CROT, FASN* since this pathway was already

known to cause G1/S arrest when disrupted (Menendez and Lupu, 2007), (Young and Anderson, 2008), (Mashima et al., 2009), (Chuang et al., 2011; Martinez-Outschoorn et al., 2014; Menendez and Lupu, 2007). Genes encoding components of oxidative phosphorylation: PDH and electron transport chain enzymes, and glycolysis enzymes: hexokinase and enolases, were also omitted since various isoforms of these genes caused arrest at different stages of the cell cycle, and many are under study already. Genes directly involved in DNA repair and de novo nucleotide synthesis: *UCK2, RRM2B*, and *ITPA* were expected to cause G1/S arrest as their depletion would prevent progression into or through S. *TYMS* unexpectedly took place amongst G2/M candidates, yet was not chosen as the main candidate due to its extensive study (Rose et al., 2002). ABCC and HCN channels were considered as a main candidate but were decided against since these transporters had not been explored as drug targets and would require a parallel study of several members of both gene families which were amongst the candidates identified by the screen. PYCR genes were not explored further when their anti-proliferative effect on tumour growth was elucidated (Liu et al., 2015).

In determining *PDE6H* as our main candidate, the following factors were considered: the extent of cell cycle arrest induced upon the knockdown of the gene, the novelty of the gene in relation to cancer and whether the gene was differentially expressed in cancer cells. *PDE6H* was selected for further study as its knockdown caused cell cycle across various cell lines, and since there were already drugs, albeit non-specific, developed to target PDE5/6. Cone phosphodiesterase 6H gene (*PDE6H*) or its protein PDE6gamma of the retina (PDE6H) had not been studied in the cancer context, which made it an interesting candidate to investigate to understand the mechanism through which it causes G1/S arrest, and whether it has a role in cancer cell proliferation and metabolism.

CHAPTER 5: PDE6H CONTROLS G1 PROGRESSION AND CELL METABOLISM

A) Abstract

As part of the nucleotide metabolism, *PDE6H*, which encodes the gamma subunit of PDE6 family responsible for the turnover of cyclic guanosine monophosphate (cGMP) in the retina cone, was selected for further study. PDE6H was identified as the member of PDE6 family the depletion of which resulted in the most striking anti-proliferative effect on HCT116 cells. PDE6H was then verified to be important for G1/S progression and mitochondrial metabolism in various cancer cells. Besides causing G1 cell cycle arrest and disruption of G1/S checkpoint mechanism, *PDE6H* knockdown induced apoptosis, increased mitochondrial ROS and dysfunctional mitochondria. *PDE6H* depletion increased cGMP levels and mitochondrial ROS, also resulted in activation of signalling pathways including ERK1/2, mTORC1, and HIF-1α . PDE6H was also identified as a controller of glycolysis and oxidative phosphorylation as its depletion lowered basal energy metabolism. Effects of *PDE6H* depletion were verified through siRNA knockdown as well as through CRISPR/Cas9 gene knockout.

B) Introduction

PDE6H was identified in the metabolic siRNA screen as a G1/S candidate. the knockdown of which caused cell cycle arrest in HCT116 cells. *PDE2A* was another phosphodiesterase gene the depletion of which resulted in G1/S arrest. Some members of the PDE family –PDE2, PDE3, PDE4, PDE5, and PDE9 have previously been studied as potential chemotherapeutic targets (Savai et al., 2009). However, PDE6 has not been explored as a target and the only study that investigates the role of PDE6 in cancer remains one that studied its protein expression in breast cancer cell lines and patients' primary breast cancer tissues (Dong et al., 2013). That study reported high expression of PDE6beta in MCF7 cells and patients' tissues by immunohistochemistry, yet no expression of the *PDE6H* gene. Despite a lack of studies on *PDE6H* or the PDE6gamma subunit (PDE6H) it encodes, *PDE6H* is mutated in several cancer cell lines and tumours, based on Oncomine and CBioPortal genomic expression data (Rhodes et al., 2004) (Gao et al., 2013). Due to its novelty and significance as a controller of cancer cell cycle and growth, potentially targetable with inhibitors, PDE6H was selected for further study as the result of the metabolic siRNA screen.

After confirming the selection of *PDE6H* amongst other PDE6 family genes as the candidate for further study, effect of *PDE6H* depletion on cancer cells was explored in more detail. siRNA knockdown and CRISPR/Cas9 knockout of HCT116 cells was used to understand PDE6H's control of cell cycle, metabolism and oncogenic signalling.

C) PDE6 is at the crossroads of cancer metabolism and retinal physiology

1. Purine synthesis is a link between cell cycle progression and metabolism

Purine biosynthesis connects oncogenic signalling, cell cycle and energy

metabolism. As cell cycle progression relies upon synthesis of new DNA, purine metabolism regulates cell cycle. Depletion of purine pools cause G1/S arrest. Purine nucleotides are synthesised from ribose-5-phosphate, the end-product of PPP. Inosine monophosphate (IMP) a common precursor of AMP and GMP (Figure 5.1) (Berg JM, 2002). *De novo* purine synthesis diverges from pyrimidine synthesis as IMP is oxidised to xanthosine monophosphate (XMP), from which GMP is produced in a glutamine and ATP dependent manner. Guanosine and guanine can be produced from GMP, which can be salvaged from guanine.

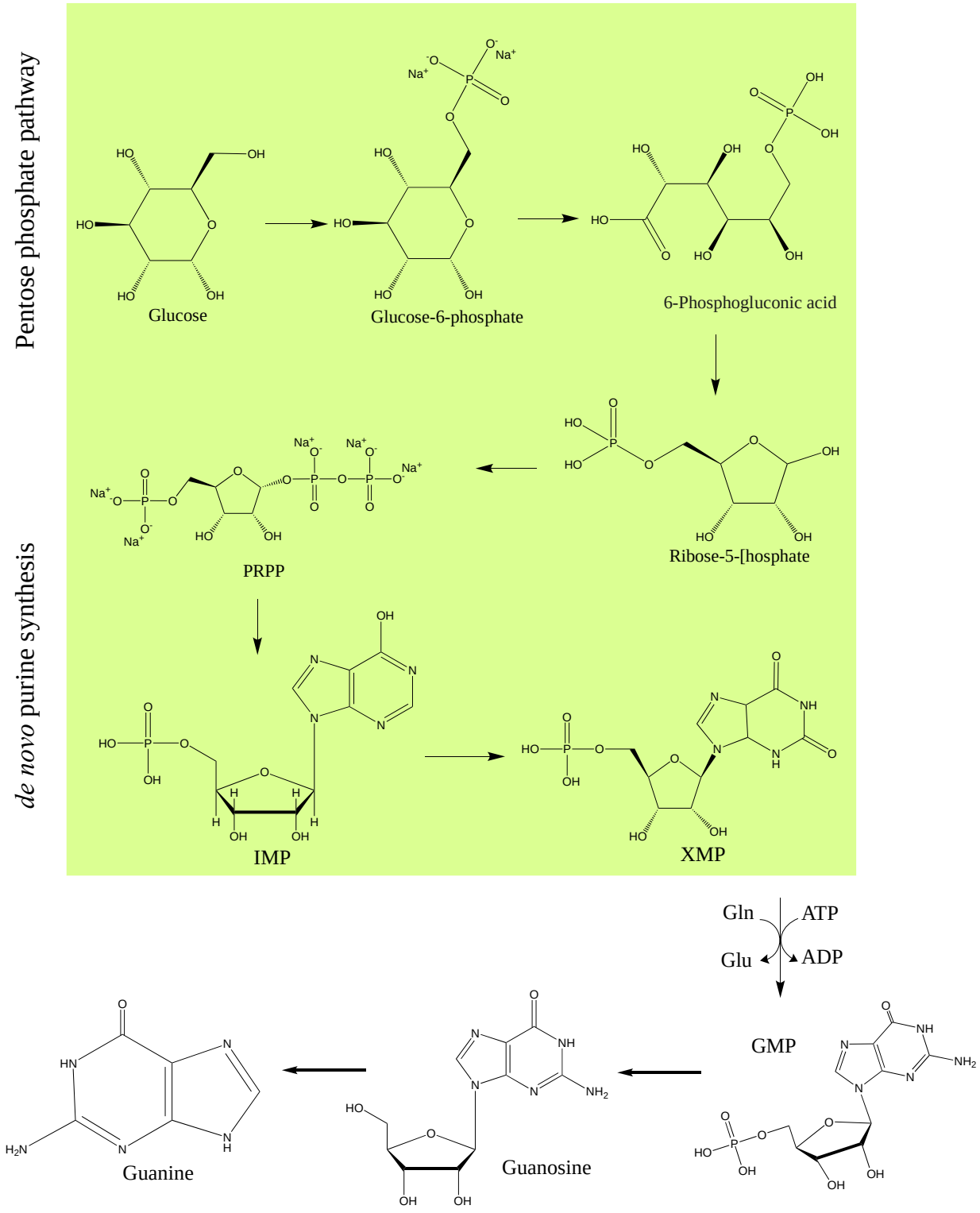


Figure 5.1: Pentose phosphate pathway and guanine pools sustain purine production.

High levels of ribose-5-phosphate were noticed during the metabolic profiling of the tumour tissue of primary lung cancer that also showed a significant accumulation of

glycolysis products lactate and pyruvate, as well as TCA cycle intermediates malate and fumarate (Moreno et al., 2018). Fumarate is an AMP production intermediate and also plays role in ROS amplification as it covalently bonds to glutathione, preventing the latter from performing its antioxidant function through increasing $NADPH/NADP^+$ ratio (Sullivan et al., 2013).

mTORC1 activation and presence of purine pools lead to de novo synthesis of purine and pyrimidines (Ben-Sahra and Manning, 2017). In response to amino acids, mTORC1 activation is initiated by its translocation to lysosomal surfaces to interact with Rag proteins. Rag GTPases interact with mTORC1 and aids its colocalisation with membrane-bound Rheb (Sancak et al., 2010). Due to the lowering of GTP levels, purine depletion also leads to mTORC1 inactivation by lowering the GTP bound Rgeb. Purine pools can stimulate pyrimidine and amino acid synthesis via mTORC1 activity (Emmanuel et al., 2017).

mTORC1 activity regulation through changes in purine levels can occur independent of AMPK in a TSC dependent manner, which can be switched on and off during the depletion or supplementation of purine nucleotides (Hoxhaj et al., 2017). AVN-944 is a selective inhibitor of de novo synthesis of guanine nucleotides that acts by targeting IMP dehydrogenase. Its depletion of purine pools in U2OS and MCF7 cells leads to disappearance of nucleostemin by disrupting GTP binding to this positive regulator of cell proliferation (Huang et al., 2009).

Phosphodiesterases (PDEs) break the phosphodiesterase bond in secondary messengers cAMP and cGMP. cGMP specific PDEs hydrolyse guanylyl cyclase product cGMP to produce GMP. Through controlling GMP levels, they affect purine pools and metabolism and has implications in cancer development that are not thoroughly studied (Tiwari, 2007). A point mutation in *PDE2A*, leads to malignant melanoma cell cycle progression and can be part of prognosis (Morita et al., 2013).

PDE6 of the retina is known for its function in the phototransduction pathway. By controlling GMP levels, phosphodiesterases partake in purine metabolism. The role of

PDE2A in cell melanoma, as well as the similarity between the retinal metabolism and the role of PDEs in purine metabolism suggest that PDE6 can act through the purine metabolism of cancer cells.

2. Retinal protein PDE6 takes part in purine metabolism

Structure and activity of PDE6

PDE6 was discovered as a protein in the retina as part of the light perception pathway. While PDE6 is inactive, the cGMP bound to CNG channels sustain a "dark-current", caused by the entry of Na^+ and Ca^{2+} ions into the photoreceptor cell, depolarising the outer membrane of the retina. Light transduction starts as light hits the retina, activating the G-protein transducin. A Gα-subunit dissociates from the activated transducin and binds to PDE6 complex to displace its inhibitory γ-subunits, resulting in the activation of the PDE6 complex (Figure 5.2) (Brennenstuhl et al., 2015).

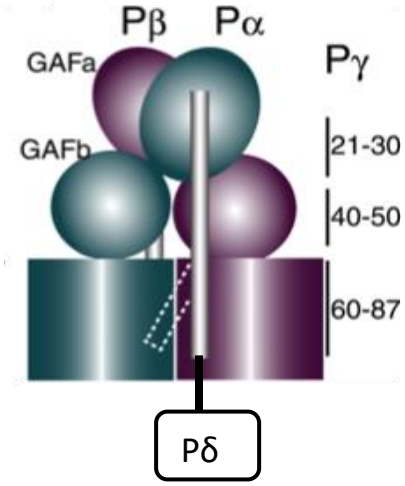


Figure 5.2: PDE6 complex structure.
PDE6 complex consists of a pair of catalytic subunits: Pα and Pβ, a pair of inhibitory subunits Pγ, and regulatory subunit Pδ. PDE6G gene produces the rod PDE6gamma whereas PDE6H produces the cone isoform. The catalytic subunits have two GAF domains at the N-terminal and a catalytic domain at the C-terminal. cGMP binds to the catalytic domain for hydrolysis and GAF domain for allosteric regulation of gamma subunit binding. (Modified from (Guo and Ruoho, 2008)).

Activation of PDE6 complex causes a rapid decrease in cGMP concentration, which leads to closure of cyclic nucleotide gated channels in the plasma membrane (Figure 5.3). The reduction of cytoplasmic cGMP followed by PDE6 activation results in the hyperpolarisation of photoreceptor membrane and release of glutamate at the photoreceptor synaptic terminal (Azevedo et al., 2014).

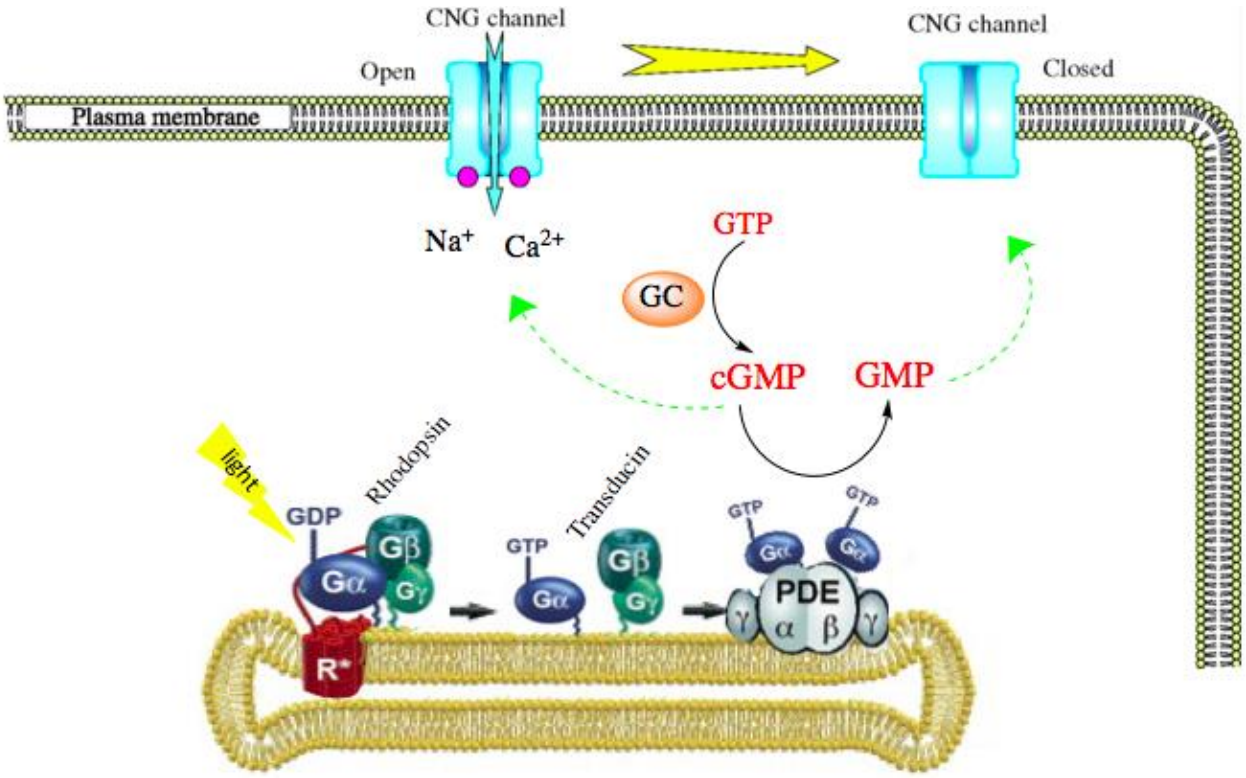


Figure 5.3: Visual signal transduction.
Visual signal transduction involves coordination of rhodopsin and transducin activation, followed by PDE6 and CNG (cyclic nucleotide gated) channel activity. Guanylate cyclase (GC) enzyme converts GTP to cGMP. CNG channels are open in the dark, when PDE6 is inactive, causing an influx of Ca^{2+} and Na^{+} ions. Upon absorption of light by retina, the G protein transducin activated PDE6 catalytic subunits by releasing the inhibitory gamma subunit from the active site of PDE6 protein complex. This stimulated the cGMP hydrolysis by PDE6, resulting in closure of photoreceptor ion channels.
Adapted from (Kramer and Molokanova, 2001), (Calvert et al., 2006), and (Veleri et al., 2015).

To ensure fast photoresponse, PDE6 gamma must bind and dissociate from the catalytic domain rapidly (Arshavsky et al., 2002). A W70A substitution of PDE6 gamma both activation and inactivation of the PDE6 complex, as it prevents PDE6 gamma from activating transducin GTPase and also reduces PDEgamma's affinity for

transducin (Slepak et al., 1995).

PDEs 2, 5, 6, 10, and 11 have consecutive GAF domains that bind to cyclic nucleotides. PDE6 GAF-A domain has the highest affinity for cGMP over cAMP. This non-catalytic binding causes conformational changes that affect the activity of the phosphodiesterase (Heikaus et al., 2009). In PDE5 and 6 enzymes, binding of cGMP to GAF-A domain is necessary for the dimerisation of the entire protein (Heikaus et al., 2008). Across all PDEs, The GAF domains have more sequence variety than the catalytic domains (Heikaus et al., 2009), which make GAF domains a potential target for PDE specific drug development. PDE specific inhibitor development remains a challenge, as current inhibitors affect more than one member of the family (Tiwari, 2007).

Differences between the rod and cone PDE6gamma-subunits

PDE6 is structurally distinct from the other PDEs in that it has two forms of dimerisation, including a homodimer of alpha'-subunits in cones and a heterodimer of alpha- and beta-subunits in rods (Azevedo et al., 2014). The implications of this cell-specific dimerisation still have not been clearly understood. Another feature by which PDE6 differs from other PDEs is that it has an inhibitory gamma-subunit, which speeds up its response time.

PDE6G gene produces the rod PDE6gamma whereas *PDE6H* produces the cone isoform. Each rod and cone PDE6s have two identical gamma-subunits. Rod PDE6gamma is thought to bind the alpha- and beta-subunits linearly and simultaneously, "stapling" the two catalytic subunits together (Guo et al., 2006). The interaction between the catalytic and inhibitory subunits within complex is critical for visual signalling. Work on rod PDE6 shows that the N-terminal (amino acids 16-30) of the gamma subunit interacts with the GAF-A domain of the complex, whereas the C-terminal (amino acids 73-87) interacts with the catalytic domain; the middle region of gamma subunit (amino acids 40-50) interact with GAF-B and the region between GAF-B and catalytic domain (Guo and Ruoho, 2008).

The two catalytic subunits of PDE6 are prenylated (alpha by farnesylation and beta by geranylgeranylation), this modification is necessary for the membrane attachment of the PDE complex (Anant et al., 1992). The transport of prenylated protein to the outer segment is aided by the delta-subunit, which can also transport farnesylated Rheb, farnesylated INPP5E-peptide, and farnesylated KRAS4B (Qureshi et al., 2018).

Besides their structural differences, cone and rod PDE6s have physiological and developmental differences. Cone cells have higher metabolic rates and need to endure periods of hypoxia Cone PDE6 precursor cells are sensitive to *Rb1* knockdown, which induces their proliferation in intact and isolated retina. Rb-deficiency also leads to acquisition of non-cone features in these cells. This dedifferentiation is not seen in rod precursors, suggesting that cone cells have similar oncogenic routes with retinoblastoma tumour cells (Xu et al., 2014). RB1 mutations lead to eye tumours before the age of 5 despite the global expression of the gene (Bremner and Sage, 2014).

3. Parallels between retinal and cancer metabolism

The retina has high demands for glucose and fatty acids. Proliferating retinal photoreceptor cells undergo aerobic glycolysis, a Warburg trait that they share with cancer cells (Fiske and Vander Heiden, 2012). Developing and highly proliferative frog retina preferentially relies on glycolysis and less on OXPHOS for ATP production compared to differentiated retina, as long as there is sufficient glycogen. Terminally differentiating retinal cells cause them to switch to OXPHOS (Agathocleous et al., 2012). Another common feature is the predominance of PKM2 isoform of pyruvate kinase in the retina (Rajala et al., 2016). This isoform of PKM has prognostic significance for its high mRNA expression in gastric, ovarian cancer and its high protein expression in ovarian, cervical pancreatic, breast, colorectal cancer and melanoma (Hsu and Hung, 2018).

Photoreceptors, like cancer cells, are sensitive to supplies of fatty acids and use them as an energy source, along with glucose (Ng et al., 2015). Like cancer cells, they

also can resort to neovasculature in times of nutrient deficiency. As in other tissues of high metabolic rate such as heart and skeletal muscle, that rely on lipid oxidation, photoreceptors have very-low-density-lipoprotein receptors (VLDLR). The latter facilitates transport of free fatty acids into tissue for oxidation (Joyal et al., 2016). Vldlr-/- mice model displays an example of interplay of oncogenic signalling and energy metabolism in the retina. Vldlr-/- mice retina have low levels of intracellular glucose due to activation of Ffar1 that inhibits glucose uptake when levels of fatty acids in blood are high. They also have low a-KG levels due to downregulation of fatty acid uptake. This depletion of a-KG leads to greater VEGFA transcription, stabilisation of Hif-1a and hence, neovascularisation. In addition to neovascularisation phenotype, Vldlr deletion also leads to age-related macular degeneration.

D) PDE6 might play a role in tissue protection from exposure to hypoxia and reactive oxygen species

Age related macular degeneration was studied in senescent-accelerated OXYS rats that develop a retinopathy similar to the one in humans (Kozhevnikova et al., 2014). The age-related changes in OXYS rat transcriptome are thought to serve as adaptive resources to prevent neurodegenerative changes. Aged (12 months old) OXYS rats display cerebral and retinal blood vessels with reduced reactivity, indicative of chronic ischemia that results from inadequate blood supply (Stefanova et al., 2014).It was observed that genes associated with cell adhesion and angiogenesis as well as the light perception genes Pde6c, Opn1mw, Col1a1, Pde6h and Aanat were downregulated significantly in 18 month OXYS rats compared to 3 month OXYS rats, but remained unchanged between 3 and 18 month old Winstar rats (control) (Kozhevnikova et al., 2014).

While it is known that PDE6gamma’s loss-of-function mutations contribute to the

gene signature for achromatopsia and retinitis pigmentosa, intracellular effects of PDE6H depletion remain understudied. Retinitis pigmentosa (ADRP) is accompanied with a dysregulation of calcium homeostasis and unfolded protein folding (Shinde, 2015). *PDE6A*, *PDE6B*, and *PDE6G* mutations cause recessive retinitis pigmentosa or autosomal dominant night blindness in humans, suggesting role of PDE6 in regulation of apoptosis (Brennenstuhl et al., 2015).

While the retina as a whole goes through periods of hypoxia, the photoreceptors of the outer retina are in greater danger of hypoxia compared to the rest of the retina. In dark, due to the high energy demands of exporting the sodium and water from rod cells, depolarised cells have to spend a lot of energy to repolarize. This increases oxygen consumption and lowers the oxygen concentration in the outer layers of retina, resulting in relative hypoxia compared to inner layers of retina (Sivaprasad and Arden, 2015). In the outer segments of the retina, oxygen concentration drops as the distance from the choroid increases. This also corresponds to an increase in membrane potential (Haugh et al., 1990).

Retinal photoreceptors activate hypoxia signalling via HIF-1α as the retina uses large amounts of oxygen and becomes hypoxic. Sustained upregulation of HIF-1α pathway in Vhl knockdown mice helps preserve photoreceptor morphology and function after light exposure by evading cell death. HIF-1α signalling is protective of short periods of hypoxia but long term hypoxia can still lead to retinal degeneration (Lange et al., 2011).

Due to the cycles of ischemia and oxygenation they face, photoreceptors need to cope with oxidative stress. Superoxide dismutases, encoded by SOD1 and SOD2, are part of the antioxidant system. This is important to protect from DNA damage and p53 activation as superoxide radical accumulation leads to growth arrest, apoptosis, and dysfunctional mitochondria (Watanabe et al., 2013). Ischemia in retinal and brain tissue can lead to tissue damage due to accumulation of ROS, which initiates cell death pathways. Low levels of ROS, however, can be neuroprotective due to ischemic

preconditioning (W. Thompson et al., 2012).

Although cones and rod photoreceptors have similar subunits for the same functions, their physiological responses to light signal are different. Cone photoreceptors do not saturate with background illumination and are responsive to more orders of magnitude of intensities of light; they also terminate their response and recover from a bright flash of light faster than rods (Knox and Solessio, 2006), (Ma et al., 2013).

Human cone cells are more mitochondria rich than rods (Hoang et al., 2002). Light dependent cGMP turnover is a process that increases oxygen consumption, which can be inhibited by PDE inhibitors (Wang et al., 2010). It is therefore possible that PDE6 activity, especially in cones, is necessary for mitochondrial function. Other organs that are prone to ischemia/reoxygenation injury are the brain, heart, testis and kidneys (Minutoli et al., 2016). Interestingly, these are the tissues where extra-retinal expression of cone *PDE6H* is observed (Su et al., 2004), (Su et al., 2002), (Roth et al., 2006), (Ramaswamy et al., 2001), (Shyamsundar et al., 2005a). While *PDE6G* is highly expressed in parts of the brain, it is not differentially expressed in heart, testis, or kidneys.

E) PDE6 isoforms are differentially expressed in cancer

Oncomine data showed the differential expression of mRNA levels of PDE6 genes in various healthy tissues. *PDE6A* is highly expressed in pituitary gland, vulva, lung, oesophagus, heart, testis, pancreas, and kidney (Ramaswamy et al., 2001), (Hsiao et al., 2001), (Su et al., 2004), (Shyamsundar et al., 2005b), (Roth, 2007). *PDE6A* copy number is high in prostate gland (Rothenberg et al., 2010). *PDE6A* is lowly expressed in ovary, breast, prostate gland, brain, bladder, lymph node, hematopoietic and lymphoid cell, and liver (Ramaswamy et al., 2001), (Hsiao et al., 2001), (Su et al., 2004), (Shyamsundar et al., 2005a), (Roth, 2007).

PDE6B is highly expressed in pancreas, bone marrow, thyroid gland, kidney, spinal cord, and brain (corpus callosum) (Roth, 2007), (Ramaswamy et al., 2001), (Shyamsundar et al., 2005a), (Su et al., 2002). *PDE6B* is lowly expressed in liver, oesophagus, vulva, pituitary gland, and prostate gland (Hsiao et al., 2001), (Roth, 2007).

PDE6C is highly expressed in pancreas and is under-expressed in lung, liver, and brain tissue (substantia nigra) (Ramaswamy et al., 2001), (Hsiao et al., 2001), (Roth et al., 2006).

PDE6D mRNA is highly expressed in testis, lung, parathyroid gland, oesophagus and hematopoietic and lymphoid cells (Su et al., 2004), (Shyamsundar et al., 2005b), (Roth, 2007), (Chang et al., 2008). *PDE6D* is lowly expressed in liver and breast tissue as well as epithelial and connective & soft tissue cells (Chang et al., 2008), (Su et al., 2004).

PDE6G is highly expressed in kidney (Ramaswamy et al., 2001).

PDE6H is highly expressed in epithelial cells, prostate gland, ovary, and brain (corpus callosum) ((Ramaswamy et al., 2001), (Su et al., 2002), (Su et al., 2004), (Roth et al., 2006). *PDE6H* is lowly expressed in prostate gland and bladder (Ramaswamy et al., 2001).

Genes encoding PDE6 isoforms are upregulated or downregulated in certain cancer types compared to normal tissue (Figure 5.4). Oncomine data that compares tumour samples with normal tissue, which show at least a two-fold increase in mRNA levels, were considered. This analysis showed that *PDE6A* is upregulated in uterine cancer (Leiomyosarcoma) (Quade et al., 2004), and leukaemia (T-cell prolymphocytic) (Dürig et al., 2007); *PDE6B* in breast (Mixed lobular and ductal adenocarcinoma) (Radvanyi et al., 2005) (Atlas), 2011b), ovarian (Serous adenocarcinoma) (Yoshihara et al., 2009), gastric cancers (Diffuse and mixed adenocarcinoma) (D'Errico et al., 2009) and lymphoma (Mantle cell lymphoma) (Basso et al., 2005); *PDE6C* in lung (Lung adenocarcinoma) (Beer et al., 2002) and brain cancers (Medulloblastoma) (Pomeroy et al., 2002); *PDE6D* in melanoma (cutaneous, and benign melanocytic skin) (Talantov,

2005) (Riker et al., 2008), and breast (lobular) (Perou et al., 1999) (Sørlie et al., 2003), brain (Oligodendroglioma) (Shai et al., 2003), bladder (Superficial bladder and infiltrating bladder urothelial carcinoma) (Blaveri, 2005), and renal (Clear cell renal cell carcinoma) (Gumz et al., 2007) cancers; *PDE6G* in uterine (Leiomyosarcoma) and breast (Lobular) (Perou et al., 1999) cancers and leukaemia (Acute myeloid and B-cell acute lymphoblastic leukaemia) (Andersson et al., 2007); *PDE6H* in renal (Chromophobe renal cell and renal pelvis urothelial carcinomas) (Jones, 2005), prostate (Carcinoma) (Luo et al., 2002) and breast (ductal in situ) (Radvanyi et al., 2005) cancer.

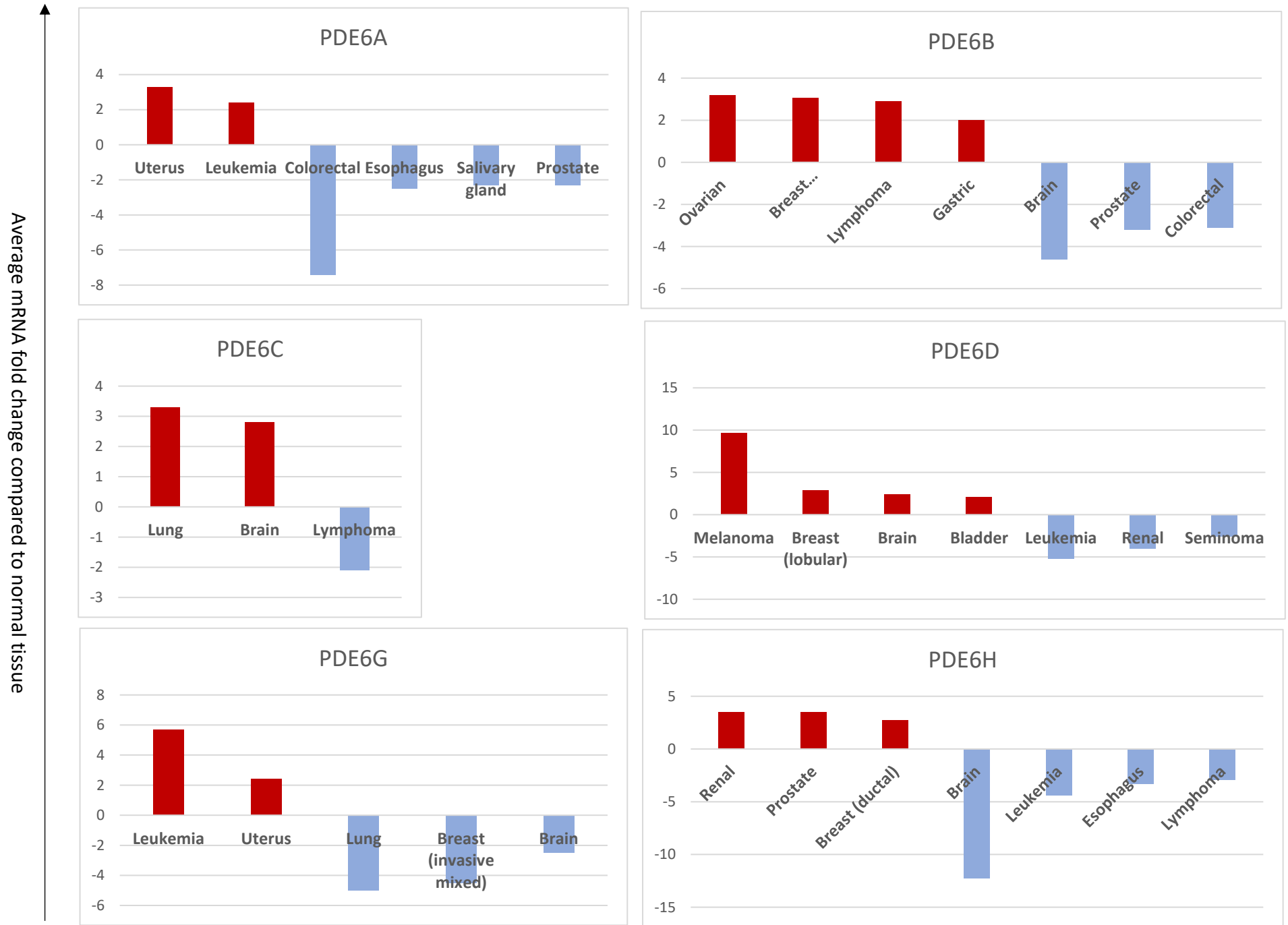

Average mRNA fold change compared to normal tissue
PDE6A
4
2
0
-2
-4
-6
-8
Uterus
Leukemia
Colorectal
Esophagus
Salivary gland
Prostate
PDE6B
4
2
0
-2
-4
-6
Ovarian
Breast...
Lymphoma
Gastric
Brain
Prostate
Colorectal
PDE6C
4
3
2
1
0
-1
-2
-3
Lung
Brain
Lymphoma
PDE6D
15
10
5
0
-5
-10
Melanoma
Breast (lobular)
Brain
Bladder
Leukemia
Renal
Seminoma
PDE6G
8
6
4
2
0
-2
-4
-6
Leukemia
Uterus
Lung
Breast (invasive mixed)
Brain
PDE6H
5
0
-5
-10
-15
Renal
Prostate
Breast (ductal)
Brain
Leukemia
Esophagus
Lymphoma

Figure 5.4: PDE6 family member genes are differentially expressed at the mRNA level in various cancers compared to normal tissue.
Results were compiled from Oncomine studies where at least a two-fold change is observed. Bars represent the average fold change of the studies presented.

Oncomine data on tumour samples that show at least a twofold decrease in mRNA levels (Figure 5.4), compared to normal tissue, reveal that *PDE6A* is downregulated in colorectal (Colon and rectal adenocarcinoma and adenoma and mucinous adenocarcinoma) (Gaedcke et al., 2010) (Hong et al., 2010) (Sabates-Bellver et al., 2007) (Khanin et al., 2010) (Kaiser et al., 2007), oesophagus (Barrett's oesophagus) (Kimchi et al., 2005), salivary gland (salivary gland adenoid cystic carcinoma) (Frierson et al., 2002) and prostate (Carcinoma) (Welsh et al., 2001) cancers; *PDE6B* in brain (atypical teratoid/rhabdoid tumour) (Pomeroy et al., 2002) (Gutmann et al., 2002), prostate (Carcinoma) (LaTulippe et al., 2002), colorectal (Rectal and colon adenocarcinoma) (Atlas), 2011a) and breast (Invasive lobular) cancers (Turashvili et al., 2007); *PDE6D* in leukaemia (acute myeloid leukaemia) (Stegmaier et al., 2004), renal cancer (Clear cell sarcoma) (Cutcliffe, 2005), and seminoma (Testicular seminoma, yolk sac tumour, and teratoma) (Korkola et al., 2006) (Sperger et al., 2003); *PDE6G* in lung (small cell lung carcinoma) (Bhattacharjee et al., 2001), breast (invasive mixed carcinoma) (Radvanyi et al., 2005) and brain (Oligodendroglioma, glioblastoma, atypical teratoid/rhabdoid tumour) (Pomeroy et al., 2002) (Shai et al., 2003) cancers; *PDE6H* in brain (malignant glioma, atypical teratoid/rhabdoid tumour, and oligodendroglioma) (Pomeroy et al., 2002) (Bredel et al., 2005), oesophagus (Barrett's oesophagus) (Hao et al., 2006), and breast (invasive lobular) (Turashvili et al., 2007) cancers, leukaemia (acute myeloid, B-cell and T-cell acute lymphoblastic leukaemia) (Andersson et al., 2007), and lymphoma (mantle cell lymphoma) (Basso et al., 2005).

For certain cancers, PDE6 genes are highly expressed while they are lowly expressed in the healthy tissue of origin, and vice versa. While *PDE6A* is highly expressed in oesophagus and prostate, it is downregulated in Barrett's Oesophagus and prostate carcinoma. *PDE6A* is lowly expressed in hematopoietic and lymphoid cells

while being upregulated in prolymphocytic leukaemia. *PDE6B* is highly expressed in brain tissue and downregulated in brain tumours. *PDE6C* is lowly expressed in healthy lung and liver while being upregulated in lung adenocarcinoma and medulloblastoma. *PDE6D* is lowly expressed in testis and is downregulated in seminoma. *PDE6H* is highly expressed in brain tissue and is downregulated in brain tumour. It is also lowly expressed in prostate gland while being upregulated in prostate carcinoma. This trend of expression can point out cancers where an over- or sunder-expression of PDE6 gene might have tumorigenic effect.

Unlike the other subunits of PDE6, PDE6gamma expression is cyclical and fluctuates with the various steps of the circadian rhythm. The mRNA for chick retina PDE6 rod gamma subunit (*PDE6G*) under daily darkness (LD) and constant darkness (DD) was evaluated. *PDE6G* expression was lowest after 6 hours of light and highest after 6 hours of dark (Bailey et al., 2004), with the latter being twice the minimum value. *PDE6G* expression in zebrafish retina also fluctuated; it is at its lowest value between 12:00 and 20:00 and rose to its maximum value of a 20-fold increase at 08:00 (Lagman et al., 2016). Fluctuations of zebrafish *PDE6H* took place to an even greater degree in a reverse trend to that of *PDE6G*, reaching a maximum between 12:00-17:00 and dropping 120 fold until the middle of the night at 04:00 (Lagman et al., 2016) Expression profile of *PDE6H* is also unique since a significant number of *PDE6H* amplified cancer cell lines also have amplified or gain-of-function mutated KRAS, unlike the other PDE6-family genes (Figure 5.5) (Gao et al., 2013).

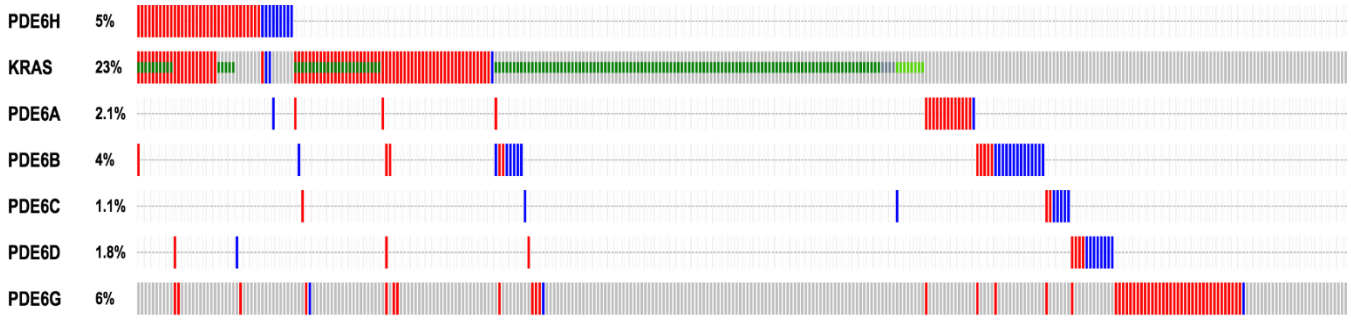


Figure 5.5: Cancer cell lines (CCLE) data show that the majority of cell lines with PDE6H amplification also have amplification or gain-of-function mutations of KRAS.
Other isoforms of PDE6 do not display this common mutation trend with KRAS. Generated using CBioPortal (Gao et al., 2013).

F) Knockdown of PDE6 genes caused cell cycle arrest, cell death and accumulation of mitochondrial ROS in HCT116

Following the screen, which was conducted in high glucose concentrations (25 mM) and the where the transfection duration was three days, the follow-up work was conducted with cell culture of low glucose concentrations (5 mM) to better mimic normal plasma glucose level (Tirosh et al., 2005). The transfection duration was kept at three days, but media were changed after the first 48 hours of transfection to prevent starvation of the cells. RNA extractions were conducted on 48th hour of transfection, prior to medium change.

As part of the process of determining PDE6H as the candidate of interest, the other PDE6 family genes were inhibited via siRNA. Cell cycle distribution of the cells was determined based on dual propidium iodide (PI) substitute, FxCycle, and 5-Ethynyl-2´-deoxyuridine (EdU) staining (Figure 5.6). Compared to PI staining method utilised during our cell cycle screen, this method is better able differentiate between the G1 and S stages, as EdU staining displays S population more accurately. This method was deemed suitable to measure cell cycle distribution, as it confirmed the positive controls used in the siRNA screen described in Chapters 3 and 4.

Similar results were obtained with PI staining with the FxCycle and EdU staining of HCT116 cells. siCCND1 increased percentages of G1 (15%) with decreased percentages of S and increased percentages of G2. Due to its greater increase in %G1, siCCND1 was chosen as the G1 positive control. siANAPC1, siCDC2, and siPLK1 caused increases in G2 as expected (15%, 25%, and 57%) with decreases in %S. siCDC2 was chosen as the G2 positive control since it caused a greater increase in G2 population than siANAPC1 and did not cause drastic cell death as did siPLK1.

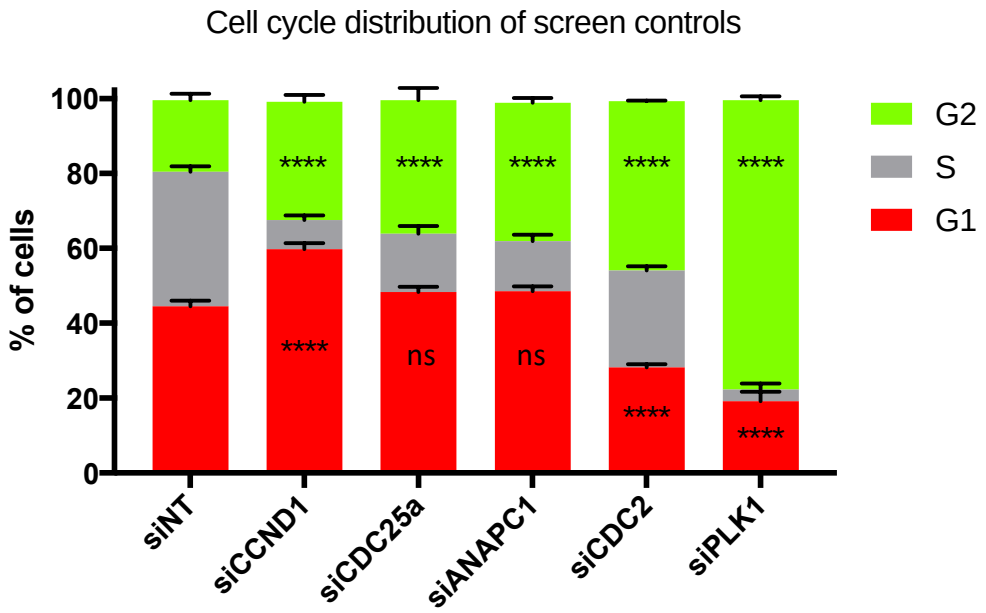


Figure 5.6: FxCycle and EdU staining was used to determine cell cycle distribution of HCT116 cells following transfection with positive control siRNAs.
*Data are mean±standard deviation, representative of three independent experiments, n=3 biological replicates. 2-way ANOVA, followed by Dunnett's multiple comparisons test was used to determine the statistical significance while comparing the percentage of G1 and G2 cells of each sample to siNT values. (ns P>0.05, **** P<0.0001).*

Following siRNA transfection in 5 mM glucose media, knockdown of *PDE6A*, *PDE6D* and *PDE6H* increased the G1 population compared to the negative control siNT group 10%, 10% and 18% respectively (Figure 5.7). siPDE6H caused the largest increase in G1 population amongst all isoforms.

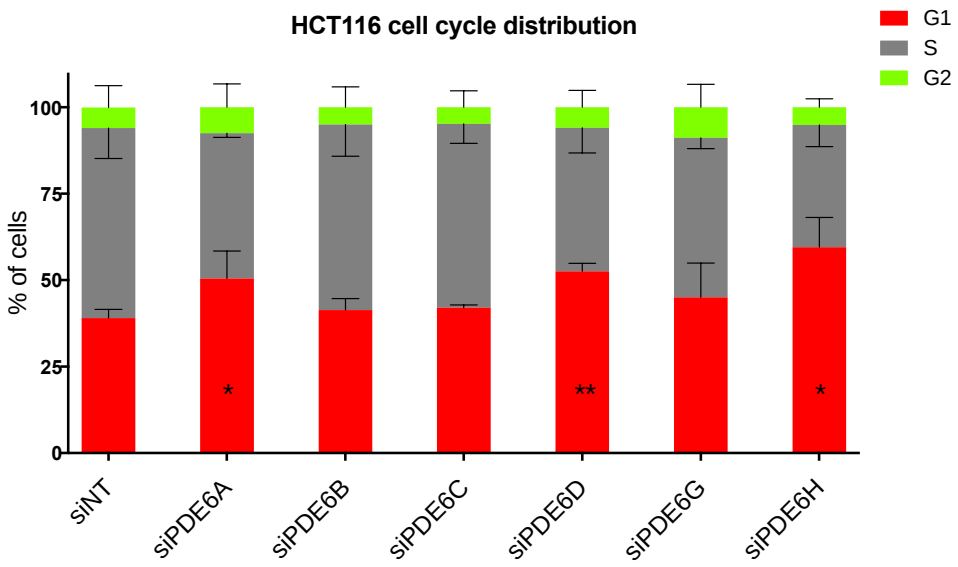


Figure 5.7: PDE6A, PDE6D, and PDE6H knockdowns caused G1/S arrest in HCT116 cells.
*Samples were analysed for FxCycle and EdU staining on the third day of siRNA transfection via flow cytometry. Data are mean±standard deviation, representative of three independent experiments, n=3 biological replicates. 2-way ANOVA, followed by Dunnett's multiple comparisons test was used to determine the statistical significance between percentage of cells in G1/S compared to the values of siNT group.*P<0.05, **P<0.01.*

Apoptotic HCT116 cell populations were determined by Annexin V and PI staining via flow cytometry following knockdown of PDE6 isoforms. The Annexin V and PI staining revealed the percentage increase in the apoptotic populations of cells (Figure 5.8). siPDE6H was the group that had the largest percentage necrotic cells (18%), and the only one that displayed a significant increase in percentage of apoptotic cells (2.5%). *PDE6G*, the other inhibitory subunit encoding gene, was the gene the knockdown of which caused the second largest increase in necrotic cell population (13%).

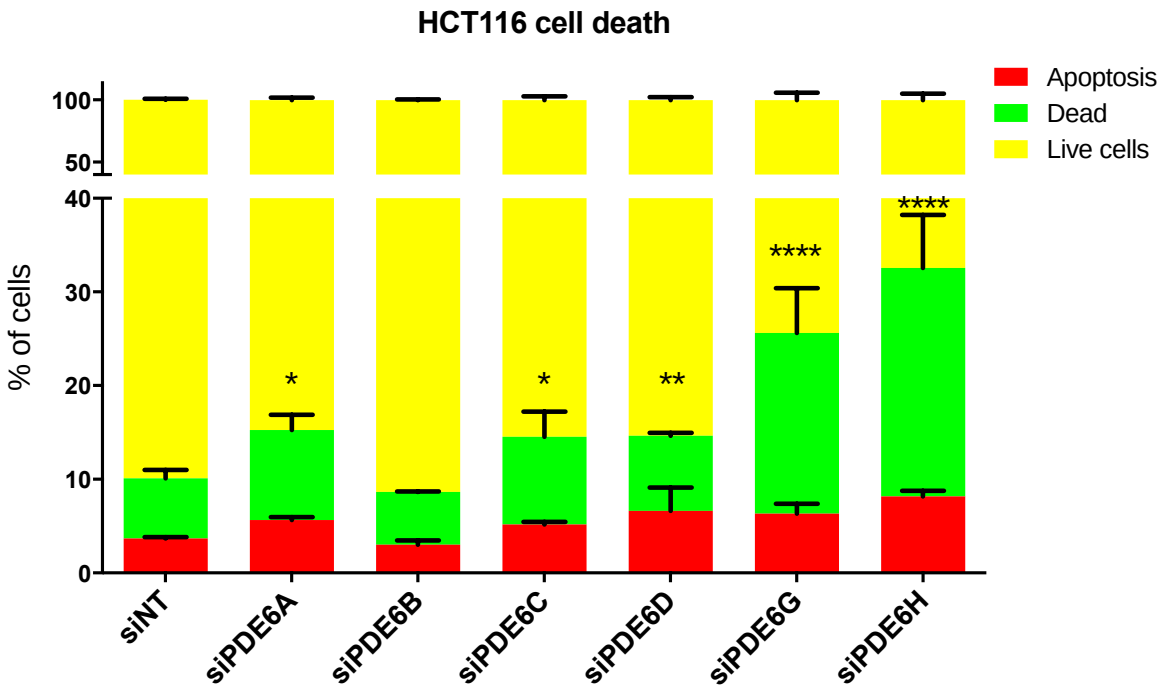


Figure 5.8: PDE6A, PDE6C, PDE6D, PDE6G and PDE6H knockdowns caused an increase in HCT116 cell death.
*Samples were analysed for PI and Annexin V staining on the third day of siRNA transfection via flow cytometry. Data are mean±standard deviation, representative of three independent experiments, n=3 biological replicates. 2-way ANOVA, followed by Dunnett's multiple comparisons test was used to determine the statistical significance between percentage of apoptotic+necrotic cells compared to the values of siNT group. Increase in apoptotic+necrotic cell populations from siNT values were statistically significant in all siRNA transfections except for siPDE6B. * P<0.05, ** P<0.01, **** P<0.0001.*

Mitochondrial specific ROS indicator probe MitoSOX-Red was used to detect mitochondrial superoxide ROS production (Figure 5.9). Median of the BL2 channel was used to present MFI (median fluorescence intensity) as the indicator of MitoSOX signal.

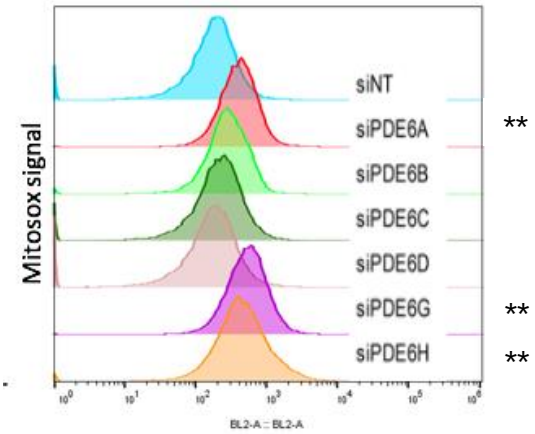


Figure 5.9: Knockdown of PDE6 isoforms caused an increase in mitochondrial ROS in HCT116 cells.
MitoSOX signal is an indication of mitochondrial ROS; its median was highest in siPDE6A, siPDE6G and siPDE6H groups (**). Samples were analysed on the third day of siRNA transfection via flow cytometry. Data are representative of three independent experiments.

Knockdown of PDE6 isoforms *PDE6A*, *PDE6G*, and *PDE6H* resulted in increased in MitoSOX signal as well as increased cell death. These results suggest that an increase in mitochondrial ROS might lead to or is caused by dysfunctional mitochondria.

G) *PDE6H* knockdown caused arrest at the G1/S checkpoint in colorectal and breast cancer cell lines

siPDE6H transfection caused G1 arrest in HCT116, MDA-MB-231 and MDA-MB-468 cells (Figure 5.10). The arrest was characterised by the percentage cell cycle distribution determined based on propidium iodide (PI) and EdU staining. Cell cycle distributions reveal a 11% increase in G1 in HCT116, 10% in MDA-MB-231 cells and an increase of 15% in MDA-MB-468 cells. There was a slight yet statistically insignificant (5%) increase in G1 population of DLD1 cells and the MCF7 cells showed no indication of a cell cycle arrest based on their FxCycle-EdU staining.

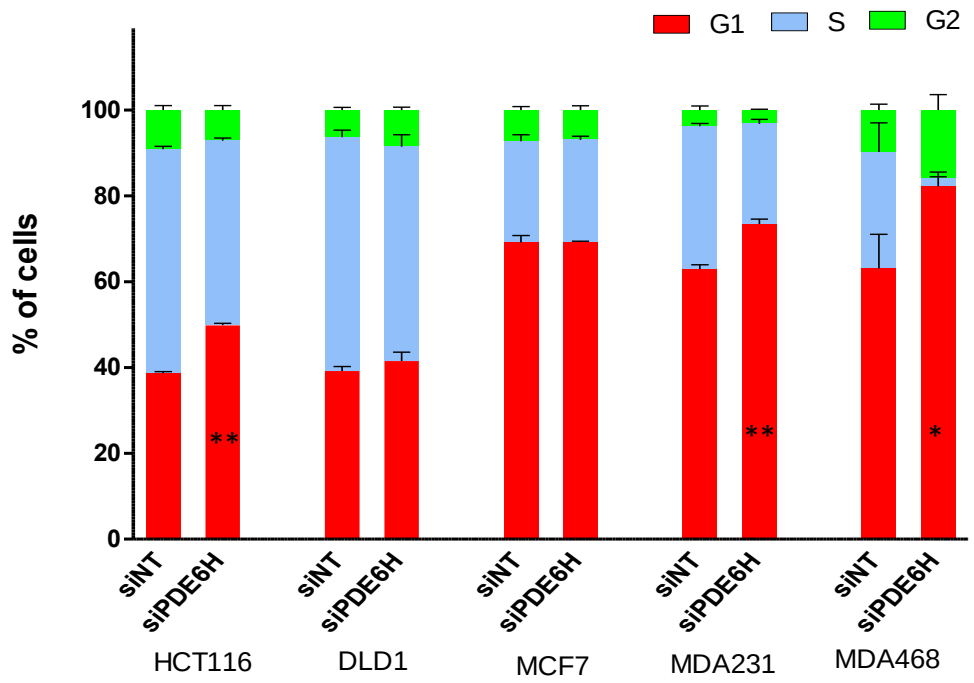


Figure 5.10: siPDE6H transfection caused G1 arrest in HCT116, MDA-MB-23 and MDA-MB-468 cells.
*Samples were analysed for FxCycle and EdU staining on the third day of siRNA transfection via flow cytometry. Data represent n=3 biological replicates. 2-way ANOVA was used to determine the statistical significance between percentage of cells in G1/S compared to the values of siNT group.*P<0.05, **P<0.01.*

Amongst the PDE6 family members, *PDE6H* was the gene the knockdown which caused the most notable G1 arrest. The results of the screen had shown that siPDE6H transfection caused a greater G1/S arrest than that the other cone gene, siPDE6C which encodes the catalytic subunit of cone PDE6 protein complex. Protein expression of G1 regulators support this finding. Both siPDE6C and siPDE6H transfections resulted in an increase of cyclin D1 protein levels (Figure 5.11). In the case of a G1 arrest, cyclin D1 protein levels accumulate when the protein is not being utilised in the complex with CDK4/6 for progression into S phase. The decrease in the amount of phosphorylated Rb protein also supported the G1 arrest. In accordance with the previous results which showed that siPDE6H transfection caused a significant G1 arrest unlike that of siPDE6C, the increase in cyclin D1 protein levels of and the corresponding decrease in phospho-RB were observed to a lesser extent in the *PDE6C* knockdown HCT116 cells compared to the *PDE6H* knockdown group.

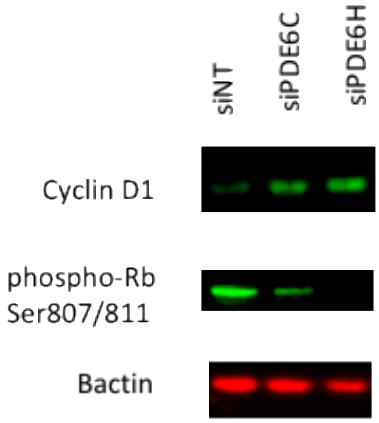


Figure 5.11: Knockdown of the cone PDE6 isoforms, PDE6C and PDE6H, caused an increase in cyclin D1 and a decrease in phospho-RB Ser807/811 protein levels in HCT116 cells.
Data are representative of three independent experiments.

Besides causing an accumulation of cyclin D1, *PDE6H* knockdown lowered protein levels of cell cycle regulators that were necessary for progression through G1 and into S phase. Levels of CDK4 and CDK6 lowered both at mRNA (Figure 5.12) and protein levels (Figure 5.13). Cyclin D1 needs to form a complex with CDK4 and CDK6

to complete G1 phase and go on to the S phase. Increase in both mRNA and protein levels of cyclin D1 might also have an inhibitory effect on CDK2 activity which would

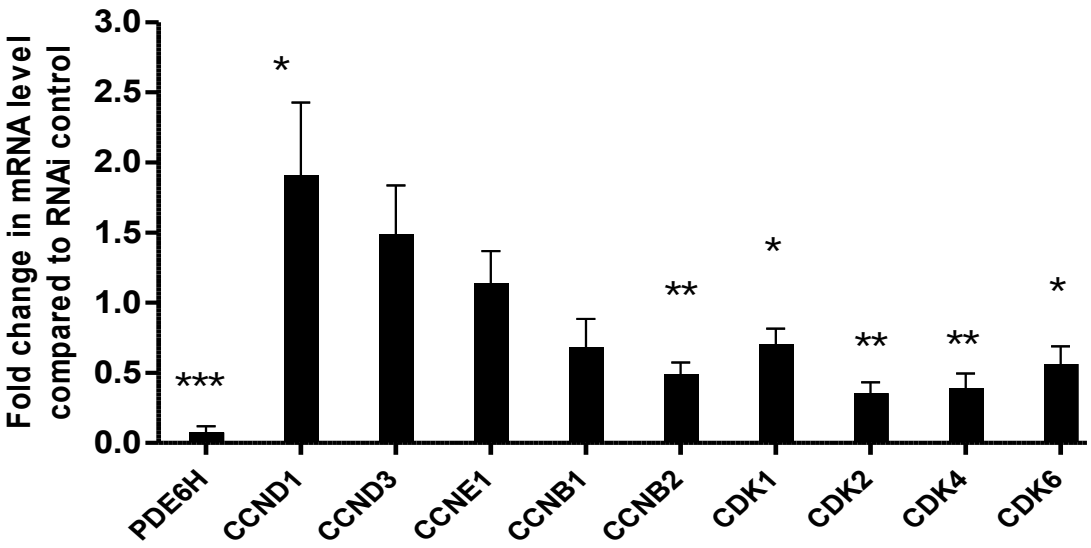


Figure 5.12: PDE6H knockdown changed mRNA expression of cell cycle regulators in HCT116.
*Data shown are mean values of n=4 technical replicates from one experiment, representative of two independent experiments; error bars represent standard deviation. *P<0.05, **P<0.01, ***P<0.001, ****P<0.0001 One-way ANOVA with Dunnett's multiple comparisons test was used to determine the statistical significance between mRNA expressions of each siRNA compared to the values of siNT for each gene.*

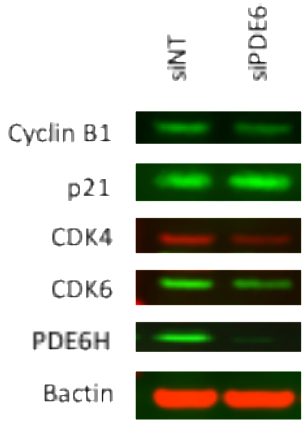


Figure 5.13: PDE6H depletion resulted in lower levels of G1 regulators in HCT116 cells. Data are representative of three independent experiments.

result in arrest before S stage (Fukami-Kobayashi and Mitsui, 1999).

PDE6H knockdown also changed mRNA expression of cell cycle components

that continue accumulating thorough further stages of cell cycle and reach a maxima in S (cyclin A1), G2 (cyclin B1) (Hochegger et al., 2008). mRNA levels of CDK1 which acts in G2, and CDK2 which act in S phases, also decreased. Experiments presented in Figure 5.12 need to be repeated with at least three biological replicates; the statistical analysis merely indicates technical reproducibility. These preliminary results suggest that the arrest upon PDE6H depletion occurred before S phase in HCT116 cells which did not reach S or G2/M where the corresponding cell cycle regulators would have been needed. In addition to the decrease in transcription of CDK1, 2, 4, and 6, the CDK inhibitor p21 protein levels increased slightly (1.5 fold) with siPDE6H transfection. Since the increase in p21 levels were not sufficient to cause cell cycle arrest on its own (Carter et al., 2009), the decrease in cyclin-CDK complex activity might have been independent of p21 activity (Figure 5.13).

H) *PDE6H* knockdown induced cell death and dysfunctional mitochondria

PDE6H inhibition resulted in an increase of necrotic populations of HCT116 (10%) and apoptotic populations of MDA-MB-231 (18%) and MDA-MB-468 (12%) (Figure 5.14).

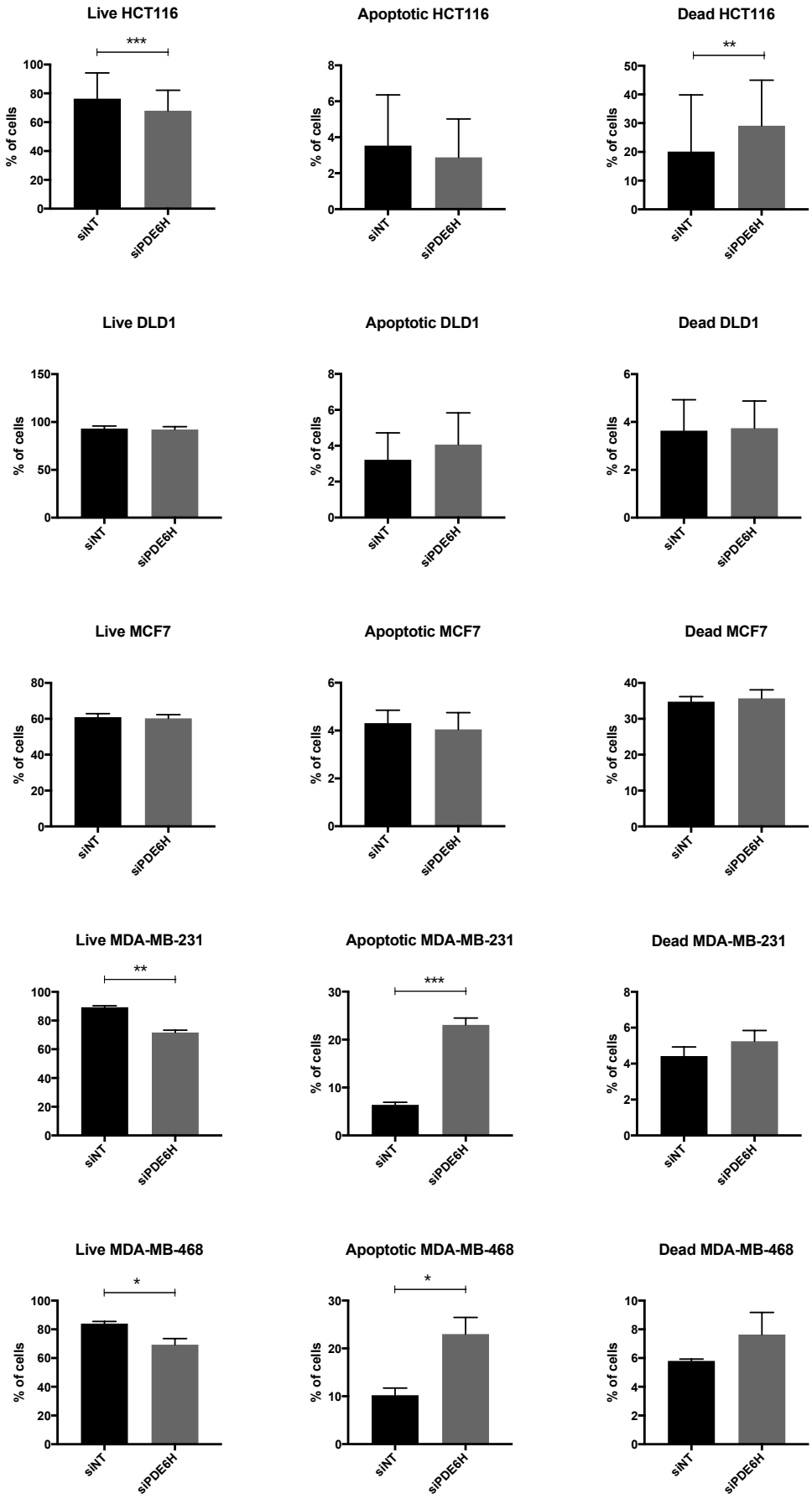

Live HCT116
***
% of cells
100
80
60
40
20
0
siNT
siPDE6H
Apoptotic HCT116
8
6
4
2
Dead HCT116
**
50
40
30
10
Live DLD1
150
50
Apoptotic DLD1
Dead DLD1
Live MCF7
Apoptotic MCF7
Dead MCF7
Live MDA-MB-231
Apoptotic MDA-MB-231
Dead MDA-MB-231
Live MDA-MB-468
Apoptotic MDA-MB-468
Dead MDA-MB-468

Figure 5.14: siPDE6H transfection increased cell death in HCT116, MDA-MB-231 and MDA-MB-468 cell populations.
*Apoptotic cell populations were determined by Annexin V and PI staining via flow cytometry following knockdown of PDE6H. Ratio-paired two-tailed t-tests were applied to compare the fold changes in percentage of cells between siNT and siPDE6H groups, n=6 biological replicates. * P<0.05, ** P<0.01, *** P<0.001.*

PDE6H knockdown increased MitoSOX MFI in HCT116, DLD1, MDA-MB-231, and MDA-MB-468 (Figure 5.15).

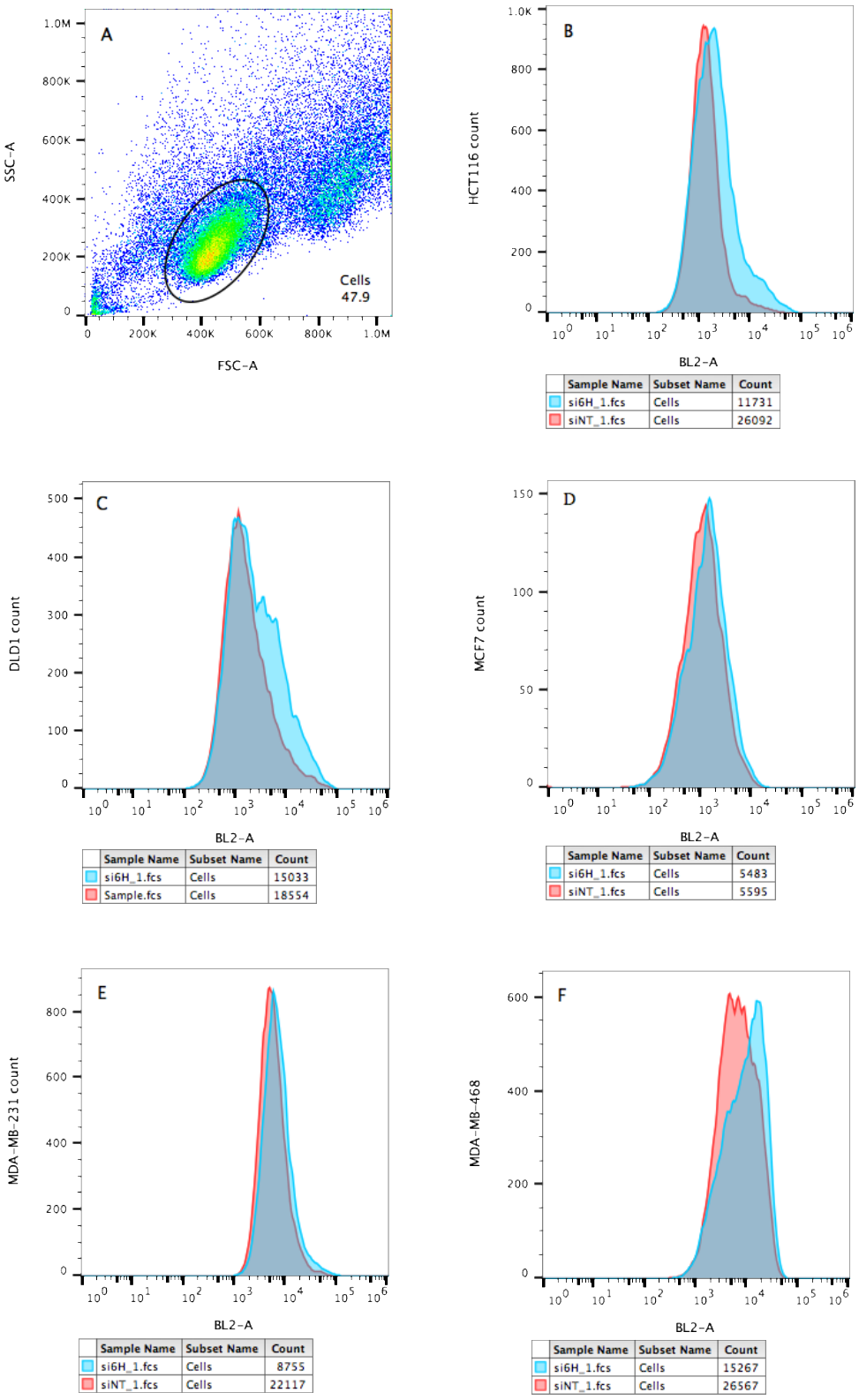


Figure 5.15: Knockdown of PDE6 isoforms caused an increase in mitochondrial ROS in HCT116, DLD1, MDA-MB-231, and MDA-MB-468 cells.

Percentage of dysfunctional mitochondria was measured as described in Figure 5.16.

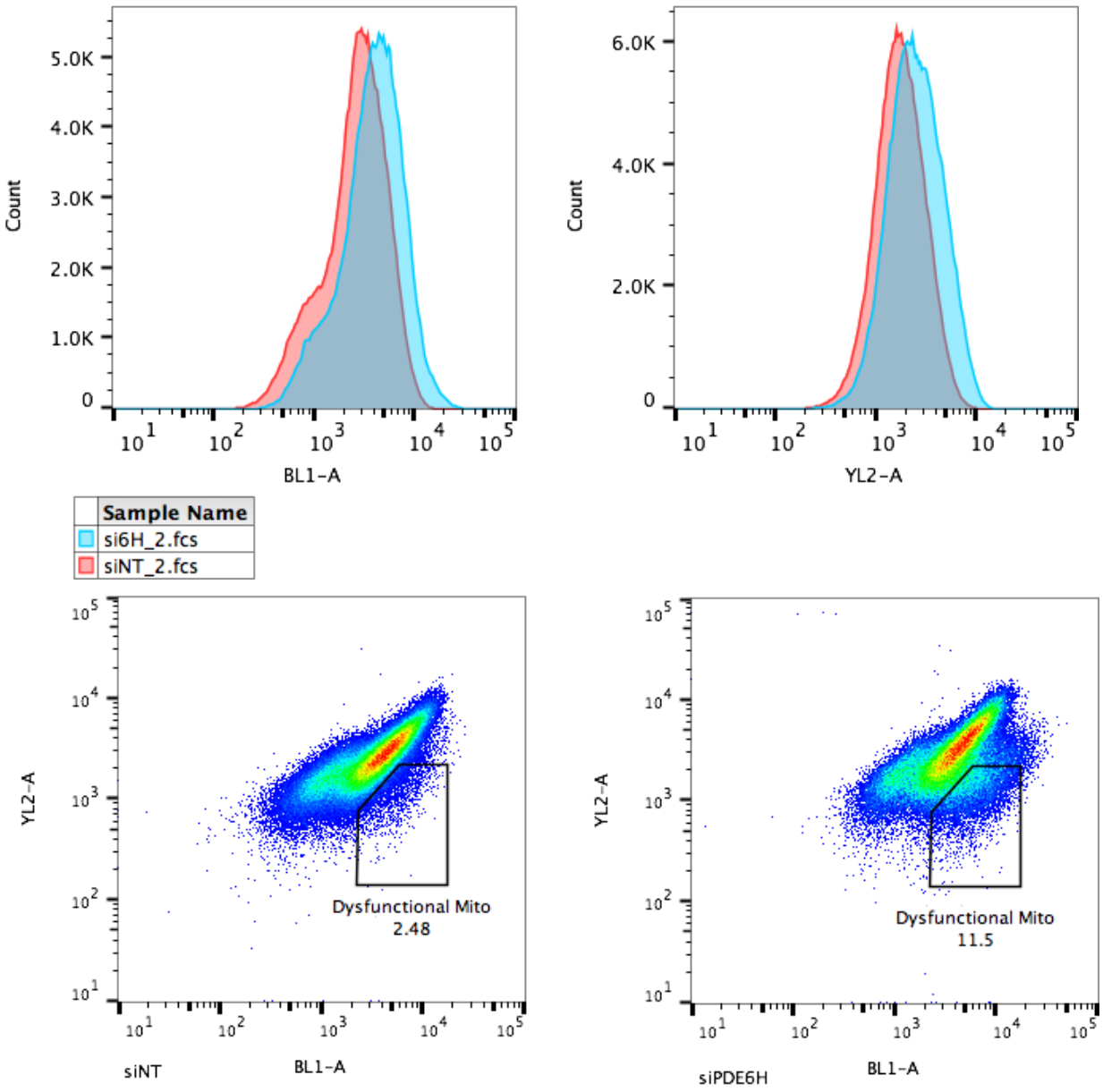
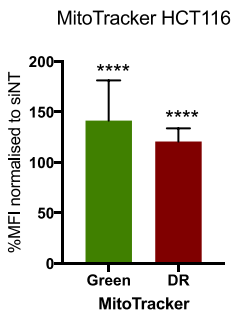
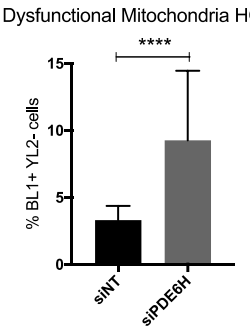
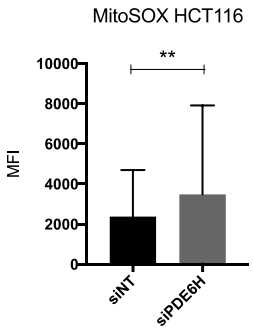


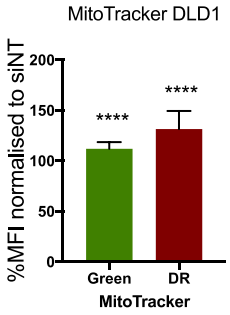
Figure 5.16: Calculating dysfunctional mitochondria in HCT116 cells based on MitoTracker signals.
MitoTracker Green (BL1) and MitoTracker Deep Red (YL2) signals were used to represent total mitochondria density and functional/respiring mitochondria density, respectively. BL1+ YL2- cell population was measured to indicate % of cells with non-respiring (dysfunctional) mitochondria.

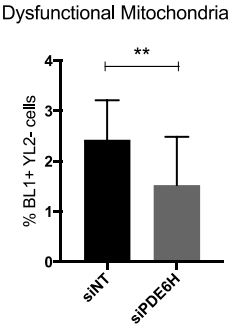
There was also a 2.6-fold increase in HCT116, a 1.2-fold increase in MCF7, a 1.3-fold increase in MDA-MB-231, and a 1.6-fold increase in MDA-MB-468 of dysfunctional mitochondria (Figure 5.17) There was a two-fold decrease in percentage of DLD1 cells with dysfunctional mitochondria.

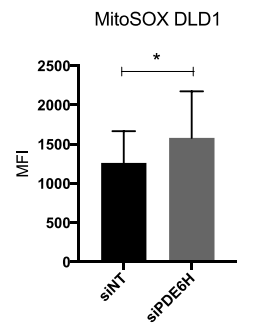

MitoTracker HCT116
%MFI normalised to siNT
****
****
Green
DR
MitoTracker

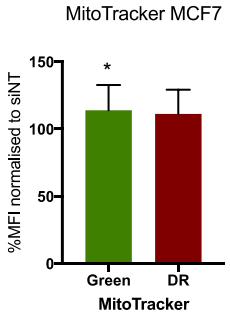

Dysfunctional Mitochondria HCT116
% BL1+ YL2- cells
****
siNT
siPDE6H

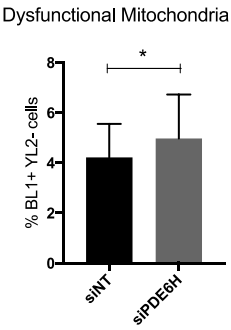

MitoSOX HCT116
MFI
**
siNT
siPDE6H

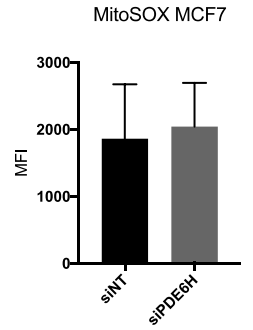

MitoTracker DLD1
%MFI normalised to siNT
****
****
Green
DR
MitoTracker

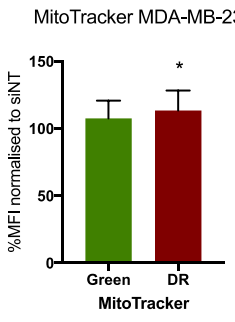

Dysfunctional Mitochondria DLD1
% BL1+ YL2- cells
**
siNT
siPDE6H

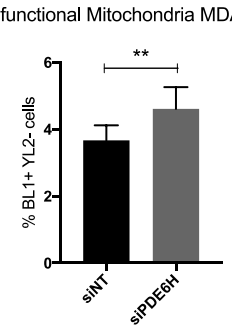

MitoSOX DLD1
MFI
*
siNT
siPDE6H

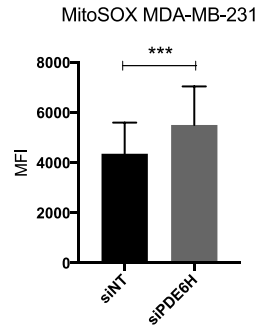

MitoTracker MCF7
%MFI normalised to siNT
*
Green
DR
MitoTracker

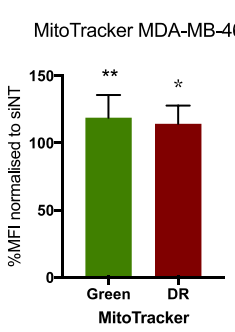

Dysfunctional Mitochondria MCF7
% BL1+ YL2- cells
*
siNT
siPDE6H

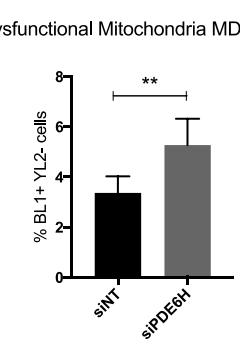

MitoSOX MCF7
MFI
siNT
siPDE6H


MitoTracker MDA-MB-231
%MFI normalised to siNT
*
Green
DR
MitoTracker


Dysfunctional Mitochondria MDA-MB-231
% BL1+ YL2- cells
**
siNT
siPDE6H


MitoSOX MDA-MB-231
MFI
***
siNT
siPDE6H


MitoTracker MDA-MB-468
%MFI normalised to siNT
**
*
Green
DR
MitoTracker


Dysfunctional Mitochondria MDA-MB-468
% BL1+ YL2- cells
**
siNT
siPDE6H

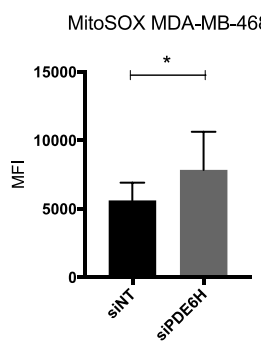

MitoSOX MDA-MB-468
MFI
*
siNT
siPDE6H

Figure 5.17: MitoTracker and MitoSOX MFI analyses following siPDE6H transfection. PDE6H knockdown increased both MitoTracker Green and DR MFI in HCT116, DLD1, and MDA-MB-468. PDE6H knockdown increased MitoTracker Green MFI in MCF7. PDE6H knockdown increased MitoTracker DR MFI in MDA-MB-231. PDE6H knockdown caused accumulation of dysfunctional mitochondria in HCT116, MCF7, MDA-MB-231 and MDA-MB-468 cells.
*Dysfunctional mitochondria were quantified based on the fraction of Mitotracker Green positive and MitoTracker Deep Red negative cells. Samples were analysed on the third day of siRNA transfection via flow cytometry. Data are mean±standard deviation, representative of three independent experiments. For MitoTracker and dysfunctional mitochondria measurements, n=9 biological replicates. For MitoSOX measurements, n=6 biological replicates. Ratio-paired two-tailed t-tests were used to compare the fold changes in MitoTracker Green and Deep Red MFI. Ratio-paired two-tailed t-tests were used to compare differences in percentage of dysfunctional mitochondria in siPDE6H to those of siNT control group. *P<0.05, **P<0.01, ***P<0.001, ****P<0.0001.*

In HCT116, MDA-MB-231, and MDA-MB-468 cells, increases in both dysfunctional mitochondria and MitoSOX MFI were observed. While we do not know the fold change in dysfunctional mitochondria necessary for causing an increase in mitochondrial ROS, dysfunctional mitochondria might be caused by or might contribute to the production of mitochondrial ROS (Weinberg et al., 2015). Dysfunctional mitochondria were higher in *PDE6H* knockdown MCF7 cells compared to siNT group. However, an increase in percentage of MitoSOX MFI was not detected in this cell line. DLD1 *PDE6H* knockdown caused a decrease in percentage of dysfunctional mitochondria despite increasing MitoSOX MFI.

PDE6H knockdown increased MitoTracker Green MFI in HCT116, DLD1, MCF7, and MDA-MB-468, while increasing MitoTracker DR in HCT116, DLD1, MDA-MB-231, and MDA-MB-468. Considering that the percentage dysfunctional mitochondria and MitoSOX also increased in HCT116 and MDA-MB-468 cells, these cell lines potentially showed an accumulation of mitochondrial mass that was not matched with an adequate increase in mitochondrial potential. Interestingly, *PDE6H* knockdown in MDA-MB-231 resulted in increased MitoSOX MFI and percentage of dysfunctional mitochondria despite a lack of mitochondrial accumulation and a slight increase in MitoTracker DR signal. HCT116, MDA-MB-231, and MDA-MB-468 are the cell lines that showed increased MitoSOX MFI, % dysfunctional mitochondria and cell death following *PDE6H*

knockdown. The decrease in dysfunctional mitochondria in DLD1 might be attributed to the increase in mitochondrial potential despite the increase in mitochondrial ROS. The increase in dysfunctional mitochondria of MCF7 can be explained by the accumulation of mitochondrial mass despite an increase in membrane potential.

It must be noted that quantifying MitoTracker Green+ MitoTracker DR- cells as those with dysfunctional mitochondria is an indirect way of describing this phenotype (Figure 5.17). An increase in MitoTracker Green-positive, MitoTracker DR-negative cell population denote an increase in dysfunctional non-respiring mitochondria (Tal et al., 2009) (Ip et al., 2017). An increase MitoTracker Green MFI indicates an increase in mitochondrial mass and an increase in MitoTracker DR MFI should indicate an increase in mitochondrial membrane potential (Puleston, 2015). Therefore, if cells fail to sufficiently increase their membrane potential (MitoTracker DR MFI) despite an increase of mitochondrial mass (MitoTracker Green MFI), we assume that there is an accumulation of dysfunctional mitochondria. However, there is no defined ratio that of MitoTracker DR MFI/ MitoTracker Green MFI that would indicate mitochondrial health. Additionally, some reports show that both MitoTracker Green and DR signals depends on mitochondrial potential and ROS levels (Xiao et al, 2016). A live/dead stain can also be incorporated to MitoTracker and MitoSOX gating since dead cells might interfere with staining (Puleston 2015). Further markers of mitochondrial morphology and function should be taken into consideration for a more accurate representation of effect of *PDE6H* knockdown on mitochondria, such as quantification of mitochondrial DNA by determining mtDNA copy number relative to that of nuclear DNA via qPCR (Rooney et al., 2015).

I) siPDE6H transfection altered oxidative phosphorylation and glycolysis profiles of various cancer cell lines

Due to an increase cell death along with changes in mitochondrial density and potential following *PDE6H* knockdown, the effect of PDE6H depletion on cell metabolism became of interest. Levels of oxidative phosphorylation and glycolysis were determined by OCR (oxygen consumption rate) and ECAR (extracellular acidification rate) respectively, measured through the Seahorse assay. The assay consisted of three measurements of basal OCR and ECAR levels followed by three consecutive measurements taken after each drug injection as explained in Chapter 2, section I.

Each time point (tp) represents an OCR/ECAR measurement taken during the assay. siPDE6H transfection resulted in lowering of basal OCR and ECAR in the colorectal cancer cell lines HCT116 (Figure 5.18), DLD1 (Figure 5.19), and triple-negative breast cancer cell line MDA-MB-468 (5.20).

The mitochondrial stress test results helped determine the maximal respiration capacity based on OCR readings following FCCP injection. The maximal respiration capacities of HCT116 WT, DLD1, MDA-MB-468, and MDA-MB-231 (Figure 5.21) were lower in the siPDE6H group. The ECAR and OCR values of MCF7 cells did not change following *PDE6H* knockdown (Figure 5.22).

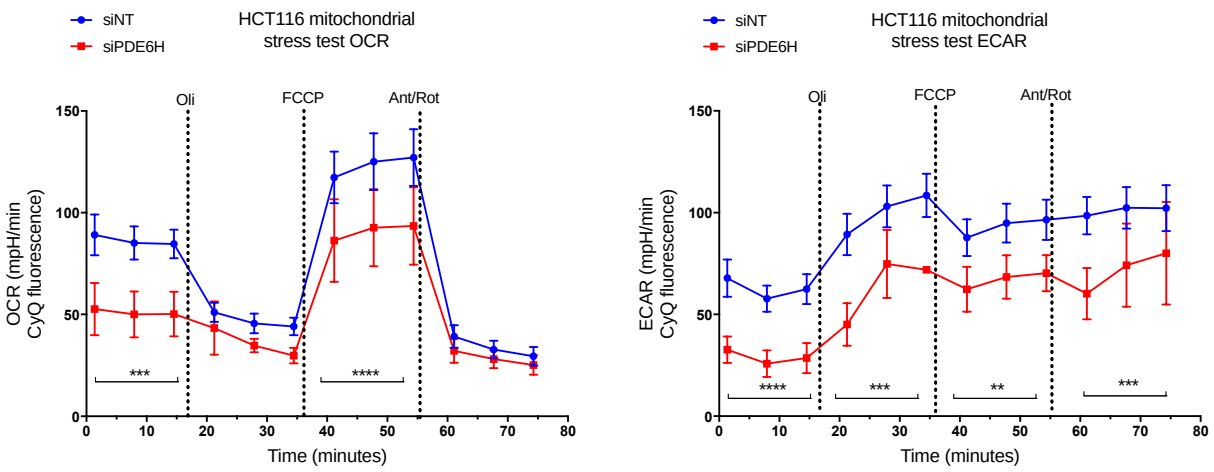


Figure 5.19: PDE6H knockdown lowered basal levels of oxidative phosphorylation and glycolysis in HCT116 cells.
*Data are mean±standard deviation, from a single experiment, representative of three independent experiments, n=5 technical replicates. 2-way ANOVA test with Sidak's multiple comparisons was used to compare the levels of OCR and ECAR between samples at each time point. ** P<0.01, *** P<0.001, **** P<0.0001.*

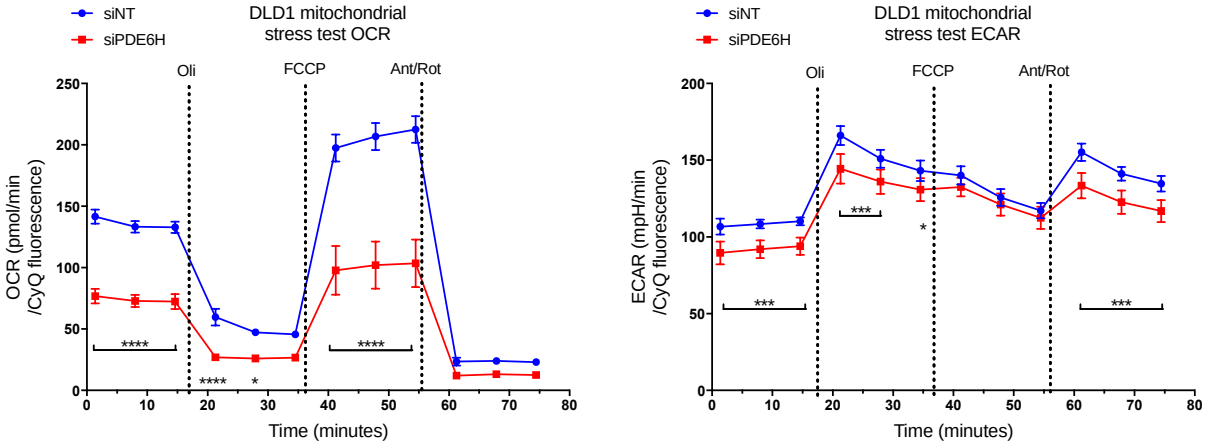


Figure 5.18: PDE6H knockdown lowered basal levels of oxidative phosphorylation and glycolysis as well as the maximal respiration capacity in DLD1 cells.
*Data are mean±standard deviation, from a single experiment, representative of three independent experiments, n=5 technical replicates. 2-way ANOVA test with Sidak's multiple comparisons was used to compare the levels of OCR and ECAR between samples at each time point. * P<0.05, ** P<0.01, *** P<0.001, **** P<0.0001.*

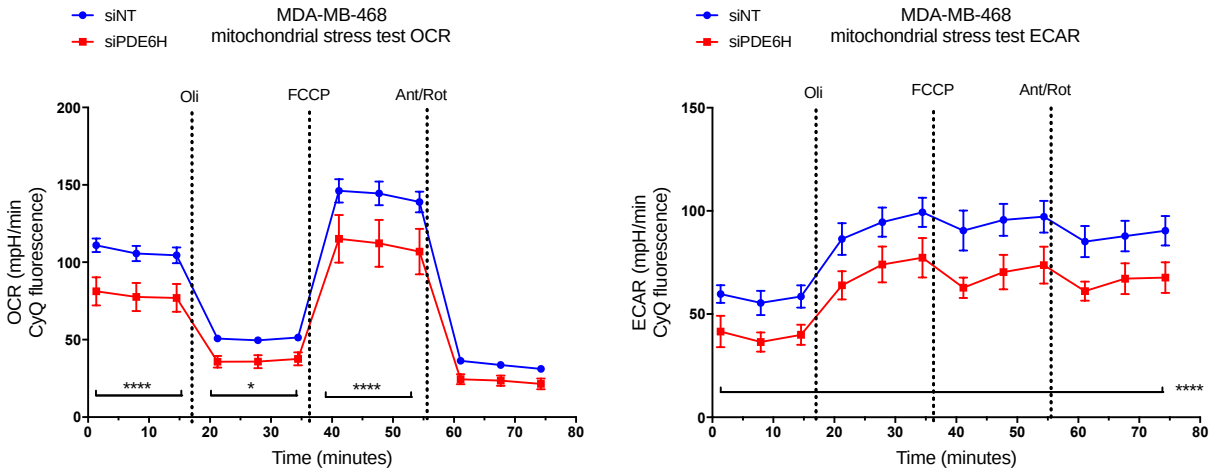


Figure 5.20: PDE6H knockdown lowered basal levels of oxidative phosphorylation and glycolysis as well as the maximal respiration capacity in MDA-MB-468 cells.
*Data are mean±standard deviation, from a single experiment, representative of three independent experiments, n=6 technical replicates. 2-way ANOVA test with Sidak's multiple comparisons was used to compare the levels of OCR and ECAR between samples at each time point. * P<0.05, ** P<0.01, *** P<0.001, **** P<0.0001.*

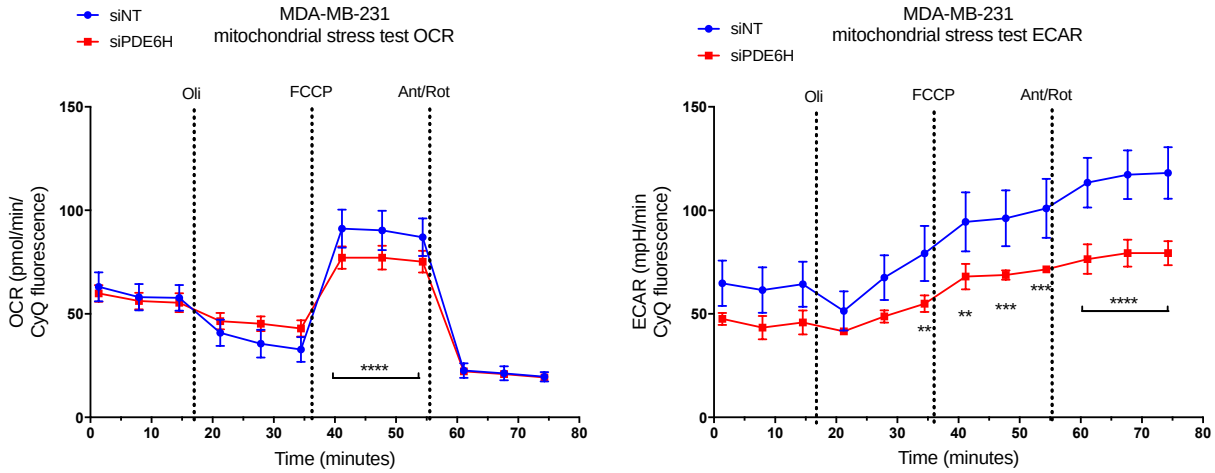


Figure 5.21: PDE6H knockdown lowered ECAR levels and maximum OCR capacity in MDA-MB-231.
*Data are mean±standard deviation, from a single experiment, representative of three independent experiments, n=5 technical replicates. 2-way ANOVA test with Sidak's multiple comparisons was used to compare the levels of OCR and ECAR between samples at each time point; * P<0.05, ** P<0.01, *** P<0.001, **** P<0.0001.*

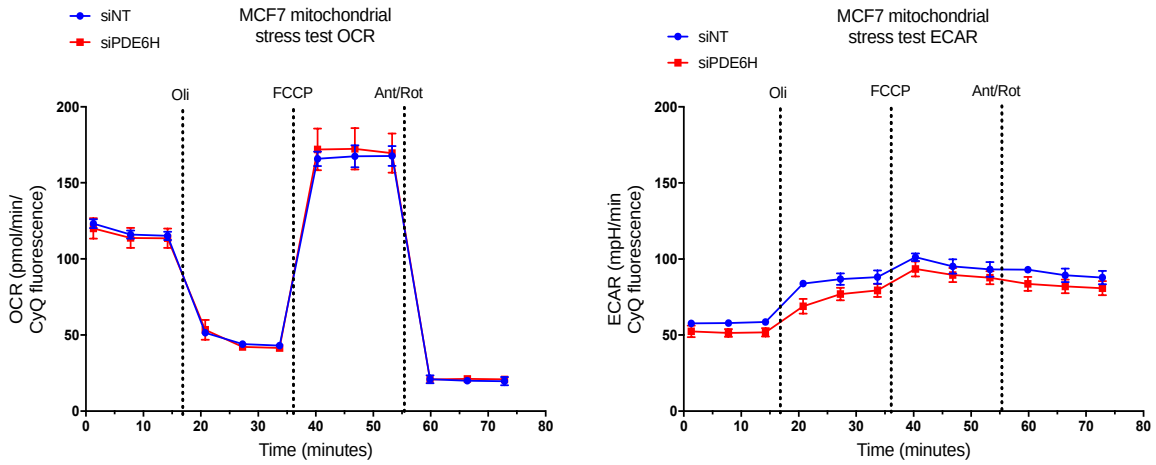


Figure 5.22: PDE6H knockdown did not affect basal levels of oxidative phosphorylation or glycolysis in MCF7 cells.
Data are mean±standard deviation, from a single experiment, representative of three independent experiments, n=5 technical replicates.

The results of the mitochondrial stress test were used to derive different parameters of respiration described in Chapter 2: basal respiration, ATP production, maximal respiration, spare capacity, and proton leak. OCR values at 3rd time-points (as per standard Seahorse protocol) following each drug injection were used for calculation. Non-mitochondrial respiration is the OCR value obtained when ETC function is shut down following addition of Complex 3 inhibitors antimycin and Complex 1 inhibitor rotenone. Basal respiration was derived by subtracting non-mitochondrial respiration from baseline cellular OCR. Oligomycin is a complex V inhibitor; when the resulting OCR after its addition is subtracted from baseline OCR, ATP-linked respiration is derived, indicating ATP production. Following injection of FCCP, which uncouples the proton transfer across the mitochondrial inner-membrane from the proton channel of ATP synthase complex V, OCR reaches its maximum from which non-mitochondrial respiration is subtracted to obtain maximal respiratory capacity. Reserve/spare capacity is the difference between maximal and basal OCR values. (Fern, 2003) (Rose et al., 2014) (Van der Windt et al., 2016).

PDE6H knockdown lowered basal and maximal respiration of HCT116, DLD1, and MDA-MB-468 cells; ATP-production (ATP-linked OCR) of HCT116, DLD1, MDA-MB-468, and MDA-MB-231; spare/reserve capacity of DLD1; proton leak OCR of all cell

lines (Figure 5.23).

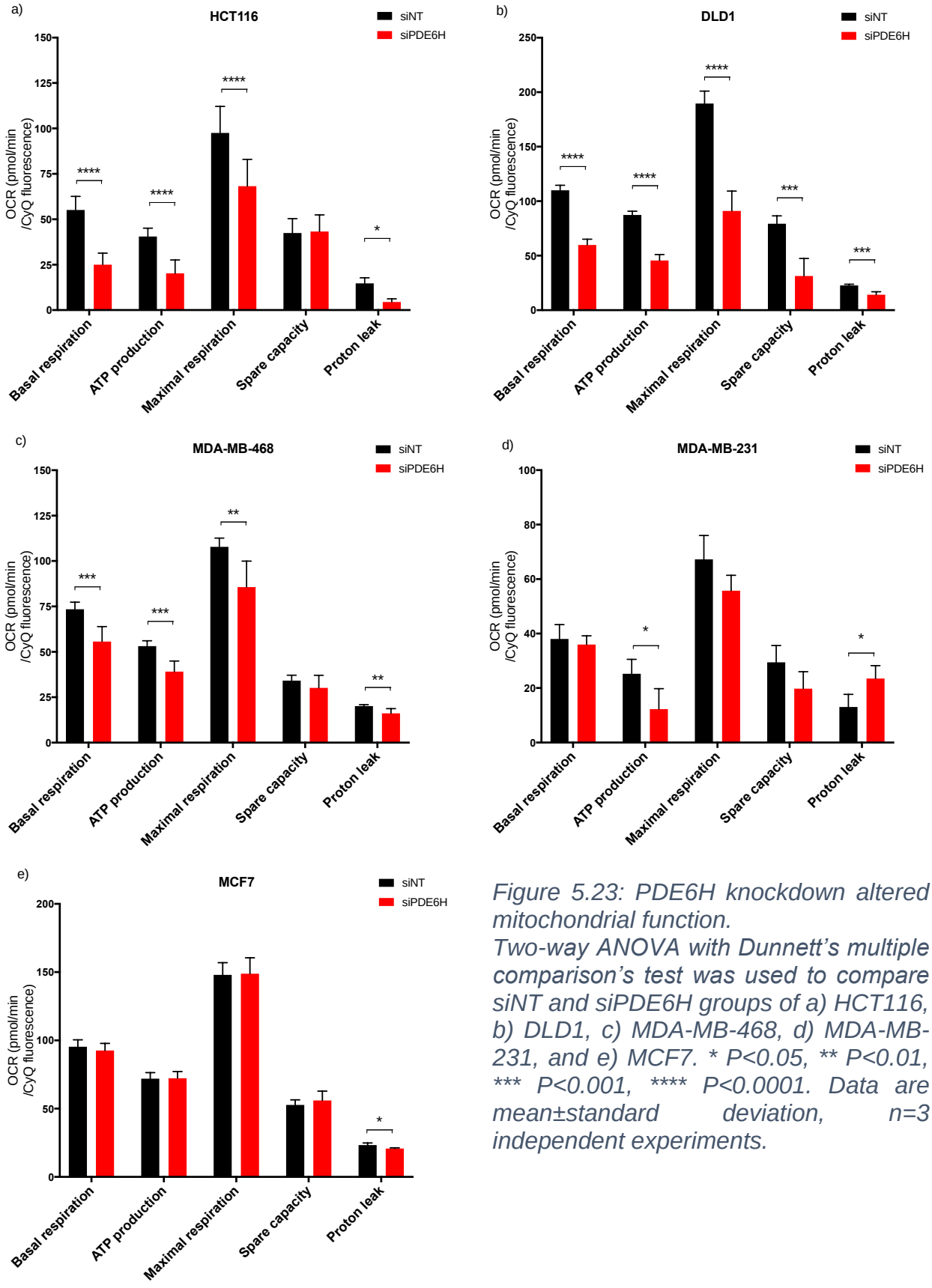


Figure 5.23: PDE6H knockdown altered mitochondrial function.
*Two-way ANOVA with Dunnett's multiple comparison's test was used to compare siNT and siPDE6H groups of a) HCT116, b) DLD1, c) MDA-MB-468, d) MDA-MB-231, and e) MCF7. * P<0.05, ** P<0.01, *** P<0.001, **** P<0.0001. Data are mean±standard deviation, n=3 independent experiments.*

J) PDE6H depletion altered cell signalling pathways

1. PDE6H inhibition increased cGMP levels in HCT116

Since phosphodiesterases are the only enzymes that break down secondary messengers cAMP and cGMP (Mullershausen et al., 2001), it was expected that the knockdown of one of the cGMP specific PDEs would result in an increase of intracellular cGMP, unless another PDE compensates. Our results suggest show that inhibition of PDE6 cone genes resulted in cGMP upregulation in HCT116 cells (Figure 5.24). The PDE5/6 inhibitor zaprinast and the cGMP analogue 8-Br-cGMP, which were included as positive controls of the cGMP assay, also increased cGMP levels. PDE6H depletion caused a greater increase in the cGMP levels than that of the other cone isomer PDE6C. PDE6H inhibition was anticipated to contribute to both cGMP accumulation and degradation for the PDE6-inhibitory-activity of PDE6gamma, which is encoded by

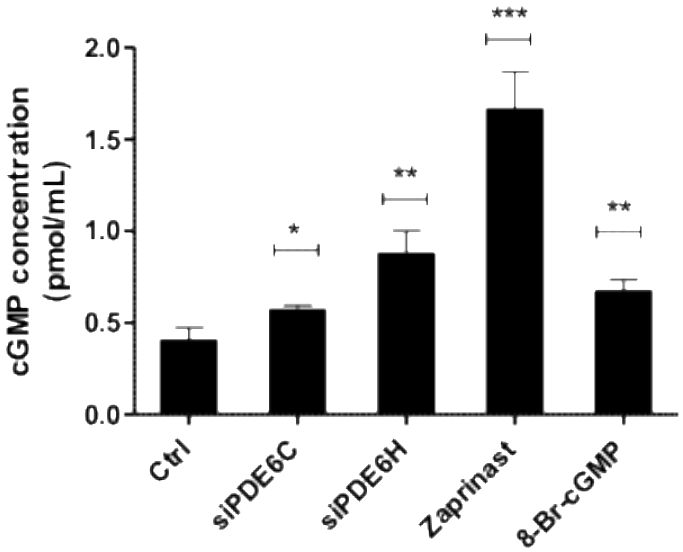


Figure 5.24: PDE6 inhibition via siPDE6C and siPDE6H as well through zaprinast and administration of cGMP analogue increase cGMP levels in HCT116.
*Samples were obtained on third day of siRNA transfection or 24-hour drug treatment and were analysed via cGMP ELISA. Ctrl (untreated) and siNT HCT116 cells had the same cGMP concentrations. Data are mean±standard deviation, n=3 biological replicates. One-way ANOVA with Dunnett's multiple comparisons test was used to determine the statistical significance between cGMP concentrations of each group compared to the Ctrl values. *P<0.05, **P<0.01, ***P<0.001.*

PDE6H in cone cells, due to its function as a PDE6 complex chaperone (Gopalakrishna et al., 2016). The significant increase in intracellular cGMP upon PDE6H inhibition highlights the gene's control over cGMP levels.

2. *PDE6H* knockdown affected MAPK and mTOR signalling

To elucidate the mechanism of cell cycle arrest observed upon siPDE6H transfection, protein levels of signalling pathways that are known to affect both cell cycle and cell metabolism, ERK1/2, HIF-1α and mTOR, were measured (Figure 5.25). mTOR was of interest as mTORC1 activation leads to *de novo* synthesis of purine and pyrimidines (Ben-Sahra and Manning, 2017), the levels of which might be disrupted upon *PDE6H* knockdown that elevates cGMP levels. cGMP-PKG activation in vascular endothelial cells by cGMP analogue increases ERK1/2 activation (Zaragoza et al., 2002). PKG activation by cGMP analogue also stimulates HUVEC proliferation (Hood and Granger, 1998). ERK1 activity activates mTORC1 (Carriere et al., 2011) and HIF1 under normoxia (Sang et al., 2003). HIF-1α levels were also measured, since naked mole rats which have high levels of HIF-1α expression, also have a loss-of-function mutation of *PDE6H* (Kim et al., 2011).

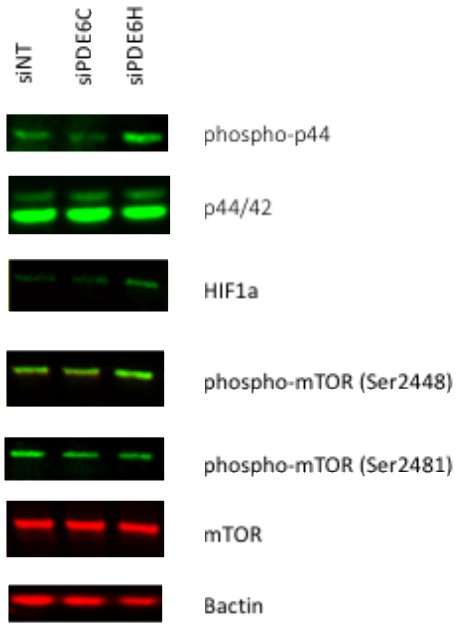


Figure 5.25: PDE6H knockdown caused mTORC1 and ERK1/2 activation, HIF-1α stabilisation. Data are representative of three independent experiments.

Phopho-ERK1, phopho-mTOR (Ser2448), and HIF-1α protein levels of siPDE6H group were greater than those of control and siPDE6C group. Transfection with the siRNA for the other cone isomer, PDE6C, did not cause a change in the activation of the three kinases. These results further support that the cone gene *PDE6H* is specific in its control of cell cycle.

Amongst the PDE6 family genes, PDE6H was determined as the gene the knockdown of which caused the greatest level of cell cycle arrest, cell death, and dysfunctional mitochondria. In order to investigate the effect of constitutive depletion of PDE6H, which is advantageous for studying 3D spheroid growth and *in vivo* work, CRISPR/Cas9 knockout of the gene was carried out in HCT116 cells.

K) sgRNA templates were designed for CRISPR/Cas9 double nickase gene editing

1. Rationale for the selection of sgRNA-targeting site

The double nickase strategy developed by Zhang lab, that uses the mtCas9 is an optimised chimeric design with lower off-target effects was used to design guide RNAs (Ran et al., 2013a). Exon 2 of *PDE6H* was selected for targeting by the sgRNAs, since it is used in the template of both of the two PDE6H mRNA (Figure 5.26) (Zerbino et al., 2018). It was important to target this exon since it encloses the part of PDE6H cDNA that is both protein coding and precedes the part of the sequence that encodes an amino acid sequence almost identical to that of the rod PDE6gamma encoding gene *PDE6G*, which is located on chromosome 17. Exon 2 corresponds to base pairs 137-240 of the PDE6H cDNA. Base pair 147 onwards *PDE6H* translates to an amino acid sequence almost identical to that of *PDE6G*. There is no alignment between the cDNAs of the two PDE6gamma subunits. A nucleotide alignment of about 350 base pairs falls between exons 1 and 2 of *PDE6H*.

The cDNA sequence of PDE6H is as follows. Each exon is denoted by a different colour and the CRISPR/Cas9 targeted region is highlighted.

```
1   caaagatcct tttgtctttt gcaaagaagg cagctgggca gctgatagga acaacattca
61  gctccgaggc tgaaagggaa acatcagccg cccgggggga gttaaaatga gtgacaacac
121 tactctgcct gctccagctt caaaccaggg tcctaccacc ccacgcaaag gccctcccaa
181 gttcaagcag aggcagactc gccaattcaa gagtaaacct ccaaagaaag gtgtgaaagg
241 atttggagat gacattccag gaatggaggg gctaggaaca ga tatcacag tgatttgtcc
301 atgggaggca ttcagccacc tggaattgca tgagctcgct cagtttggga ttatctgaag
361 tgccagaggt tctgccactc tcaatgacat ctgctgtaat tttggttgct tttgccctgt
421 tgatctgccg gagtcttgaa attcagctga ttggaagtgg tttctttgac tttcaaggtc
481 attccctatc agttactact aagagttctc ttactgtcag aatctcttct gcagtacagc
541 tcaaaatagt ggatgcattt caaacttgac caccttttcc taccagctag ttagaagtca
601 tcaatatttc tctacatttt gtttatctgt aagtccttta aatctatttt tgctaggcat
661 tcattatgat taatagtaga cttttaagac aacatttatg tcactcccca cctcctcata
721 tttaataaag gagatattta ccttgaaaaa  aaaaaaaaaa aaa
```

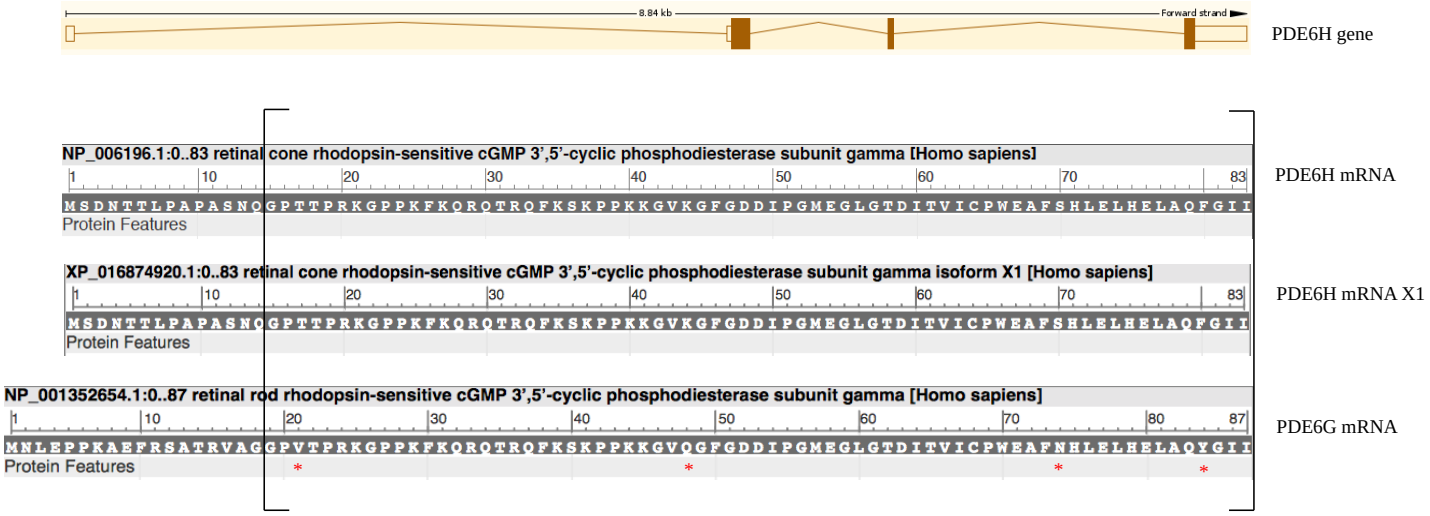


Figure 5.26: cDNA template and amino acid sequence of PDE6H.
PDE6H gene includes four exons with two mRNA transcripts (PDE6H mRNA and PDE6H mRNA X1). Both mRNAs produce identical PDE6H proteins of 83 amino acids. The first 17 amino acids translated are specific to PDE6H. Amino acid sequence that is common between PDE6H and PDE6G fall within the bracket, excluding the amino acids marked with "". Adapted from (Zerbino et al., 2018).*

The first 17 amino acids (aa) at the N-terminal make up the portion of *PDE6H* encoded gamma subunit, one that is not shared with *PDE6G*. Aa 22-87 of rod PDE6gamma, encoded by *PDE6G*, are almost identical to aa 18-83 of cone PDE6gamma, encoded by *PDE6H*. Cone PDE6gamma has not been structurally investigated like rod PDE6gamma. It is accepted that the high affinity interaction of rod PDE6gamma with the catalytic dimer occurs at the 18-41 aa in the central domain of rod PDE6gamma (Guo and Ruoho, 2008). The PDE6gamma binding site of the rod PDE6

overlaps with the PDE5/6 inhibitor sildenafil binding site. Therefore, while PDE5 does not have an inhibitory subunit, the drug might be allosterically competing with the gamma subunit of PDE6 (Barren et al., 2009).

Therefore, to eliminate a protein product by deleting an amino acid sequence that is specific to only PDE6H, we could target only a limited part of the genomic DNA. An additional restriction was the necessity for the target sequence to contain a PAM region, as explained below.

2. Design of sgRNA primer pairs

PDE6H sgRNA were designed based on the Zhang lab protocol. The PAM sequence is necessary for target binding and was 3' NGG for the mtCas9 protein that is used. An "NGG" sequence was searched for within the exon 2 of PDE6H to find a suitable target sequence. "CACC" and "AAAC" cloning hangs were added to the sgRNAs (Tables 5.1 and 5.2).

Cas9 cuts 3-4 base pairs upstream of the PAM sequences (highlighted in red in the sgRNA target sequence list). Through our target selection, the part of the cDNA that would not be transcribed following gene deletion was ascribed to base pairs 130-195 of the cDNA. It was estimated that this modification via CRISPR/Cas9 nickase would result in deletion of the PDE6gamma subunit encoded by *PDE6H*. The base pair (bp) locations, that the sgRNA primer pairs target, are noted below.

Table 5.1: PDE6H CRISPR/Cas9 sgRNA primer pair 1

sgRNA of the positive strand
Position on positive strand: 137-156

5' to 3' Template 1	CCAGCTTCAAACCAGGGTCCTAC
5' to 3' Template 1 without PAM	GCTTCAAACCAGGGTCCTAC
5' to 3' Template 1 change G	GCTTCAAACCAGGGTCCTAC
5' to 3' Template 1 +AAAC overhang	AAACGCTTCAAACCAGGGTCCTAC

sgRNA of the negative strand
Position on positive strand: 134-155

5' to 3' Template 2	GTAGGACCCTGGTTTGAAGCTGG
5' to 3' Template 2 without PAM	GTAGGACCCTGGTTTGAAGC
5' to 3' Template 2 change G	GTAGGACCCTGGTTTGAAGC
5' to 3' Template 2 +CACC overhang	CACCGTAGGACCCTGGTTTGAAGC

Table 5.2: PDE6H CRISPR/Cas9 sgRNA primer pair 2.

sgRNA for the positive strand
Position on positive strand: 172-193

5' to 3' Template 3	GCCCTCCCAAGTTCAAGCAGAGG
5' to 3' Template 3 without NGG	GCCCTCCCAAGTTCAAGCAG
5' to 3' Template 3 change G	GCCCTCCCAAGTTCAAGCAG
5' to 3' Template 3 +CACC overhang	CACCGCCCTCCCAAGTTCAAGCAG

sgRNA for the negative strand
Position on negative strand: 171-190

5' to 3' Template 4	CCTCTGCTTGAACTTGGGAGGGC
5' to 3' Template 4 without DGG	CTGCTTGAACTTGGGAGGGC
5' to 3' Template 4 change G	CTGCTTGAACTTGGGAGGGC
5' to 3' Template 4 +AAAC overhang	AAACCTGCTTGAACTTGGGAGGGC

3. Verification of *PDE6H* knockout in selected clones

Following puromycin selection of the transfected HCT116 cells with dual sgRNA primers, the surviving cells were pooled and were seeded in 96-well plates as single cells. The cells were cultured for 10 days to allow them to grow into colonies. Only single-cell colonies that were formed from individual cells were selected for further study of knockout validation (Figure 5.27). The single cell colonies were then replated in 6-well plates and only the ones that reached above 50% confluency within 5 days of seeding were selected for validation. The selected colonies numbered 1-16 were further

expanded; colony number 15 was later omitted due to low viability following the first few passages.

The ABCAM antibody against PDE6H product, ab156104, was determined to be the only antibody that covered part of the PDE6 gamma amino acid that is specific to the cone isoform. Since there are no publications featuring images of western blots with this antibody, the estimate of cone PDE6gamma product on the blot relied on the protein size reported by ABCAM (9 kDa). HCT116 siNT and WT lysates were included as controls to show unspecific bands detected by this PDE6gamma antibody (Figure 5.27).

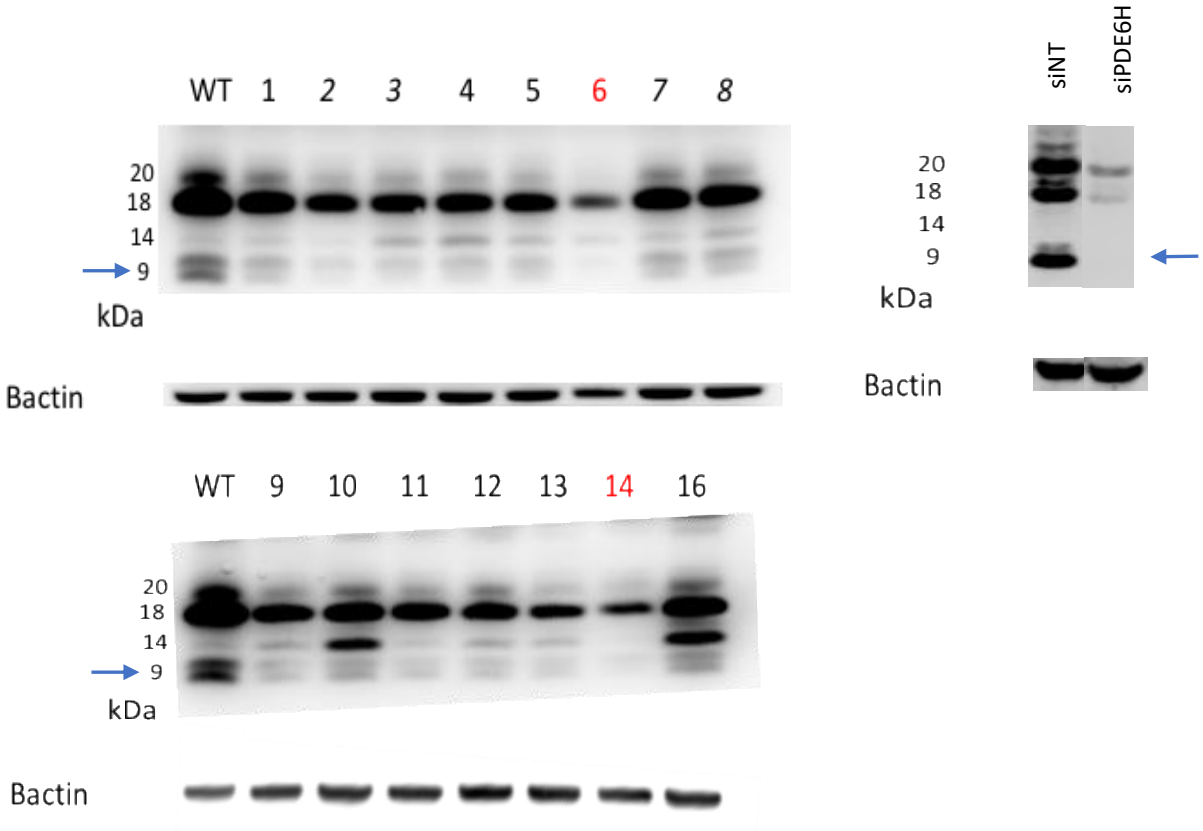


Figure 5.27: PDE6H CRISPR knockout and knockdown HCT116 cells were depleted of cone PDE6 gamma protein.
PDE6H band is located at 9 kDa. Data are representative of three independent experiments.

It was observed that the CRISPR knockout and knockdown of *PDE6H* yielded unspecific bands. The unspecific bands in *PDE6H* kd or ko samples were present but were much fainter compared to the siNT or WT samples. It is crucial that we identify the unspecific bands. Thus far we only have an estimate for the nature of the 14 kDa band.

Firstly, we checked for peptides that might have formed upon deletion or knockdown of PDE6H. The alternative amino acid sequence, that might have been translated based on the next open reading frame (ORF) after exon 2 region targeted by both the sgRNA pair and siRNA, was generated. This amino acid sequence is of similar size to cone PDE6gamma; but it is does not align with the sequence targeted by this antibody, and is unlikely to be detected by this antibody. However, five amino acids of rod PDE6gamma protein shows alignment with this antibody's targeted-region. Therefore, the 14 kDa band might represent rod PDE6gamma; as the band matches this protein' weight. A blot of siPDE6G can be used to check whether the 14 kDa band disappears.

The constitutive deletion of *PDE6H* via siRNA knockdown, a constitutive deletion of the gene via CRISPR/Cas9 in HCT116, also demonstrated PDE6H's role in kinase signalling (Figure 5.28). *PDE6H* knockout clones had higher levels of phospho-4EBP1 and phospho-ERK1/2 indicating mTORC1 and MAPK activation. Levels of phospho-VASP, phosphorylated preferentially by protein kinase G at Ser239, also increase, suggesting an increase of the cGMP/PKG pathway.

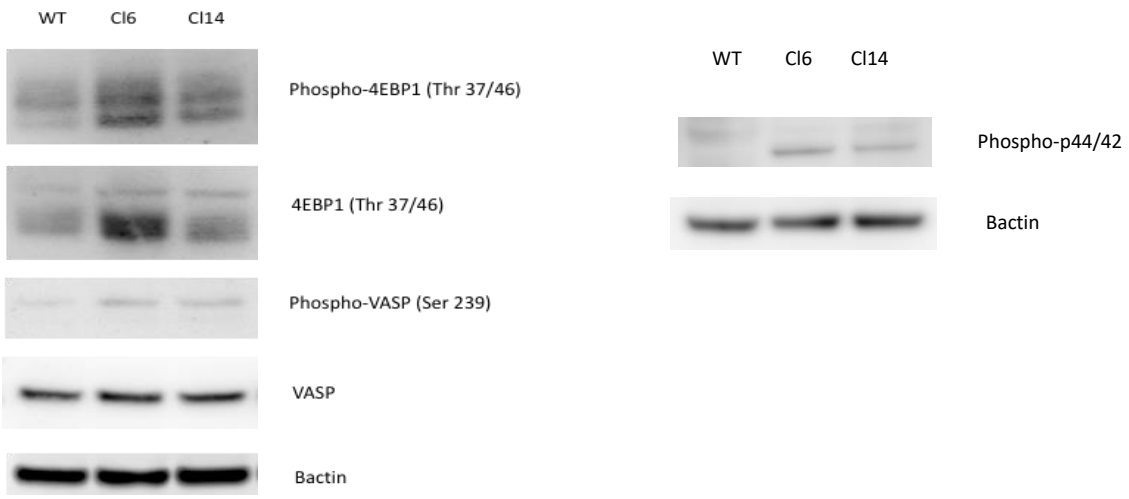


Figure 5.28: PDE6H knockout HCT116 clones had activated mTORC1, VASP and ERK1/2. Data are representative of two independent experiments.

Cell cycle profiles of *PDE6H* ko clones were the same as that of WT HCT116 (Figure 5.29). While we would expect the ko clones to have a greater percentage of cells in G1 compared to WT, it is possible that the clones that we were able to expand were the cells that do not get arrested in G1, unlike *PDE6H* kd cells which do not have the time to adapt. An arrest-release experiment could reveal whether the clones recover from a reversible cell cycle arrest induced by nocodazole or palbociclib at the same rate as WT HCT116. A longer EdU incubation (longer than the 2-hour incubation used to determine population of cells in S-phase) or quantification of Ki-67 positive cells can also help determine whether proliferation levels of *PDE6H* knockout HCT116 cells are different to those of WT.

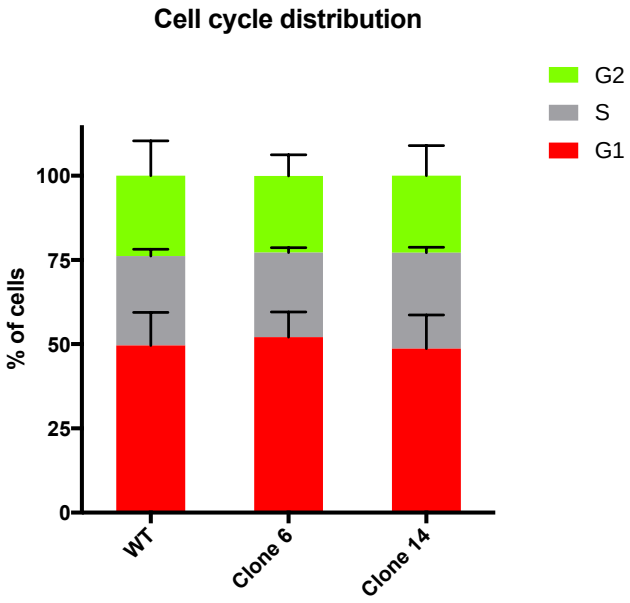


Figure 5.29: PDE6H knockout clones do not have altered cell cycle profiles.
2-way ANOVA followed by Dunnett's multiple comparisons test was used to determine the statistical significance between percentage of cells in G1, S, and G2 compared to the values of WT group. N=3 biological replicates.

L) *PDE6H* knockout clones had altered basal OXPHOS and glycolysis compared to WT HCT116

The CRISPR/Cas9 colonies that were expanded were also evaluated for their basal OCR and ECAR values (Figure 5.30). While control cell lines that had not been treated with CRISPR reagents were used, it is recognised that a more appropriate control may be cells treated and selected without deletion. Additionally, cells selected

but without deletions could be used. A lower expression of cone PDE6gamma protein corresponded to the lowering of basal levels of both glycolysis and oxidative phosphorylation. The clones with the lowest PDE6gamma expression, Clone 6 and Clone 14 (Figure 5.27) also had the lowest levels of basal OCR and ECAR (Figure 5.30). Clones 3, and 13 had high levels of OCR despite their low ECAR values. For the screening tests only 2 biological replicates were used, with three points in each experiment. These were used for exploratory selection of clones, recognising that for a publication, 3 biological replicates will be needed.

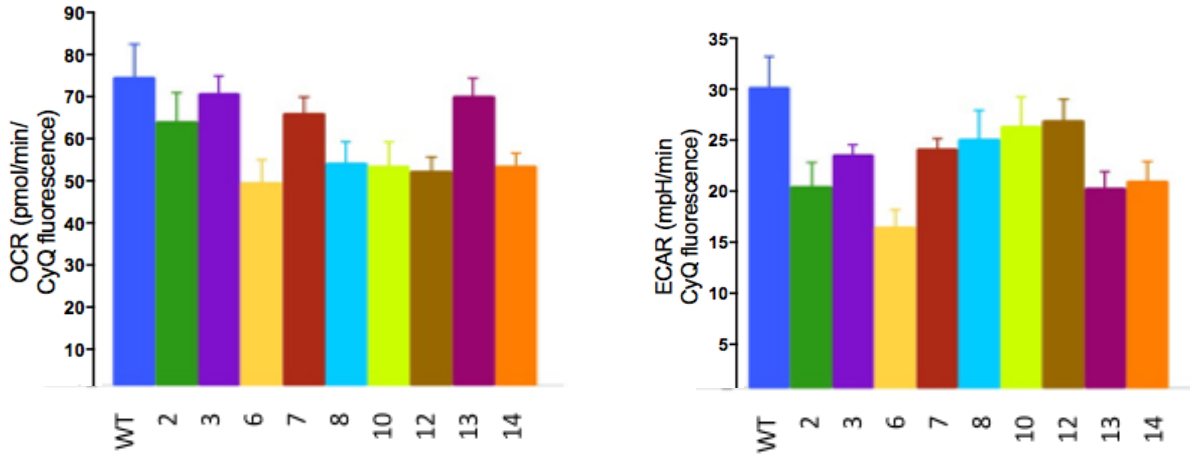


Figure 5.30: PDE6H knockout clones had altered basal OXPHOS and glycolysis compared to WT HCT116.
Data are mean±standard deviation, 3 technical replicates per experiment. N=2.

Clones 6 and 14 were selected for *in vivo* studies to examine growth of *PDE6H* knockout HCT116 tumours in mouse model, as they had the lowest level of PDE6gamma, and the knockout resulted in lowering of basal metabolism (Figure 5.31).

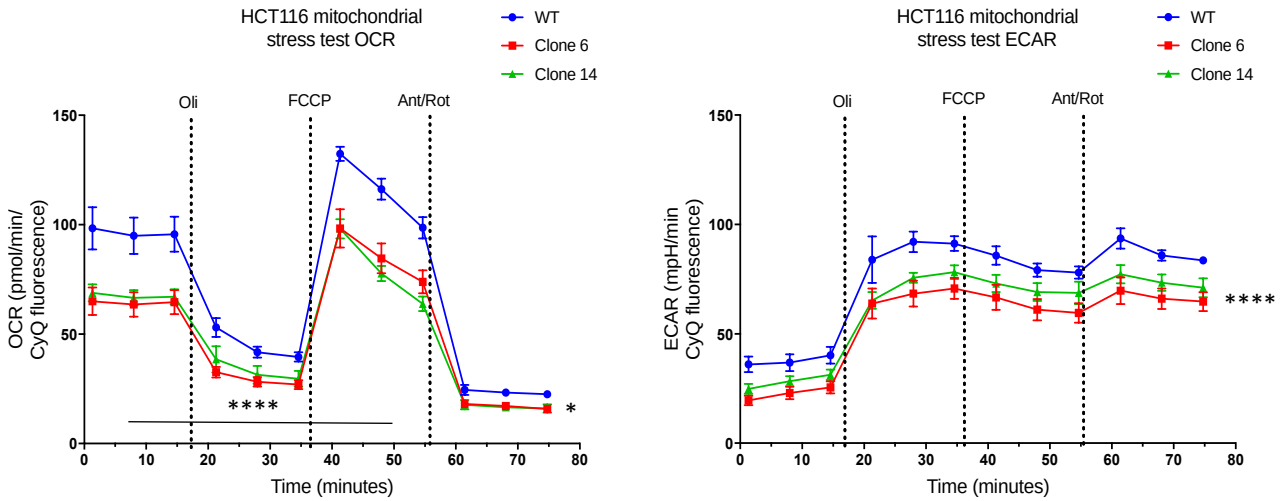


Figure 5.31: PDE6H knockout clones 6 and 14 had lower levels of oxidative phosphorylation and glycolysis compared to WT HCT116.
*Data are mean±standard deviation, representative of three independent experiments, n=6 technical replicates. 2-way ANOVA test with Sidak's multiple comparisons was used to compare the levels of OCR and ECAR between samples at each time point; clone 6 and clone 14 OCR were significantly lower on 1-9 (****) and 10-12 (*). Clone 6 and 14 ECAR values were significantly lower starting throughout the assay (****). * P<0.05, **** P<0.0001.*

The results of the mitochondrial stress test were used to derive different parameters of respiration described in Chapter 2, Section I: basal respiration, ATP production, maximal respiration, spare capacity, and proton leak. OCR values at 3rd time-points following each drug injection were used for calculation, except for maximal respiration for which the OCR value at the first time-point following FCCP injection was used. Mitochondrial functions of *PDE6H* knockout HCT116 clones were different from that of WT HCT116 with respect to all parameters of respiration (Figure 5.32). Basal, ATP production linked, maximal, spare, and proton-leak OCR of both Clone 6 and Clone 14 were lower than those of WT HCT116.

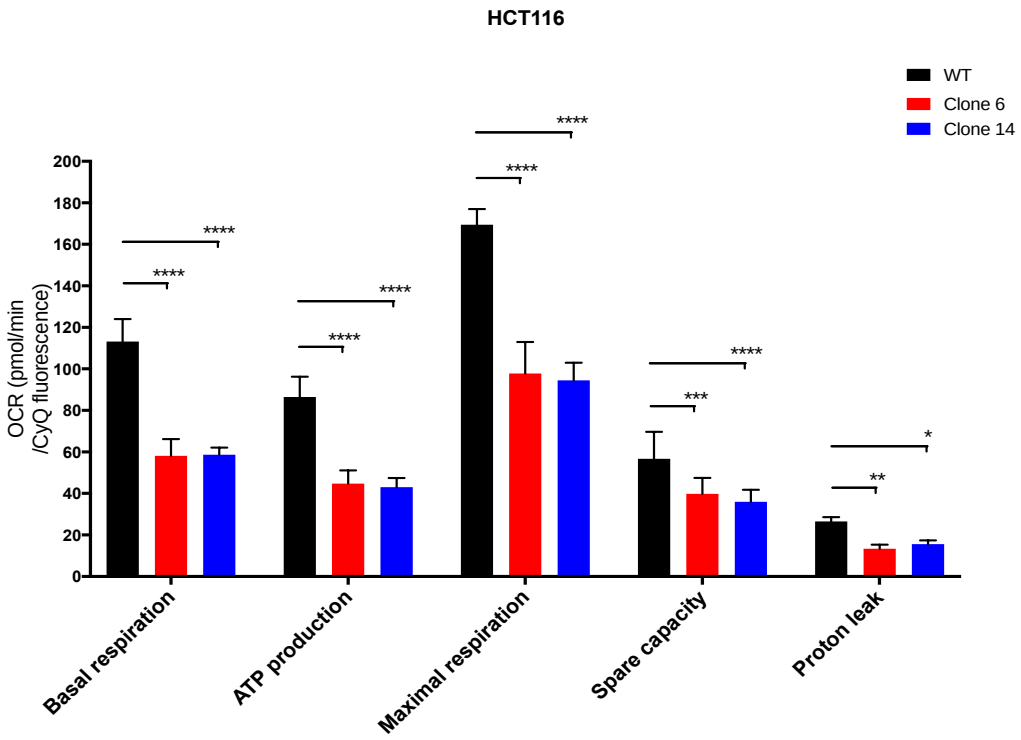


Figure 5.32: PDE6H knockout alters mitochondrial function.
** P<0.05, ** P<0.01, *** P<0.001, **** P<0.0001. Data are mean±standard deviation, n=3 independent experiments. 2-way ANOVA test with Dunnett's multiple comparisons to compare respiration parameters of clones to those of WT.*

Seahorse experiments of *PDE6H* knockout clones were carried out after glutamine depletion for two reasons: 1) PDE6H is a step in of purine metabolism, cell lines lacking PDE6H might have a rewired Gln metabolism that affect the way Gln is utilised (Figure 5.33). PDE6H depletion might lower GMP pools, resulting in an upregulation of PPP. In this mechanism, glutamine and glucose are shunted to PPP to sustain purine production, at the expense of glutaminolysis/TCA cycle and glycolysis, respectively. 2) The PDE5/6 inhibitor zaprinast has been reported to be a glutaminase (GLS) inhibitor (Elhammali et al., 2014). Therefore, the response of the *PDE6H* knockout clones to glutamine depletion was tested.

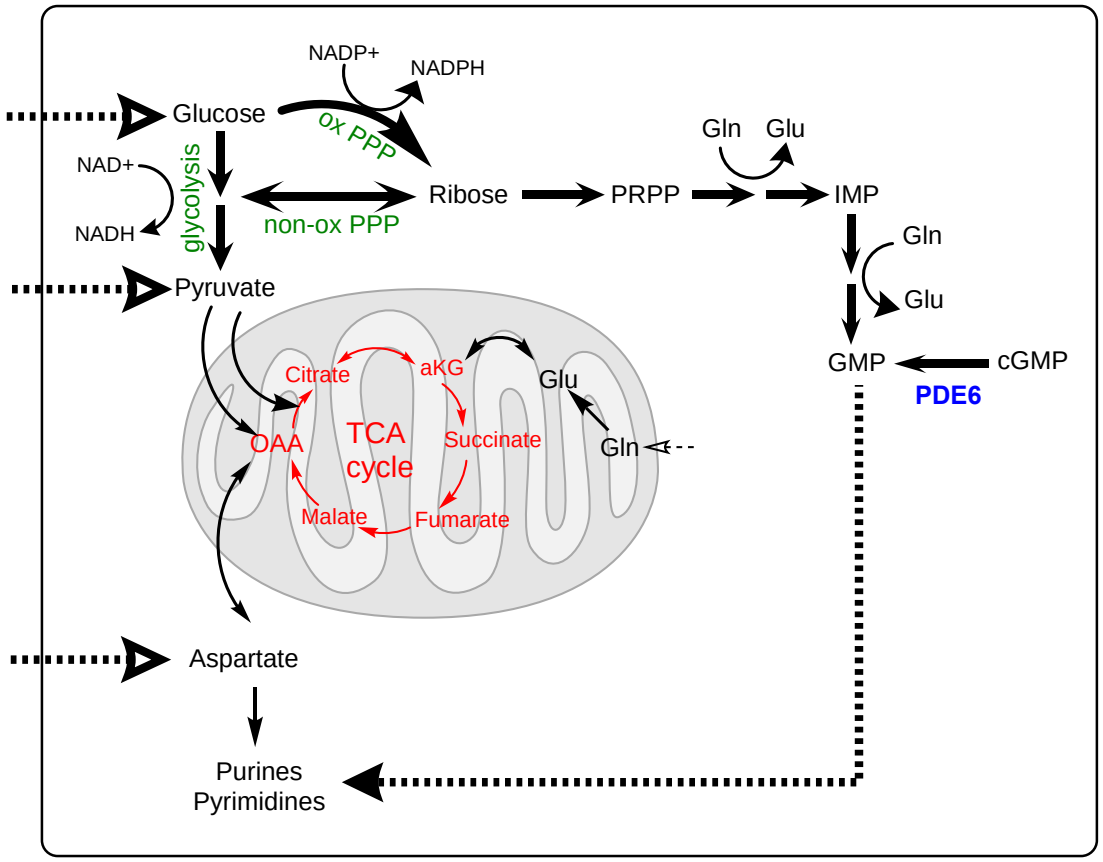


Figure 5.33: PDE6H inhibition might affect metabolism through modulation of glucose and glutamine use.
Hollow arrowhead indicate transport. ox-PPP: oxidative pentose phosphate pathway.

Seahorse results indicate that ECAR levels of WT and *PDE6H* knockout HCT116 cells showed a similar response to glutamine depletion (Figure 5.34), while basal values of both OCR and ECAR were lower in ko clones than WT HCT116. At the beginning of the assay (t=0 min), the OCR values of glutamine depleted PDE6H ko HCT116 cells were lower than those of WT cells. After a ten-hour glutamine depletion, the percentage decrease of OCR levels upon glutamine depletion is the same in both WT and clones (about 50%). While this suggests that while PDE6H depletion disrupted basal energy metabolism, we cannot determine whether PDE6H ko cells use glutamine differently than WT HCT116. We need to repeat this experiment with more replicates to check whether there is differential response to acute glutamine depletion between the WT and ko HCT116. Mass spectroscopy studies are also planned to test whether *PDE6H* ko

clones use glucose or glutamine preferentially in PPP, resulting in lower levels of glycolysis and OXPHOS.

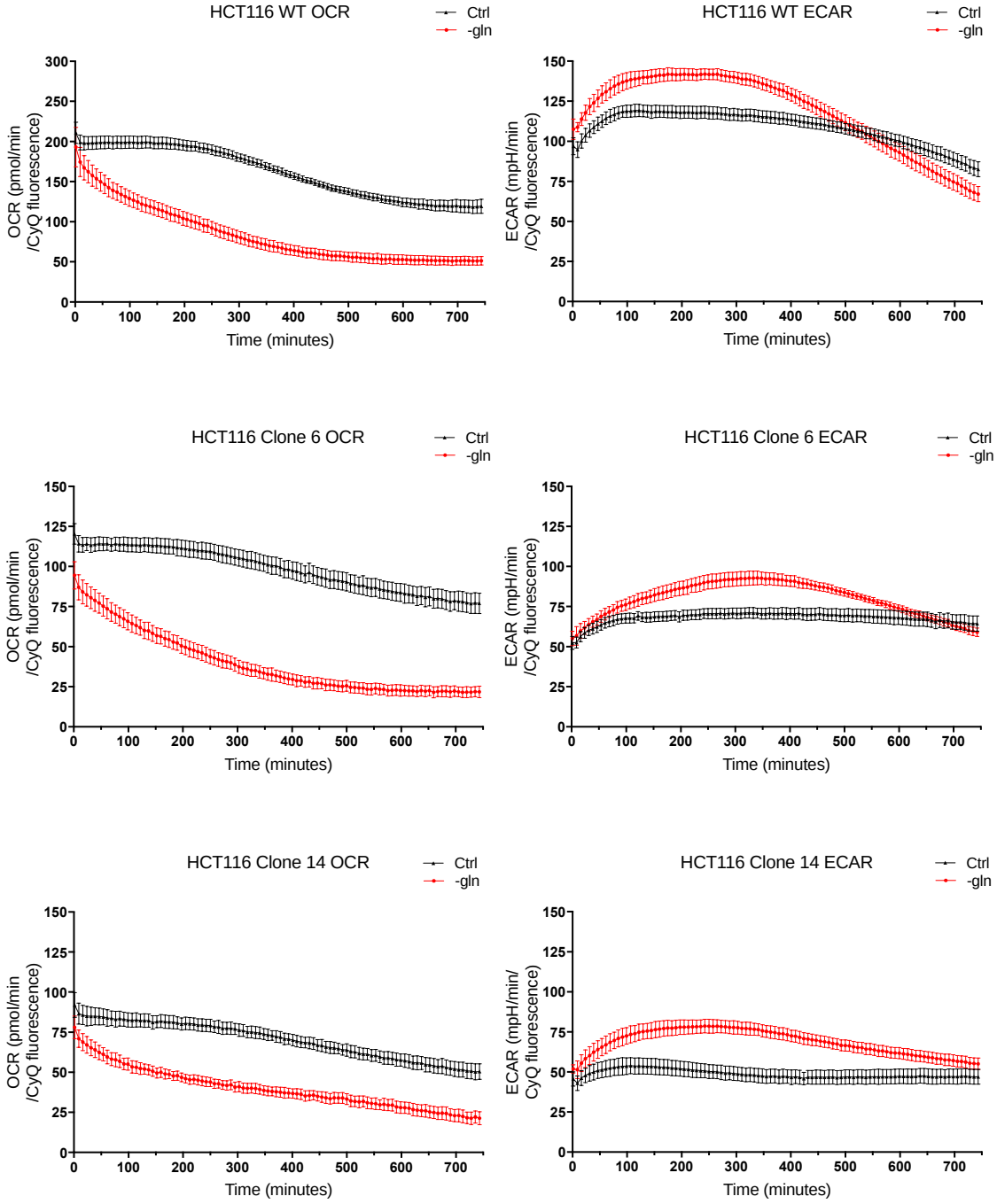


Figure 5.34: OCR and ECAR levels of PDE6H ko HCT116 clones over a 12-hour Gln depletion.
ECAR levels of HCT116 WT reached maximum sooner than those of PDE6H knockout clones while OCR levels of both HCT116 WT and PDE6H knockout clones were halved upon glutamine depletion.

M) Discussion

This chapter describes the metabolic consequences of PDEH6 downregulation. Under low glucose conditions, the depletion of *PDE6A*, *PDE6D*, and *PDE6H* caused the greatest G1 arrest. It was the depletion the two PDE6 inhibitory subunits that caused the greatest increase in dead cell population. The isoforms, the knockdowns of which caused the greatest increase in necrosis, were also the siRNAs that caused the greatest increase of mitochondrial ROS (PDE6A, PDE6G, and PDE6H). The G1 arrest caused by siPDE6H transfection was not limited to HCT116 cells. Importantly, there was specificity in the way PDE6 gene knockdowns affected growth and proliferation, suggesting that the function of one gene isoform could not compensate for that of another.

Cell cycle regulators involved in HCT116 G1/S arrest upon siPDE6H transfection were determined in an effort to understand the mechanism of arrest. Results suggest that there is a decrease in CDK4/6-cylin D complex activity. This inhibition was likely to be independent from an increase in p21 levels which did not show a striking difference compared the control group. While the effects of *PDE6H* depletion on cell cycle and metabolism was not limited to HCT116 cells, they were cell line dependent and are summarised in Table 5.3. “X” denotes the presence of an effect.

Table 5.3: Summary of effects of PDE6H knockdown in various cancer cell lines

	Cell cycle arrest	Cell death	Dysfunctional mitochondria	Basal OCR lowered	Basal ECAR lowered
HCT116	X	X	X	X	X
DLD1				X	X
MCF7			X		
MDA-MB-231	X	X	X		X
MDA-MB-468	X	X	X	X	X

The increase in cGMP levels (Figure 5.24) followed by the activation of signalling pathways, as well as a metabolic deficit might be the drivers of cell cycle arrest induced

by PDE6H depletion. The increase in cGMP caused by siPDE6H transfection might have led to the cellular signalling response: increase in levels of ERK1/2 activity that is accompanied by mTORC1 activity, as well as HIF-1α stabilisation (Figure 5.25). HIF-1α stabilisation might be due to mitochondrial ROS (Okamoto et al., 2017), and contribute to a lowering of OXPHOS (Wang et al., 2010).

ERK1 activity can activate mTORC1 (Carriere et al., 2011), which would explain our results that show an increase in phospho-mTOR (Ser2448) expression that accompanied an increase in phospho-p44 (phospho-ERK1) protein levels in the siPDE6H cells. However, it is interesting that despite a greater activation of growth signals compared to siPDE6C group, PDE6H depleted HCT116 had a more significant cell cycle arrest. The growth signals may be activated to overcome, or accumulate during, a cell cycle arrest.

The lowering of oxidative phosphorylation *PDE6H* ko clones might be due mitochondrial dysfunction due to cGMP accumulation (Oldenburg et al., 2004), an increase in mTORC1 activity (Schieke et al., 2006), or an independent mechanism through which PDE6H controls mitochondrial function/morphology. The decrease in both OXPHOS and glycolysis might be due to a preferential utilisation of glucose and glutamine in the pentose phosphate pathway (PPP) over glycolysis and OXPHOS, respectively. In case of a shortage of purine pools due to lack of GMP production under PDE6 depletion, cells could be upregulating PPP to produce GMP. PPP uses up glutamine which could have been used for supplementing TCA cycle after being converted to glutamate via glutaminolysis. PPP also uses glucose supplies that diverge from the glycolysis pathway through ribose intermediate, from which PRPP is produced (Figure 5.35).

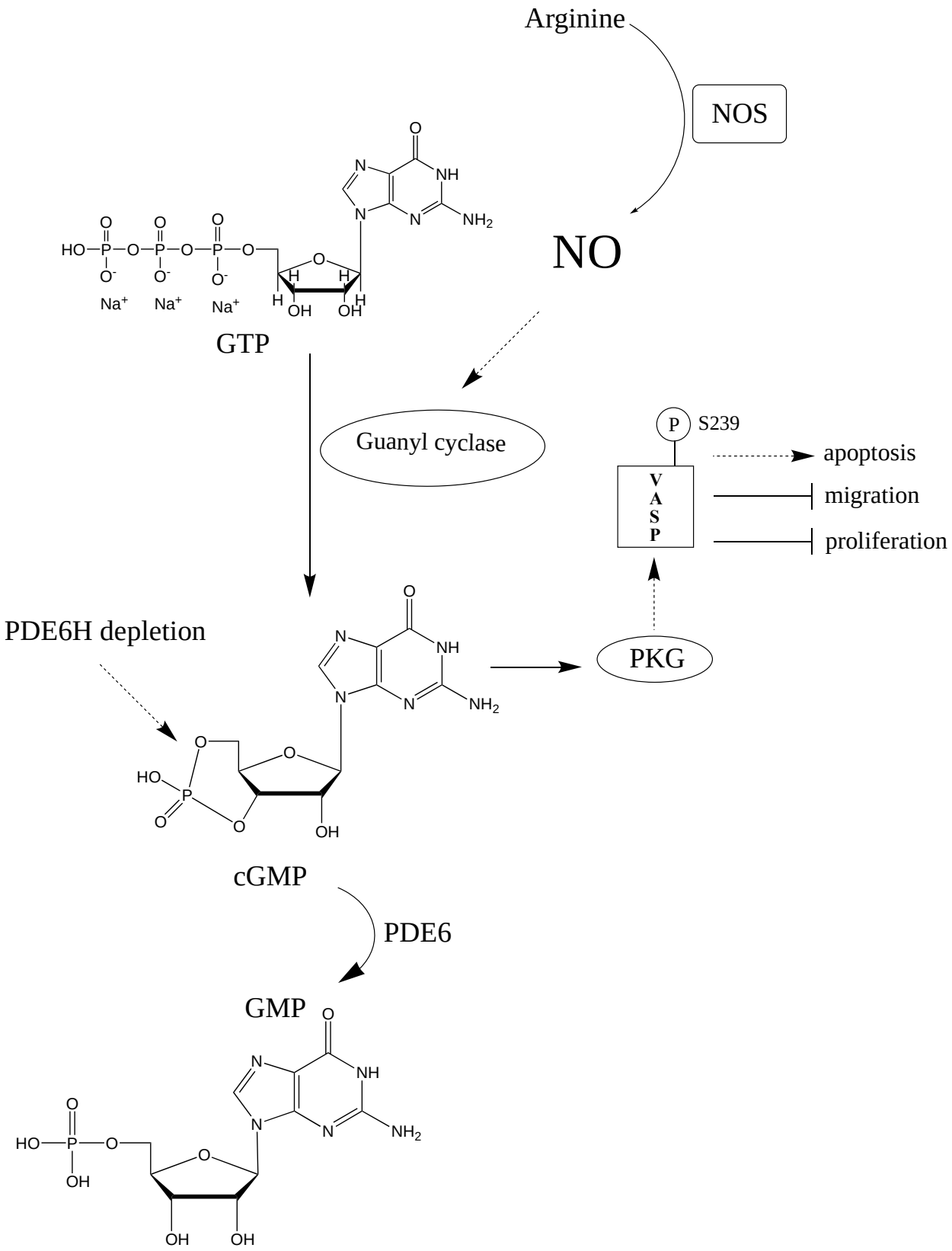


Figure 5.35: Summary of NO/GC/cGMP/PKG pathway. NO produced from arginine activates GC which produces cGMP from GTP. cGMP is hydrolysed to GMP by PDE6; it also stimulates PKG which phosphorylates VASP at the S239 site (Beavo et al., 2006).

The activation of ERK1/2 and mTORC1 pathways might also be due to PKG activity that increases with cGMP. PKG signalling activates mTORC1 by phosphorylation of Raptor in brown adipose tissue (Liu et al., 2018). Another report supports the effect of cGMP on mTORC1 activation, as PKG phosphorylates TSC2 to alleviate its inhibition of mTORC1 (Ranek et al., 2019). cGMP accumulation also results in an increase of VASP phosphorylation at Ser239 due to PKG activity (Figure 5.28). This leads to apoptosis as well as inhibition of proliferation and migration (Ali et al., 2015), (Jackson and Ceresa, 2016). PKG activates 1) VASP pathway causing cell adhesion and migration (through phosphorylation at Ser157), as well as apoptosis (through phosphorylation at Ser239), 2) CREB pathway leading to cell survival and proliferation and 3) ERK1/2 pathway leading to angiogenesis and smooth muscle contraction (Gallo and Iadecola, 2011), (Park et al., 2018).

The downstream effects of PKG related VASP activity, taken together with the lowering of oxidative phosphorylation and glycolysis due to PDE6H depletion, suggest that *PDE6H* deletion could potentially slow down tumour growth and metastasis by several mechanisms. An *in vivo* study comparing tumour growth of HCT116 WT and HCT116 *PDE6H* ko clones in mice was conducted and is presented in Chapter 6.

CHAPTER 6: EFFECTS OF PDE6H DELETION ON GROWTH IN HCT116 XENOGRAFT TUMOURS

A) Abstract

PDE6H depletion slowed down tumour growth and improved survival in *PDE6H* knockout xenograft model of HCT116. *PDE6H* knockdown, as well as that of the other PDE6 family genes led to decreased cell viability in HCT116, under both normoxia and hypoxia *in vitro*. Upon establishing that both PDE6H siRNA knockdown and gene deletion through CRISPR/Cas9 lowered the level of HCT116 colony formation, we tested the tumour growth of *PDE6H* ko HCT116 cells in a xenograft model. We also tested the potential therapeutic effect of zaprinast treatment, via intratumoural injection over 4 weeks on HCT116 tumour growth. Our results showed that *PDE6H* deletion slowed down HCT116 tumour growth while zaprinast treatment had no effect on tumour volume while it did effect tumour cell viability. Based on immunohistochemistry results we concluded that both PDE6 inhibition through zaprinast and *PDE6H* deletion led to a lowering of tumour cell viability, increased necrosis and tumour hypoxia. Our results support that PDE6 function is important for tumour growth and its regulation of cell metabolism that might regulate tumour microenvironment.

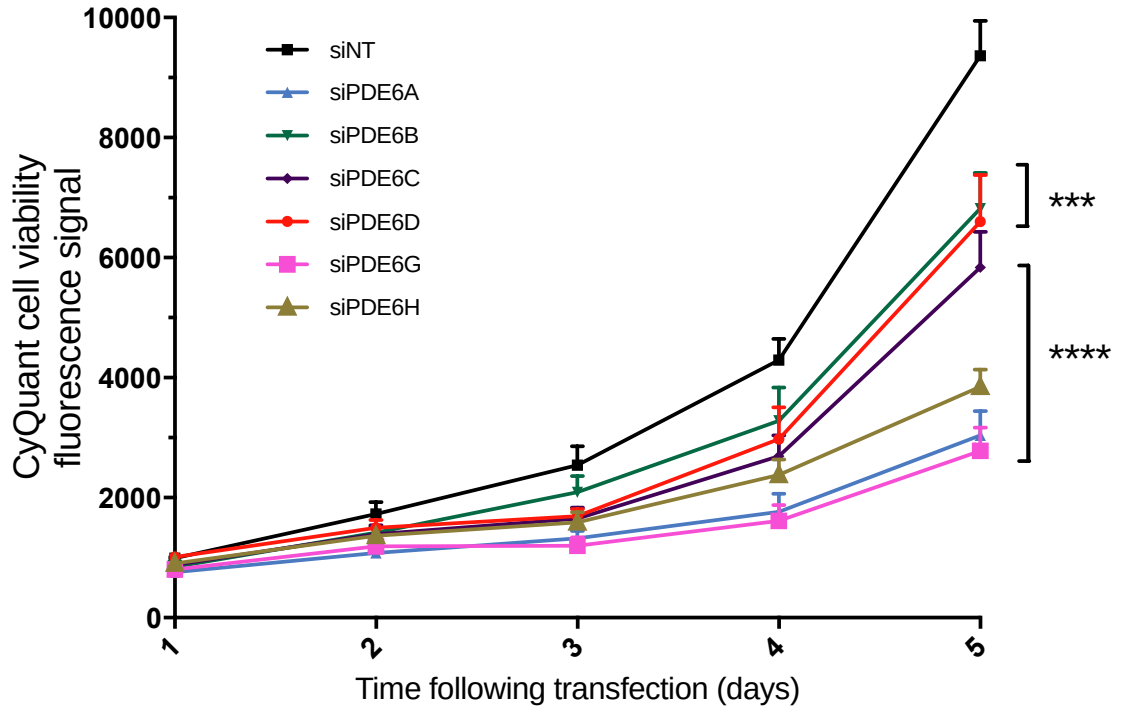
B) Introduction

It was established that the siPDE6H transfection causes G1 arrest and cell death. It was additionally shown that PDE6H depletion, both via siRNA transcriptional inhibition and by CRISPR deletion of *PDE6H*, altered cell signalling pathways and lowered levels of oxidative phosphorylation and glycolysis. This chapter presents the *in vitro* effect of *PDE6H* depletion on HCT116 viability in 2D in normoxia and hypoxia, as well as on spheroid growth. Clonogenic assays were also conducted on HCT116 to observe the effect of *PDE6H* depletion on colony formation. The effect of *PDE6H* depletion on cancer cell cycle and signalling, as well as energy metabolism led to a mouse xenograft experiment to test the tumour growth of WT HCT116, the two HCT116 clones in which *PDE6H* gene is deleted via CRISPR/Cas9 nickase, as well as a drug treatment group with a PDE6 inhibitor.

C) PDE6 depletion has antiproliferative effects on HCT116

All PDE6 isoforms lowered HCT116 viability upon their depletion through siRNA transfection as shown via a 5-day CyQuant assay. Cell viability was lower in siPDE6 groups both under normoxia (Figure 6.1a) and hypoxia (Figure 6.1b). Under both normoxic and hypoxic conditions, siRNAs that caused the biggest decrease in HCT116 viability were siPDE6A, siPDE6G, and siPDE6H. These are the same siRNAs that had caused an increase in MitoSOX signal, which is an indicator of mitochondrial ROS, upon their transfection.

a) siPDE6 tranfection of HCT116 in normoxia



b) siPDE6 tranfection of HCT116 in hypoxia

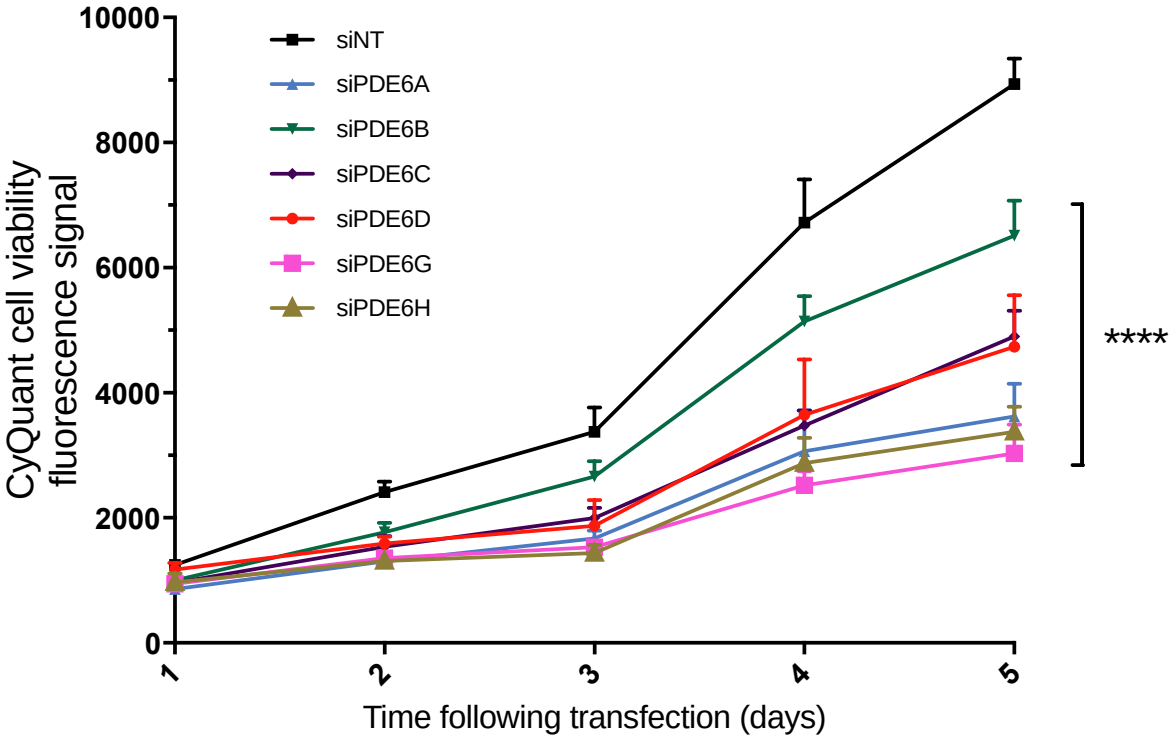


Figure 6.1: Cell viability of HCT116 cells decreased following siPDE6 transfection under both normoxic and hypoxic (1% O_2) conditions.
*HCT116 cells were replated in 96-well format on Day 3 of transfection and cell viability was measured via CyQuant fluorescent cell proliferation assay. Knockdown of each member of the PDE6 family genes cause significant lowering of nuclei staining intensity measured through CyQuant cell viability signal on Day5 of replating under a) normoxia: siPDE6A (****), siPDE6B (***), siPDE6C (****), siPDE6D (***), siPDE6G (****), siPDE6H (****), and b) under hypoxia of 1% O_2 (all siPDE6s ****). 2-way ANOVA test with Sidak's multiple comparisons was used for analysis on Day 5 of replating. Data represent mean of 6 technical replicates n=1.*

Due to HIF-1α stabilising effect of siPDE6H transfection described in Chapter 5 (Figure 5.18), viability assays of HCT116 cells were carried out under hypoxia (1% O_2) as well as normoxia. Knockdown of each PDE6 family member lowered viability in HCT116 cells grown in 2D (Figure 6.1). In both normoxic and hypoxic conditions, inhibition of *PDE6A*, PDE6G or *PDE6H* resulted in about a 3.5-fold decrease in HCT116 viability. Depletion of *PDE6B* resulted in about a 35% decrease in cell viability under both normoxia and hypoxia. Under normoxia, knockdowns of *PDE6C* and *PDE6D* also resulted in about 40% and 35% decreases HCT116 viability respectively. Under hypoxia, a greater decrease was observed at 50% for both siPDE6C and siPDE6D transfection groups.

PDE6H depletion resulted in formation of fewer colonies in both siRNA transfected (Figure 6.2a) and CRISPR/Cas9 ko (Figure 6.2b) HCT116 cells. Numbers of colonies formed after a ten-day incubation of siRNA transfected cells were counted. We acknowledge that results presented in Figures 6.1 and 6.2 are from single experiments and that these experiments need to be repeated to present results in triplicates. Further repeats of the clonogenic assays are also planned to observe colony growth under hypoxic (1%) growth conditions and post-irradiation.

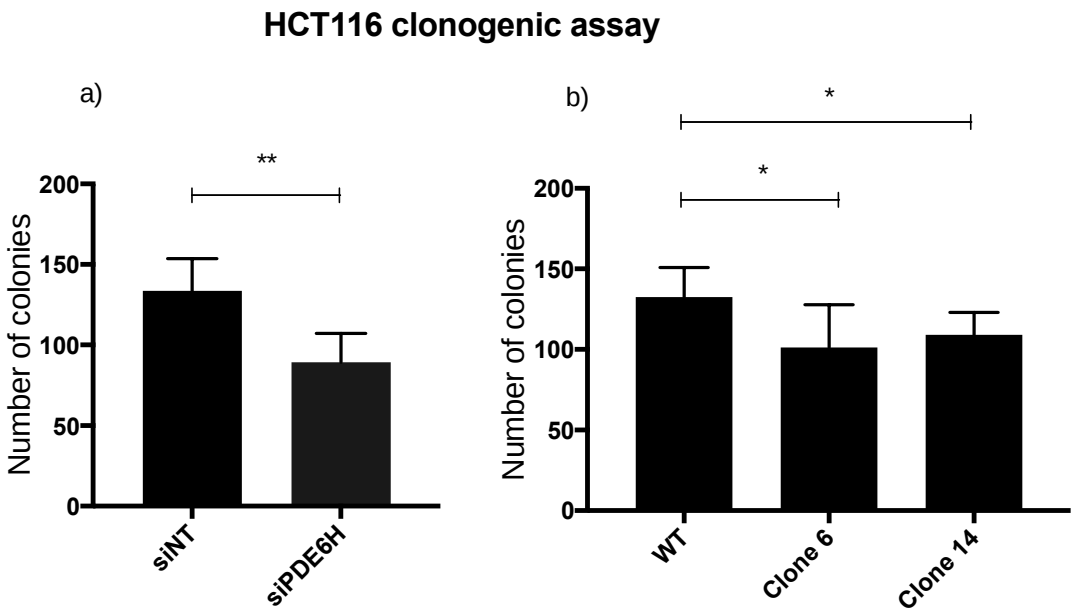


Figure 6.2: PDE6H depletion through a) siPDE6H transfection and b) CRISPR/Cas9 gene deletion resulted in formation of fewer HCT116 colonies.
*a) Unpaired t-test and b) One-way ANOVA with Dunnett's multiple comparisons test were used compare the number of colonies. *P<0.05, **P<0.1. Error bars show standard deviation. Data represent 6 technical replicates, n=1.*

A strategy to alleviate tumour hypoxia is to decrease the level of oxygen consumption in tumours to increase the O_2 concentration (Kelly et al., 2014). Reducing tumour hypoxia is important to relieve its effect on radiotherapy, which it deems ineffective (Gray et al., 1953). The lowering of oxidative phosphorylation levels in HCT116 cells upon siPDE6H transfection can help alleviate tumour hypoxia and potentially improve efficacy of radiation treatment.

PDE6H depletion inhibited spheroid growth of HCT116 cells (Figure 6.3). Spheroid growth of siPDE6H transfected HCT116 cells was measured in parallel with siPDE6C and compared to siNT. It was observed that compared to negative control group, *PDE6H* depleted HCT116 grew into smaller spheroids (mean r=125 µM in siPDE6H group and

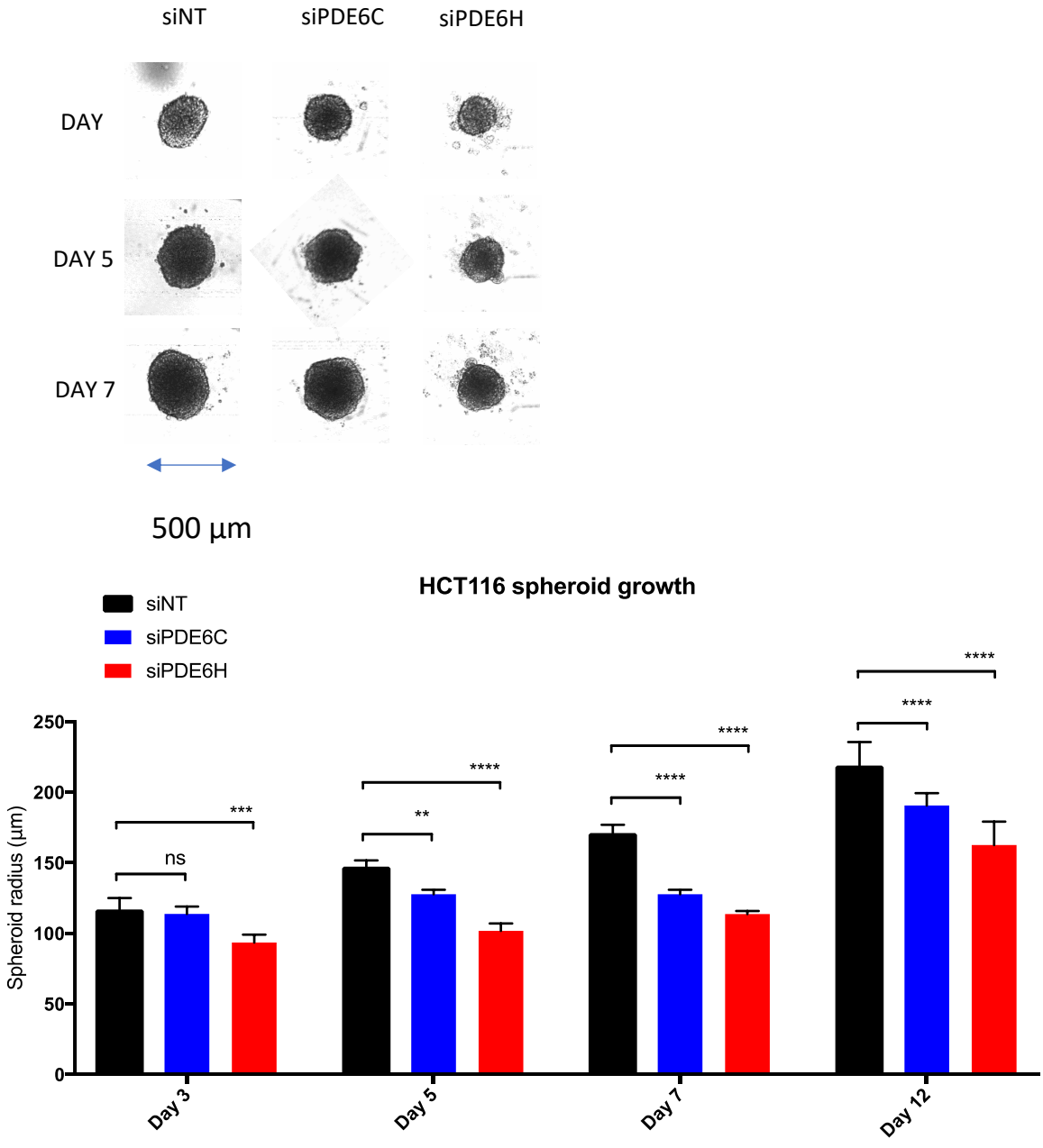


Figure 6.3: PDE6H depletion disrupted spheroid growth in HCT116. One-way ANOVA, followed by Dunnett's multiple comparisons test was used to compare the spheroid radii. Error bars show standard deviation. Data represent n=5 technical replicates.

mean r=175 μM in siNT group). As with Figure 6.2 we acknowledge that, while the available data were presented, the experiment needs to be repeated to present statistical analysis with at least three biological replicates. Depletion of the other cone isoform, *PDE6C* did not decrease the spheroid size. These results suggested that PDE6H inhibition would be worth testing *in vivo.*

D) *In vivo* experiment design

1. Zaprinast was selected as the PDE6 inhibitor

Zaprinast is a phosphodiesterase inhibitor that inhibits PDE5, 6, and 9. It is the only PDE6 inhibitor that inhibits PDE6 more potently than it does PDE5. Zaprinast's IC50 values for PDE5, PDE6, PDE9 are 0.5–0.76, 0.15, and 35 μM (Taniguchi et al., 2006). Due to the similarity of the catalytic subunits, PDE5 inhibitors also inhibit PDE6; this is the explanation provided for the visual defects that are attributed as a side-effect of erectile dysfunction drugs (Beavo et al., 2006).

Zaprinast and siPDE6H induced increases of cGMP in HCT116 cells were shown in Chapter 5 (Figure 5.17). This suggests that zaprinast, like inhibition of PDE6 activity, would result in an accumulation of cGMP. Zaprinast also resulted in an increase of dysfunctional mitochondria (Figure 6.4).

Despite the increase in apoptotic+necrotic HCT116 population following siPDE6H transfection (Chapter 5), neither zaprinast nor 8-Br-cGMP treatments cause cell death in HCT116 (Figure 6.5). This might be explained by a possible hormesis with the initial increase in cGMP leading to cell death, followed by an adaptive period where apoptosis or necrosis does not take place (Mattson, 2009). A time-course experiment of zaprinast and 8-Br-cGMP treatments of HCT116 can help explain if there are biphasic responses in cell death to these agents. Additionally, higher concentrations of 8-Br-cGMP can be used. The concentration of 8-Br-cGMP that causes significant decrease in MCF7 and MDA-MB-468 cell viability after a 24-hour treatment was determined as 10 μM.

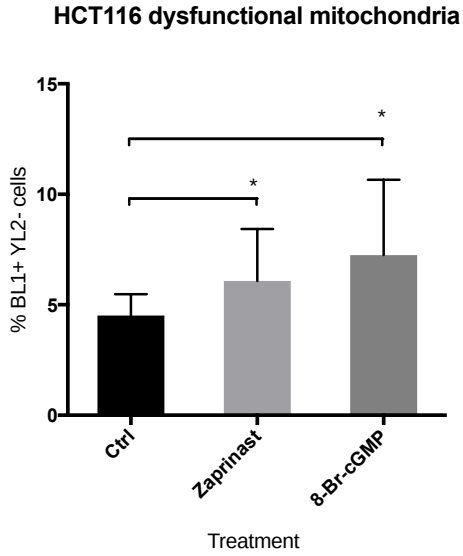


Figure 6.4: PDE6 inhibitor zaprinast and cGMP analogue induced dysfunctional mitochondria in HCT116.
*A 24-hour treatment with 100 nM zaprinast caused a 1,4-fold increase in percentage of dysfunctional mitochondria and a 24-hour treatment with 1 μM 8-Br-cGMP caused a 1.6-fold increase in percentage of dysfunctional mitochondria population. Dysfunctional mitochondria were measured by the fraction of Mitotracker Green positive and Mitotracker Deep Red negative cells. Samples were analysed on the third day of siRNA transfection via flow cytometry. Data are mean±standard deviation, n=9 biological replicates. One-way ANOVA followed by Dunnett's multiple comparisons test was used to compare the percentage of dysfunctional mitochondria to the values of siNT control group *P<0.05.*

Zaprinast caused a similar effect on HCT116 cell cycle distribution as siPDE6H transfection (Figure 6.6). Zaprinast treatment resulted in a G1 arrest, increasing G1

population of HCT116 by 14%. 8-Br-cGMP treatment increased G1 population by 10%. Zaprinast and cGMP analogue 8-Br-cGMP induced similar effects in terms of induction of dysfunctional mitochondria and G1 arrest.

Additionally, zaprinast and 8-Br-cGMP have multiple targets. Zaprinast is known to inhibit both PDE5 and PDE6 (Zhang et al., 2005) and was also identified as a GLS inhibitor (Elhammali et al., 2014). Changes in cGMP levels also influence activity of dual specific PDEs, PDE2 and PDE3 which are activated and inhibited by cGMP, respectively (Larsen et al., 2016). Effects of cAMP and cGMP signalling on mitochondria, are discussed in detail in Chapter 7. cAMP-PKA signalling takes place at mitochondria as PDE2A can be found on both cytoplasm and intermembrane space sides of outer mitochondrial membrane and its inhibition can protect from apoptotic cell death (Monterisi et al., 2017). The non-specificity of zaprinast on PDE6, the multitude of controllers of cGMP-PKG/cAMP-PKA pathways and the interplay between the two make it challenging to assess how total intracellular levels of cGMP would explain changes in dysfunctional mitochondria and cell death. In addition to the cGMP levels, activity and localisation of PDEs other than PDE6 need to be tested as part of future work. The effects of zaprinast and 8-Br-cGMP treatments of several concentrations and durations also need to be tested.

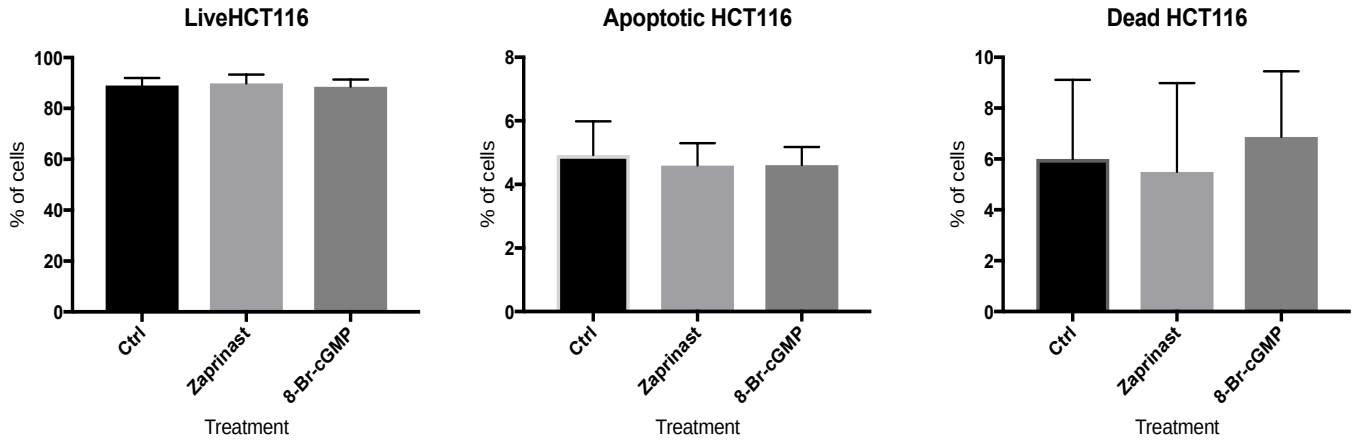


Figure 6.5: 24-hour treatment of HCT116 with Zaprinast (100nM) and 8-Br-cGMP (1 μM) did not change the percentage of live/apoptotic/dead cells.
Samples were analysed for PI and Annexin V staining on the third day of siRNA transfection via flow cytometry. Data are mean±standard deviation, n=6 biological replicates. 2-way ANOVA followed by Dunnett's multiple comparisons test was used to determine the statistical significance between percentage of apoptotic and necrotic cells compared to the values of siNT group.

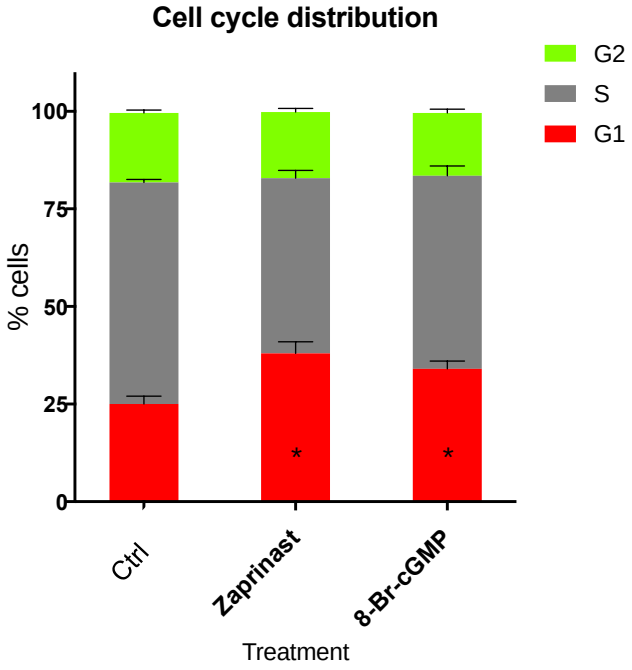


Figure 6.6: Zaprinast and 8-Br-cGMP treatments resulted in G1 arrest in HCT116.
*Samples were analysed for PI and EdU staining after two-day treatments with zaprinast (100 nM) or 8-Br-cGMP (1 μM). 2-way ANOVA, followed by Dunnett's multiple comparisons test was used to determine the statistical significance between percentage of cells in G1/S compared to the values of siNT group.*P<0.05.*

A previous xenograft tumour study tested zaprinast as a potential inhibitor of glutaminase (Elhammali et al., 2014). This study included a single intratumoural injection

of 600 μM zaprinast dissolved in DMSO. As per the methods of that study, since the pharmacokinetics of the drug have not been established, intratumoural injection of the drug was planned to ensure its uptake by the tumour. A low dose of the drug is desirable to minimize its effect on PDE and PDE9, since the IC50 values of zaprinast for PDE6 are lower than those for the other two PDE family members. Published work used peritumoral zaprinast (600 μM, every two days for four weeks, 50% DMSO in saline solution) (Li et al., 2015) and intraperitoneal injections of mice (3 or 10 mg/kg, single injection, dissolved in DMSO supplemented saline solution) (Akar et al., 2014), and intravenous injection or infusion of rats (5 mg/kg, single dose, dissolved in 5% triethanolamine in saline solution) (Wibberley et al., 2002). Periodic intratumoural injections at a high (3 mg/kg) dose were decided as the method of zaprinast delivery upon Dr. Bridges' advice, to ensure delivery to the tumour. We aimed to observe whether the drug would have any effect on tumour growth in this preliminary xenograft study.

2. Tumour growth conditions

Dr. Esther Bridges conducted the xenograft study. Tumour growth of four groups was studied, 1) Ctrl A -control group of wild type HCT116 tumour, 2) Drug -wild type HCT116 tumours injected with zaprinast, and 3) Clone 6 and 4) Clone 14 –HCT116 tumours with CRISPR/Cas9 deleted *PDE6H.* Each group consisted of 6 mice. Day 0 of measurement was determined as the point at which spherical tumours were started to be observed, which on average took place 14 days following tumour injection.

E) *PDE6H* deletion slowed HCT116 tumour growth

Growth of HCT116 tumours with *PDE6H* deletion, Clones 6 and 14 started to diverge from WT tumours at Day 28 of tumour volume measurement (Figure 6.7, Figure 6.8). Control group tumours (Ctrl) grew faster compared to clones and reached the

maximum volume by Day 40. At 40 days following initiation of tumour growth, almost all of the subjects of the control group had been culled due to their tumours having reached the maximum volume, but all of the clones were still in study. It was observed that tumours lacking PDE6H grew slower and that PDE6 inhibitor zaprinast did not have a significant effect on tumour growth.

Four mice were excluded from average tumour growths and survival curves as mice were sick during study. They presented with anaemia and were culled on welfare issues. Two Ctrl and one Drug subjects past day 37, and one Clone 6 subject past day 51, were therefore excluded from the results. These animals had not grown spherical tumours larger than 150 mm^3 at the time of their cull. Intratumoural injections were given to the zaprinast group when tumours reached an average group tumour volume of 50 mm^3, on day 16.

Raw data curves for individual mice show that on week 6 of measurements, all of the Ctrl and Drug group subjects had to be sacrificed while two of Clone 6 and 5 of Clone 14 subjects survived past week 6 of the study.

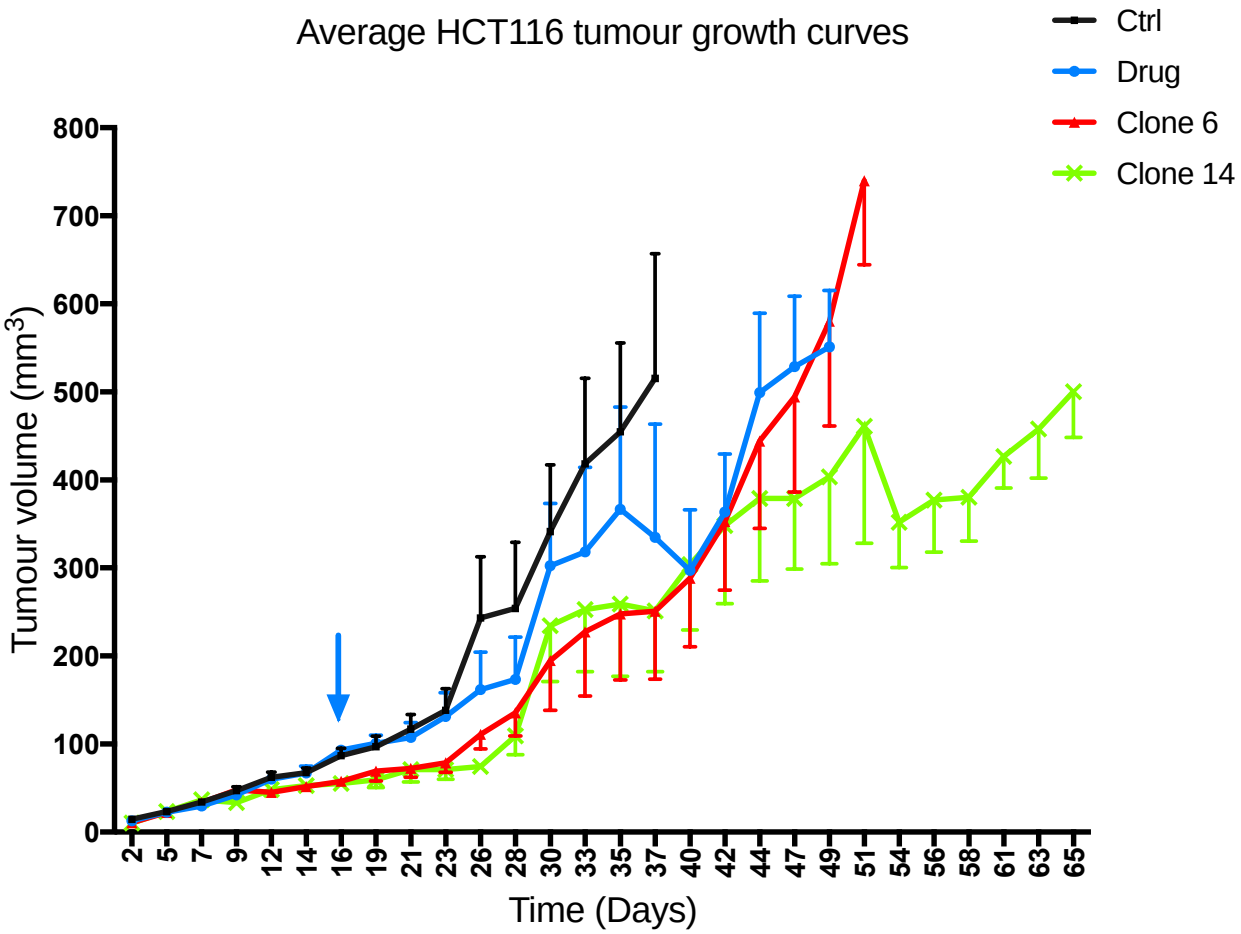


Figure 6.7: PDE6H knockout tumours took longer to reach maximum volume than control or zaprinast treatment group, on average.
Tumour volume of the HCT116 xenograft models was measured. Measurements were carried out until the endpoint mark (9 weeks) or until the tumours reached maximum size. Blue arrow indicates when zaprinast drug treatment started in corresponding group. 4 Mice were excluded in average tumour growths as mice were sick during study; presented with anaemia and were culled on welfare issues (2 from Ctrl, 1 from Clone 6, and 1 from Clone 14 groups). Presented here are n=4 in Ctrl group, n=5 in Drug, n=5 in Clone 6 group, n=6 in Clone 14 group. Error bars represent SEM. Two Ctrl and one Drug subjects past day 37, and one Clone 6 subject past day 51, were excluded from this graph; they are shown in Figure 6.8.

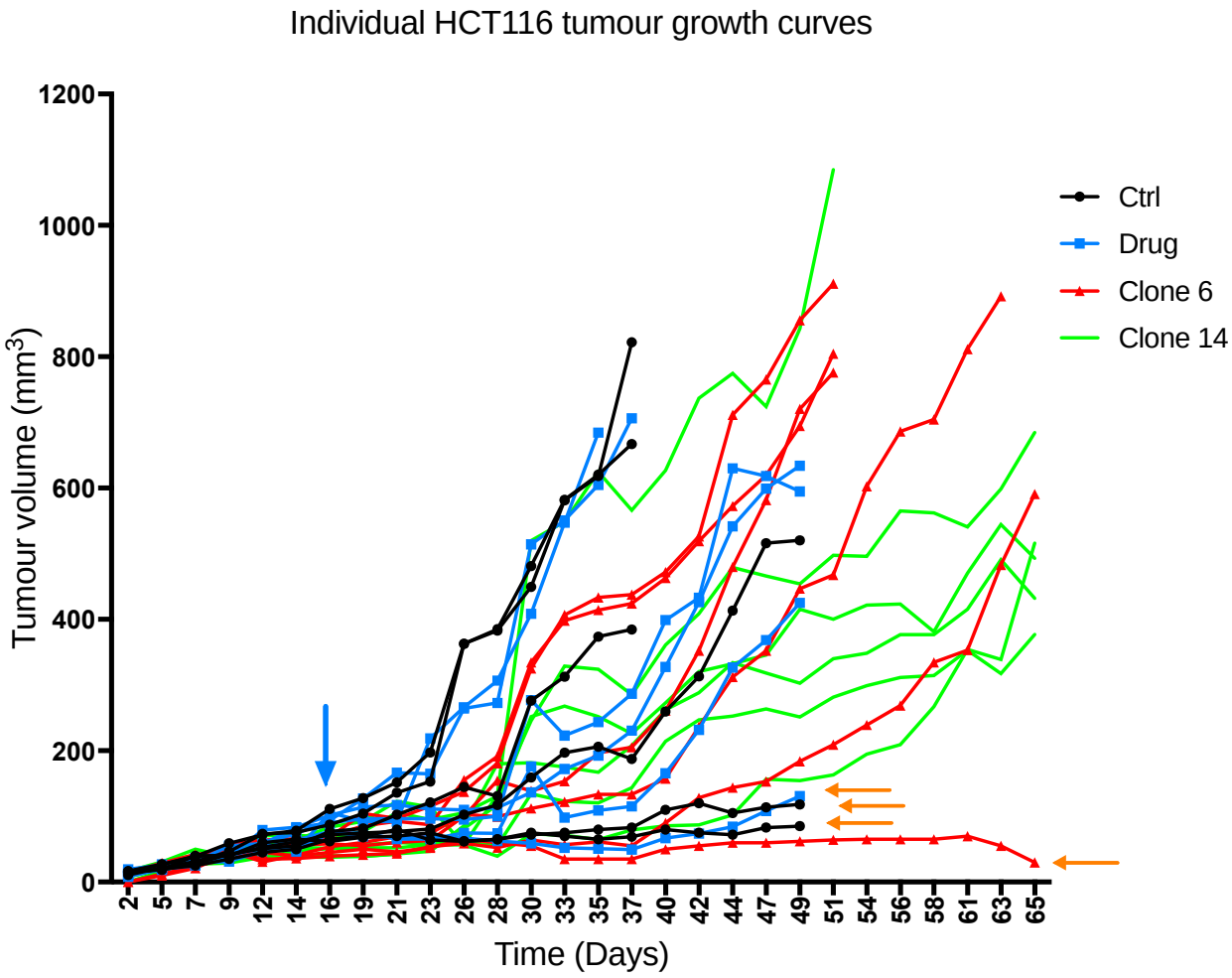
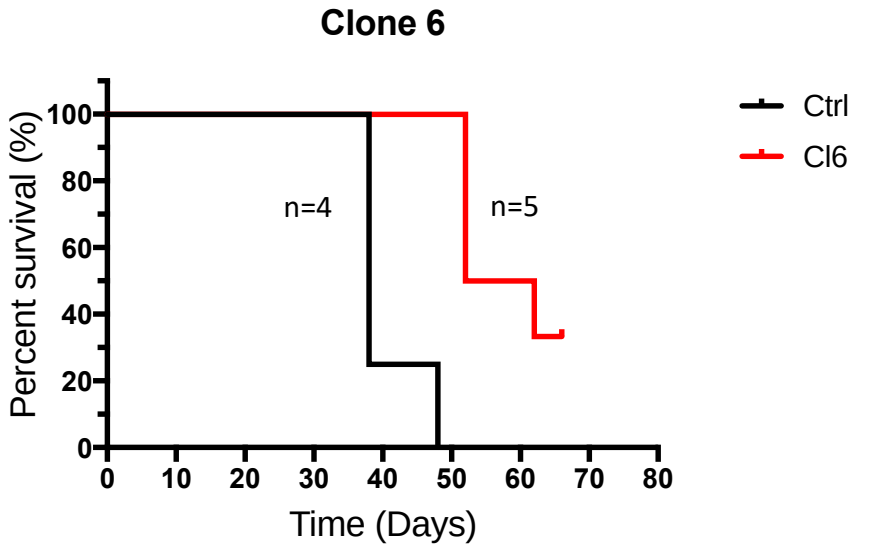
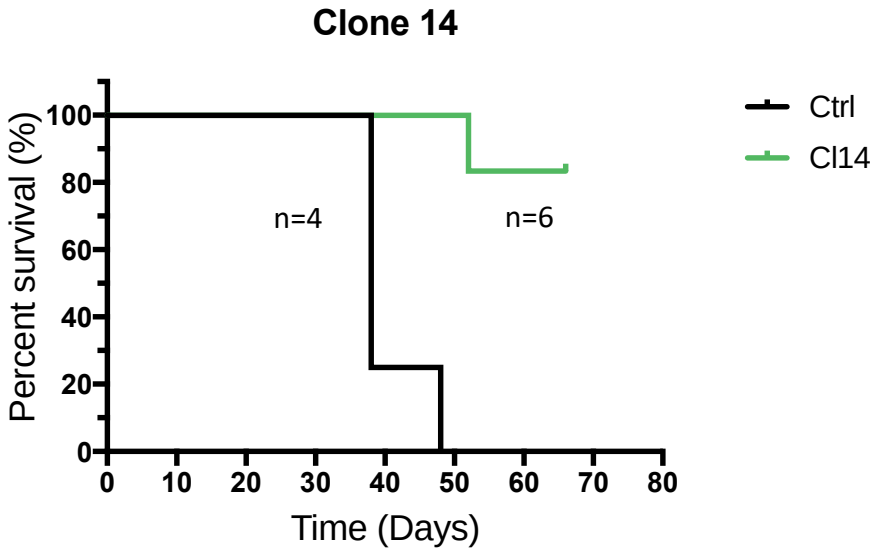


Figure 6.8: HCT116 tumours with PDE6H deletion grew slower compared to WT group. Zaprinast treatment did not affect tumour growth significantly.
Tumour volume of the HCT116 xenograft models was measured. Measurements were carried out until the endpoint mark (9 weeks) or until the tumours reached maximum size. Blue arrow indicates when zaprinast drug treatment started in corresponding group. 4 Mice were excluded in average tumour growths as mice were sick during study; presented with anaemia and were culled on welfare issues (2 from Ctrl, 1 from Clone 6, and 1 from Clone 14 groups). Culled mice are shown with orange arrows. N=4 in Ctrl group, n=5 in Drug, n=5Clone 6 group, n=6 in Clone 14 group. Error bars represent SEM.

a)


Clone 6
Percent survival (%)
100
80
60
40
20
0
0
10
20
30
40
50
60
70
80
Time (Days)
n=4
n=5
Ctrl
Cl6

b)


Clone 14
Percent survival (%)
100
80
60
40
20
0
0
10
20
30
40
50
60
70
80
Time (Days)
n=4
n=6
Ctrl
Cl14

c)

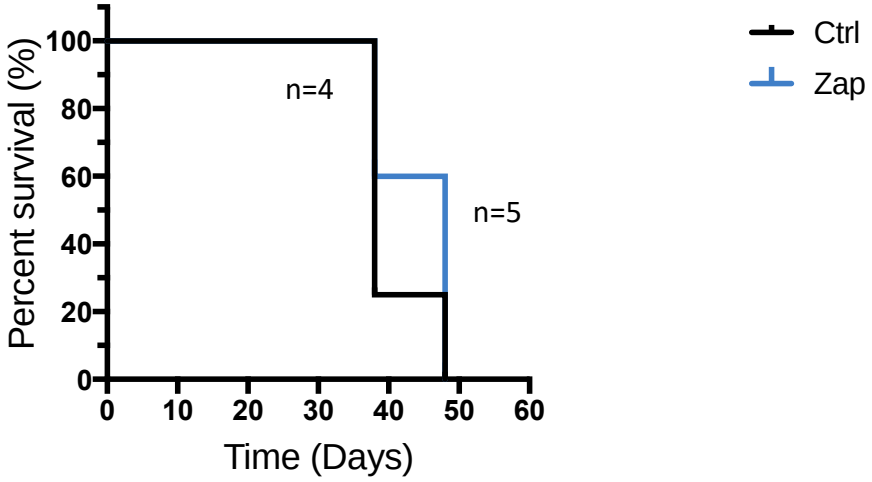

Zaprinast
Percent survival (%)
100
80
60
40
20
0
0
10
20
30
40
50
60
Time (Days)
n=4
n=5
Ctrl
Zap

Figure 6.9: PDE6H deletion in HCT116 affected animal survival.
*Zaprinast slowed tumour growth between Days 38-49 but did not significantly affect survival overall. 4 Mice were excluded in average tumour growths as mice were sick during study; presented with anaemia and were culled on welfare issues (2 from Ctrl, 1 from Clone 6, and 1 from Clone 14 groups). N=4 in Ctrl group, n=5 in Drug and Clone 6 group, n=6 in Clone 14 group. Error bars represent SEM. 1 Ctrl subject past day 37 and two Clone 6 subjects past day 51, which were shown in Figure 6.7, were excluded from this graph. Log-rank (Mantel-Cox) and Gehan-Breslow-Wilcoxon tests were used to determine the median survival of Ctrl, zaprinast treatment and PDE6H ko subjects, and to compare a) Clone 6, b) Clone 14, and c) Zaprinast median survivals to that of the control group. Median survival values were calculated as Ctrl: 38 days, Clone 6: 57 days (**) Clone 14: undefined, as all subjects, except for one, were alive at the end of the study (**), and Zaprinast/Drug: 38 (not significant). **P<0.01.*

PDE6H deletion slowed down tumour growth (Figure 6.7, Figure 6.8) and improved animal survival (Figure 6.9 a,b) in a preliminary analysis from which the culled mice were excluded. Zaprinast had no significant effect on overall survival (Figure 6.9 c). This result is consistent with the inability of zaprinast to change percentage of live HCT116 cells (Figure 6.5).

One-way ANOVA analysis followed by Tukey's multiple comparisons test showed that Ctrl vs Drug, Ctrl vs Clone 6, Drug vs Clone 6, Clone 6 vs Clone 14 tumour volume comparisons yielded non-significant (P>0.05) differences. Ctrl vs Clone 14 and Drug vs Clone 14 groups were significantly different (* P<0.05 and ** P<0.01, respectively).

We then combined control groups from a xenograft experiment also conducted with HCT116 cells of identical growth conditions (DL), as well as merging the two *PDE6H* ko clones as one group to plot another survival curve (Figure 6.10) with n=10 (Ctrl) and n=11 (Clones). The endpoint of tumour growth was determined to be the third timepoint once the tumour had reached 500 mm^3, which was representative of the endpoint used in the original xenograft experiment (ALH29). While data of this compiled experiment revealed a significant difference in survival between WT and *PDE6H* ko HCT116 tumours, it must be noted that this was a preliminary analysis and indicated the size of groups needed for definitive experiments.

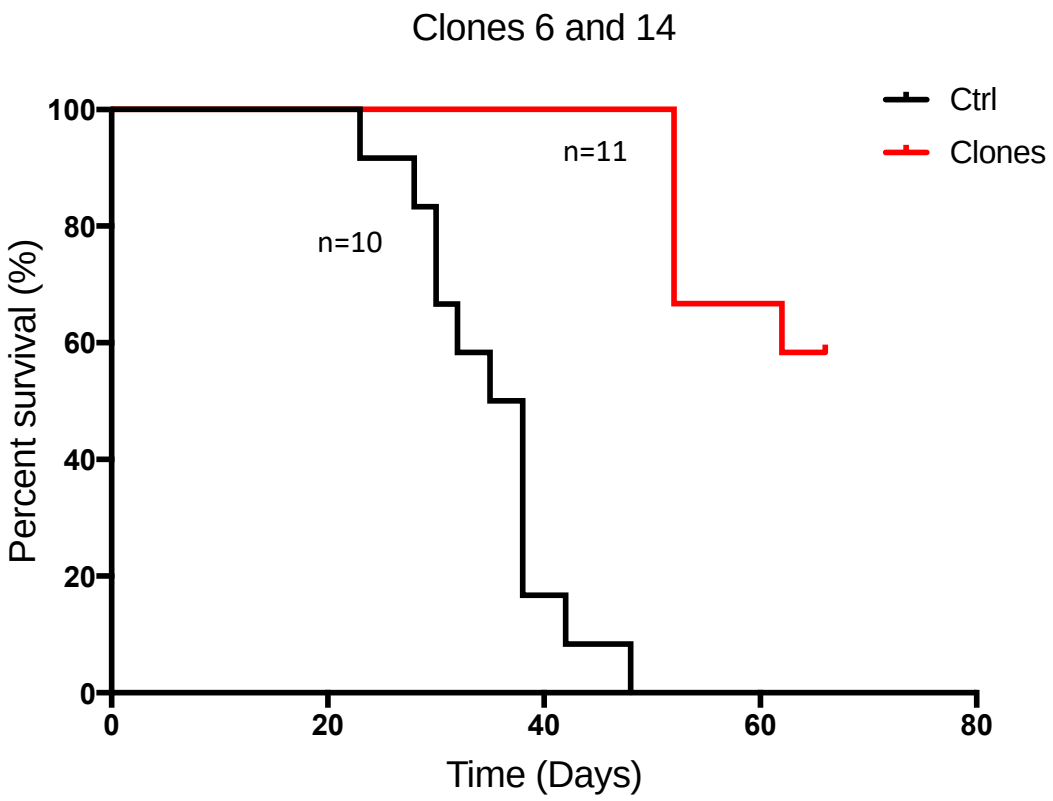
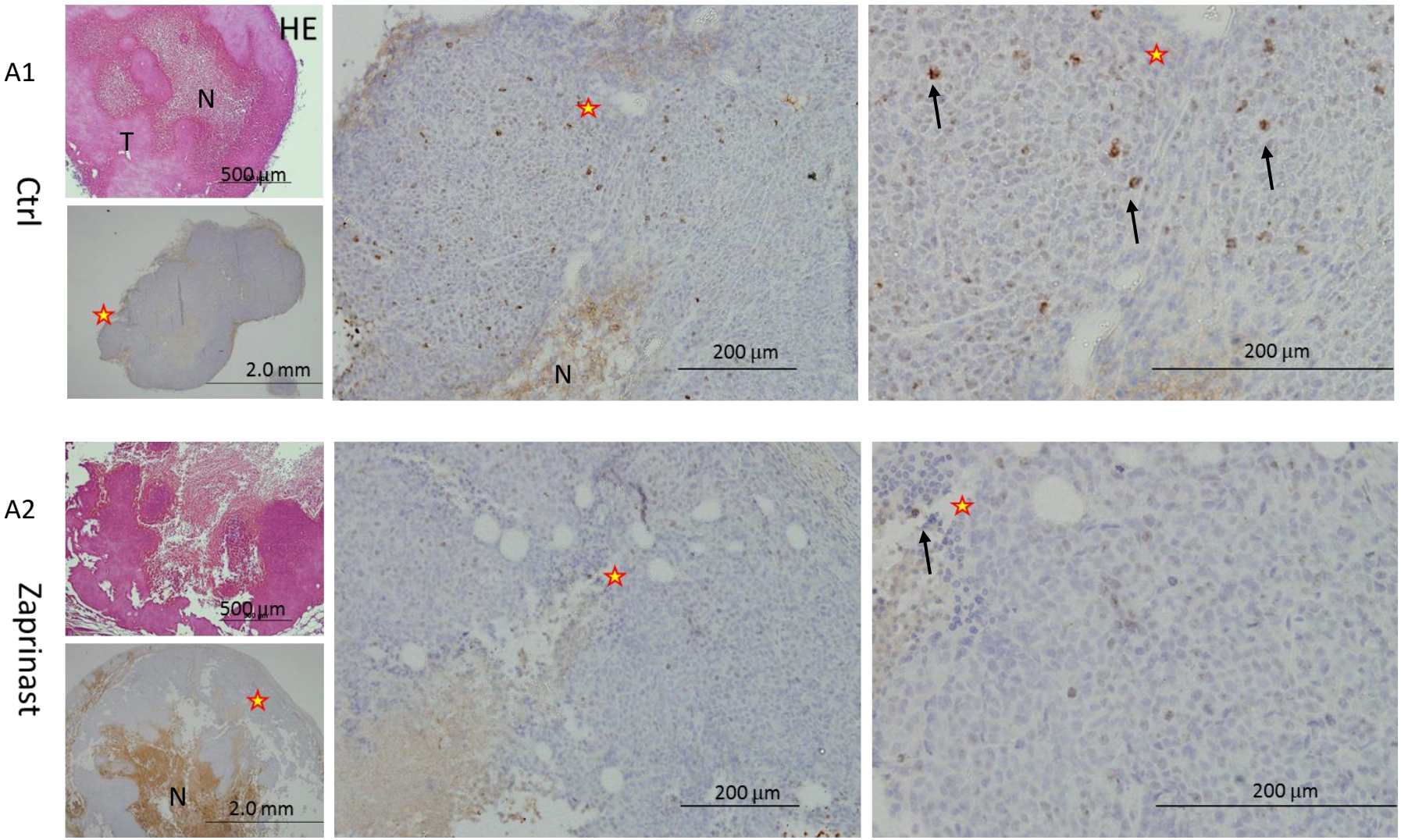
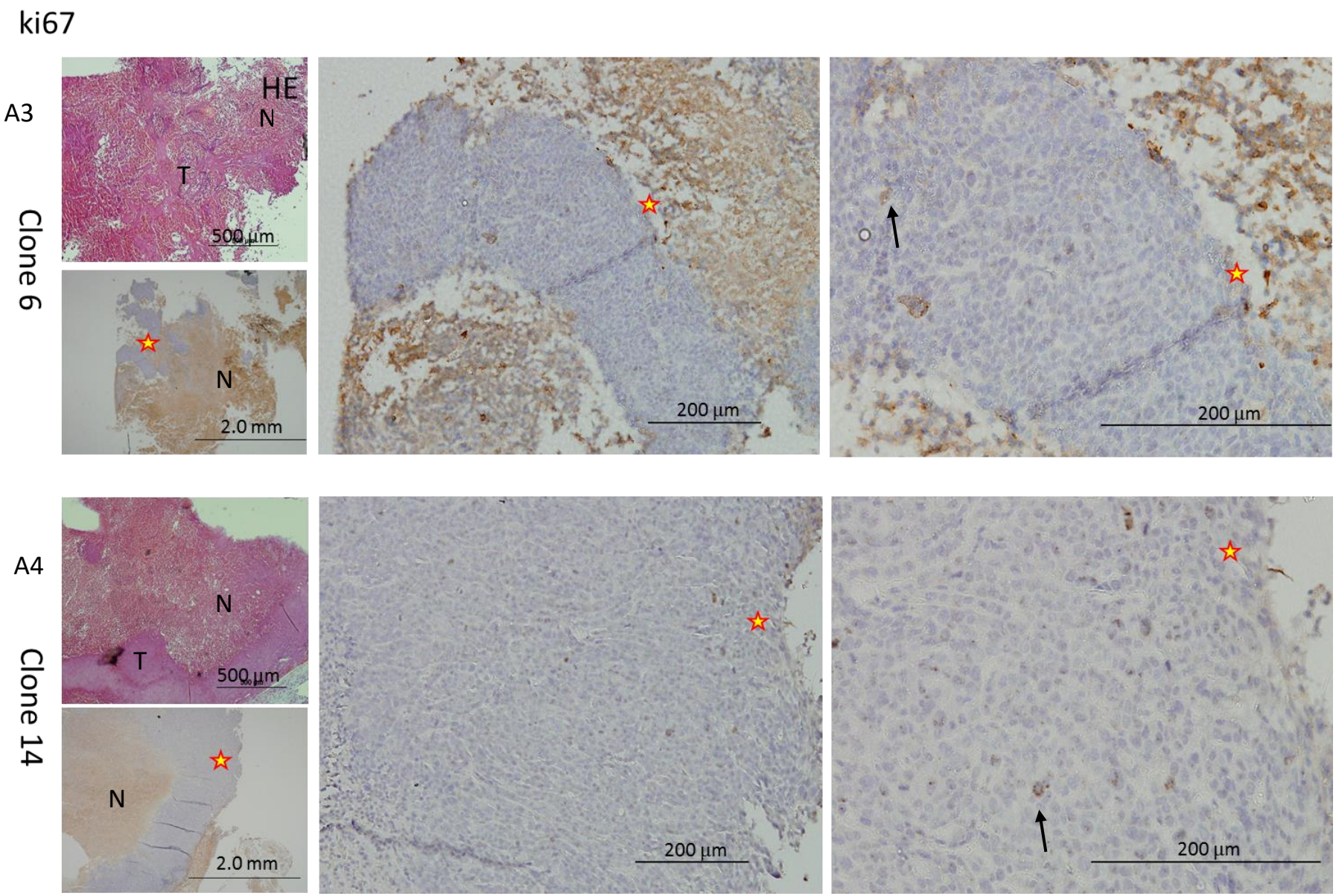


Figure 6.10: Survival curve of complied PDE6H ko tumour growth data revealed that animals with PDE6H ko tumours had improved survival.
*Ctrl group is a compilation of tumour growth data of two HCT116 WT xenograft experiments (ALH29 and DL). Clones group is a compilation of tumour growth data of the two clones; 6 and 14, from xenograft experiment ALH29. n=10 (Ctrl) and n=11 (Clones). Log-rank (Mantel-Cox) and Gehan-Breslow-Wilcoxon tests were used to determine the median survival of Ctrl and PDE6H ko (Clones) subjects. Median survival of Ctrl group was determined as 36.5 days. Median survival of the Clones could not be determined as all subjects but four were alive at the end of the study. Difference between median survivals was statistically significant, ****: P<0.0001.*

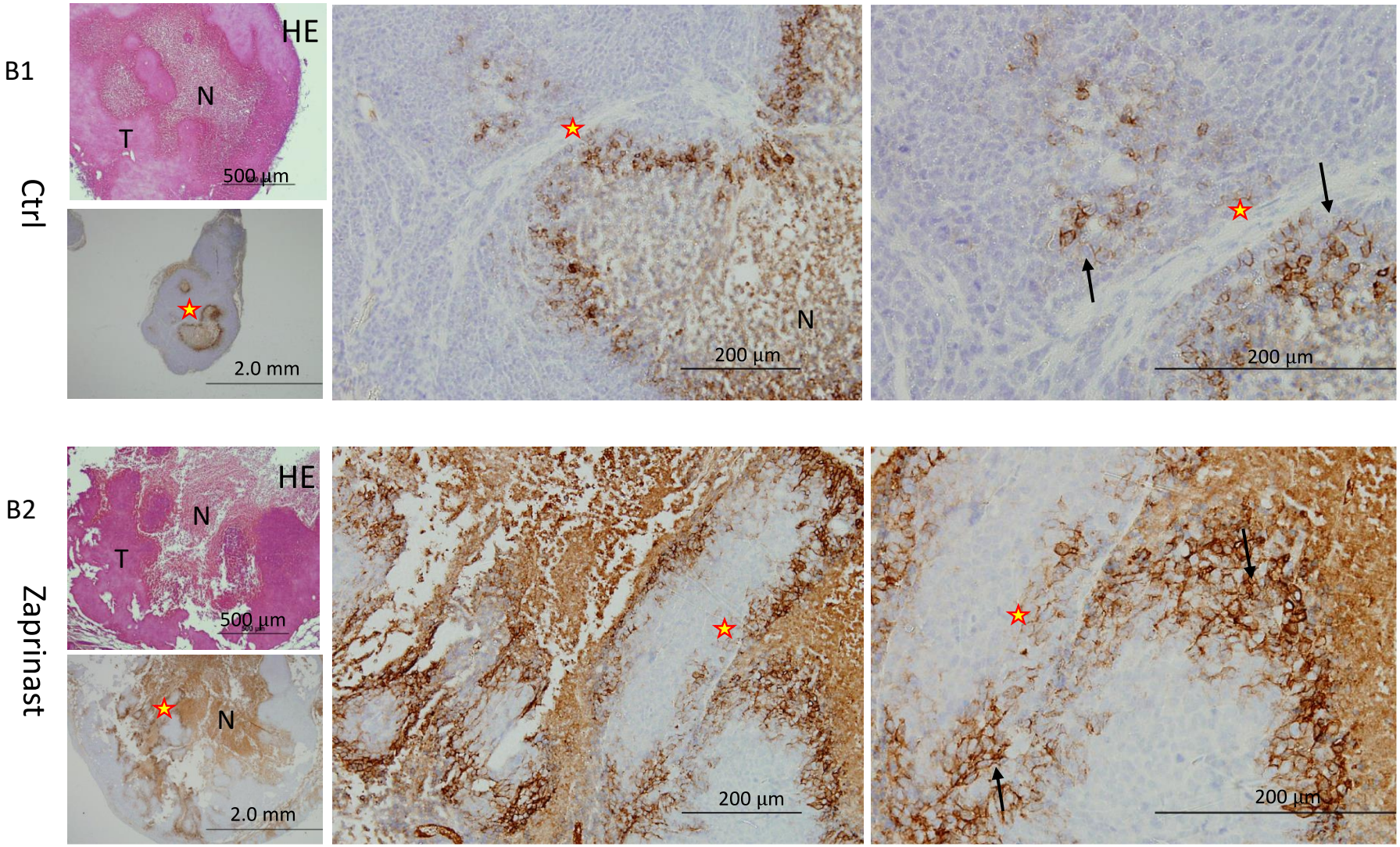
Tumour section staining showed that zaprinast treatment had a similar antiproliferative effect as the *PDE6H* deletion (Figure 6.11). This was displayed through the haematoxylin & eosin (HE), Ki-67, carbonic anhydrase 9 (CA9) staining of Ctrl vs zaprinast, Clone 6 and Clone 14 sections, which also showed that Ctrl group tumour had less necrosis compared to the rest.

ki67


A1
Ctrl
HE
N
T
500 μm
2.0 mm
N
200 μm
200 μm
A2
Zaprinast
500 μm
N
2.0 mm
200 μm
200 μm


ki67
A3
Clone 6
HE
N
T
500 µm
N
2.0 mm
200 µm
200 µm
A4
Clone 14
N
T
500 µm
N
2.0 mm
200 µm
200 µm

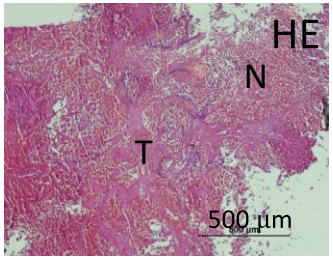
CA9

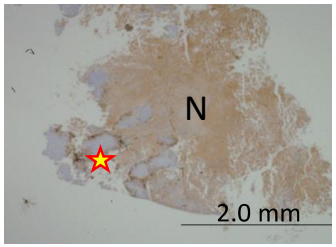

B1
Ctrl
HE
N
T
500 µm
2.0 mm
N
200 µm
200 µm
B2
Zaprinast
HE
N
T
500 µm
N
2.0 mm
200 µm
200 µm

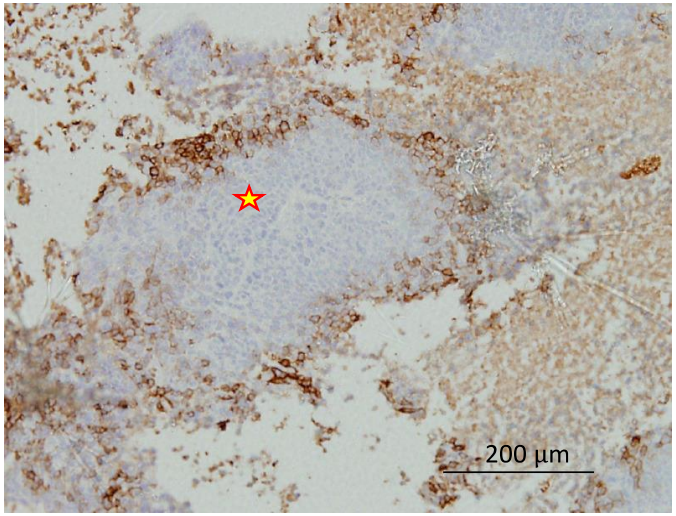
CA9

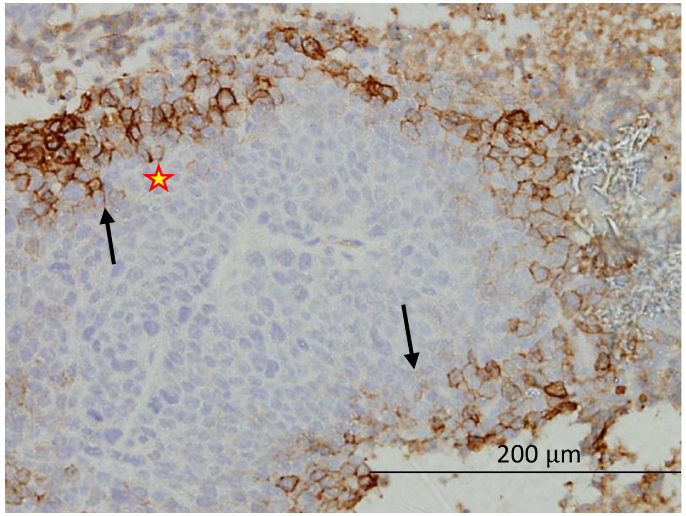
B3

Clone 6



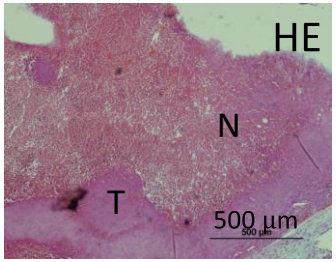


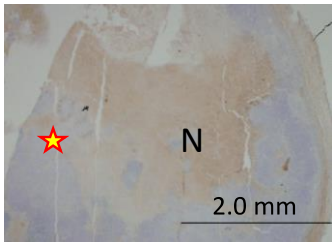


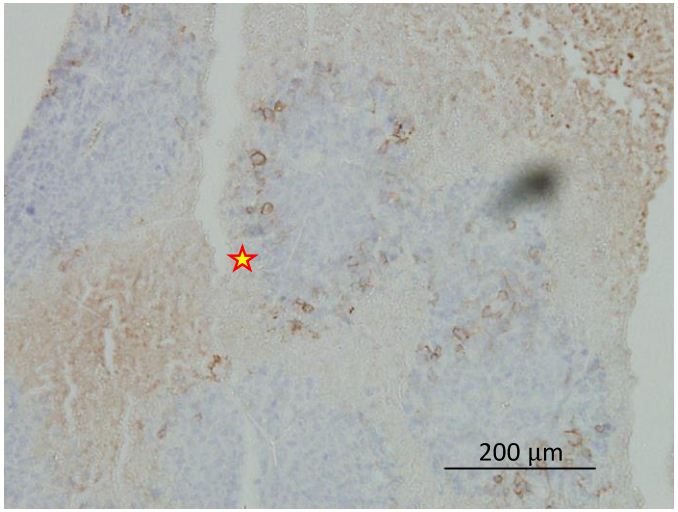


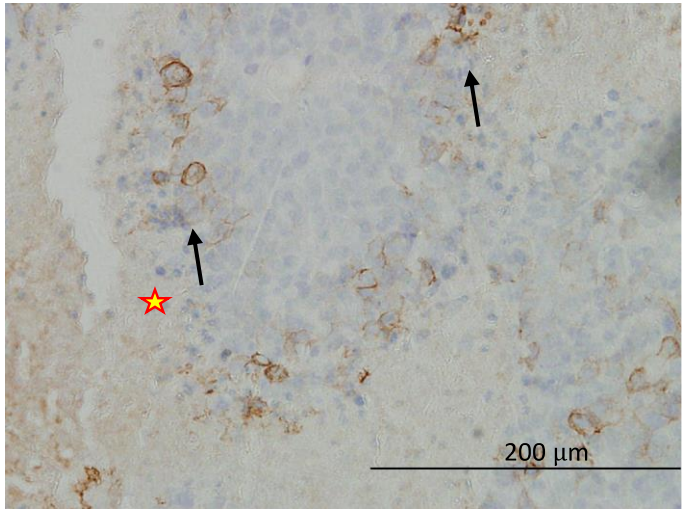
B4

Clone 14

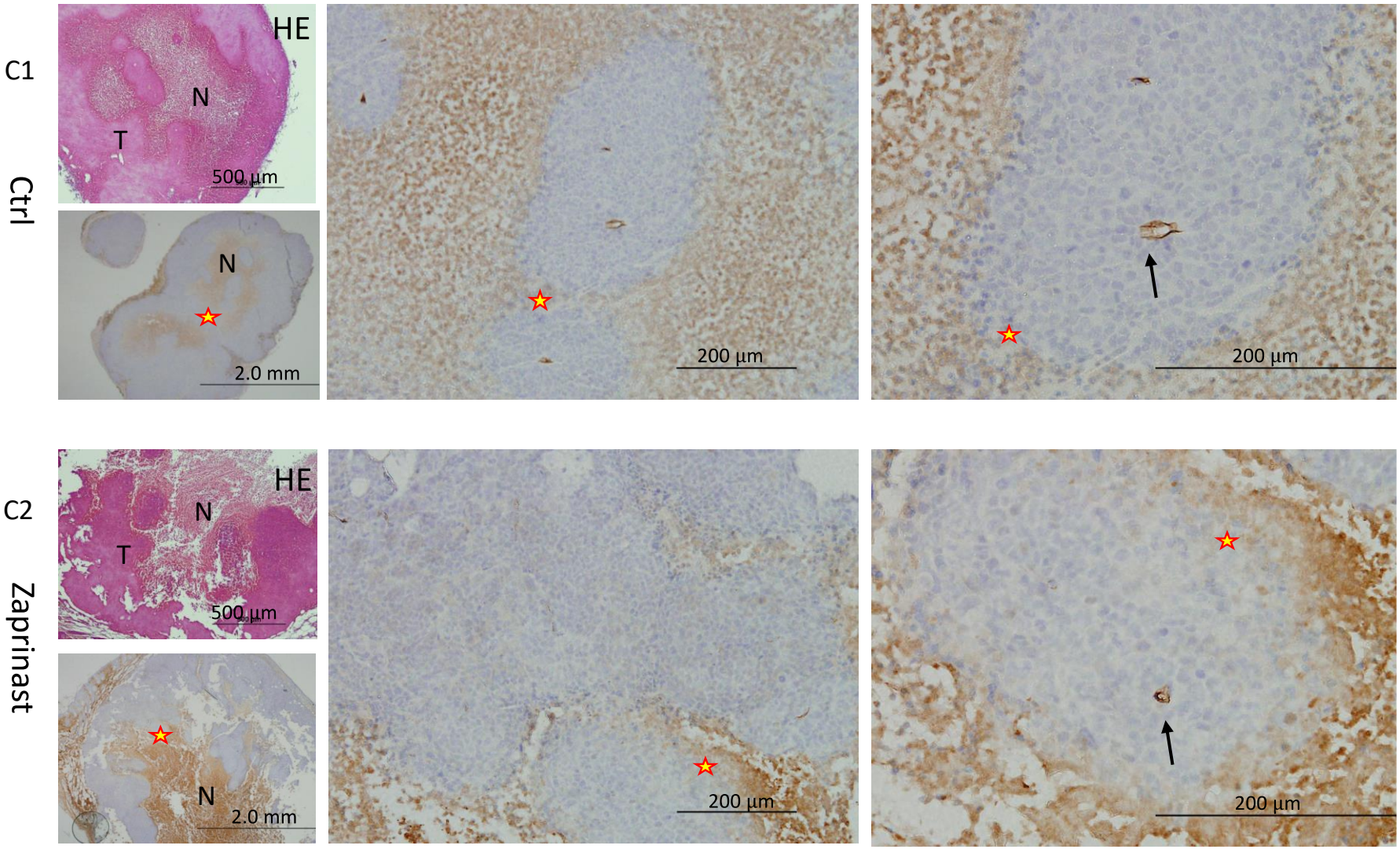






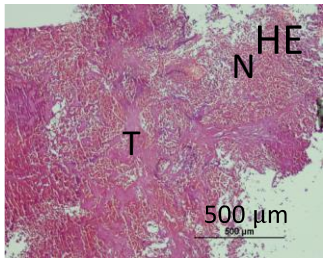


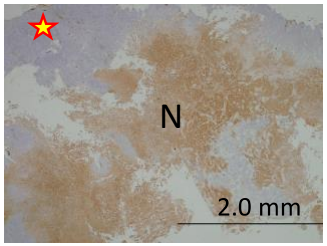
Endomucin

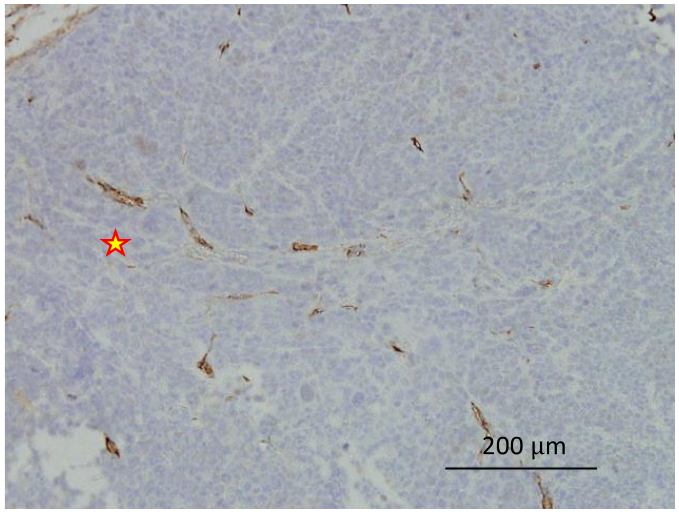

C1
Ctrl
HE
N
T
500 µm
N
2.0 mm
200 µm
200 µm
C2
Zaprinast
HE
N
T
500 µm
N
2.0 mm
200 µm
200 µm

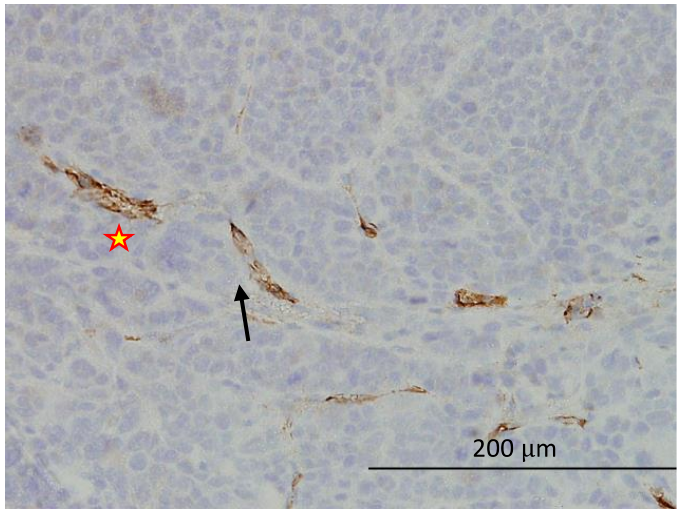
Endomucin

C3 Clone 6

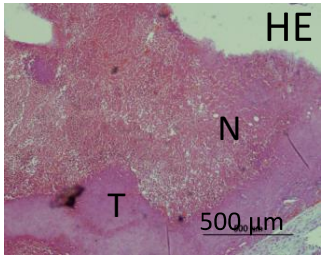


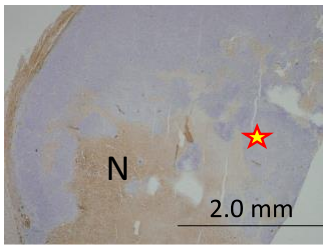


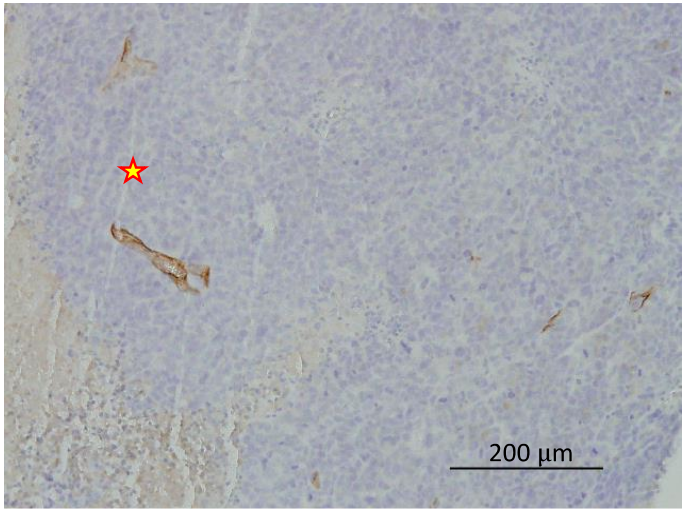




C4 Clone 14







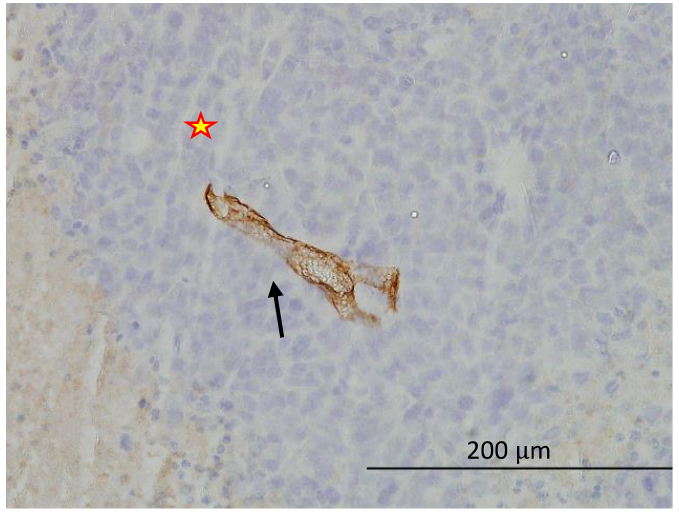


Figure 6.12: Immunostaining of tumour sections.
Vessels were stained with endomucin. Haematoxylin & eosin (HE) staining show tumour structure. Ki-67 is a marker for proliferation and CA9 for hypoxia. Arrows show representative Ki-67, CA9, or endomucin positive cells.

Tumour histology (HE) of zaprinast and *PDE6H* ko clone tumours displayed more necrotic areas compared to those of Ctrl group (Figure 6.11). Compared to WT, necrotic areas of zaprinast, Clone 6, and Clone 14 were greater by 40%, 26%, and 36%, respectively (Figure 6.12a). Cell proliferation marker Ki-67 was expressed higher in the Ctrl group (Figure 6.12b) compared to zaprinast and Clone 14 groups by 8.8% and 9.2%, respectively. Hypoxia marker CA9 displayed a single large hypoxic region in the Ctrl group, whereas zaprinast and clone groups' sections had smaller yet disperse hypoxic regions (Figure 6.11). CA9 score of Clone 14 was greater than that of WT control by 15.5% (Figure 6.12c).

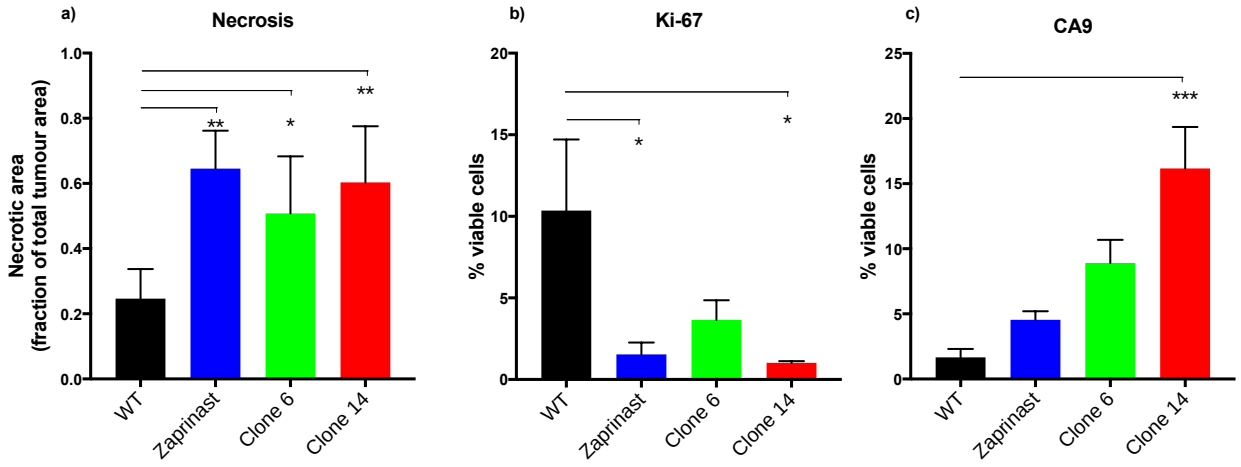


Figure 6.11: PDE6 inhibition and PDE6H deletion caused necrosis in HCT116 xenografts. N=4 in Ctrl group, n=5 in Drug, Clone 6 and Clone 14 groups. Mean values are shown, error bars denote SEM. One-way ANOVA followed by Dunnett's multiple comparisons test was used to compare quantification of each group to the values of WT (P<0.05, **P<0.01, ***P<0.001).*

Vessel count and length scoring are to be completed using Visiopharm Integrator System protocol that is being developed by Dr Nasullah Khalid Alham. A preliminary assessment prior to quantification of endomucin staining that marks endothelial cells, showed that zaprinast treated tumours had fewer blood vessels compared to the control. Blood vessels of Clones 6 and 14, however, were larger in size and number compared

to tumours of zaprinast and Ctrl groups. To explain how tumours of Clone 6 and Clone 14 groups had more blood vessels while displaying more regions of hypoxia, we need to assess vessel functionality. Therefore, tomato leptin staining is under way, to understand the blood perfusion of the intratumoural vessels.

F) Discussion

1. *In vitro* work

PDE6H knockdown decreased HCT116 cell viability (Figure 6.1) and spheroid growth (Figure 6.3), while *PDE6H* knockdown and knockout both disrupted colony formation (Figure 6.2) These results need to be replicated with three biological samples and the current statistical analysis is only a measure of technical reproducibility.

Based on the G1 cell cycle arrest, increase in cell death and increase in percentage dysfunctional mitochondria following siPDE6H transfection (Chapter 5), one would predict zaprinast and 8-Br-cGMP treatments to have the same effects. While zaprinast and 8-Br-cGMP increased percentage dysfunctional mitochondria (Figure 6.4) and caused G1 arrest in HCT116 (Figure 6.6), they did not induce cell death (Figure 6.5). Time-course and dose-response experiments will be performed to find conditions of treatment that result in similar increase in cGMP as siPDE6H transfection. The differential effect of the drugs might also have to do with a potential hormesis that occurs with initial increase in cGMP leading to cell death, followed by an adaptive period where apoptosis or necrosis does not take place (Mattson, 2009).

2. *In vivo* work

A pilot xenograft study has been completed on *PDE6H* deletion in HCT116 tumours. *PDE6H* knockout groups had reduced tumour when taking into account animal welfare and tumour establishment conditions. These results were in accordance with

the effect of *PDE6H* deletion on lowering HCT116 viability *in vitro* under normoxia and hypoxia, and on disrupting colony formation and spheroid growth.

The HE and Ki-67 staining showed that the WT tumours were denser with more viable cells compared to the PDE6H depleted tumours: zaprinast treated WT and *PDE6H* knockout clones 6 and 14.

Zaprinast treatment did not improve survival in our pilot xenograft experiment. However, according to our initial histochemistry data, it did result in a decrease of the proliferation marker Ki-67. Complete staining and scoring of the tumour sections are under way. It is possible that, over a longer treatment regimen, zaprinast treated animals would experience a reconstruction of their tumours, leading to slowing down of tumour growth. Another layer of complexity stems from zaprinast's inhibition of both PDE5 and PDE6, making it difficult to attribute its effects solely to PDE6 inhibition.

Results from the zaprinast group were consistent with those of the clones 6 and 14 in that, compared to the WT control group, they had fewer Ki-67 positive regions and displayed more hypoxic regions stained for CA9. The WT tumour section also had a hypoxic ring which was not dispersed across the tumour as observed in the zaprinast, Clone 6, and Clone 14 groups. Additionally, PDE6H depletion resulted in fewer blood vessels compared to the WT group, as displayed in the zaprinast and Clone 6 & 14 groups. CA9 rings of zaprinast group and clones enclosed viable regions and were surrounded by necrotic areas. The vessels of Clone 6 and Clone 14 sections were larger compared to those of both the zaprinast and WT groups.

While we need more detailed markers of angiogenesis and vessel functionality, the preliminary staining of tumour sections suggests that the larger blood vessels of Clone 6 and Clone 14 might fail to properly oxygenate the tumour.

The results of the xenograft study suggest that *PDE6H* deletion slows down HCT116 tumour growth and is to be repeated with more animals and a control cell line that has been through the CRISPR selection, to establish the effect of *PDE6H* deletion on survival. The inhibition of HCT116 tumour growth upon *PDE6H* deletion can be

ascribed to the contribution of the gene to cell cycle progression, and cancer cell or tumour microenvironment energy metabolism.

CHAPTER 7: DISCUSSION

We identified genes that link metabolic pathways of energy production and biosynthesis to cell cycle progression. The results of the study contribute to a better understanding of the metabolic regulation of cell cycle which has the potential to elucidate specific targets for cell growth, proliferation and tumourigenesis, as well as interactions between drugs that affect cancer cell cycle and metabolism.

A)Future work

1. Senescence

As part of future work, I will make the distinction between quiescence and senescence that accompanies the G1 arrest observed upon PDE6H depletion. The presence of a terminal differentiation is marked by a cell cycle exit. Quiescence and senescence in animals can be distinguished by whether the cell cycle arrest was reversible or not (Velappan et al., 2017). Senescence is marked by cell cycle arrest in presence of growth signals (Blagosklonny, 2011).Activated mTOR and ERK1/2 in siPDE6H transfected and PDE6H CRISPR/Cas9 knockout HCT116 cells suggest that these cells have undergone senescence. It is important to understand the root of cell signalling pathway activation in PDE6H depleted cells (ERK1/2, mTORC1, and HIF-1α).

mTOR signalling is necessary for a stable but reversible arrest. Rapamycin leads to reversal of cell cycle arrest upon p21 removal, transforming otherwise irreversible arrest (Demidenko et al., 2014). mTOR activity that is regulated by p53 can therefore

make the difference between senescence and quiescence, as the former is caused by a hyperactive p53 that inhibits mTOR (Dulic, 2011). P53 can suppress senescence to induce quiescence (Demidenko et al., 2010). Assessing the length of cell cycle arrest in presence of mTOR inhibitors and studying arrest upon PDE6H depletion in cell lines of various p53 statuses will help us understand p53's relation to G1 arrest observed. One way the senescent cells can sustain themselves in absence of autophagy, which has been inhibited by mTOR, is senescence-associated secretory phenotype (SASP). SAPS can be measured by IL-6 IL-8 expression (Coppé et al., 2010). Quantification of Ki-67 expression, an indication of CDK 4/6 activity and an important marker of proliferation, and beta-galactosidase assay can also inform us of senescence. The activation of growth signalling can also be due to abundance of growth factors in the media, so there is merit to testing oncogenic signalling in PDE6H depleted and WT cells under various concentrations of serum.

2. Metabolomics

Mass spectroscopy assessment of WT and PDE6H depleted cells can enable a better analysis of which metabolic pathways are altered in absence of PDE6H. Since glutamine is important fuel for nucleotide signalling and oxidative phosphorylation, we have initiated a mass spectroscopy analysis of WT and PDE6H deleted HCT116 cells with and in absence of glutamine. Along with glutamine and glucose uptake assays, the mass spectroscopy analysis will allow us to understand if nutrients are preferentially used in pentose phosphate pathway at the expense of TCA cycle and glycolysis (Figure 5.26). Mass spectroscopy can supplement cGMP ELISA assays in measuring PDE6 activity of cells. Mass spectroscopy can detect levels of cGMP and GMP, which are the substrate and product of PDE catalysed hydrolysis reaction, respectively.

Preliminary quantification of mass spectroscopy results suggests that PDE6H depleted clones have lower levels of glucose, glutamine and pyrimidine pools compared to WT HCT116. Initial results suggest that in *PDE6H* ko cells, available glucose was not

used solely for elevating glycolysis levels. In these cells, glucose and glutamine might be used through pentose phosphate pathway to sustain production of nucleotides.

Preliminary mass spectroscopy results indicated a difference in levels of pyrimidines, glutamine, and glycolysis intermediates between wild type and *PDE6H* knockout clones. Therefore, we are planning to conduct flux studies to understand changes to energy and biosynthesis pathways by examining alterations to glycolysis, glutaminolysis, TCA cycle and PPP. We are also working on clarifying the source of ROS production through superoxide ELISA, in presence of established ROS scavengers and inducers, following PDE6H depletion and how it explains the effect of the latter on cell proliferation and tumour growth. These findings can help us explore a potential synergy between ROS inducing drugs and PDE6 inhibitors to induce cancer cell death.

Due to changes in nucleotide pools in PDE6H depleted clones, we are currently performing clonogenic assays of *PDE6H* knockout clones following radiation treatment. These results can help us understand if PDE6H function plays a role in DNA repair mechanisms.

More replicates of the western blots of HIF-1α and PKG signalling pathways are planned for quantification. Histology work is also continuing to stain for glutamine and glucose transporters, PKG pathway components phospho-VASP and CREB, as well as markers of angiogenesis. We are also planning to assess hypoxia within spheroids grown from *PDE6H* ko HCT116 cells.

3. Downstream targets

cAMP/PKA signalling and mitochondria

Some phosphodiesterases have dual specificity. Intracellular cyclic nucleotide pools are controlled by PDE1, PDE2, PDE3, PDE10, and PDE11 which hydrolyse both cAMP and cGMP, PDE4, PDE7, and PDE8 which hydrolyse cAMP and PDE5, PDE6, and PDE9 which hydrolyse cGMP (Beavo et al., 2006). PDE2 is activated by cGMP

while PDE3 is inhibited by cAMP. An interplay between cAMP and cGMP levels is controlled by PDE2 and PDE3 activity (Larsen et al., 2016). With increased cGMP levels, cAMP could go up (due to PDE3 inhibition) or go down (due to PDE2 activation).

Preliminary results from our mass spectroscopy experiments show that cAMP levels are higher in PDE6H ko clones compared to PDE6H WT. This led us to consider cAMP as the key player of mitochondrial effects of PDE6H inhibition. Effects of cAMP on mitochondria have been widely studied; PKA signalling in mitochondria have also been discovered (Monterisi et al., 2017) Despite reports of the effect of changes in cGMP levels on mitochondrial function, PKG has not been discovered in mitochondrial matrix.

cAMP pools in mitochondrial matrix and on mitochondrial membranes

cAMP does not travel far in the cell as its concentration is controlled by phosphodiesterases, as shown by the presence of cAMP microdomains in rat cardiac myocytes (Zaccolo, 2002). Multiple groups have shown that cytosolic cAMP cannot enter the mitochondria (Lefkimmiatis et al., 2013) (Di Benedetto et al., 2013). Therefore, reports of mitochondrial cAMP/PKA signalling have been crucial in showing a direct effect of cAMP on mitochondrial function. In addition to electron microscopy evidence of mitochondrial PKA (Schwoch et al., 1990), mitochondrial soluble adenyl cyclase (sAC) that is activated by bicarbonate has been reported (Zippin et al., 2003). It was also reported that cAMP, that is produced in mitochondria by sAC, enhanced OXPHOS and increased ATP production through mitochondrial PKA activation in HeLa, HEK293T, and COS-1 cells (Acin-Perez et al., 2009).

PDE2A localised in mitochondrial matrix has been identified as the controller of mitochondrial cAMP levels, based on work done on mitochondria isolated from rat brain and liver (Acin-Perez et al., 2011). Same work reported that the N-terminal residues of PDE2A2 promoted its mitochondrial localisation, resulting in the binding of the protein to mitochondria without showing how PDE2A enters the matrix.

Another group reported that the mitochondrial outer membrane (MOM) is another site cAMP/PKA activity, thereby showing distinct cAMP cascades on MOM and matrix (Lefkimmiatis et al., 2013). The function of PDE2A on the MOM of cardiac myocytes and embryonic fibroblasts has also been studied (Monterisi et al., 2017). PDE2A located outside of the matrix, on the cytosolic and intermembrane space (IMS) sides of MOM, as well as the IMS of the inner mitochondrial membrane (IMM), has been shown to control mitochondrial form and function (Monterisi et al., 2017). This PDE2A controlled cAMP generated by plasma membrane- associated adenylyl cyclase (pmAC), not sAC in the matrix. Same group showed that inhibition of PDE2A results in protection from apoptosis and an increase in membrane potential.

While PKG has not been detected in mitochondria, cGMP/PKG signalling has an impact on mitochondrial function. Addition of PKG + cGMP to isolated rat mitochondria results in opening of the K_{ATP} channels on IMM (Costa et al., 2005). The opening of this channel leads to increased mitochondrial ROS production (Costa et al 2008). Increased levels of cGMP were detected in isolated cardiac mitochondria after treatment with membrane permeable 8-Br-cGMP, resulted in cytochrome c release from mitochondria and apoptosis (Seya et al., 2007). Mitochondrial cytochrome c release in isolated rat cardiac mitochondria is induced by Ca^{2+} and inhibited by KT5823, a PKG inhibitor (Seya et al., 2012).

Remaining questions

While our mass spectroscopy results show an increase in intracellular cAMP levels in *PDE6H* ko clones compared to WT HCT116, they might not reflect mitochondrial cAMP levels. It is likely that such an increase does not take place in mitochondria since cytoplasm and mitochondria have separate cAMP pools (Lefkimmiatis et al., 2013) (Di Benedetto et al., 2013). Increase in cellular cGMP, as seen in PDE6H depleted cells, may result in the activation of PDE2 in the cytoplasm. PDE2 may then travel to the mitochondria to downregulate cAMP/PKA signalling,

potentially affecting OXPHOS and apoptosis (Acin-Perez et al., 2009) (Monterisi et al., 2017). Alternatively, if there is an overall increase in cAMP levels throughout the *PDE6H* ko HCT116 cells, mitochondria included, this increase might be due to PDE3 inactivation. The question of the effect of cytoplasmic PDE2 on cAMP levels also remains to be addressed.

A further challenge of assessing mitochondrial activity of cAMP and cGMP signalling stems from the opposite effects of each on apoptosis. Unlike PKG signalling which promotes apoptosis, (Jackson and Ceresa, 2016), intermembrane space anchored PKA activity inactivates BAD following IL-3 Stimulation in hematopoietic cells (Harada et al., 1999); it also inactivates Drp1, resulting in mitochondrial elongation in cardiac muscle cells (Cribbs and Strack, 2007). Inactivation of both BAD and Drp1 confers resistance to apoptosis. cAMP signalling is predicted to enhance survival and antagonise the effects of cGMP.

Plans for future experiments

To test whether changes in cAMP levels following PDE6H inhibition result in mitochondrial dysfunction and lowering of OXPHOS, we plan on testing how changes in cGMP levels correspond with changes in cAMP levels in *PDE6H* knockdown cells at various time-points. We will investigate PDE2 and PDE3 as regulators of cAMP levels in *PDE6H* ko HCT116 cells. Therefore, we are planning to use inhibitors against PDE2 and PDE3 on siPDE6H transfected cells as well as PDE6H ko HCT116 cells to test whether the changes in cAMP levels can be prevented following *PDE6H* knockdown and deletion, respectively. We also plan to test cAMP and cGMP levels in isolated mitochondria upon PDE6H depletion. A better understanding of cGMP/PKG signalling will help distinguish between its direct role or indirect effect through cAMP/PKA on mitochondrial morphology and function.

Recently, SponGee (sponge-inhibiting cGMP signalling) was developed to enable subcellular control of cGMP levels (Ros et al., 2019). This variant of PKG, from

which the kinase domain is excluded, can be used *in vitro* and *in vivo* to modify cGMP signalling without interacting with cAMP or cGMP producing/hydrolysing enzymes. We plan to express SponGee protein in cell lines, starting with HCT116 and investigate ways to target it to mitochondria as a means to control intracellular cGMP levels.

Elevating PKG signalling in cancer cells has therapeutic potential. Loss of PGK1 expression in SW480 colon cancer inhibited colony formation and induced apoptosis, while its overexpression decreases cellular levels of β-catenin cyclin D1 and increased p21 (Deguchi et al., 2004). Activation of PKG through phosphodiesterase inhibition downregulates β-catenin mRNA and protein levels (Piazza, 2016). The negative regulator of β-catenin, (adenomatous polyposis coli (APC), prevents colorectal cancer (Novellasdemunt et al., 2015). While the most commonly studied PDE inhibitors, those of PDE5 such as sildenafil and vardenafil, are suggested for colorectal cancer prevention and treatment (Yarla et al., 2019), these, have not concluded in a strong trend of chemotherapeutic potential. Therefore, to investigate if PKG is a key player in effects of PDE6H, rather than using PDE5 inhibitors, we plan to test the effect of PKG inhibition via KT5823 on proliferation of PDE6H ko cells.

We aim to test the effect of IMPDH inhibitor AVN-944 on siPDE6H transfected or zaprinast treated cells. This drug suppresses GTP production and levels of guanine-based nucleotides (Emmanuel et al., 2017) and might cause a greater cell cycle arrest than PDE6H inhibition alone. The drug MitoQ prevents MPT (Davidson et al., 2012). Comparing mitochondrial ROS production and cell viability MitoQ treated PDE6H ko with MitoQ treated PDE6H WT cells would inform us whether targeting MPT would elicit further sensitivity in PDE6H ko cells.

4. Xenografts

A more comprehensive animal experiment would entail a separate control group for the drug treatment experiment. A group with the 1% DMSO + PBS vehicle treatment would be included to account for the effect of intratumoural injection. This would allow

us to differentiate between the effect of the drug on tumour growth, both in size and shape, and that of the method of drug administration. Intratumoural injection of any liquid can potentially cause tumour collapse and restructuring, and it needs to be accounted for when investigating the chemical effect of the drug itself, and not its method of delivery. Zaprinast was used at a concentration much higher than what had been used *in vitro* studies (11 mM as opposed to 100 nM). Concentration of zaprinast administered was significantly greater than not only IC_{50} for PDE6 (150 nM) but also than those for PDE5 and PDE9. During our study, zaprinast treatment could have resulted in the inhibition of several PDEs, as well as other potential unknown targets. An improved experiment to study the effect of zaprinast on HCT116 tumour growth would include various concentrations of the drug. Treatment groups where zaprinast is injected to *PDE6H* knockout clone tumours would also be included in such a study. We are planning on resorting to oral or iv administration methods of zaprinast.

The antiproliferative effect of PDE6H depletion was verified through results from siPDE6H, CRISPR/Cas9 *PDE6H* knockout and PDE6 inhibiting drug zaprinast. Future plans include understanding effects of *PDE6H* induction on cancer cell proliferation and tumour growth.

5. Antibodies

Moving forward, issues regarding antibody specificity need to be resolved. Dual bands were observed at the PDE6H location might be due to the farnesylation modification of PDE6gamma. The farnesyl moiety can make the protein more hydrophobic and cause it to travel slower than the unmodified protein. Therefore, the upper band might indicate the protein with the farnesyl moiety. This can be checked by a pull-down assay for blotting with farnesyl antibody, using a farnesyl transferase inhibitor as a control. The extra band might also belong to PDE6G. Improved PDE6H antibodies that robustly stain formalin-fixed paraffin-embedded tissue specimens are needed to open up possibilities of clinical work to investigate PDE6H's role in primary

and secondary cancer formation. cDNA genomic sequencing of the *PDE6H* knockout clones also need to be conducted to ensure deletion within exon 2 of PDE6H.

B) Summarising PDE6H's control over cell cycle and metabolism

PDE6H depletion results in a decrease of cGMP specific PDE6 (Figure 7.1), which causes an accumulation of cGMP and lowering of GMP levels (a) (Azevedo et al., 2014).

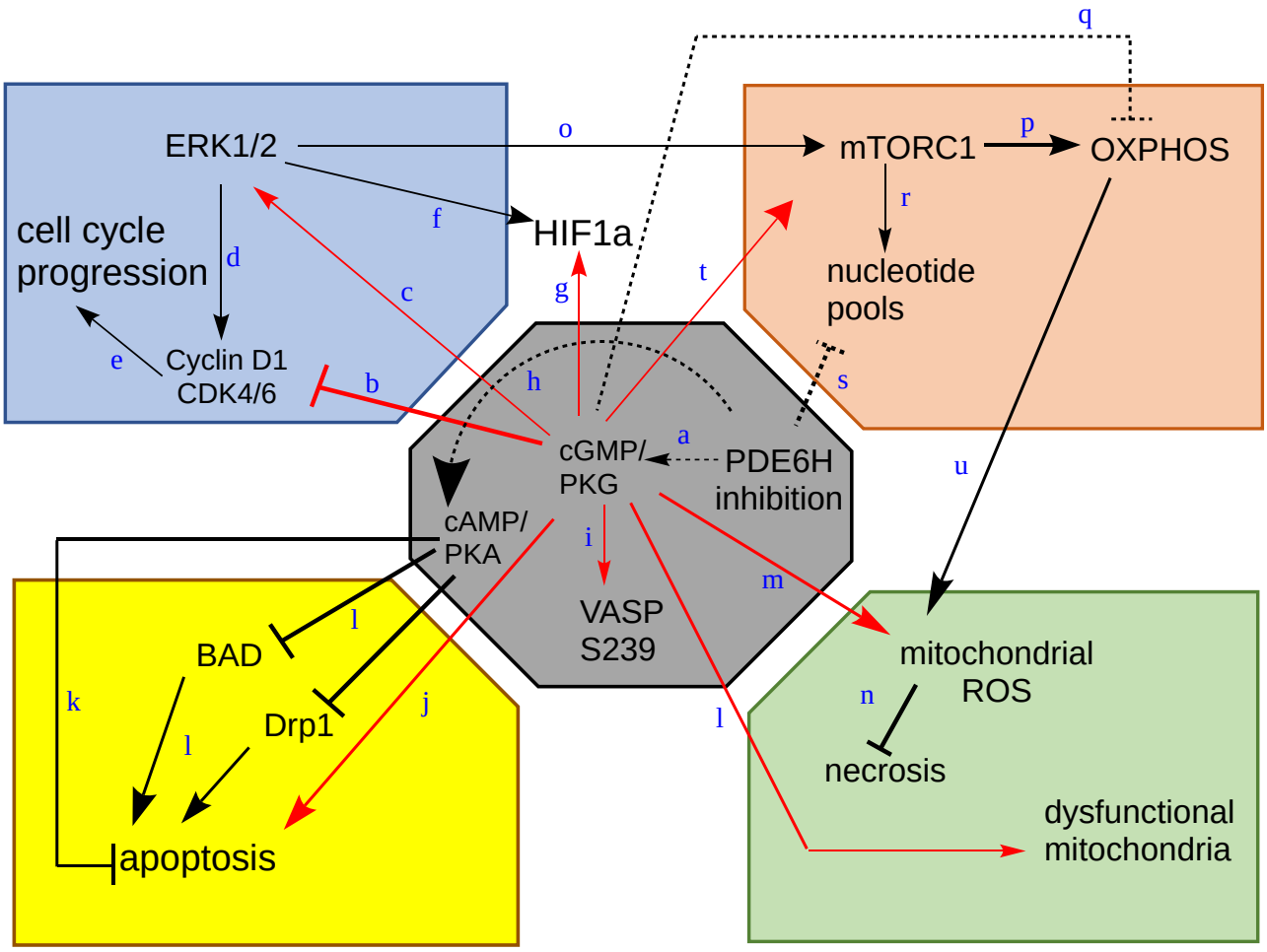


Figure 7.1: Working hypothesis on effect of PDE6H depletion on cell cycle progression, metabolism, mitochondrial function, and apoptosis.
Red arrows: results supported by literature and our results. Black arrows: results supported by literature. Dashed black arrows: results supported by our data.

Cell cycle progression

In vascular smooth muscle cells, cGMP inhibits cyclin D1 and CDK4 activation (b) (Fukumoto et al., 1999); this is in accordance with G1/S arrest caused by PDE6H depletion we observed. However, cGMP also results in activation of ERK1/2 pathway (c) (Zaragoza et al., 2002) which induces cyclin D1 expression (d) and is critical for G1 progression (e) (Lavoie et al., 1996) (Baldin et al., 1993). ERK1 is required for HIF-1α activation (f) (Sang et al., 2003).

cGMP/PKG signalling stabilises HIF-1α under normoxic conditions (g)

We also observed that *PDE6H* knockdown led to HIF-1α stabilisation in HCT116 cells, under normoxia. We know from literature that PKG inhibitor KT5823 suppresses the normoxic stabilisation of HIF-1α that is induced by membrane-type 1 matrix metalloproteinase (MT1-MMP)/Mint3 in HT1080 cells (Okajima et al., 2013). NO donors also lead to normoxic stimulation of HIF-1α in macrophages.

Pro-apoptotic effect of cGMP and anti-apoptotic effect of cAMP

A preliminary analysis of our mass spectroscopy results shows an increase in cAMP in PDE6H ko HCT116 clones compared to WT HCT116 (h). Since cGMP/PKG signalling affects PDE2 and PDE3 activity, cAMP/PKA signalling need to be taken into account when explaining effects of PDE6H depletion. We aim to understand the time-course and localisation of changes in cAMP and cGMP signalling upon PDE6H depletion, as described in section 7.A.3.

PKG activity, induced by cGMP analogues and measured by VASP-S239 phosphorylation (i), results in apoptosis in MDA-MB-468 cells (j) (Jackson and Ceresa, 2016). Inhibition of VASP phosphorylation at the cAMP site S157 by use of phosphomutants increased apoptosis (k), while a similar inhibition at the cGMP S239 site reduced apoptosis in human colon carcinoma cells (Ali et al., 2015). PKA activity

inactivates BAD (Harada et al., 1999) and Drp1 (Cribbs and Strack, 2007) (l), antagonising the apoptotic effect of cGMP.

Anti-necrotic role of cGMP through ROS production (m)

Although cGMP does not enter mitochondria, it turns on a signalling cascade across mitochondrial membranes. Mitochondrial permeability transition (MPT) pore opening occurs following calcium overload in response to oxidative stress (Davidson et al., 2012). cGMP is hypothesized to open mitoKATP by activating a PKG at the MOM, which then transmits the signal to a protein kinase C (PKC) at the IMM; the opening of mitoKATP results in increased K^+ uptake, increased ROS production (m) and the activation of a second PKC pool which ultimately inhibits MPT, reducing cell necrosis (n) (Costa et al., 2007). Increased cGMP production in cardiac cells by bradykinin or direct activation of PKG, also generates mitochondrial ROS and mitoKATP opening, (m) (Oldenburg et al., 2004).

mTORC1's control over OXPHOS and nucleotide synthesis (i, j)

ER1/2 mediates Raptor phosphorylation and activates mTORC1 (Carriere et al., 2011) (o). mTORC1 stimulates mitochondrial function (p) by inducing transcription of mitochondria-related mRNAs (Morita et al., 2013; Schieke et al., 2006), and protein expression of mitochondrial ETC complexes (Rosario et al., 2019). Therefore, the decrease in OXPHOS we observe upon PDE6H depletion (q) might result from mitochondrial dysfunction, despite the activation of mTORC1 due to ERK1/2 or cGMP/PKG activity.

mTORC1 stimulates glutamine dependent de novo purine production by upregulating pentose phosphate pathway (r) (Ben-Sahra et al., 2016). Acute purine depletion (e.g. AMP and GMP) (Hoxhaj et al., 2017) and sustained depletion of GTP leads to inhibition of mTORC1 (Emmanuel et al., 2017). We speculate that mTORC1

activation we observe in PDE6H depleted cells is important for replenishing the nucleotide pools that are depleted, considering the GMP levels should go down upon PDE6 inhibition (s).

PKG signalling activates mTORC1 (t) by direct phosphorylation of Raptor (Liu et al., 2018) and by phosphorylation of TSC2 that alleviates its inhibition of mTORC1 (Ranek et al., 2019).

Mitochondrial dysfunction and ROS production

There are several sites of ROS production (Brown and Borutaite, 2012), and in mitochondria complex 1 and 3 activity is a major source of superoxide production in mitochondria (Chen et al., 2003) (u). While potentially causing ATP deficit due to presence of dysfunctional mitochondria, a lowering of OXPHOS could also help sustain cell survival under mitochondrial ROS in PDE6H depleted cells. Increased cytosolic superoxide production is observed in p62 deficient cells where complex 1 activity is inhibited and mitochondrial membrane potential reduced (Bartolome et al., 2017). We plan to measure cellular ROS generation using dihydroethidium.

En route to targeted therapy, drug specificity is a challenge common to PDE inhibitors caused by the compensatory effect of PDE family members. Additionally, PDE6H depletion led to more hypoxic regions in the tumour, which might pose a challenge to radiotherapy. The dual effect of PDE6H depletion on preventing cancer cell proliferation and disrupting energy metabolism suggests that PDE6H would be a new target worth assessing. Our future work aims to understand how to maximise the effectiveness of PDE6H inhibition.

Bibliography

1. Abolhassani, N., Iyama, T., Tsuchimoto, D., Sakumi, K., Ohno, M., Behmanesh, M., and Nakabeppu, Y. (2010). NUDT16 and ITPA play a dual protective role in maintaining chromosome stability and cell growth by eliminating dIDP/IDP and dITP/ITP from nucleotide pools in mammals. Nucleic Acids Research *38*, 2891-2903.
2. Abu-Jamous, B., Buffa, F.M., Harris, A.L., and Nandi, A.K. (2017). In vitro downregulated hypoxia transcriptome is associated with poor prognosis in breast cancer. Molecular Cancer *16*.
3. Acharya, A., Das, I., Chandhok, D., and Saha, T. (2010). Redox Regulation in Cancer: A Double-edged Sword with Therapeutic Potential. Oxidative Medicine and Cellular Longevity *3*, 23-34.
4. Acin-Perez, R., Russwurm, M., Günnewig, K., Gertz, M., Zoidl, G., Ramos, L., Buck, J., Levin, L.R., Rassow, J., Manfredi, G., et al. (2011). A Phosphodiesterase 2A Isoform Localized to Mitochondria Regulates Respiration. Journal of Biological Chemistry *286*, 30423-30432.
5. Acin-Perez, R., Salazar, E., Kamenetsky, M., Buck, J., Levin, L.R., and Manfredi, G. (2009). Cyclic AMP Produced inside Mitochondria Regulates Oxidative Phosphorylation. Cell Metabolism *9*, 265-276.
6. Addgene (2017). CRISPR guide.
7. Adli, M. (2018). The CRISPR tool kit for genome editing and beyond. Nat Commun *9*, 1911.
8. Agathocleous, M., Love, N.K., Randlett, O., Harris, J.J., Liu, J., Murray, A.J., and Harris, W.A. (2012). Metabolic differentiation in the embryonic retina. Nature Cell Biology *14*, 859-864.
9. Akar, F., Mutlu, O., Celikyurt, I.K., Bektas, E., Tanyeri, M.H., Ulak, G., Tanyeri, P., and Erden, F. (2014). Effects of Zaprinast and Rolipram on Olfactory and Visual Memory in the Social Transmission of Food Preference and Novel Object Recognition Tests in Mice. Drug Target Insights *8*.
10. Ali, M., Rogers, L.K., and Pitari, G.M. (2015). Serine phosphorylation of vasodilator-stimulated phosphoprotein (VASP) regulates colon cancer cell survival and apoptosis. Life Sciences *123*, 1-8.
11. Almeida, A., Bolanos, J.P., and Moncada, S. (2010). E3 ubiquitin ligase APC/C-Cdh1 accounts for the Warburg effect by linking glycolysis to cell proliferation. Proceedings of the National Academy of Sciences of the United States of America *107*, 738-741.
12. Alves, C.L., Elias, D., Lyng, M., Bak, M., Kirkegaard, T., Lykkesfeldt, A.E., and Ditzel, H.J. (2016). High CDK6 Protects Cells from Fulvestrant-Mediated Apoptosis and is a Predictor of Resistance to Fulvestrant in Estrogen Receptor–Positive

Metastatic Breast Cancer. Clinical Cancer Research *22*, 5514-5526.
13. Anant, J.S., Ong, O.C., Xie, H.Y., Clarke, S., O'Brien, P.J., and Fung, B.K. (1992). In vivo differential prenylation of retinal cyclic GMP phosphodiesterase catalytic subunits. The Journal of biological chemistry *267*, 687-690.
14. Andersson, A., Ritz, C., Lindgren, D., Edén, P., Lassen, C., Heldrup, J., Olofsson, T., Råde, J., Fontes, M., Porwit-MacDonald, A., et al. (2007). Microarray-based classification of a consecutive series of 121 childhood acute leukemias: prediction of leukemic and genetic subtype as well as of minimal residual disease status. Leukemia *21*, 1198-1203.
15. Arshavsky, V.Y., Lamb, T.D., and Pugh, E.N. (2002). G Proteins and Phototransduction. Annual Review of Physiology *64*, 153-187.
16. Ashton, T.M., Fokas, E., Kunz-Schughart, L.A., Folkes, L.K., Anbalagan, S., Huether, M., Kelly, C.J., Pirovano, G., Buffa, F.M., Hammond, E.M., et al. (2016). The anti-malarial atovaquone increases radiosensitivity by alleviating tumour hypoxia. Nature Communications *7*.
17. Atlas), T.T.C.G. (2011a). The Cancer Genome Atlas - Colon and Rectum Adenocarcinoma Gene Expression Data
18. Atlas), T.T.C.G. (2011b). The Cancer Genome Atlas - Invasive Breast Carcinoma Gene Expression Data.
19. Atsumi, T., Chesney, J., Metz, C., Leng, L., Donnelly, S., Makita, Z., Mitchell, R., and Bucala, R. (2002). High expression of inducible 6-phosphofructo-2-kinase/fructose-2, 6-bisphosphatase (iPFK-2; PFKFB3) in human cancers. Cancer research *62*, 5881-5887.
20. Aubrey, B.J., Kelly, G.L., Janic, A., Herold, M.J., and Strasser, A. (2017). How does p53 induce apoptosis and how does this relate to p53-mediated tumour suppression? Cell Death and Differentiation *25*, 104-113.
21. Azevedo, M.F., Faucz, F.R., Bimpaki, E., Horvath, A., Levy, I., de Alexandre, R.B., Ahmad, F., Manganiello, V., and Stratakis, C.A. (2014). Clinical and Molecular Genetics of the Phosphodiesterases (PDEs). Endocrine Reviews *35*, 195-233.
22. Bailey, M.J., Beremand, P.D., Hammer, R., Reidel, E., Thomas, T.L., and Cassone, V.M. (2004). Transcriptional Profiling of Circadian Patterns of mRNA Expression in the Chick Retina. Journal of Biological Chemistry *279*, 52247-52254.
23. Baldin, V., Lukas, J., Marcote, M.J., Pagano, M., and Draetta, G. (1993). Cyclin D1 is a nuclear protein required for cell cycle progression in G1. Genes Dev *7*, 812-821.
24. Bao, Y., Mukai, K., Hishiki, T., Kubo, A., Ohmura, M., Sugiura, Y., Matsuura, T., Nagahata, Y., Hayakawa, N., Yamamoto, T., et al. (2013). Energy management by enhanced glycolysis in G1-phase in human colon cancer cells in vitro and in vivo. Mol Cancer Res *11*, 973-985.
25. Barren, B., Gakhar, L., Muradov, H., Boyd, K.K., Ramaswamy, S., and Artemyev, N.O. (2009). Structural basis of phosphodiesterase 6 inhibition by the C-terminal region of the γ-subunit. The EMBO Journal *28*, 3613-3622.
26. Bartolome, F., Esteras, N., Martin-Requero, A., Boutoleau-Bretonniere, C., Vercelletto, M., Gabelle, A., Le Ber, I., Honda, T., Dinkova-Kostova, A.T., Hardy, J., et al. (2017). Pathogenic p62/SQSTM1 mutations impair energy metabolism through limitation of mitochondrial substrates. Sci Rep *7*, 1666.
27. Basso, K., Margolin, A.A., Stolovitzky, G., Klein, U., Dalla-Favera, R., and Califano, A. (2005). Reverse engineering of regulatory networks in human B cells. Nature Genetics *37*, 382-390.

28. Beavo, J.A., Francis, S.H., and Houslay, M.D. (2006). Cyclic nucleotide phosphodiesterases in health and disease.
29. Beer, D.G., Kardia, S.L.R., Huang, C.-C., Giordano, T.J., Levin, A.M., Misek, D.E., Lin, L., Chen, G., Gharib, T.G., Thomas, D.G., et al. (2002). Gene-expression profiles predict survival of patients with lung adenocarcinoma. Nature Medicine *8*, 816-824.
30. Ben-Sahra, I., Hoxhaj, G., Ricoult, S.J.H., Asara, J.M., and Manning, B.D. (2016). mTORC1 induces purine synthesis through control of the mitochondrial tetrahydrofolate cycle. Science *351*, 728-733.
31. Ben-Sahra, I., and Manning, B.D. (2017). mTORC1 signaling and the metabolic control of cell growth. Current opinion in cell biology *45*, 72-82.
32. Bender, D.A. (2003). Oxidative Phosphorylation. 4295-4301.
33. Bensaad, K., Favaro, E., Lewis, Caroline A., Peck, B., Lord, S., Collins, Jennifer M., Pinnick, Katherine E., Wigfield, S., Buffa, Francesca M., Li, J.-L., et al. (2014). Fatty Acid Uptake and Lipid Storage Induced by HIF-1α Contribute to Cell Growth and Survival after Hypoxia-Reoxygenation. Cell Reports *9*, 349-365.
34. Bensaad, K., and Harris, A.L. (2014). Hypoxia and Metabolism in Cancer. *772*, 1-39.
35. Bensaad, K., Tsuruta, A., Selak, M.A., Vidal, M.N.C., Nakano, K., Bartrons, R., Gottlieb, E., and Vousden, K.H. (2006). TIGAR, a p53-Inducible Regulator of Glycolysis and Apoptosis. Cell *126*, 107-120.
36. Berg JM, T.J., Stryer L. (2002). Purine Bases Can Be Synthesized de Novo or Recycled by Salvage Pathways. In Biochemistry, 5th edition (New York: W H Freeman).
37. Bhattacharjee, A., Richards, W.G., Staunton, J., Li, C., Monti, S., Vasa, P., Ladd, C., Beheshti, J., Bueno, R., Gillette, M., et al. (2001). Classification of human lung carcinomas by mRNA expression profiling reveals distinct adenocarcinoma subclasses. Proceedings of the National Academy of Sciences *98*, 13790-13795.
38. Bhutia, Y.D., Babu, E., Ramachandran, S., and Ganapathy, V. (2015). Amino Acid Transporters in Cancer and Their Relevance to "Glutamine Addiction": Novel Targets for the Design of a New Class of Anticancer Drugs. Cancer Research *75*, 1782-1788.
39. Birmingham, A., Anderson, E.M., Reynolds, A., Ilsley-Tyree, D., Leake, D., Fedorov, Y., Baskerville, S., Maksimova, E., Robinson, K., Karpilow, J., et al. (2006). 3′ UTR seed matches, but not overall identity, are associated with RNAi off-targets. Nature Methods *3*, 199-204.
40. Birsoy, K., Wang, T., Chen, W.W., Freinkman, E., Abu-Remaileh, M., and Sabatini, D.M. (2015). An essential role of the mitochondrial electron transport chain in cell proliferation is to enable aspartate synthesis. Cell *162*, 540-551.
41. Blagosklonny, M.V. (2011). Cell cycle arrest is not senescence. Aging *3*, 94-101.
42. Blaveri, E. (2005). Bladder Cancer Outcome and Subtype Classification by Gene Expression. Clinical Cancer Research *11*, 4044-4055.
43. Bougnoux, P., Hajjaji, N., Maheo, K., Couet, C., and Chevalier, S. (2010). Fatty acids and breast cancer: Sensitization to treatments and prevention of metastatic re-growth. Progress in Lipid Research *49*, 76-86.
44. Bredel, M., Bredel, C., Juric, D., Harsh, G.R., Vogel, H., Recht, L.D., and Sikic, B.I. (2005). Functional Network Analysis Reveals Extended Gliomagenesis Pathway Maps and Three Novel MYC-Interacting Genes in Human Gliomas. Cancer Research

65, 8679-8689.
45. Bremner, R., and Sage, J. (2014). Cancer: The origin of human retinoblastoma. Nature *514*, 312-313.
46. Brennenstuhl, C., Tanimoto, N., Burkard, M., Wagner, R., Bolz, S., Trifunovic, D., Kabagema-Bilan, C., Paquet-Durand, F., Beck, S.C., Huber, G., et al. (2015). Targeted Ablation of the Pde6h Gene in Mice Reveals Cross-species Differences in Cone and Rod Phototransduction Protein Isoform Inventory. Journal of Biological Chemistry *290*, 10242-10255.
47. Bretones, G., Delgado, M.D., and León, J. (2015). Myc and cell cycle control. Biochimica et Biophysica Acta (BBA) - Gene Regulatory Mechanisms *1849*, 506-516.
48. Bric, A., Miething, C., Bialucha, C.U., Scuoppo, C., Zender, L., Krasnitz, A., Xuan, Z., Zuber, J., Wigler, M., Hicks, J., et al. (2009). Functional Identification of Tumor-Suppressor Genes through an In Vivo RNA Interference Screen in a Mouse Lymphoma Model. Cancer Cell *16*, 324-335.
49. Brown, G.C., and Borutaite, V. (2012). There is no evidence that mitochondria are the main source of reactive oxygen species in mammalian cells. Mitochondrion *12*, 1-4.
50. Busino, L., Chiesa, M., Draetta, G.F., and Donzelli, M. (2004). Cdc25A phosphatase: combinatorial phosphorylation, ubiquitylation and proteolysis. Oncogene *23*, 2050-2056.
51. Cai, L., and Tu, B.P. (2012). Driving the cell cycle through metabolism. Annu Rev Cell Dev Biol *28*, 59-87.
52. Cairns, R.A., Harris, I.S., and Mak, T.W. (2011). Regulation of cancer cell metabolism. Nature Reviews Cancer *11*, 85-95.
53. Calvert, P.D., Strissel, K.J., Schiesser, W.E., Pugh, E.N., and Arshavsky, V.Y. (2006). Light-driven translocation of signaling proteins in vertebrate photoreceptors. Trends in Cell Biology *16*, 560-568.
54. Cantor, J.R., and Sabatini, D.M. (2012). Cancer Cell Metabolism: One Hallmark, Many Faces. Cancer Discovery *2*, 881-898.
55. Carracedo, A., Cantley, L.C., and Pandolfi, P.P. (2013). Cancer metabolism: fatty acid oxidation in the limelight. Nature Reviews Cancer *13*, 227-232.
56. Carriere, A., Romeo, Y., Acosta-Jaquez, H.A., Moreau, J., Bonneil, E., Thibault, P., Fingar, D.C., and Roux, P.P. (2011). ERK1/2 Phosphorylate Raptor to Promote Ras-dependent Activation of mTOR Complex 1 (mTORC1). Journal of Biological Chemistry *286*, 567-577.
57. Cascone, T., McKenzie, J.A., Mbofung, R.M., Punt, S., Wang, Z., Xu, C., Williams, L.J., Wang, Z., Bristow, C.A., Carugo, A., et al. (2018). Increased Tumor Glycolysis Characterizes Immune Resistance to Adoptive T Cell Therapy. Cell Metabolism *27*, 977-987.e974.
58. Chang, H.Y., Yu, K., Ganesan, K., Tan, L.K., Laban, M., Wu, J., Zhao, X.D., Li, H., Leung, C.H.W., Zhu, Y., et al. (2008). A Precisely Regulated Gene Expression Cassette Potently Modulates Metastasis and Survival in Multiple Solid Cancers. PLoS Genetics *4*.
59. Chen, Q., Vazquez, E.J., Moghaddas, S., Hoppel, C.L., and Lesnefsky, E.J. (2003). Production of reactive oxygen species by mitochondria: central role of complex III. J Biol Chem *278*, 36027-36031.
60. Chiarugi, P., and Cirri, P. (2016). Metabolic exchanges within tumor microenvironment. Cancer Letters *380*, 272-280.
61. Cho, S.W., Kim, S., Kim, Y., Kweon, J., Kim, H.S., Bae, S., and Kim, J.S.

(2013). Analysis of off-target effects of CRISPR/Cas-derived RNA-guided endonucleases and nickases. Genome Research *24*, 132-141.
62. Chou, A., Froio, D., Nagrial, A.M., Parkin, A., Murphy, K.J., Chin, V.T., Wohl, D., Steinmann, A., Stark, R., Drury, A., et al. (2018). Tailored first-line and second-line CDK4-targeting treatment combinations in mouse models of pancreatic cancer. Gut *67*, 2142-2155.
63. Christofk, H.R., Vander Heiden, M.G., Harris, M.H., Ramanathan, A., Gerszten, R.E., Wei, R., Fleming, M.D., Schreiber, S.L., and Cantley, L.C. (2008a). The M2 splice isoform of pyruvate kinase is important for cancer metabolism and tumour growth. Nature *452*, 230.
64. Christofk, H.R., Vander Heiden, M.G., Wu, N., Asara, J.M., and Cantley, L.C. (2008b). Pyruvate kinase M2 is a phosphotyrosine-binding protein. Nature *452*, 181-186.
65. Chuang, H.-Y., Chang, Y.-F., and Hwang, J.-J. (2011). Antitumor effect of orlistat, a fatty acid synthase inhibitor, is via activation of caspase-3 on human colorectal carcinoma-bearing animal. Biomedicine & Pharmacotherapy *65*, 286-292.
66. Chumakov, S., Ballesteros, E., Rodriguez Sanchez, J.E., Chavez, A., Zhang, M., Pettit, B.M., and Fofanov, Y. (2006). Using Mutual Information to Discover Temporal Patterns in Gene Expression Data. In AIP Conference Proceedings, pp. 25-30.
67. Collins, I., and Garrett, M.D. (2005). Targeting the cell division cycle in cancer: CDK and cell cycle checkpoint kinase inhibitors. Curr Opin Pharmacol *5*, 366-373.
68. Colombo, S.L., Palacios-Callender, M., Frakich, N., Carcamo, S., Kovacs, I., Tudzarova, S., and Moncada, S. (2011). Molecular basis for the differential use of glucose and glutamine in cell proliferation as revealed by synchronized HeLa cells. Proceedings of the National Academy of Sciences of the United States of America *108*, 21069-21074.
69. Colombo, S.L., Palacios-Callender, M., Frakich, N., De Leon, J., Schmitt, C.A., Boorn, L., Davis, N., and Moncada, S. (2010). Anaphase-promoting complex/cyclosome-Cdh1 coordinates glycolysis and glutaminolysis with transition to S phase in human T lymphocytes. Proceedings of the National Academy of Sciences of the United States of America *107*, 18868-18873.
70. Commisso, C., Davidson, S.M., Soydaner-Azeloglu, R.G., Parker, S.J., Kamphorst, J.J., Hackett, S., Grabocka, E., Nofal, M., Drebin, J.A., Thompson, C.B., et al. (2013). Macropinocytosis of protein is an amino acid supply route in Ras-transformed cells. Nature *497*, 633-637.
71. Coppé, J.-P., Desprez, P.-Y., Krtolica, A., and Campisi, J. (2010). The Senescence-Associated Secretory Phenotype: The Dark Side of Tumor Suppression. Annual Review of Pathology: Mechanisms of Disease *5*, 99-118.
72. Costa, A., Scholer-Dahirel, A., and Mechta-Grigoriou, F. (2014). The role of reactive oxygen species and metabolism on cancer cells and their microenvironment. Seminars in Cancer Biology *25*, 23-32.
73. Costa, A.D.T., Garlid, K.D., West, I.C., Lincoln, T.M., Downey, J.M., Cohen, M.V., and Critz, S.D. (2005). Protein Kinase G Transmits the Cardioprotective Signal From Cytosol to Mitochondria. Circulation Research *97*, 329-336.
74. Costa, A.D.T., Pierre, S.V., Cohen, M.V., Downey, J.M., and Garlid, K.D. (2007). cGMP signalling in pre- and post-conditioning: the role of mitochondria. Cardiovascular Research *77*, 344-352.
75. Cribbs, J.T., and Strack, S. (2007). Reversible phosphorylation of Drp1 by cyclic

AMP-dependent protein kinase and calcineurin regulates mitochondrial fission and cell death. EMBO reports *8*, 939-944.
76. Cutcliffe, C. (2005). Clear Cell Sarcoma of the Kidney: Up-regulation of Neural Markers with Activation of the Sonic Hedgehog and Akt Pathways. Clinical Cancer Research *11*, 7986-7994.
77. Dang, C.V. (2013). MYC, metabolism, cell growth, and tumorigenesis. Cold Spring Harb Perspect Med *3*.
78. Dang, L., White, D.W., Gross, S., Bennett, B.D., Bittinger, M.A., Driggers, E.M., Fantin, V.R., Jang, H.G., Jin, S., Keenan, M.C., et al. (2009). Cancer-associated IDH1 mutations produce 2-hydroxyglutarate. Nature *462*, 739-744.
79. Davidson, Shawn M., Papagiannakopoulos, T., Olenchock, Benjamin A., Heyman, Julia E., Keibler, Mark A., Luengo, A., Bauer, Matthew R., Jha, Abhishek K., O'Brien, James P., Pierce, Kerry A., et al. (2016). Environment Impacts the Metabolic Dependencies of Ras-Driven Non-Small Cell Lung Cancer. Cell Metabolism *23*, 517-528.
80. Davidson, S.M., Yellon, D.M., Murphy, M.P., and Duchen, M.R. (2012). Slow calcium waves and redox changes precede mitochondrial permeability transition pore opening in the intact heart during hypoxia and reoxygenation. Cardiovasc Res *93*, 445-453.
81. De Saedeleer, C.J., Porporato, P.E., Copetti, T., Perez-Escuredo, J., Payen, V.L., Brisson, L., Feron, O., and Sonveaux, P. (2014). Glucose deprivation increases monocarboxylate transporter 1 (MCT1) expression and MCT1-dependent tumor cell migration. Oncogene *33*, 4060-4068.
82. DeBerardinis, R.J., Mancuso, A., Daikhin, E., Nissim, I., Yudkoff, M., Wehrli, S., and Thompson, C.B. (2007). Beyond aerobic glycolysis: transformed cells can engage in glutamine metabolism that exceeds the requirement for protein and nucleotide synthesis. Proceedings of the National Academy of Sciences *104*, 19345-19350.
83. Deguchi, A., Thompson, W.J., and Weinstein, I.B. (2004). Activation of Protein Kinase G Is Sufficient to Induce Apoptosis and Inhibit Cell Migration in Colon Cancer Cells. Cancer Research *64*, 3966-3973.
84. Demidenko, Z.N., Korotchkina, L.G., Gudkov, A.V., and Blagosklonny, M.V. (2010). Paradoxical suppression of cellular senescence by p53. Proceedings of the National Academy of Sciences *107*, 9660-9664.
85. Demidenko, Z.N., Zubova, S.G., Bukreeva, E.I., Pospelov, V.A., Pospelova, T.V., and Blagosklonny, M.V. (2014). Rapamycin decelerates cellular senescence. Cell Cycle *8*, 1888-1895.
86. DeNicola, G.M., Karreth, F.A., Humpton, T.J., Gopinathan, A., Wei, C., Frese, K., Mangal, D., Kenneth, H.Y., Yeo, C.J., and Calhoun, E.S. (2011). Oncogene-induced Nrf2 transcription promotes ROS detoxification and tumorigenesis. Nature *475*, 106.
87. Denko, N.C. (2008). Hypoxia, HIF1 and glucose metabolism in the solid tumour. Nat Rev Cancer *8*, 705-713.
88. Dharmacon (2014). Dharmacon: Reverse Transfection of siRNA.
89. Dharmacon (2018). DharmaFECT Transfection Reagent Cell Type Guide.
90. Diaz-Ruiz, R., Rigoulet, M., and Devin, A. (2011). The Warburg and Crabtree effects: On the origin of cancer cell energy metabolism and of yeast glucose repression. Biochimica et biophysica acta *1807*, 568-576.
91. Di Benedetto, G., Scalzotto, E., Mongillo, M., and Pozzan, T. (2013). Mitochondrial Ca2+ Uptake Induces Cyclic AMP Generation in the Matrix and

Modulates Organelle ATP Levels. Cell Metabolism *17*, 965-975.
92. Dolfi, S.C., Chan, L.L.-Y., Qiu, J., Tedeschi, P.M., Bertino, J.R., Hirshfield, K.M., Oltvai, Z.N., and Vazquez, A. (2013). The metabolic demands of cancer cells are coupled to their size and protein synthesis rates. Cancer & Metabolism *1*.
93. Dong, H., Claffey, K.P., Brocke, S., and Epstein, P.M. (2013). Expression of phosphodiesterase 6 (PDE6) in human breast cancer cells. SpringerPlus *2*, 680.
94. Dreger, H., Westphal, K., Weller, A., Baumann, G., Stangl, V., Meiners, S., and Stangl, K. (2009). Nrf2-dependent upregulation of antioxidative enzymes: a novel pathway for proteasome inhibitor-mediated cardioprotection. Cardiovascular research *83*, 354-361.
95. Du, W., Jiang, P., Mancuso, A., Stonestrom, A., Brewer, M.D., Minn, A.J., Mak, T.W., Wu, M., and Yang, X. (2013). TAp73 enhances the pentose phosphate pathway and supports cell proliferation. Nature Cell Biology *15*, 991-1000.
96. Duan, G., Shi, M., Xie, L., Xu, M., Wang, Y., Yan, H., Zhuge, Y., and Zou, X. (2018). Increased Glutamine Consumption in Cisplatin-Resistant Cells Has a Negative Impact on Cell Growth. Scientific Reports *8*.
97. Duan, S., and Pagano, M. (2011). Linking metabolism and cell cycle progression via the APC/CCdh1 and SCFbetaTrCP ubiquitin ligases. Proceedings of the National Academy of Sciences of the United States of America *108*, 20857-20858.
98. Dulic, V. (2011). Be quiet and you'll keep young: does mTOR underlie p53 action in protecting against senescence by favoring quiescence? Aging *3*, 3-4.
99. Dürig, J., Bug, S., Klein-Hitpass, L., Boes, T., Jöns, T., Martin-Subero, J.I., Harder, L., Baudis, M., Dührsen, U., and Siebert, R. (2007). Combined single nucleotide polymorphism-based genomic mapping and global gene expression profiling identifies novel chromosomal imbalances, mechanisms and candidate genes important in the pathogenesis of T-cell prolymphocytic leukemia with inv(14)(q11q32). Leukemia *21*, 2153-2163.
100. D'Errico, M., Rinaldis, E.d., Blasi, M.F., Viti, V., Falchetti, M., Calcagnile, A., Sera, F., Saieva, C., Ottini, L., Palli, D., et al. (2009). Genome-wide expression profile of sporadic gastric cancers with microsatellite instability. European Journal of Cancer *45*, 461-469.
101. Elhammali, A., Ippolito, J.E., Collins, L., Crowley, J., Marasa, J., and Piwnica-Worms, D. (2014). A High-Throughput Fluorimetric Assay for 2-Hydroxyglutarate Identifies Zaprinast as a Glutaminase Inhibitor. Cancer Discovery *4*, 828-839.
102. Emmanuel, N., Ragunathan, S., Shan, Q., Wang, F., Giannakou, A., Huser, N., Jin, G., Myers, J., Abraham, R.T., and Unsal-Kacmaz, K. (2017). Purine Nucleotide Availability Regulates mTORC1 Activity through the Rheb GTPase. Cell Reports *19*, 2665-2680.
103. Eom, T.-Y., and Jope, R.S. (2009). GSK3β N-terminus binding to p53 promotes its acetylation. Molecular Cancer *8*.
104. Favot, L., Keravis, T., and Lugnier, C. (2004). Modulation of VEGF-induced endothelial cell cycle protein expression through cyclic AMP hydrolysis by PDE2 and PDE4. Thrombosis and Haemostasis.
105. Fiori, M.E., Di Franco, S., Villanova, L., Bianca, P., Stassi, G., and De Maria, R. (2019). Cancer-associated fibroblasts as abettors of tumor progression at the crossroads of EMT and therapy resistance. Molecular Cancer *18*.
106. Fiske, B.P., and Vander Heiden, M.G. (2012). Seeing the Warburg effect in the developing retina. Nature Cell Biology *14*, 790-791.
107. FlowJo (2018). FlowJo v10.0.7 Documentation. Graphs and Gating.

108. Fogal, V., Richardson, A.D., Karmali, P.P., Scheffler, I.E., Smith, J.W., and Ruoslahti, E. (2010). Mitochondrial p32 protein is a critical regulator of tumor metabolism via maintenance of oxidative phosphorylation. Molecular and cellular biology *30*, 1303-1318.
109. Franco, J., Balaji, U., Freinkman, E., Witkiewicz, Agnieszka K., and Knudsen, Erik S. (2016). Metabolic Reprogramming of Pancreatic Cancer Mediated by CDK4/6 Inhibition Elicits Unique Vulnerabilities. Cell Reports *14*, 979-990.
110. Frierson, H.F., El-Naggar, A.K., Welsh, J.B., Sapinoso, L.M., Su, A.I., Cheng, J., Saku, T., Moskaluk, C.A., and Hampton, G.M. (2002). Large Scale Molecular Analysis Identifies Genes with Altered Expression in Salivary Adenoid Cystic Carcinoma. The American Journal of Pathology *161*, 1315-1323.
111. Fritz, V., and Fajas, L. (2010). Metabolism and proliferation share common regulatory pathways in cancer cells. Oncogene *29*, 4369-4377.
112. Fry, D.C., and Vassilev, L.T. (2005). Targeting protein-protein interactions for cancer therapy. J Mol Med (Berl) *83*, 955-963.
113. Fujiwara, S., Kawano, Y., Yuki, H., Okuno, Y., Nosaka, K., Mitsuya, H., and Hata, H. (2012). PDK1 inhibition is a novel therapeutic target in multiple myeloma. British Journal of Cancer *108*, 170-178.
114. Fukami-Kobayashi, J., and Mitsui, Y. (1999). Cyclin D1 inhibits cell proliferation through binding to PCNA and cdk2. Exp Cell Res *246*, 338-347.
115. Fukumoto, S., Koyama, H., Hosoi, M., Yamakawa, K., Tanaka, S., Morii, H., and Nishizawa, Y. (1999). Distinct role of cAMP and cGMP in the cell cycle control of vascular smooth muscle cells: cGMP delays cell cycle transition through suppression of cyclin D1 and cyclin-dependent kinase 4 activation. Circ Res *85*, 985-991.
116. Furse, S., and Shearman, G.C. (2018). Do lipids shape the eukaryotic cell cycle? Biochimica et Biophysica Acta (BBA) - Molecular and Cell Biology of Lipids *1863*, 9-19.
117. Gaedcke, J., Grade, M., Jung, K., Camps, J., Jo, P., Emons, G., Gehoff, A., Sax, U., Schirmer, M., Becker, H., et al. (2010). Mutated KRAS results in overexpression of DUSP4, a MAP-kinase phosphatase, and SMYD3, a histone methyltransferase, in rectal carcinomas. Genes, Chromosomes and Cancer *49*, 1024-1034.
118. Gallagher, E.J., and LeRoith, D. (2011). Diabetes, cancer, and metformin: connections of metabolism and cell proliferation. Annals of the New York Academy of Sciences *1243*, 54-68.
119. Gallo, E.F., and Iadecola, C. (2011). Neuronal Nitric Oxide Contributes to Neuroplasticity-Associated Protein Expression through cGMP, Protein Kinase G, and Extracellular Signal-Regulated Kinase. Journal of Neuroscience *31*, 6947-6955.
120. Gao, J., Aksoy, B.A., Dogrusoz, U., Dresdner, G., Gross, B., Sumer, S.O., Sun, Y., Jacobsen, A., Sinha, R., Larsson, E., et al. (2013). Integrative Analysis of Complex Cancer Genomics and Clinical Profiles Using the cBioPortal. Science Signaling *6*, pl1-pl1.
121. Garcia-Bermudez, J., Baudrier, L., La, K., Zhu, X.G., Fidelin, J., Sviderskiy, V.O., Papagiannakopoulos, T., Molina, H., Snuderl, M., and Lewis, C.A. (2018). Aspartate is a limiting metabolite for cancer cell proliferation under hypoxia and in tumours. Nature cell biology *20*, 775.
122. Garcia-Cao, I., Song, M.S., Hobbs, R.M., Laurent, G., Giorgi, C., De Boer, V.C.J., Anastasiou, D., Ito, K., Sasaki, A.T., and Rameh, L. (2012). Systemic elevation of PTEN induces a tumor-suppressive metabolic state. Cell *149*, 49-62.

123. Gartel, A.L., Ye, X., Goufman, E., Shianov, P., Hay, N., Najmabadi, F., and Tyner, A.L. (2001). Myc represses the p21(WAF1/CIP1) promoter and interacts with Sp1/Sp3. Proceedings of the National Academy of Sciences *98*, 4510-4515.
124. Gogvadze, V., Orrenius, S., and Zhivotovsky, B. (2008). Mitochondria in cancer cells: what is so special about them? Trends in Cell Biology *18*, 165-173.
125. Gopalakrishna, K.N., Boyd, K., Yadav, R.P., and Artemyev, N.O. (2016). Aryl Hydrocarbon Receptor-interacting Protein-like 1 Is an Obligate Chaperone of Phosphodiesterase 6 and Is Assisted by the γ-Subunit of Its Client. Journal of Biological Chemistry *291*, 16282-16291.
126. Gray, J.V., Petsko, G.A., Johnston, G.C., Ringe, D., Singer, R.A., and Werner-Washburne, M. (2004). "Sleeping Beauty": Quiescence in Saccharomyces cerevisiae. Microbiology and Molecular Biology Reviews *68*, 187-206.
127. Gray, L.H., Conger, A.D., Ebert, M., Hornsey, S., and Scott, O.C.A. (1953). The Concentration of Oxygen Dissolved in Tissues at the Time of Irradiation as a Factor in Radiotherapy. The British Journal of Radiology *26*, 638-648.
128. Graziano, F., Ruzzo, A., Giacomini, E., Ricciardi, T., Aprile, G., Loupakis, F., Lorenzini, P., Ongaro, E., Zoratto, F., Catalano, V., et al. (2016). Glycolysis gene expression analysis and selective metabolic advantage in the clinical progression of colorectal cancer. The Pharmacogenomics Journal *17*, 258-264.
129. Grimes, D.R., Kannan, P., McIntyre, A., Kavanagh, A., Siddiky, A., Wigfield, S., Harris, A., and Partridge, M. (2016). The role of oxygen in avascular tumor growth. PloS one *11*, e0153692.
130. Gueven, N., Rose, S., Frye, R.E., Slattery, J., Wynne, R., Tippett, M., Pavliv, O., Melnyk, S., and James, S.J. (2014). Oxidative Stress Induces Mitochondrial Dysfunction in a Subset of Autism Lymphoblastoid Cell Lines in a Well-Matched Case Control Cohort. PLoS ONE *9*.
131. Gumz, M.L., Zou, H., Kreinest, P.A., Childs, A.C., Belmonte, L.S., LeGrand, S.N., Wu, K.J., Luxon, B.A., Sinha, M., Parker, A.S., et al. (2007). Secreted Frizzled-Related Protein 1 Loss Contributes to Tumor Phenotype of Clear Cell Renal Cell Carcinoma. Clinical Cancer Research *13*, 4740-4749.
132. Guo, J.Y., Karsli-Uzunbas, G., Mathew, R., Aisner, S.C., Kamphorst, J.J., Strohecker, A.M., Chen, G., Price, S., Lu, W., and Teng, X. (2013). Autophagy suppresses progression of K-ras-induced lung tumors to oncocytomas and maintains lipid homeostasis. Genes & development *27*, 1447-1461.
133. Guo, L.-W., Muradov, H., Hajipour, A.R., Sievert, M.K., Artemyev, N.O., and Ruoho, A.E. (2006). The Inhibitory γ Subunit of the Rod cGMP Phosphodiesterase Binds the Catalytic Subunits in an Extended Linear Structure. Journal of Biological Chemistry *281*, 15412-15422.
134. Guo, L.W., and Ruoho, A.E. (2008). The retinal cGMP phosphodiesterase gamma-subunit - a chameleon. Curr Protein Pept Sci *9*, 611-625.
135. Gutmann, D.H., Hedrick, N.M., Li, J., Nagarajan, R., Perry, A., and Watson, M.A. (2002). Comparative gene expression profile analysis of neurofibromatosis 1-associated and sporadic pilocytic astrocytomas. Cancer Res *62*, 2085-2091.
136. Haider, S., McIntyre, A., van Stiphout, R.G.P.M., Winchester, L.M., Wigfield, S., Harris, A.L., and Buffa, F.M. (2016). Genomic alterations underlie a pan-cancer metabolic shift associated with tumour hypoxia. Genome Biology *17*.
137. Halliwell, B. (2006). Oxidative stress and neurodegeneration: where are we now? Journal of Neurochemistry *97*, 1634-1658.
138. Hamanaka, R.B., and Chandel, N.S. (2012). Targeting glucose metabolism for

cancer therapy. J Exp Med *209*, 211-215.
139. Hanahan, D., and Weinberg, R.A. (2011). Hallmarks of cancer: the next generation. Cell *144*, 646-674.
140. Hao, Y., Triadafilopoulos, G., Sahbaie, P., Young, H.S., Omary, M.B., and Lowe, A.W. (2006). Gene Expression Profiling Reveals Stromal Genes Expressed in Common Between Barrett's Esophagus and Adenocarcinoma. Gastroenterology *131*, 925-933.
141. Harada, H., Becknell, B., Wilm, M., Mann, M., Huang, L.J., Taylor, S.S., Scott, J.D., and Korsmeyer, S.J. (1999). Phosphorylation and inactivation of BAD by mitochondria-anchored protein kinase A. Mol Cell *3*, 413-422.
142. Harris, A.L. (2002). Hypoxia — a key regulatory factor in tumour growth. Nature Reviews Cancer *2*, 38-47.
143. Harvey, C.J., Thimmulappa, R.K., Singh, A., Blake, D.J., Ling, G., Wakabayashi, N., Fujii, J., Myers, A., and Biswal, S. (2009). Nrf2-regulated glutathione recycling independent of biosynthesis is critical for cell survival during oxidative stress. Free Radical Biology and Medicine *46*, 443-453.
144. Haugh, L.M., Linsenmeier, R.A., and Goldstick, T.K. (1990). Mathematical models of the spatial distribution of retinal oxygen tension and consumption, including changes upon illumination. Annals of Biomedical Engineering *18*, 19-36.
145. He, G., Siddik, Z.H., Huang, Z., Wang, R., Koomen, J., Kobayashi, R., Khokhar, A.R., and Kuang, J. (2005). Induction of p21 by p53 following DNA damage inhibits both Cdk4 and Cdk2 activities. Oncogene *24*, 2929-2943.
146. He, W., Bennett, M.J., Luistro, L., Carvajal, D., Nevins, T., Smith, M., Tyagi, G., Cai, J., Wei, X., Lin, T.-A., et al. (2014). Discovery of siRNA Lipid Nanoparticles to Transfect Suspension Leukemia Cells and Provide In Vivo Delivery Capability. Molecular Therapy *22*, 359-370.
147. Heikaus, C.C., Pandit, J., and Klevit, R.E. (2009). Cyclic Nucleotide Binding GAF Domains from Phosphodiesterases: Structural and Mechanistic Insights. Structure *17*, 1551-1557.
148. Heikaus, C.C., Stout, J.R., Sekharan, M.R., Eakin, C.M., Rajagopal, P., Brzovic, P.S., Beavo, J.A., and Klevit, R.E. (2008). Solution structure of the cGMP binding GAF domain from phosphodiesterase 5: insights into nucleotide specificity, dimerization, and cGMP-dependent conformational change. The Journal of biological chemistry *283*, 22749-22759.
149. Hoang, Q.V., Linsenmeier, R.A., Chung, C.K., and Curcio, C.A. (2002). Photoreceptor inner segments in monkey and human retina: Mitochondrial density, optics, and regional variation. Visual Neuroscience *19*, 395-407.
150. Hochegger, H., Takeda, S., and Hunt, T. (2008). Cyclin-dependent kinases and cell-cycle transitions: does one fit all? Nat Rev Mol Cell Biol *9*, 910-916.
151. Hong, Y., Downey, T., Eu, K.W., Koh, P.K., and Cheah, P.Y. (2010). A 'metastasis-prone' signature for early-stage mismatch-repair proficient sporadic colorectal cancer patients and its implications for possible therapeutics. Clinical & Experimental Metastasis *27*, 83-90.
152. Hood, J., and Granger, H.J. (1998). Protein Kinase G Mediates Vascular Endothelial Growth Factor-induced Raf-1 Activation and Proliferation in Human Endothelial Cells. Journal of Biological Chemistry *273*, 23504-23508.
153. Horvath, P., and Barrangou, R. (2010). CRISPR/Cas, the Immune System of Bacteria and Archaea. Science *327*, 167-170.
154. Hosios, A.M., Hecht, V.C., Danai, L.V., Johnson, M.O., Rathmell, J.C.,

Steinhauser, M.L., Manalis, S.R., and Vander Heiden, M.G. (2016). Amino acids rather than glucose account for the majority of cell mass in proliferating mammalian cells. Developmental cell *36*, 540-549.
155. Hoxhaj, G., Hughes-Hallett, J., Timson, R.C., Ilagan, E., Yuan, M., Asara, J.M., Ben-Sahra, I., and Manning, B.D. (2017). The mTORC1 Signaling Network Senses Changes in Cellular Purine Nucleotide Levels. Cell Reports *21*, 1331-1346.
156. Hsiao, L.-L., Dangond, F., Yoshida, T., Hong, R., Jensen, R.V., Misra, J., Dillon, W., Lee, K.F., Clark, K.E., Haverty, P., et al. (2001). A compendium of gene expression in normal human tissues. Physiological Genomics *7*, 97-104.
157. Hsu, M.-C., and Hung, W.-C. (2018). Pyruvate kinase M2 fuels multiple aspects of cancer cells: from cellular metabolism, transcriptional regulation to extracellular signaling. Molecular Cancer *17*.
158. Hsu, P.P., and Sabatini, D.M. (2008). Cancer Cell Metabolism: Warburg and Beyond. Cell *134*, 703-707.
159. Hu, J.-w., Sun, P., Zhang, D.-x., Xiong, W.-j., and Mi, J. (2014). Hexokinase 2 regulates G1/S checkpoint through CDK2 in cancer-associated fibroblasts. Cellular Signalling *26*, 2210-2216.
160. Hu, W., Zhang, C., Wu, R., Sun, Y., Levine, A., and Feng, Z. (2010). Glutaminase 2, a novel p53 target gene regulating energy metabolism and antioxidant function. Proceedings of the National Academy of Sciences *107*, 7455-7460.
161. Hu, Y., Rosen, D.G., Zhou, Y., Feng, L., Yang, G., Liu, J., and Huang, P. (2005). Mitochondrial manganese-superoxide dismutase expression in ovarian cancer role in cell proliferation and response to oxidative stress. Journal of Biological Chemistry *280*, 39485-39492.
162. Huang, M., Itahana, K., Zhang, Y., and Mitchell, B.S. (2009). Depletion of Guanine Nucleotides Leads to the Mdm2-Dependent Proteasomal Degradation of Nucleostemin. Cancer Research *69*, 3004-3012.
163. Hui, S., Ghergurovich, J.M., Morscher, R.J., Jang, C., Teng, X., Lu, W., Esparza, L.A., Reya, T., Le, Z., Yanxiang Guo, J., et al. (2017). Glucose feeds the TCA cycle via circulating lactate. Nature *551*, 115-118.
164. Hulikova, A., Black, N., Hsia, L.-T., Wilding, J., Bodmer, W.F., and Swietach, P. (2016). Stromal uptake and transmission of acid is a pathway for venting cancer cell-generated acid. Proceedings of the National Academy of Sciences *113*, E5344-E5353.
165. Ischenko, I., Zhi, J., Hayman, M.J., and Petrenko, O. (2017). KRAS-dependent suppression of MYC enhances the sensitivity of cancer cells to cytotoxic agents. Oncotarget *8*.
166. Ishikawa, K., Takenaga, K., Akimoto, M., Koshikawa, N., Yamaguchi, A., Imanishi, H., Nakada, K., Honma, Y., and Hayashi, J.-I. (2008). ROS-generating mitochondrial DNA mutations can regulate tumor cell metastasis. Science *320*, 661-664.
167. Isidoro, A., Martínez, M., Fernández, P.L., Ortega, Á.D., Santamaría, G., Chamorro, M., and Cuezva, J.M. (2004). Alteration of the bioenergetic phenotype of mitochondria is a hallmark of breast, gastric, lung and oesophageal cancer. Biochemical Journal *378*, 17-20.
168. Israelsen, William J., Dayton, Talya L., Davidson, Shawn M., Fiske, Brian P., Hosios, Aaron M., Bellinger, G., Li, J., Yu, Y., Sasaki, M., Horner, James W., et al. (2013). PKM2 Isoform-Specific Deletion Reveals a Differential Requirement for Pyruvate Kinase in Tumor Cells. Cell *155*, 397-409.
169. Jackson, A.L. (2006). Position-specific chemical modification of siRNAs reduces

"off-target" transcript silencing. Rna *12*, 1197-1205.
170. Jackson, N.M., and Ceresa, B.P. (2016). Protein Kinase G facilitates EGFR-mediated cell death in MDA-MB-468 cells. Experimental Cell Research *346*, 224-232.
171. Jacobs, K.M., Bhave, S.R., Ferraro, D.J., Jaboin, J.J., Hallahan, D.E., and Thotala, D. (2012). GSK-3: A Bifunctional Role in Cell Death Pathways. International Journal of Cell Biology *2012*, 1-11.
172. Jia, W., Zhao, X., Zhao, L., Yan, H., Li, J., Yang, H., Huang, G., and Liu, J. (2018). Non-canonical roles of PFKFB3 in regulation of cell cycle through binding to CDK4. Oncogene.
173. Jiang, P., Du, W., and Wu, M. (2014). Regulation of the pentose phosphate pathway in cancer. Protein & Cell *5*, 592-602.
174. Jingwen, B., Yaochen, L., and Guojun, Z. (2017). Cell cycle regulation and anticancer drug discovery. Cancer Biology & Medicine *14*.
175. Jones, J. (2005). Gene Signatures of Progression and Metastasis in Renal Cell Cancer. Clinical Cancer Research *11*, 5730-5739.
176. Jones, R.G., and Thompson, C.B. (2009). Tumor suppressors and cell metabolism: a recipe for cancer growth. Genes Dev *23*, 537-548.
177. Joyal, J.-S., Sun, Y., Gantner, M.L., Shao, Z., Evans, L.P., Saba, N., Fredrick, T., Burnim, S., Kim, J.S., Patel, G., et al. (2016). Retinal lipid and glucose metabolism dictates angiogenesis through the lipid sensor Ffar1. Nature Medicine *22*, 439-445.
178. Kaiser, S., Park, Y.-K., Franklin, J.L., Halberg, R.B., Yu, M., Jessen, W.J., Freudenberg, J., Chen, X., Haigis, K., Jegga, A.G., et al. (2007). Transcriptional recapitulation and subversion of embryonic colon development by mouse colon tumor models and human colon cancer. Genome Biology *8*.
179. Kaminskyy, V.O., and Zhivotovsky, B. (2014). Free Radicals in Cross Talk Between Autophagy and Apoptosis. Antioxidants & Redox Signaling *21*, 86-102.
180. Kamphorst, J.J., Cross, J.R., Fan, J., de Stanchina, E., Mathew, R., White, E.P., Thompson, C.B., and Rabinowitz, J.D. (2013). Hypoxic and Ras-transformed cells support growth by scavenging unsaturated fatty acids from lysophospholipids. Proceedings of the National Academy of Sciences *110*, 8882-8887.
181. Kanehisa, M., and Goto, S. (2000). KEGG: kyoto encyclopedia of genes and genomes. Nucleic Acids Res *28*, 27-30.
182. Kanehisa, M., Goto, S., Sato, Y., Kawashima, M., Furumichi, M., and Tanabe, M. (2014). Data, information, knowledge and principle: back to metabolism in KEGG. Nucleic Acids Research *42*, D199-D205.
183. Kelly, C.J., Hussien, K., Fokas, E., Kannan, P., Shipley, R.J., Ashton, T.M., Stratford, M., Pearson, N., and Muschel, R.J. (2014). Regulation of O2 consumption by the PI3K and mTOR pathways contributes to tumor hypoxia. Radiotherapy and Oncology *111*, 72-80.
184. Kerr, E.M., and Martins, C.P. (2018). Metabolic rewiring in mutant Kras lung cancer. The FEBS Journal *285*, 28-41.
185. Khanin, R., Skrzypczak, M., Goryca, K., Rubel, T., Paziewska, A., Mikula, M., Jarosz, D., Pachlewski, J., Oledzki, J., and Ostrowsk, J. (2010). Modeling Oncogenic Signaling in Colon Tumors by Multidirectional Analyses of Microarray Data Directed for Maximization of Analytical Reliability. PLoS ONE *5*.
186. Kim, E.B., Fang, X., Fushan, A.A., Huang, Z., Lobanov, A.V., Han, L., Marino, S.M., Sun, X., Turanov, A.A., Yang, P., et al. (2011). Genome sequencing reveals insights into physiology and longevity of the naked mole rat. Nature *479*, 223-227.
187. Kim, J.-w., Gao, P., Liu, Y.-C., Semenza, G.L., and Dang, C.V. (2007). Hypoxia-

inducible factor 1 and dysregulated c-Myc cooperatively induce vascular endothelial growth factor and metabolic switches hexokinase 2 and pyruvate dehydrogenase kinase 1. Molecular and cellular biology *27*, 7381-7393.
188. Kim, J.-w., Tchernyshyov, I., Semenza, G.L., and Dang, C.V. (2006). HIF-1-mediated expression of pyruvate dehydrogenase kinase: a metabolic switch required for cellular adaptation to hypoxia. Cell metabolism *3*, 177-185.
189. Kimchi, E.T., Posner, M.C., Park, J.O., Darga, T.E., Kocherginsky, M., Karrison, T., Hart, J., Smith, K.D., Mezhir, J.J., Weichselbaum, R.R., et al. (2005). Progression of Barrett's Metaplasia to Adenocarcinoma Is Associated with the Suppression of the Transcriptional Programs of Epidermal Differentiation. Cancer Research *65*, 3146-3154.
190. Knox, B.E., and Solessio, E. (2006). Shedding Light On Cones. The Journal of General Physiology *127*, 355-358.
191. Korkola, J.E., Houldsworth, J., Chadalavada, R.S.V., Olshen, A.B., Dobrzynski, D., Reuter, V.E., Bosl, G.J., and Chaganti, R.S.K. (2006). Down-Regulation of Stem Cell Genes, Including Those in a 200-kb Gene Cluster at 12p13.31, Is Associated withIn vivoDifferentiation of Human Male Germ Cell Tumors. Cancer Research *66*, 820-827.
192. Koshiji, M., Kageyama, Y., Pete, E.A., Horikawa, I., Barrett, J.C., and Huang, L.E. (2004). HIF-1α induces cell cycle arrest by functionally counteracting Myc. The EMBO Journal *23*, 1949-1956.
193. Koukourakis, M.I., Giatromanolaki, A., Sivridis, E., Gatter, K.C., Harris, A.L., Tumor, and Angiogenesis Research, G. (2005). Pyruvate dehydrogenase and pyruvate dehydrogenase kinase expression in non small cell lung cancer and tumor-associated stroma. Neoplasia *7*, 1-6.
194. Kozhevnikova, O.S., Korbolina, E.E., Ershov, N.I., and Kolosova, N.G. (2014). Rat retinal transcriptome: Effects of aging and AMD-like retinopathy. Cell Cycle *12*, 1745-1761.
195. Kramer, R.H., and Molokanova, E. (2001). Modulation of cyclic-nucleotide-gated channels and regulation of vertebrate phototransduction. J Exp Biol *204*, 2921-2931.
196. Kroemer, G., and Pouyssegur, J. (2008). Tumor cell metabolism: cancer's Achilles' heel. Cancer cell *13*, 472-482.
197. Kumari, S., Badana, A.K., G, M.M., G, S., and Malla, R. (2018). Reactive Oxygen Species: A Key Constituent in Cancer Survival. Biomarker Insights *13*, 117727191875539.
198. Labuschagne, C.F., Zani, F., and Vousden, K.H. (2018). Control of metabolism by p53 – Cancer and beyond. Biochimica et Biophysica Acta (BBA) - Reviews on Cancer *1870*, 32-42.
199. Lagman, D., Franzén, I.E., Eggert, J., Larhammar, D., and Abalo, X.M. (2016). Evolution and expression of the phosphodiesterase 6 genes unveils vertebrate novelty to control photosensitivity. BMC Evolutionary Biology *16*.
200. Lane, A.N., and Fan, T.W.M. (2015). Regulation of mammalian nucleotide metabolism and biosynthesis. Nucleic Acids Research *43*, 2466-2485.
201. Lane, D.P. (1992). Cancer. p53, guardian of the genome. Nature *358*, 15-16.
202. Lange, C., Heynen, S.R., Tanimoto, N., Thiersch, M., Le, Y.-Z., Meneau, I., Seeliger, M.W., Samardzija, M., Caprara, C., and Grimm, C. (2011). Normoxic Activation of Hypoxia-Inducible Factors in Photoreceptors Provides Transient Protection against Light-Induced Retinal Degeneration. Investigative Opthalmology &

Visual Science *52*, 5872.
203. Lapenna, S., and Giordano, A. (2009). Cell cycle kinases as therapeutic targets for cancer. Nature reviews. Drug discovery *8*, 547-566.
204. Larsen, H.E., Bardsley, E.N., Lefkimmiatis, K., and Paterson, D.J. (2016). Dysregulation of Neuronal Ca 2+ Channel Linked to Heightened Sympathetic Phenotype in Prohypertensive States. The Journal of Neuroscience *36*, 8562-8573.
205. LaTulippe, E., Satagopan, J., Smith, A., Scher, H., Scardino, P., Reuter, V., and Gerald, W.L. (2002). Comprehensive gene expression analysis of prostate cancer reveals distinct transcriptional programs associated with metastatic disease. Cancer Res *62*, 4499-4506.
206. Lavoie, J.N., L'Allemain, G., Brunet, A., Müller, R., and Pouysségur, J. (1996). Cyclin D1 expression is regulated positively by the p42/p44MAPK and negatively by the p38/HOGMAPK pathway. J Biol Chem *271*, 20608-20616.
207. Lee, I.H., and Finkel, T. (2013). Metabolic regulation of the cell cycle. Current opinion in cell biology *25*, 724-729.
208. Lee, Y., Dominy, J.E., Choi, Y.J., Jurczak, M., Tolliday, N., Camporez, J.P., Chim, H., Lim, J.-H., Ruan, H.-B., Yang, X., et al. (2014). Cyclin D1–Cdk4 controls glucose metabolism independently of cell cycle progression. Nature *510*, 547-551.
209. Lefkimmiatis, K., Leronni, D., and Hofer, A.M. (2013). The inner and outer compartments of mitochondria are sites of distinct cAMP/PKA signaling dynamics. The Journal of Cell Biology *202*, 453-462.
210. Leuschner, P.J., Ameres, S.L., Kueng, S., and Martinez, J. (2006). Cleavage of the siRNA passenger strand during RISC assembly in human cells. EMBO Rep *7*, 314-320.
211. Li Chen, X., Huan Ren, K., He, H.-W., and Shao, R.-G. (2014). Involvement of PI3K/AKT/GSK3ÃŸ pathway in tetrandrine-induced G1 arrest and apoptosis. Cancer Biology & Therapy *7*, 1073-1078.
212. Li, D., Fu, Z., Chen, R., Zhao, X., Zhou, Y., Zeng, B., Yu, M., Zhou, Q., Lin, Q., Gao, W., et al. (2015). Inhibition of glutamine metabolism counteracts pancreatic cancer stem cell features and sensitizes cells to radiotherapy. Oncotarget *6*.
213. Li, M., and Zhang, P. (2009). The function of APC/CCdh1 in cell cycle and beyond. Cell division *4*, 2.
214. Li, X., Jiang, Y., Meisenhelder, J., Yang, W., Hawke, D.H., Zheng, Y., Xia, Y., Aldape, K., He, J., and Hunter, T. (2016). Mitochondria-translocated PGK1 functions as a protein kinase to coordinate glycolysis and the TCA cycle in tumorigenesis. Molecular cell *61*, 705-719.
215. Liou, G.-Y., and Storz, P. (2010). Reactive oxygen species in cancer. Free radical research *44*, 479-496.
216. Liu, D., Ceddia, R.P., and Collins, S. (2018). Cardiac natriuretic peptides promote adipose 'browning' through mTOR complex-1. Molecular Metabolism *9*, 192-198.
217. Liu, W., Hancock, C.N., Fischer, J.W., Harman, M., and Phang, J.M. (2015). Proline biosynthesis augments tumor cell growth and aerobic glycolysis: involvement of pyridine nucleotides. Scientific Reports *5*.
218. Liu, W., Le, A., Hancock, C., Lane, A.N., Dang, C.V., Fan, T.W.M., and Phang, J.M. (2012). Reprogramming of proline and glutamine metabolism contributes to the proliferative and metabolic responses regulated by oncogenic transcription factor c-MYC. Proceedings of the National Academy of Sciences *109*, 8983-8988.
219. Liu, W., and Phang, J.M. (2012). Proline dehydrogenase (oxidase) in cancer.

BioFactors *38*, 398-406.
220. Liu, X., Zhou, B., Xue, L., Shih, J., Tye, K., Qi, C., and Yen, Y. (2005). The ribonucleotide reductase subunit M2B subcellular localization and functional importance for DNA replication in physiological growth of KB cells. Biochemical Pharmacology *70*, 1288-1297.
221. Liu, Y., Borchert, G.L., Donald, S.P., Diwan, B.A., Anver, M., and Phang, J.M. (2009). Proline Oxidase Functions as a Mitochondrial Tumor Suppressor in Human Cancers. Cancer Research *69*, 6414-6422.
222. Luo, J.H., Yu, Y.P., Cieply, K., Lin, F., Deflavia, P., Dhir, R., Finkelstein, S., Michalopoulos, G., and Becich, M. (2002). Gene expression analysis of prostate cancers. Mol Carcinog *33*, 25-35.
223. Ma, E.Y., Lewis, A., Barabas, P., Stearns, G., Suzuki, S., Krizaj, D., and Brockerhoff, S.E. (2013). Loss of Pde6 reduces cell body Ca2+ transients within photoreceptors. Cell Death and Disease *4*, e797.
224. Ma, X., Wang, L., Huang, D., Li, Y., Yang, D., Li, T., Li, F., Sun, L., Wei, H., He, K., et al. (2017). Polo-like kinase 1 coordinates biosynthesis during cell cycle progression by directly activating pentose phosphate pathway. Nature Communications *8*.
225. Madhok, B.M., Yeluri, S., Perry, S.L., Hughes, T.A., and Jayne, D.G. (2010). Dichloroacetate induces apoptosis and cell-cycle arrest in colorectal cancer cells. British Journal of Cancer *102*, 1746-1752.
226. Manchado, E., Guillamot, M., and Malumbres, M. (2012). Killing cells by targeting mitosis. Cell Death & Differentiation *19*, 369-377.
227. Martinez-Outschoorn, U.E., Pestell, R.G., Howell, A., Tykocinski, M.L., Nagajyothi, F., Machado, F.S., Tanowitz, H.B., Sotgia, F., and Lisanti, M.P. (2014). Energy transfer in "parasitic" cancer metabolism. Cell Cycle *10*, 4208-4216.
228. Mashima, T., Seimiya, H., and Tsuruo, T. (2009). De novo fatty-acid synthesis and related pathways as molecular targets for cancer therapy. British Journal of Cancer *100*, 1369-1372.
229. Matoba, S., Kang, J.-G., Patino, W.D., Wragg, A., Boehm, M., Gavrilova, O., Hurley, P.J., Bunz, F., and Hwang, P.M. (2006). p53 regulates mitochondrial respiration. Science *312*, 1650-1653.
230. McIntyre, A., Patiar, S., Wigfield, S., Li, J.l., Ledaki, I., Turley, H., Leek, R., Snell, C., Gatter, K., Sly, W.S., et al. (2012). Carbonic Anhydrase IX Promotes Tumor Growth and Necrosis In Vivo and Inhibition Enhances Anti-VEGF Therapy. Clinical Cancer Research *18*, 3100-3111.
231. Meister, G., and Tuschl, T. (2004). Mechanisms of gene silencing by double-stranded RNA. Nature *431*, 343-349.
232. Menendez, J.A., and Lupu, R. (2007). Fatty acid synthase and the lipogenic phenotype in cancer pathogenesis. Nature Reviews Cancer *7*, 763-777.
233. Milani, P., Gagliardi, S., Cova, E., and Cereda, C. (2011). SOD1 Transcriptional and Posttranscriptional Regulation and Its Potential Implications in ALS. Neurology Research International *2011*, 1-9.
234. Minutoli, L., Puzzolo, D., Rinaldi, M., Irrera, N., Marini, H., Arcoraci, V., Bitto, A., Crea, G., Pisani, A., Squadrito, F., et al. (2016). ROS-Mediated NLRP3 Inflammasome Activation in Brain, Heart, Kidney, and Testis Ischemia/Reperfusion Injury. Oxidative Medicine and Cellular Longevity *2016*, 1-10.
235. Mitsuishi, Y., Motohashi, H., and Yamamoto, M. (2012). The Keap1–Nrf2 system in cancers: stress response and anabolic metabolism. Frontiers in Oncology *2*.

236. Miyaoka, Y., Berman, J.R., Cooper, S.B., Mayerl, S.J., Chan, A.H., Zhang, B., Karlin-Neumann, G.A., and Conklin, B.R. (2016). Systematic quantification of HDR and NHEJ reveals effects of locus, nuclease, and cell type on genome-editing. Sci Rep *6*, 23549.
237. Montal, Emily D., Dewi, R., Bhalla, K., Ou, L., Hwang, Bor J., Ropell, Ashley E., Gordon, C., Liu, W.-J., DeBerardinis, Ralph J., Sudderth, J., et al. (2015). PEPCK Coordinates the Regulation of Central Carbon Metabolism to Promote Cancer Cell Growth. Molecular Cell *60*, 571-583.
238. Monterisi, S., Lobo, M.J., Livie, C., Castle, J.C., Weinberger, M., Baillie, G., Surdo, N.C., Musheshe, N., Stangherlin, A., Gottlieb, E., et al. (2017). PDE2A2 regulates mitochondria morphology and apoptotic cell death via local modulation of cAMP/PKA signalling. eLife *6*.
239. Moreno, P., Jiménez-Jiménez, C., Garrido-Rodríguez, M., Calderón-Santiago, M., Molina, S., Lara-Chica, M., Priego-Capote, F., Salvatierra, Á., Muñoz, E., and Calzado, M.A. (2018). Metabolomic profiling of human lung tumor tissues: nucleotide metabolism as a candidate for therapeutic interventions and biomarkers. Molecular Oncology.
240. Morita, H., Murata, T., Shimizu, K., Okumura, K., Inui, M., and Tagawa, T. (2013). Characterization of phosphodiesterase 2A in human malignant melanoma PMP cells. Oncology Reports *29*, 1275-1284.
241. Muir, A., Danai, L.V., Gui, D.Y., Waingarten, C.Y., Lewis, C.A., and Vander Heiden, M.G. (2017). Environmental cystine drives glutamine anaplerosis and sensitizes cancer cells to glutaminase inhibition. Elife *6*, e27713.
242. Mukherji, M., Bell, R., Supekova, L., Wang, Y., Orth, A.P., Batalov, S., Miraglia, L., Huesken, D., Lange, J., Martin, C., et al. (2006). Genome-wide functional analysis of human cell-cycle regulators. Proceedings of the National Academy of Sciences of the United States of America *103*, 14819-14824.
243. Mullershausen, F., Russwurm, M., Thompson, W.J., Liu, L., Koesling, D., and Friebe, A. (2001). Rapid nitric oxide–induced desensitization of the cGMP response is caused by increased activity of phosphodiesterase type 5 paralleled by phosphorylation of the enzyme. The Journal of Cell Biology *155*, 271-278.
244. Murata, D. (2004). A Crucial Role of Uridine/Cytidine Kinase 2 in Antitumor Activity of 3'-Ethynyl Nucleosides. Drug Metabolism and Disposition *32*, 1178-1182.
245. Nakakuki, M., Shimano, H., Inoue, N., Tamura, M., Matsuzaka, T., Nakagawa, Y., Yahagi, N., Toyoshima, H., Sato, R., and Yamada, N. (2007). A transcription factor of lipid synthesis, sterol regulatory element-binding protein (SREBP)-1a causes G1 cell-cycle arrest after accumulation of cyclin-dependent kinase (cdk) inhibitors. FEBS Journal *274*, 4440-4452.
246. Natarajan, S.K., Zhu, W., Liang, X., Zhang, L., Demers, A.J., Zimmerman, M.C., Simpson, M.A., and Becker, D.F. (2012). Proline dehydrogenase is essential for proline protection against hydrogen peroxide-induced cell death. Free Radical Biology and Medicine *53*, 1181-1191.
247. Nayak, G., and Cooper, G.M. (2012). p53 is a major component of the transcriptional and apoptotic program regulated by PI 3-kinase/Akt/GSK3 signaling. Cell Death & Disease *3*, e400-e400.
248. Ng, S.K., Wood, J.P.M., Chidlow, G., Han, G., Kittipassorn, T., Peet, D.J., and Casson, R.J. (2015). Cancer-like metabolism of the mammalian retina. Clinical & Experimental Ophthalmology *43*, 367-376.
249. Nigg, E.A. (1995). Cyclin-dependent protein kinases: key regulators of the

eukaryotic cell cycle. Bioessays *17*, 471-480.
250. Norberg, E., Karlsson, M., Korenovska, O., Szydlowski, S., Silberberg, G., Uhlén, P., Orrenius, S., and Zhivotovsky, B. (2010). Critical role for hyperpolarization-activated cyclic nucleotide-gated channel 2 in the AIF-mediated apoptosis. The EMBO Journal *29*, 3869-3878.
251. Novellasdemunt, L., Antas, P., and Li, V.S.W. (2015). Targeting Wnt signaling in colorectal cancer. A Review in the Theme: Cell Signaling: Proteins, Pathways and Mechanisms. American Journal of Physiology-Cell Physiology *309*, C511-C521.
252. Obach, M., Navarro-Sabaté, À., Caro, J., Kong, X., Duran, J., Gómez, M., Perales, J.C., Ventura, F., Rosa, J.L., and Bartrons, R. (2004). 6-Phosphofructo-2-kinase (pfkfb3) gene promoter contains hypoxia-inducible factor-1 binding sites necessary for transactivation in response to hypoxia. Journal of Biological Chemistry *279*, 53562-53570.
253. Okajima, M., Kokura, S., Ishikawa, T., Mizushima, K., Tsuchiya, R., Matsuyama, T., Adachi, S., Okayama, T., Sakamoto, N., Kamada, K., et al. (2013). Anoxia/reoxygenation induces epithelial-mesenchymal transition in human colon cancer cell lines. Oncology Reports *29*, 2311-2317.
254. Okamoto, A., Sumi, C., Tanaka, H., Kusunoki, M., Iwai, T., Nishi, K., Matsuo, Y., Harada, H., Takenaga, K., Bono, H., et al. (2017). HIF-1-mediated suppression of mitochondria electron transport chain function confers resistance to lidocaine-induced cell death. Sci Rep *7*, 3816.
255. Oldenburg, O., Qin, Q., Krieg, T., Yang, X.-M., Philipp, S., Critz, S.D., Cohen, M.V., and Downey, J.M. (2004). Bradykinin induces mitochondrial ROS generation via NO, cGMP, PKG, and mitoKATP channel opening and leads to cardioprotection. American Journal of Physiology-Heart and Circulatory Physiology *286*, H468-H476.
256. Owusu-Ansah, E., Yavari, A., Mandal, S., and Banerjee, U. (2008). Distinct mitochondrial retrograde signals control the G1-S cell cycle checkpoint. Nature Genetics *40*, 356-361.
257. Pacilli, A., Calienni, M., Margarucci, S., D'Apolito, M., Petillo, O., Rocchi, L., Pasquinelli, G., Nicolai, R., Koverech, A., Calvani, M., et al. (2013). Carnitine-Acyltransferase System Inhibition, Cancer Cell Death, and Prevention of Myc-Induced Lymphomagenesis. JNCI: Journal of the National Cancer Institute *105*, 489-498.
258. Park, M., Sandner, P., and Krieg, T. (2018). cGMP at the centre of attention: emerging strategies for activating the cardioprotective PKG pathway. Basic Research in Cardiology *113*.
259. Patsoukis, N., Li, L., Sari, D., Petkova, V., and Boussiotis, V.A. (2013). PD-1 Increases PTEN Phosphatase Activity While Decreasing PTEN Protein Stability by Inhibiting Casein Kinase 2. Molecular and Cellular Biology *33*, 3091-3098.
260. Perou, C.M., Jeffrey, S.S., van de Rijn, M., Rees, C.A., Eisen, M.B., Ross, D.T., Pergamenschikov, A., Williams, C.F., Zhu, S.X., Lee, J.C., et al. (1999). Distinctive gene expression patterns in human mammary epithelial cells and breast cancers. Proceedings of the National Academy of Sciences of the United States of America *96*, 9212-9217.
261. Pezuk, J.A., Brassesco, M.S., Morales, A.G., de Oliveira, J.C., de Paula Queiroz, R.G., Machado, H.R., Carlotti, C.G., Neder, L., Scrideli, C.A., and Tone, L.G. (2013). Polo-like kinase 1 inhibition causes decreased proliferation by cell cycle arrest, leading to cell death in glioblastoma. Cancer Gene Therapy *20*, 499-506.
262. Phang, J.M., Liu, W., Hancock, C., and Christian, K.J. (2012). The Proline Regulatory Axis and Cancer. Frontiers in Oncology *2*.

263. Piazza, K.L.A.G. (2016). The interaction between the Wnt/β-catenin signaling cascade and PKG activation in cancer. Journal of Biomedical Research *31*, 189-196.
264. Pomeroy, S.L., Tamayo, P., Gaasenbeek, M., Sturla, L.M., Angelo, M., McLaughlin, M.E., Kim, J.Y.H., Goumnerova, L.C., Black, P.M., Lau, C., et al. (2002). Prediction of central nervous system embryonal tumour outcome based on gene expression. Nature *415*, 436-442.
265. Porporato, P.E., Filigheddu, N., Pedro, J.M.B.-S., Kroemer, G., and Galluzzi, L. (2017). Mitochondrial metabolism and cancer. Cell Research *28*, 265-280.
266. Pozarowski, P., and Darzynkiewicz, Z. (2004). Analysis of Cell Cycle by Flow Cytometry. In Checkpoint Controls and Cancer, pp. 301-312.
267. Prior, I.A., Lewis, P.D., and Mattos, C. (2012). A comprehensive survey of Ras mutations in cancer. Cancer research *72*, 2457-2467.
268. Qi, X.F., Zheng, L., Lee, K.J., Kim, D.H., Kim, C.S., Cai, D.Q., Wu, Z., Qin, J.W., Yu, Y.H., and Kim, S.K. (2013). HMG-CoA reductase inhibitors induce apoptosis of lymphoma cells by promoting ROS generation and regulating Akt, Erk and p38 signals via suppression of mevalonate pathway. Cell Death & Disease *4*, e518-e518.
269. Qi, Y., Tu, Y., Yang, D., Chen, Q., Xiao, J., Chen, Y., Fu, J., Xiao, X., and Zhou, Z. (2007). Cyclin a but not cyclin D1 is essential for c-myc-modulated cell-cycle progression. Journal of Cellular Physiology *210*, 63-71.
270. Quade, B.J., Wang, T.-Y., Sornberger, K., Cin, P.D., Mutter, G.L., and Morton, C.C. (2004). Molecular pathogenesis of uterine smooth muscle tumors from transcriptional profiling. Genes, Chromosomes and Cancer *40*, 97-108.
271. Qureshi, B.M., Schmidt, A., Behrmann, E., Bürger, J., Mielke, T., Spahn, C.M.T., Heck, M., and Scheerer, P. (2018). Mechanistic insights into the role of prenyl-binding protein PrBP/δ in membrane dissociation of phosphodiesterase 6. Nature Communications *9*.
272. Radvanyi, L., Singh-Sandhu, D., Gallichan, S., Lovitt, C., Pedyczak, A., Mallo, G., Gish, K., Kwok, K., Hanna, W., Zubovits, J., et al. (2005). The gene associated with trichorhinophalangeal syndrome in humans is overexpressed in breast cancer. Proceedings of the National Academy of Sciences *102*, 11005-11010.
273. Rajala, R.V.S., Rajala, A., Kooker, C., Wang, Y., and Anderson, R.E. (2016). The Warburg Effect Mediator Pyruvate Kinase M2 Expression and Regulation in the Retina. Scientific Reports *6*.
274. Ramaswamy, S., Tamayo, P., Rifkin, R., Mukherjee, S., Yeang, C.H., Angelo, M., Ladd, C., Reich, M., Latulippe, E., Mesirov, J.P., et al. (2001). Multiclass cancer diagnosis using tumor gene expression signatures. Proceedings of the National Academy of Sciences *98*, 15149-15154.
275. Ran, F.A., Hsu, Patrick D., Lin, C.-Y., Gootenberg, Jonathan S., Konermann, S., Trevino, A.E., Scott, David A., Inoue, A., Matoba, S., Zhang, Y., et al. (2013a). Double Nicking by RNA-Guided CRISPR Cas9 for Enhanced Genome Editing Specificity. Cell *154*, 1380-1389.
276. Ran, F.A., Hsu, P.D., Wright, J., Agarwala, V., Scott, D.A., and Zhang, F. (2013b). Genome engineering using the CRISPR-Cas9 system. Nature Protocols *8*, 2281-2308.
277. Ranek, M.J., Kokkonen-Simon, K.M., Chen, A., Dunkerly-Eyring, B.L., Vera, M.P., Oeing, C.U., Patel, C.H., Nakamura, T., Zhu, G., Bedja, D., et al. (2019). PKG1-modified TSC2 regulates mTORC1 activity to counter adverse cardiac stress. Nature *566*, 264-269.
278. Raspé, E., Coulonval, K., Pita, J.M., Paternot, S., Rothé, F., Twyffels, L.,

Brohée, S., Craciun, L., Larsimont, D., Kruys, V., et al. (2017). CDK4 phosphorylation status and a linked gene expression profile predict sensitivity to palbociclib. EMBO Molecular Medicine *9*, 1052-1066.
279. Ravi Hingorani, J.D., Jeanne Elia, Catherine McIntyre, and Dev Mittar (2011). Detection of Apoptosis Using the BD Annexin V FITC Assay on the BD FACSVerseTM System. (BD Biosciences).
280. Reynolds, A. (2006). Induction of the interferon response by siRNA is cell type- and duplex length-dependent. Rna *12*, 988-993.
281. Rhodes, D.R., Yu, J., Shanker, K., Deshpande, N., Varambally, R., Ghosh, D., Barrette, T., Pandey, A., and Chinnaiyan, A.M. (2004). ONCOMINE: a cancer microarray database and integrated data-mining platform. Neoplasia *6*, 1-6.
282. Riker, A.I., Enkemann, S.A., Fodstad, O., Liu, S., Ren, S., Morris, C., Xi, Y., Howell, P., Metge, B., Samant, R.S., et al. (2008). The gene expression profiles of primary and metastatic melanoma yields a transition point of tumor progression and metastasis. BMC Medical Genomics *1*.
283. Roci, I., Watrous, J.D., Lagerborg, K.A., Lafranchi, L., Lindqvist, A., Jain, M., and Nilsson, R. (2019). Mapping Metabolic Events in the Cancer Cell Cycle Reveals Arginine Catabolism in the Committed SG2M Phase. Cell reports *26*, 1691-1700. e1695.
284. Romero, R., Sayin, V.I., Davidson, S.M., Bauer, M.R., Singh, S.X., LeBoeuf, S.E., Karakousi, T.R., Ellis, D.C., Bhutkar, A., Sánchez-Rivera, F.J., et al. (2017). Keap1 loss promotes Kras-driven lung cancer and results in dependence on glutaminolysis. Nature Medicine.
285. Rooney, J.P., Ryde, I.T., Sanders, L.H., Howlett, E.H., Colton, M.D., Germ, K.E., Mayer, G.D., Greenamyre, J.T., and Meyer, J.N. (2015). PCR Based Determination of Mitochondrial DNA Copy Number in Multiple Species. *1241*, 23-38.
286. Rosario, F.J., Gupta, M.B., Myatt, L., Powell, T.L., Glenn, J.P., Cox, L., and Jansson, T. (2019). Mechanistic Target of Rapamycin Complex 1 Promotes the Expression of Genes Encoding Electron Transport Chain Proteins and Stimulates Oxidative Phosphorylation in Primary Human Trophoblast Cells by Regulating Mitochondrial Biogenesis. Sci Rep *9*, 246.
287. Rose, M.G., Farrell, M.P., and Schmitz, J.C. (2002). Thymidylate Synthase: A Critical Target for Cancer Chemotherapy. Clinical Colorectal Cancer *1*, 220-229.
288. Roth, R. (2007). Human body index - transcriptional profiling.
289. Roth, R.B., Hevezi, P., Lee, J., Willhite, D., Lechner, S.M., Foster, A.C., and Zlotnik, A. (2006). Gene expression analyses reveal molecular relationships among 20 regions of the human CNS. Neurogenetics *7*, 67-80.
290. Rothenberg, S.M., Mohapatra, G., Rivera, M.N., Winokur, D., Greninger, P., Nitta, M., Sadow, P.M., Sooriyakumar, G., Brannigan, B.W., Ulman, M.J., et al. (2010). A Genome-Wide Screen for Microdeletions Reveals Disruption of Polarity Complex Genes in Diverse Human Cancers. Cancer Research *70*, 2158-2164.
291. Roy, S.K., Srivastava, R.K., and Shankar, S. (2010). Inhibition of PI3K/AKT and MAPK/ERK pathways causes activation of FOXO transcription factor, leading to cell cycle arrest and apoptosis in pancreatic cancer. Journal of Molecular Signaling *5*, 10.
292. Sabates-Bellver, J., Van der Flier, L.G., de Palo, M., Cattaneo, E., Maake, C., Rehrauer, H., Laczko, E., Kurowski, M.A., Bujnicki, J.M., Menigatti, M., et al. (2007). Transcriptome Profile of Human Colorectal Adenomas. Molecular Cancer Research *5*, 1263-1275.
293. Sakaue-Sawano, A., Kurokawa, H., Morimura, T., Hanyu, A., Hama, H., Osawa,

H., Kashiwagi, S., Fukami, K., Miyata, T., Miyoshi, H., et al. (2008). Visualizing Spatiotemporal Dynamics of Multicellular Cell-Cycle Progression. Cell *132*, 487-498.
294. Sancak, Y., Bar-Peled, L., Zoncu, R., Markhard, A.L., Nada, S., and Sabatini, D.M. (2010). Ragulator-Rag Complex Targets mTORC1 to the Lysosomal Surface and Is Necessary for Its Activation by Amino Acids. Cell *141*, 290-303.
295. Sanchez-Macedo, N., Feng, J., Faubert, B., Chang, N., Elia, A., Rushing, E.J., Tsuchihara, K., Bungard, D., Berger, S.L., Jones, R.G., et al. (2013). Depletion of the novel p53-target gene carnitine palmitoyltransferase 1C delays tumor growth in the neurofibromatosis type I tumor model. Cell Death & Differentiation *20*, 659-668.
296. Sang, N., Stiehl, D.P., Bohensky, J., Leshchinsky, I., Srinivas, V., and Caro, J. (2003). MAPK signaling up-regulates the activity of hypoxia-inducible factors by its effects on p300. Journal of Biological chemistry *278*, 14013-14019.
297. Santamaría, D., Barrière, C., Cerqueira, A., Hunt, S., Tardy, C., Newton, K., Cáceres, J.F., Dubus, P., Malumbres, M., and Barbacid, M. (2007). Cdk1 is sufficient to drive the mammalian cell cycle. Nature *448*, 811.
298. Satomura, A., Nishioka, R., Mori, H., Sato, K., Kuroda, K., and Ueda, M. (2017). Precise genome-wide base editing by the CRISPR Nickase system in yeast. Sci Rep *7*, 2095.
299. Savai, R., Pullamsetti, S.S., Banat, G.-A., Weissmann, N., Ghofrani, H.A., Grimminger, F., and Schermuly, R.T. (2009). Targeting cancer with phosphodiesterase inhibitors. Expert Opinion on Investigational Drugs *19*, 117-131.
300. Schieke, S.M., Phillips, D., McCoy, J.P., Aponte, A.M., Shen, R.-F., Balaban, R.S., and Finkel, T. (2006). The Mammalian Target of Rapamycin (mTOR) Pathway Regulates Mitochondrial Oxygen Consumption and Oxidative Capacity. Journal of Biological Chemistry *281*, 27643-27652.
301. Schmaltz, C., Hardenbergh, P.H., Wells, A., and Fisher, D.E. (1998). Regulation of Proliferation-Survival Decisions during Tumor Cell Hypoxia. Molecular and Cellular Biology *18*, 2845-2854.
302. Schoors, S., Bruning, U., Missiaen, R., Queiroz, K.C.S., Borgers, G., Elia, I., Zecchin, A., Cantelmo, A.R., Christen, S., Goveia, J., et al. (2015). Fatty acid carbon is essential for dNTP synthesis in endothelial cells. Nature *520*, 192-197.
303. Schwartzenberg-Bar-Yoseph, F., Armoni, M., and Karnieli, E. (2004). The tumor suppressor p53 down-regulates glucose transporters GLUT1 and GLUT4 gene expression. Cancer research *64*, 2627-2633.
304. Schwoch, G., Trinczek, B., and Bode, C. (1990). Localization of catalytic and regulatory subunits of cyclic AMP-dependent protein kinases in mitochondria from various rat tissues. Biochemical Journal *270*, 181-188.
305. Sciacovelli, M., Gonçalves, E., Johnson, T.I., Zecchini, V.R., da Costa, A.S.H., Gaude, E., Drubbel, A.V., Theobald, S.J., Abbo, S.R., Tran, M.G.B., et al. (2016). Fumarate is an epigenetic modifier that elicits epithelial-to-mesenchymal transition. Nature *537*, 544-547.
306. Semenza, G.L. (2009). Defining the role of hypoxia-inducible factor 1 in cancer biology and therapeutics. Oncogene *29*, 625-634.
307. Seya, K., Motomura, S., and Furukawa, K.-I. (2007). Cardiac mitochondrial cGMP stimulates cytochromecrelease. Clinical Science *112*, 113-121.
308. Seya, K., Ono, K., Fujisawa, S., Okumura, K., Motomura, S., and Furukawa, K.I. (2012). Cytosolic Ca2+-Induced Apoptosis in Rat Cardiomyocytes via Mitochondrial NO-cGMP-Protein Kinase G Pathway. Journal of Pharmacology and Experimental Therapeutics *344*, 77-84.

309. Shai, R., Shi, T., Kremen, T.J., Horvath, S., Liau, L.M., Cloughesy, T.F., Mischel, P.S., and Nelson, S.F. (2003). Gene expression profiling identifies molecular subtypes of gliomas. Oncogene *22*, 4918-4923.
310. Shinde, V. (2015). The unfolded protein response and calcium dysregulation in autosomal dominant retinitis pigmentosa animal models. (The University of Alabama at Birmingham).
311. Shyamsundar, R., Kim, Y.H., Higgins, J.P., Montgomery, K., Jorden, M., Sethuraman, A., van de Rijn, M., Botstein, D., Brown, P.O., and Pollack, J.R. (2005a). Genome Biology *6*.
312. Shyamsundar, R., Kim, Y.H., Higgins, J.P., Montgomery, K., Jorden, M., Sethuraman, A., van de Rijn, M., Botstein, D., Brown, P.O., and Pollack, J.R. (2005b). Genome Biology *6*, R22.
313. Sivaprasad, S., and Arden, G. (2015). Spare the rods and spoil the retina: revisited. Eye *30*, 189-192.
314. Slepak, V.Z., Artemyev, N.O., Zhu, Y., Dumke, C.L., Sabacan, L., Sondek, J., Hamm, H.E., Bownds, M.D., and Arshavsky, V.Y. (1995). An Effector Site That Stimulates G-protein GTPase in Photoreceptors. Journal of Biological Chemistry *270*, 14319-14324.
315. Sokolova, M., Turunen, M., Mortusewicz, O., Kivioja, T., Herr, P., Vähärautio, A., Björklund, M., Taipale, M., Helleday, T., and Taipale, J. (2016). Genome-wide screen of cell-cycle regulators in normal and tumor cells identifies a differential response to nucleosome depletion. Cell Cycle *16*, 189-199.
316. Soliman, G.A. (2011). The integral role of mTOR in lipid metabolism. Cell Cycle *10*, 861-862.
317. Son, J., Lyssiotis, C.A., Ying, H., Wang, X., Hua, S., Ligorio, M., Perera, R.M., Ferrone, C.R., Mullarky, E., and Shyh-Chang, N. (2013). Glutamine supports pancreatic cancer growth through a KRAS-regulated metabolic pathway. Nature *496*, 101.
318. Spellman, P.T., Sherlock, G., Zhang, M.Q., Iyer, V.R., Anders, K., Eisen, M.B., Brown, P.O., Botstein, D., and Futcher, B. (1998). Comprehensive identification of cell cycle-regulated genes of the yeast Saccharomyces cerevisiae by microarray hybridization. Mol Biol Cell *9*, 3273-3297.
319. Sperger, J.M., Chen, X., Draper, J.S., Antosiewicz, J.E., Chon, C.H., Jones, S.B., Brooks, J.D., Andrews, P.W., Brown, P.O., and Thomson, J.A. (2003). Gene expression patterns in human embryonic stem cells and human pluripotent germ cell tumors. Proceedings of the National Academy of Sciences *100*, 13350-13355.
320. Stefanova, N., Kozhevnikova, O., Vitovtov, A., Maksimova, K., Logvinov, S., Rudnitskaya, E., Korbolina, E., Muraleva, N., and Kolosova, N. (2014). Senescence-accelerated OXYS rats: A model of age-related cognitive decline with relevance to abnormalities in Alzheimer disease. Cell Cycle *13*, 898-909.
321. Stegmaier, K., Ross, K.N., Colavito, S.A., O'Malley, S., Stockwell, B.R., and Golub, T.R. (2004). Gene expression–based high-throughput screening(GE-HTS) and application to leukemia differentiation. Nature Genetics *36*, 257-263.
322. Su, A.I., Cooke, M.P., Ching, K.A., Hakak, Y., Walker, J.R., Wiltshire, T., Orth, A.P., Vega, R.G., Sapinoso, L.M., Moqrich, A., et al. (2002). Large-scale analysis of the human and mouse transcriptomes. Proceedings of the National Academy of Sciences *99*, 4465-4470.
323. Su, A.I., Wiltshire, T., Batalov, S., Lapp, H., Ching, K.A., Block, D., Zhang, J., Soden, R., Hayakawa, M., Kreiman, G., et al. (2004). A gene atlas of the mouse and

human protein-encoding transcriptomes. Proceedings of the National Academy of Sciences *101*, 6062-6067.
324. Sullivan, Lucas B., Martinez-Garcia, E., Nguyen, H., Mullen, Andrew R., Dufour, E., Sudarshan, S., Licht, Jonathan D., Deberardinis, Ralph J., and Chandel, Navdeep S. (2013). The Proto-oncometabolite Fumarate Binds Glutathione to Amplify ROS-Dependent Signaling. Molecular Cell *51*, 236-248.
325. Swain, J.E., Ding, J., Brautigan, D.L., Villa-Moruzzi, E., and Smith, G.D. (2007). Proper Chromatin Condensation and Maintenance of Histone H3 Phosphorylation During Mouse Oocyte Meiosis Requires Protein Phosphatase Activity1. Biology of Reproduction *76*, 628-638.
326. Sznarkowska, A., Kostecka, A., Meller, K., and Bielawski, K.P. (2016). Inhibition of cancer antioxidant defense by natural compounds. Oncotarget *8*.
327. Sørlie, T., Tibshirani, R., Parker, J., Hastie, T., Marron, J.S., Nobel, A., Deng, S., Johnsen, H., Pesich, R., Geisler, S., et al. (2003). Repeated observation of breast tumor subtypes in independent gene expression data sets. Proceedings of the National Academy of Sciences *100*, 8418-8423.
328. Tajan, M., Hock, A.K., Blagih, J., Robertson, N.A., Labuschagne, C.F., Kruiswijk, F., Humpton, T.J., Adams, P.D., and Vousden, K.H. (2018). A role for p53 in the adaptation to glutamine starvation through the expression of SLC1A3. Cell metabolism *28*, 721-736. e726.
329. Talantov, D. (2005). Novel Genes Associated with Malignant Melanoma but not Benign Melanocytic Lesions. Clinical Cancer Research *11*, 7234-7242.
330. Tan, Z., Luo, X., Xiao, L., Tang, M., Bode, A.M., Dong, Z., and Cao, Y. (2016). The Role of PGC1 in Cancer Metabolism and its Therapeutic Implications. Molecular Cancer Therapeutics *15*, 774-782.
331. Tang, G. (2005). siRNA and miRNA: an insight into RISCs. Trends in Biochemical Sciences *30*, 106-114.
332. Taniguchi, Y., Tonai-Kachi, H., and Shinjo, K. (2006). Zaprinast, a well-known cyclic guanosine monophosphate-specific phosphodiesterase inhibitor, is an agonist for GPR35. FEBS Letters *580*, 5003-5008.
333. Thompson, S.L., and Compton, D.A. (2008). Examining the link between chromosomal instability and aneuploidy in human cells. The Journal of Cell Biology *180*, 665-672.
334. Tirosh, A., Shai, I., Tekes-Manova, D., Israeli, E., Pereg, D., Shochat, T., Kochba, I., and Rudich, A. (2005). Normal Fasting Plasma Glucose Levels and Type 2 Diabetes in Young Men. New England Journal of Medicine *353*, 1454-1462.
335. Tiwari, S., Blount, M., Smith, C., Shakur, Y., Degerman, E., Pyne, N., Murray, F., Tate, R., Zhang, H.T., O'Donnell, J., Zhang, K., Wang, H., Tilley, D., Corbin, J., Bolger, G., Cote, R., Davies, S., Bender, A., Martinez, S., Manganiello, V., Conti, M., Kotera, J., Ke, H., Bessay, E., Michaeli, T., Day, J., Jin, S., Holst, L., Epperson, S., Brunton, L., Aandahl, E., Abi-Gerges, A., Castro, L., Favot, L., Lugnier, C., Maurice, D., Jeon, K.I., Movsesian, M., Nagel, D., Seebeck, T., Zoraghi, R., Vasta, V., Omori, K., Strick, C., Wentzinger, L., Richter, W., Zhao, A., Witczak, O., Tasken, K., Rochais, F., Vandecasteele, G., Silva, A., Yan, C., MacLean, M., Kruuse, C., Lerner, A., Moon, E.Y., Kambayashi, J., Liu, Y., Giembycz, M., McKenna, J., Menniti, F., Fischmeister, R., Keravis, T., Muller, G., Schmidt, C. (2007). Cyclic Nucleotide Phosphodiesterases in Health and Disease. (Boca Raton: CRC Press.).
336. Tu, B.P., and McKnight, S.L. (2007). The Yeast Metabolic Cycle: Insights into the Life of a Eukaryotic Cell. Cold Spring Harbor Symposia on Quantitative Biology *72*,

339-343.
337. Tudzarova, S., Colombo, S.L., Stoeber, K., Carcamo, S., Williams, G.H., and Moncada, S. (2011). Two ubiquitin ligases, APC/C-Cdh1 and SKP1-CUL1-F (SCF)-beta-TrCP, sequentially regulate glycolysis during the cell cycle. Proceedings of the National Academy of Sciences of the United States of America *108*, 5278-5283.
338. Turashvili, G., Bouchal, J., Baumforth, K., Wei, W., Dziechciarkova, M., Ehrmann, J., Klein, J., Fridman, E., Skarda, J., Srovnal, J., et al. (2007). Novel markers for differentiation of lobular and ductal invasive breast carcinomas by laser microdissection and microarray analysis. BMC Cancer *7*.
339. Turner, N.C., Slamon, D.J., Ro, J., Bondarenko, I., Im, S.-A., Masuda, N., Colleoni, M., DeMichele, A., Loi, S., and Verma, S. (2018). Overall survival with palbociclib and fulvestrant in advanced breast cancer. New England Journal of Medicine *379*, 1926-1936.
340. Valente, L.J., Gray, D.H., Michalak, E.M., Pinon-Hofbauer, J., Egle, A., Scott, C.L., Janic, A., and Strasser, A. (2013). p53 efficiently suppresses tumor development in the complete absence of its cell-cycle inhibitory and proapoptotic effectors p21, Puma, and Noxa. Cell Rep *3*, 1339-1345.
341. Vander Heiden, M.G., Cantley, L.C., and Thompson, C.B. (2009). Understanding the Warburg Effect: The Metabolic Requirements of Cell Proliferation. Science *324*, 1029-1033.
342. Vander Heiden, M.G., and DeBerardinis, R.J. (2017). Understanding the Intersections between Metabolism and Cancer Biology. Cell *168*, 657-669.
343. Vassilev, L.T., Tovar, C., Chen, S., Knezevic, D., Zhao, X., Sun, H., Heimbrook, D.C., and Chen, L. (2006). Selective small-molecule inhibitor reveals critical mitotic functions of human CDK1. Proceedings of the National Academy of Sciences of the United States of America *103*, 10660-10665.
344. Vazquez, F., Lim, J.-H., Chim, H., Bhalla, K., Girnun, G., Pierce, K., Clish, C.B., Granter, S.R., Widlund, H.R., and Spiegelman, B.M. (2013). PGC1α expression defines a subset of human melanoma tumors with increased mitochondrial capacity and resistance to oxidative stress. Cancer cell *23*, 287-301.
345. Velappan, Y., Signorelli, S., and Considine, M.J. (2017). Cell cycle arrest in plants: what distinguishes quiescence, dormancy and differentiated G1? Annals of Botany *120*, 495-509.
346. Veleri, S., Lazar, C.H., Chang, B., Sieving, P.A., Banin, E., and Swaroop, A. (2015). Biology and therapy of inherited retinal degenerative disease: insights from mouse models. Disease Models & Mechanisms *8*, 109-129.
347. Verbon, E.H., Post, J.A., and Boonstra, J. (2012). The influence of reactive oxygen species on cell cycle progression in mammalian cells. Gene *511*, 1-6.
348. Villunger, A., Kurosu, T., Nagao, T., Wu, N., Oshikawa, G., and Miura, O. (2013). Inhibition of the PI3K/Akt/GSK3 Pathway Downstream of BCR/ABL, Jak2-V617F, or FLT3-ITD Downregulates DNA Damage-Induced Chk1 Activation as Well as G2/M Arrest and Prominently Enhances Induction of Apoptosis. PLoS ONE *8*.
349. Vincent, Emma E., Sergushichev, A., Griss, T., Gingras, M.-C., Samborska, B., Ntimbane, T., Coelho, Paula P., Blagih, J., Raissi, Thomas C., Choinière, L., et al. (2015). Mitochondrial Phosphoenolpyruvate Carboxykinase Regulates Metabolic Adaptation and Enables Glucose-Independent Tumor Growth. Molecular Cell *60*, 195-207.
350. Visintin, R., Prinz, S., and Amon, A. (1997). CDC20 and CDH1: a family of substrate-specific activators of APC-dependent proteolysis. Science *278*, 460-463.

351. Vizán, P., Alcarraz-Vizán, G., Díaz-Moralli, S., Solovjeva, O.N., Frederiks, W.M., and Cascante, M. (2009a). Modulation of pentose phosphate pathway during cell cycle progression in human colon adenocarcinoma cell line HT29. International Journal of Cancer *124*, 2789-2796.
352. Vizán, P., Alcarraz-Vizán, G., Díaz-Moralli, S., Solovjeva, O.N., Frederiks, W.M., and Cascante, M. (2009b). Modulation of pentose phosphate pathway during cell cycle progression in human colon adenocarcinoma cell line HT29. International journal of cancer *124*, 2789-2796.
353. Vogel, A., Kasper, S., Weichert, W., Bitzer, M., Block, A., Riess, H., Schulze-Bergkamen, H., Moehler, M.H., Merx, K.E., and Endris, V. (2015). Panitumumab in combination with gemcitabine/cisplatin (GemCis) for patients with advanced kRAS WT biliary tract cancer: A randomized phase II trial of the Arbeitsgemeinschaft Internistische Onkologie (AIO). (American Society of Clinical Oncology).
354. W. Thompson, J., V. Narayanan, S., and A. Perez-Pinzon, M. (2012). Redox Signaling Pathways Involved in Neuronal Ischemic Preconditioning. Current Neuropharmacology *10*, 354-369.
355. Wallace, D.C. (2012). Mitochondria and cancer. Nature Reviews Cancer *12*, 685-698.
356. Wang, H., Nicolay, B.N., Chick, J.M., Gao, X., Geng, Y., Ren, H., Gao, H., Yang, G., Williams, J.A., Suski, J.M., et al. (2017). The metabolic function of cyclin D3–CDK6 kinase in cancer cell survival. Nature *546*, 426-430.
357. Wang, H., Yang, H., Shivalila, C.S., Dawlaty, M.M., Cheng, A.W., Zhang, F., and Jaenisch, R. (2013). One-Step Generation of Mice Carrying Mutations in Multiple Genes by CRISPR/Cas-Mediated Genome Engineering. Cell *153*, 910-918.
358. Wang, L., Li, J.-j., Guo, L.-y., Li, P., Zhao, Z., Zhou, H., and Di, L.-j. (2018). Molecular link between glucose and glutamine consumption in cancer cells mediated by CtBP and SIRT4. Oncogenesis *7*.
359. Wang, L., Zhou, H., Wang, Y., Cui, G., and Di, L.j. (2015a). CtBP maintains cancer cell growth and metabolic homeostasis via regulating SIRT4. Cell Death & Disease *6*, e1620-e1620.
360. Wang, S., Birol, G., Budzynski, E., Flynn, R., and Linsenmeier, R.A. (2010). Metabolic Responses to Light in Monkey Photoreceptors. Current Eye Research *35*, 510-518.
361. Wang, W., Heideman, L., Chung, C.S., Pelling, J.C., Koehler, K.J., and Birt, D.F. (2000). Cell-cycle arrest at G2/M and growth inhibition by apigenin in human colon carcinoma cell lines. Mol Carcinog *28*, 102-110.
362. Wang, X., Liu, H., Zhang, X., Li, X., Gu, H., Zhang, H., and Fan, R. (2015b). G6PD downregulation triggered growth inhibition and induced apoptosis by regulating STAT3 signaling pathway in esophageal squamous cell carcinoma. Tumor Biology *37*, 781-789.
363. Watanabe, K., Shibuya, S., Koyama, H., Ozawa, Y., Toda, T., Yokote, K., and Shimizu, T. (2013). Sod1 Loss Induces Intrinsic Superoxide Accumulation Leading to p53-Mediated Growth Arrest and Apoptosis. International Journal of Molecular Sciences *14*, 10998-11010.
364. Weinberg, F., Hamanaka, R., Wheaton, W.W., Weinberg, S., Joseph, J., Lopez, M., Kalyanaraman, B., Mutlu, G.M., Budinger, G.R.S., and Chandel, N.S. (2010). Mitochondrial metabolism and ROS generation are essential for Kras-mediated tumorigenicity. Proceedings of the National Academy of Sciences *107*, 8788-8793.
365. Welsh, J.B., Sapinoso, L.M., Su, A.I., Kern, S.G., Wang-Rodriguez, J.,

Moskaluk, C.A., Frierson, H.F., Jr., and Hampton, G.M. (2001). Analysis of gene expression identifies candidate markers and pharmacological targets in prostate cancer. Cancer Res *61*, 5974-5978.
366. Wen, Y.-A., Xiong, X., Zaytseva, Y.Y., Napier, D.L., Vallee, E., Li, A.T., Wang, C., Weiss, H.L., Evers, B.M., and Gao, T. (2018). Downregulation of SREBP inhibits tumor growth and initiation by altering cellular metabolism in colon cancer. Cell Death & Disease *9*.
367. Wheaton, W.W., Weinberg, S.E., Hamanaka, R.B., Soberanes, S., Sullivan, L.B., Anso, E., Glasauer, A., Dufour, E., Mutlu, G.M., and Budigner, G.R.S. (2014). Metformin inhibits mitochondrial complex I of cancer cells to reduce tumorigenesis. elife *3*, e02242.
368. Wibberley, A., Nunn, P.A., Naylor, A.M., and Ramage, A.G. (2002). An investigation of the effects of zaprinast, a PDE inhibitor, on the nitrergic control of the urethra in anaesthetized female rats. British Journal of Pharmacology *136*, 399-414.
369. Winter, S.C., Buffa, F.M., Silva, P., Miller, C., Valentine, H.R., Turley, H., Shah, K.A., Cox, G.J., Corbridge, R.J., Homer, J.J., et al. (2007). Relation of a Hypoxia Metagene Derived from Head and Neck Cancer to Prognosis of Multiple Cancers. Cancer Research *67*, 3441-3449.
370. Wise, D.R., DeBerardinis, R.J., Mancuso, A., Sayed, N., Zhang, X.Y., Pfeiffer, H.K., Nissim, I., Daikhin, E., Yudkoff, M., McMahon, S.B., et al. (2008). Myc regulates a transcriptional program that stimulates mitochondrial glutaminolysis and leads to glutamine addiction. Proceedings of the National Academy of Sciences *105*, 18782-18787.
371. Wyant, G.A., Abu-Remaileh, M., Wolfson, R.L., Chen, W.W., Freinkman, E., Danai, L.V., Vander Heiden, M.G., and Sabatini, D.M. (2017). mTORC1 activator SLC38A9 is required to efflux essential amino acids from lysosomes and use protein as a nutrient. Cell *171*, 642-654. e612.
372. Xu, X.L., Singh, H.P., Wang, L., Qi, D.-L., Poulos, B.K., Abramson, D.H., Jhanwar, S.C., and Cobrinik, D. (2014). Rb suppresses human cone-precursor-derived retinoblastoma tumours. Nature *514*, 385-388.
373. Yalcin, A., Clem, B.F., Imbert-Fernandez, Y., Ozcan, S.C., Peker, S., O'Neal, J., Klarer, A.C., Clem, A.L., Telang, S., and Chesney, J. (2014). 6-Phosphofructo-2-kinase (PFKFB3) promotes cell cycle progression and suppresses apoptosis via Cdk1-mediated phosphorylation of p27. Cell Death & Disease *5*, e1337-e1337.
374. Yang, H., Wang, H., Shivalila, Chikdu S., Cheng, Albert W., Shi, L., and Jaenisch, R. (2013). One-Step Generation of Mice Carrying Reporter and Conditional Alleles by CRISPR/Cas-Mediated Genome Engineering. Cell *154*, 1370-1379.
375. Yang, Z., Guo, F., Albers, A.E., Sehouli, J., and Kaufmann, A.M. (2019). Disulfiram modulates ROS accumulation and overcomes synergistically cisplatin resistance in breast cancer cell lines. Biomedicine & Pharmacotherapy *113*, 108727.
376. Yarla, N.S., Gali, H., Pathuri, G., Smriti, S., Farooqui, M., Panneerselvam, J., Kumar, G., Madka, V., and Rao, C.V. (2019). Targeting the paracrine hormone-dependent guanylate cyclase/cGMP/phosphodiesterases signaling pathway for colorectal cancer prevention. Seminars in Cancer Biology *56*, 168-174.
377. Ye, J., Coulouris, G., Zaretskaya, I., Cutcutache, I., Rozen, S., and Madden, T.L. (2012). Primer-BLAST: A tool to design target-specific primers for polymerase chain reaction. BMC Bioinformatics *13*.
378. Yeung, S.J., Pan, J., and Lee, M.H. (2008). Roles of p53, Myc and HIF-1 in Regulating Glycolysis — the Seventh Hallmark of Cancer. Cellular and Molecular Life

Sciences *65*, 3981-3999.
379. Yoshihara, K., Tajima, A., Komata, D., Yamamoto, T., Kodama, S., Fujiwara, H., Suzuki, M., Onishi, Y., Hatae, M., Sueyoshi, K., et al. (2009). Gene expression profiling of advanced-stage serous ovarian cancers distinguishes novel subclasses and implicatesZEB2in tumor progression and prognosis. Cancer Science *100*, 1421-1428.
380. Younes, M., Brown, R.W., Stephenson, M., Gondo, M., and Cagle, P.T. (1997). Overexpression of glut1 and glut3 in stage I nonsmall cell lung carcinoma is Associated with poor survival. Cancer *80*, 1046-1051.
381. Young, C.D., and Anderson, S.M. (2008). Sugar and fat – that's where it's at: metabolic changes in tumors. Breast Cancer Research *10*.
382. Zaccolo, M. (2002). Discrete Microdomains with High Concentration of cAMP in Stimulated Rat Neonatal Cardiac Myocytes. Science *295*, 1711-1715.
383. Zamore, P.D., and Aronin, N. (2003). siRNAs knock down hepatitis. Nat Med *9*, 266-267.
384. Zaragoza, C., Soria, E., Lopez, E., Browning, D., Balbin, M., Lopez-Otin, C., and Lamas, S. (2002). Activation of the mitogen activated protein kinase extracellular signal-regulated kinase 1 and 2 by the nitric oxide-cGMP-cGMP-dependent protein kinase axis regulates the expression of matrix metalloproteinase 13 in vascular endothelial cells. Mol Pharmacol *62*, 927-935.
385. Zawacka-Pankau, J., Grinkevich, V.V., Hünten, S., Nikulenkov, F., Gluch, A., Li, H., Enge, M., Kel, A., and Selivanova, G. (2011). Inhibition of Glycolytic Enzymes Mediated by Pharmacologically Activated p53. Journal of Biological Chemistry *286*, 41600-41615.
386. Zerbino, D.R., Achuthan, P., Akanni, W., Amode, M R., Barrell, D., Bhai, J., Billis, K., Cummins, C., Gall, A., Girón, C.G., et al. (2018). Ensembl 2018. Nucleic Acids Research *46*, D754-D761.
387. Zhang, F. (2017). Target Sequence Cloning Protocol.
388. Zhang, J.H. (1999). A Simple Statistical Parameter for Use in Evaluation and Validation of High Throughput Screening Assays. Journal of Biomolecular Screening *4*, 67-73.
389. Zhang, Y., Unnikrishnan, A., Deepa, S.S., Liu, Y., Li, Y., Ikeno, Y., Sosnowska, D., Van Remmen, H., and Richardson, A. (2017). A new role for oxidative stress in aging: The accelerated aging phenotype in Sod1−/ − mice is correlated to increased cellular senescence. Redox Biology *11*, 30-37.
390. Zippin, J.H., Chen, Y., Nahirney, P., Kamenetsky, M., Wuttke, M.S., Fischman, D.A., Levin, L.R., and Buck, J. (2003). Compartmentalization of bicarbonate-sensitive adenylyl cyclase in distinct signaling microdomains. The FASEB Journal *17*, 82-84.